UNIVERSIDADE D
COIMBRA

Elisa Cristina Marçalo Brás

Jet-cooled and matrix-isolated radicals: monitoring reactions and interactions through IR spectroscopy

Tese no âmbito do Doutoramento em Química, Ramo de Espectroscopia Molecular, orientada pelo Professor Doutor Rui Fausto Martins Ribeiro da Silva Lourenço, pelo Professor Doutor Martin Andreas Suhm, pela Professora Doutora Maria de Lurdes dos Santos Cristiano e apresentada ao Departamento de Química da Faculdade de Ciências e Tecnologia da Universidade de Coimbra.

Novembro de 2023

Jet-Cooled and Matrix-Isolated Radicals: Monitoring Interactions and Reactions through IR Spectroscopy

Elisa Cristina Marçalo Brás

Tese no âmbito do Doutoramento em Química, Ramo de Espectroscopia Molecular, orientada pelo Professor Doutor Rui Fausto Martins Ribeiro da Silva Lourenço, pelo Professor Doutor Martin Andreas Suhm, pela Professora Doutora Maria de Lurdes dos Santos Cristiano e apresentada ao Departamento de Química da Faculdade de Ciências e Tecnologia da Universidade de Coimbra.

Novembro 2023

UNIVERSIDADE D
COIMBRA

Acknowledgements

This work would not have been accomplished without the support and encouragement of many dedicated people. Therefore, I would like to express my deepest gratitude to all of them.

First, I would like to express my sincere gratitude to my PhD advisors for their invaluable contribution throughout this academic journey. I would like to thank Professor Rui Fausto for sharing his extensive academic knowledge, for giving me the freedom to develop my own research work, and for the opportunities provided. I would like to thank Professor Martin Suhm for his invaluable guidance, dedication, and for the provided opportunity to join the Suhm group at the University of Göttingen. I am truly grateful for this experience, which pushed me beyond my comfort zone and rewarded me with many opportunities for both professional and personal growth. I would like to thank Professor Maria de Lurdes Cristiano for always being available for scientific discussions, for providing me support and for encouraging me throughout this journey.

I extend my heartfelt gratitude to Professor Christopher Brett for motivating me throughout my entire academic journey, and for the given opportunity to represent the doctoral students.

I am very grateful to Professor Peter R. Schreiner for hosting me during a research stay at the University of Giessen, and Dr. Artur Mardyukov for introducing me the flash vacuum pyrolysis technique, and for the friendly welcome. I am also thankful to Dr. Igor Reva for the extraordinary opportunity to participate in this bilateral cooperation project with Germany.

Furthermore, I would like to thank Professor Manabu Abe (Hiroshima University) for the collaboration and valuable contribution to the work presented herein.

I would like to thank all the members of the Suhm and Zeuch groups for their extraordinary support during and after my research stay in Göttingen, for the collaborative work atmosphere, for making me feel so welcome and for all the board game nights. A very special thanks go to Dr. Taija L. Fischer and Dr. Charlotte Zimmermann for the collaborative teamwork, for their precious help with the jet measurements and for sharing their talents. I also want to thank Mrs. Petra Lawecki, for the warm reception and kindness, and for aiding me with bureaucratic paperwork.

I also want to thank Dr. Patrícia Amado, from the Organic Chemistry and Reactivity group of the University of Algarve, for the fruitful collaboration and for her significant contribution to the success of this work.

Another very special thanks go to all the LMCB group colleagues José Roque, Dr. Lícinia Justino, Dr. Cláudio Nunes, Dr. Bernardo Nogueira, Dr. Susy Lopes, and Dr. Timur Nikitin for all the provided support throughout these years, for their friendship and for all they taught me. I've had the privilege to work closely with many talented researchers who have strongly influenced and inspired me.

I extend my deepest gratitude to Dr. Sérgio Domingos for the incredible opportunity to join the FTMW spectroscopy group, and for the chance to contribute to the fascinating research field of molecular switches, even before completing the doctoral degree.

For the financial support, I would like to thank the Portuguese Foundation for Science and Technology (FCT) for the PhD grant (SFRH/BD/136246/2018), which enabled this work to be accomplished. I am also thankful for the financial support of both FCT and German Academic Exchange Service (Deutscher Akademischer Austauschdienst, DAAD), which funded the bilateral project "Exploring Competitive Heavy-Atom Tunneling Reactions using experiment and Theory", carried out at both University of Coimbra and University of Giessen. I also would like to acknowledge the Associate Laboratory CCMar, funded by FCT through projects UIDB/04326/2020, UIDP/04326/2020, and LA/P/0101/2020.

I am also very grateful to the IYCN IUPAC for allowing me to join the conference presence committee and to participate actively in several activities. It is a privilege to work with like-minded people towards a greener world by raising awareness and motivating people towards sustainability.

Among the most remarkable highlights of this journey was the opportunity to move to Göttingen, where I met wonderful people inside and outside the University, who have helped me in so many ways. Thus, I would like to express my gratitude to those who crossed my path and enriched my life, especially to Maximilian Dörrier for his support and patience.

Foremost, I could not be more grateful to my parents and sister for all the unconditional support throughout my life and for always being there for me. I am also very grateful to my friends who were always there for the highs and lows of this journey.

I am deeply thankful to all, and I am eager to see what the future holds.

“Denke nicht in Problemen. Denke in Lösungen.”

J. W. von Goethe

Contents

Abstract

Free radicals and radical-complexes are common intermediates in a wide range of chemical processes. With at least one unpaired electron, these species are typically more reactive than closed-shell molecules, and thus, their detection and characterisation are not always straightforward due to their short lifetimes. Nowadays, these typically short-lived species can be investigated immediately after their formation, in general in short time frames, or otherwise, be trapped under special environment conditions that allow a more detailed insight into their structures using spectroscopic tools. Experimental techniques such as low-temperature matrix isolation and supersonic jet expansions coupled with infrared spectroscopy presented in this Thesis, afford favourable conditions for the direct detection and characterisation of those species, and have provided many contributions to the development of several fields, such as mechanistic chemistry.

For the interpretation of these experimental results, there is a greater dependence on accurate quantum predictions of the vibrational spectra of the molecular species, and quantum chemical predictions can be notoriously more complicated for radicals due to their electronic structure, than for closed-shell molecules.

The work presented in this Thesis focuses on the investigations of the interactions between radicals and small solvent molecules, and photoinduced generation of radical species through suitable precursors, processes that were monitored by infrared spectroscopy and quantum chemical calculations. Chapter 1 details the motivation towards the investigation of radical species and radical-complexes with both matrix isolation and jet-FTIR spectroscopies, along with the Thesis outline.

Chapter 2 highlights matrix isolation and supersonic expansions approaches, with their advantages and limitations to study radical species, and the conditions required to prepare jet-cooled and matrix isolated radicals through photolysis or pyrolysis of suitable precursors. Furthermore, several investigations about radicals using those techniques are also addressed. The experimental results and discussions are described in the following Chapters.

Chapter 3 presents a detailed description of the jet and matrix isolation set-ups used in this work. The features of the new gas-recycling jet FTIR spectroscopy setup, abbreviated as gratin-jet (from gas-recycling atom-economic infrared spectroscopy), and the filet-jet with a fine but lengthy slit nozzle, are highlighted, as well as the cryostat used for matrix isolation experiments. Moreover, the quantum chemical calculations performed on the chemical systems investigated within the scope of this Thesis are also described, including the gold-standard method DLPNO-CCSD(T), to benchmark density functional theory methods and to decompose the interaction energy of radical-complexes through the LED (Local Energy Decomposition) analysis in the DLPNO-CCSD(T) framework.

Chapter 4 highlights the first detection of an organic radical microhydrate complex in vacuum isolation by FTIR supersonic jet spectroscopy and the extension of the investigations to other radical complexes with OH-containing solvents. The 2,2,6,6-tetramethylpiperidinyloxyl (TEMPO) radical monohydrate shows a rich conformational and coupling dynamics, which is significantly reduced upon isotopic substitution of the solvent molecule. Moreover, the metastability of the TEMPO radical is demonstrated through its detection with a gas recycling infrared setup and even under several hours of humid gas conditions. Di-tert-butylnitroxide (DTBN) and TEMPO microsolvates with one or two molecules of water, methanol, *t*-butyl alcohol, or phenol were also detected. Systematic conformational preferences were observed, depending on the conformational flexibility of the nitroxide. These IR data were collected into an experimental benchmark data set and the performance of DFT methods for the calculation of their gas-phase IR spectra was tested. The investigations on nitroxide radical water complexes were extended to matrix isolation FTIR spectroscopy, which provided complementary results to those previously obtained.

Chapter 5 focuses on the photolysis and pyrolysis of 2,2'-dipyrydyldisulfide (1), as a source of pyridyl-2-thiyl radicals (2). UV-light irradiations of matrix-isolated (1) in Ar led to the homolytic cleavage of the disulfide bond into radical pairs that have shown to survive in the matrix environment without recombining. Further matrix annealing and O_2-doping experiments supported the generation of (2), as the radical species recombine to reform 1 upon matrices warming, and pyridyl-2-thiyl peroxy were successfully identified in the IR spectrum.

Chapter 6 highlights the photochemistry of a matrix-isolated endoperoxide with the trioxolane moiety. The detection of triplet diradical species (identified as peroxy diradicals) by EPR spectroscopy supported a mechanistic route previously proposed.

Resumo

Radicais livres e complexos de radicais são intermediários numa vasta gama de reações químicas. Com pelo menos um electrão desemparelhado, estas espécies são, geralmente, mais reativas do que moléculas de camada fechada e, consequentemente, a sua detecção e caracterização nem sempre é feita de forma direta, devido ao curto tempo de vida. Atualmente, existem técnicas que permitem a investigação destas espécies imediatamente após a sua formação, nomeadamente técnicas resolvidas no tempo. Em alternativa, podem ser estudadas sob determinadas condições experimentais de temperatura e pressão, que permitem o seu isolamento e o estudo detalhado através de métodos espectroscópicos. Técnicas experimentais como a espectroscopia de infravermelho com isolamento em matrizes criogénicas e a espectroscopia de jatos supersónicos fornecem condições favoráveis para a detecção direta e caracterização de radicais e têm permitido a elucidação de um grande número de mecanismos de reacções químicas.

Por outro lado, espécies de camada aberta, cujas previsões de química quântica são notoriamente mais complicadas, têm sido menos estudadas do que espécies de camada fechada. Desta forma, existe maior necessidade em explorar métodos computacionais que reproduzam de forma satisfatória a informação espectral destes sistemas.

O trabalho apresentado nesta Tese centra-se no estudo das interacções entre radicais e pequenas moléculas de solvente que contém o grupo OH e da sua geração fotoinduzida através de moléculas precursoras, processos monitorizados por espectroscopia de infravermelho e cálculos mecânico-quânticos. O Capítulo 1 apresenta a motivação do trabalho descrito nesta dissertação acerca do estudo de radicais e de complexos de radicais através das técnicas de espectroscopia de infravermelho com isolamento em matrizes criogénicas e de espectroscopia de jatos.

No Capítulo 2 são apresentadas as técnicas experimentais, as suas vantagens e limitações no estudo de radicais e é feita uma apresentação de investigações precedentes.

No Capítulo 3 é feita uma descrição detalhada dos equipamentos. São destacadas as características da nova instrumentação de espectroscopia de jatos *gratin-jet* (do Inglês,

gas-recycling atom-economic infrared spectroscopy), nomeadamente a possibilidade da reciclagem de gás, e da instrumentação *filet-jet* mais comumente usada (do Inglês, fine but lengthy slit nozzle), bem como do criostato usado para as experiências de isolamento em matriz. Para além disso, é também feita uma descrição dos métodos mecânico-quânticos selecionados para este estudo, incluindo o método DLPNO-CCSD(T), usado para avaliar métodos de teoria do funcional de densidade e também para a avaliação e decomposição das energias de interacção dos fragmentos dos complexos, através da análise de LED (do Inglês, Local Energy Decomposition).

No capítulo 4 são apresentados os resultados da detecção de microsolvatos de radicais em vácuo através da técnica de espectroscopia de infravermelho de jatos. Os resultados revelam que o monohidrato de radical TEMPO (do Inglês, 2,2,6,6-tetramethylpiperidinyloxyl) exibe dinâmicas conformacional e de acoplamento complexas que são significativamente reduzidas após a substituição isotópica da molécula do solvente. Adicionalmente, a sua metaestabilidade é demonstrada pela detecção através do equipamento de gás reciclável. As investigações estenderam-se ao estudo de hidratos de DTBN (do Inglês, di-*tert*-butyl nitroxide) e de solvatos de metanol, *terc*-butanol, e fenol, detectados e caracterizados através de espectroscopia de jatos supersónicos. Através deste estudo, foram observadas preferências conformacionais sistemáticas em função da flexibilidade conformacional do radical nitróxido. Estes resultados foram utilizados para testar a capacidade dos métodos DFT em reproduzir os valores experimentais. Para além disso, investigações complementares sobre complexos radicais nitróxidos de água foram realizadas através da espectroscopia FTIR de isolamento de matrizes.

O Capítulo 5 é focado na fotólise e pirólise de 2,2'-dipiridildissulfeto (1) isolado em matrizes, como precursor de radicais (2). Irradiações na região do UV induziram a clivagem homolítica da ligação dissulfeto e a subsequente formação de pares de radicais (2), posteriormente estabilizados em ambiente criogénico. O aumento da temperatura, bem como a realização de experiências com matrizes de nitrogénio dopadas com oxigénio molecular, sustentaram a formação de radicais (2) através da fotólise do precursor (1), uma vez que os radicais recombinam para reformar (1) após o aumento da temperatura e reagem com o oxigénio molecular para formar novas espécies.

No Capítulo 6 são apresentados os resultados das experiências de isolamento em matriz sobre a reactividade foto-induzida de um endoperóxido. A detecção de espécies dirradicalares no estado tripleto através da espectroscopia de EPR suportaram o mecanismo de reacção anteriormente proposto para a espécie em estudo.

Chapter 1

Introduction

Radicals are common intermediates in a wide range of chemical reactions[1–3] and thus have spurred a lot of interest and investigations throughout the years since their discovery in 1900. Afterwards, a new type of chemistry emerged, no longer constrained by the valency rules – the chemistry of free radicals.[4] Because radicals are open-shell species with one or more unpaired electrons they tend to react very fast – but there are exceptions to the rules. According to Ingold's classification based on their lifetimes, radicals can be defined as transient or persistent[5]. While transient radicals are typically short-lived and exist during typically milliseconds (or less), persistent radicals have usually a longer half-life. The term persistent has been proposed to be used for the description of a radical with a lifetime substantially greater than methyl radical under the same environmental conditions.

Nitroxide radicals are among the most prominent class of radicals bearing the "persistent" and "stable" features and are the most employed class of such type of radicals in organic synthesis.[6–8] These features are based on thermodynamic effects and kinetic stabilization due to steric hindrance promoted by the presence of bulky substituents.[9] Furthermore, the electronic stabilization in nitroxide is a consequence of the overlap of the p orbitals of oxygen and nitrogen atoms of the N-O bond, leading to the delocalization of the unpaired electron through resonance (see Figure 1).

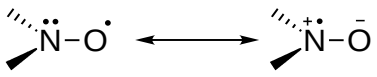

Figure 1. Resonance structures of the nitroxide radical.

TEMPO radical [(2,2,6,6-Tetramethylpiperidin-1-yl)oxyl] is the best known example of nitroxide radicals, as it can have an endless lifetime if kept under appropriate conditions, due to the kinetic stabilization provided by shielding methyl groups at the nitrogen-bound -carbon atoms that prevent its dimerisation.[9] With an exceptional persistency, and at the same time with an open-shell electronic configuration and an odd number of valence electrons, TEMPO has found many diverse applications, for example as catalyst for the oxidation of alcohols[10,11], radical-mediated polymerization reactions,[12] in radical-radical coupling reactions[8], and as a spin-trapping agent of transient radicals.[13,14] While used as catalyst in chemical reactions or with another purpose in solution, nitroxide radicals may form hydrogen-bonded complexes with small solvent molecules, such as water, through coordination with the N-O$^{\bullet}$ moiety. This interaction between radicals and solvent molecules may eventually influence the electronic structures and modulate their reactivity.[2,15,16] Indeed, open-shell radical species are capable to form hydrogen bonds,[17][18][19][20–23] and many chemical processes are controlled by coordination with small molecules, including several processes in the in Earth's Atmosphere[1][24]. Despite of its importance in several processes, the topic of weakly bound complexes involving radical open-shell species is still underexplored. Structural studies in the gas phase are scarce, thus providing challenges for the present knowledge of hydrogen bonding. Such lack of data relates with the need of low-temperatures or time resolved techniques to capture radicals because they are often highly reactive and consequently, short-lived species. The inherent challenges associated with the theoretical treatment of complexes involving radical species (and open-shell species in general) also represents another drawback. To give a contribution to this field, this work aims at exploring the microsolvation processes in nitroxides with OH-containing solvents at low temperatures. Due to the above referred stability and persistency, TEMPO radical has been selected as suitable reference system for these ground-breaking investigations on radical microsolvates through FTIR jet spectroscopy,[25,26] in combination with another well-suited technique to study small clusters: matrix isolation FTIR spectroscopy.

In a jet expansion, a gas mixture is cooled down by its expansion from a high-pressure region through a small orifice into *vacuum*. Within this environment, the molecular clusters formed within the expansion are isolated in the gas phase and complex thermal motion effects are largely avoided. Thus, the advantage in relation to the gas phase spectroscopy is that the attained conditions closely resemble the conditions of theoretical calculations performed at 0 K in *vacuum*. Consequently, jet spectroscopy is the preferred technique for clusters preparation, and it is suitable for benchmarking purposes, while matrix isolation does not serve so well for benchmarking gas phase calculations. This is a consequence of the environment perturbation in matrix isolation that leads to the shifting of the vibrational bands of the matrix isolated guest species in relation to the

spectra of the isolated molecules in the gas phase. Although the initial investigations on cluster isomerism started in inert solutions and inert matrices, it was later, with jet spectroscopy, that their rovibrational dynamics has been disclosed. Such investigations are pivotal to an in-depth understanding of condensed phases.

Nevertheless, radical species formed under jet expansion conditions are often prone to react due to collisions with other molecules at the initial stage of the expansion, and thus their lifetimes in the expansion can limit the amount of available time for their detection or detailed spectroscopic characterisation. In this regard, matrix isolation technique is far more effective for investigations on metastable complexes[27] and reactive species such as transient radicals[28–35] allowing their trapping in a solid inert environment, without the requirement of long slit jet nozzles or pulsed operations.[36–38] In fact, one of the main intentions of matrix isolation invention was to capture and stabilise free radicals.[39–44]

In this investigation, water, and water isotopologues were the first chosen solvent molecules for the investigation of open-shell radical complexes under jet expansion conditions. The selection of water was triggered by several aspects, including the water polarity, ability to form hydrogen bonds, and by the noteworthy behaviour of TEMPO radical in aqueous solution. A suitable reference system to aid the interpretation of the vibrational spectra of the open-shell TEMPO is the closed-shell ketone analogue 2,2,6,6-tetramethylcyclohexanone (TEMCO). In comparison to closed-shell molecules, investigations on radicals are quite more challenging, regarding both experimentation and theory, as it will be shown later in this Thesis, where the complexity of the spectra of TEMPO hydrates in relation to TEMCO will be highlighted.[25,26] In addition to the investigations on hydrate complexes, the investigated non-radical molecules has been extended to a series of alcohols, including methanol, *t*-butanol, and phenol, and another nitroxide, di-*tert*-butyl-nitroxide (DTBN) as depicted in Figure 2.

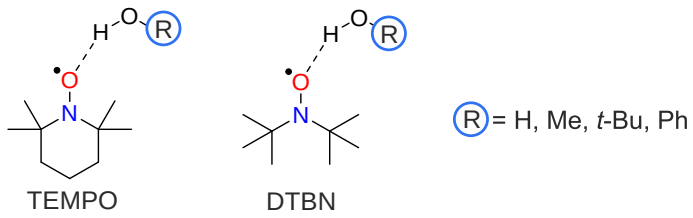

Figure 2. Mono-solvates of (2,2,6,6-Tetramethylpiperidin-1-yl)oxyl (TEMPO, right) and di-*tert*-butyl-nitroxide (DTBN, left) with OH-containing solvents.

Using different protic solvents has been proven to be useful in other investigations for elucidation of the vibrational experimental IR data and for testing the underlying

vibrational structure. As the most fundamental requirement for benchmarking studies has been met through the experimental conditions provided by jet spectroscopy, several different quantum chemical methods were employed, and their spectral predictive power was tested.

It is known that vibrational frequency calculations computed within the harmonic approximation tend to systematically overestimate experimental fundamental frequencies. To overcome the neglect of anharmonicity and the intrinsic errors resulting from the electronic treatment, scaling factors may be applied. In this work, an elaborate scaling strategy that considers the OH stretching modes of closed-shell dimers and trimers of water, methanol, *t*-butanol, and phenol has been developed.

Despite of some exceptions such as the mentioned above, nearly all known radicals are transient. For example, several heteroatom-centred radicals, like pyridyl-2-thiyl radical investigated within this work, are highly reactive and difficult to stabilise and characterise.

Transient radicals are often formed pairwise, and pairs comprised of two unbounded radicals are known to play important roles in many chemical reactions, being key intermediates in a variety of biological processes, including photosynthesis[45] and magnetoreception in birds.[46,47] The investigation of stabilized radical pairs for practical applications is also of interest in the field of materials science, as radical pairs generated and stabilized in solids may offer exclusive optical and magnetic properties. [48–52]

Radical pairs can be formed through photoinduced or thermal-induced homolytic bond breaking, through electron or hydrogen transfer reactions, and whenever two spin-correlated radicals encounter one another. In the first case, a molecule DA in its singlet ground state is photoexcited to a higher energy level, DA*, in the same spin state as the ground state precursor. Usually, the ground state precursors are diamagnetic, with few exceptions of molecules with a triplet ground state, e.g., molecular oxygen, which is the most known example. The excited state can then undergo a transition to a different multiplicity state (e.g., $S_1 \rightarrow T_1$) through intersystem crossing (ISC) - a process driven by spin-orbit coupling (SOC). Subsequent radical pair formation may then take place if a bond is broken. Once formed, the generated radical pairs retain the multiplicity of the excited precursors. According to the Pauli exclusion principle and the angular momentum (spin) conservation during chemical reactions, the singlet state can directly recombine to produce the ground state, whereas the pure triplet state cannot undergo recombination until spin-flipping has taken place. Therefore, the recombination of triplet radical pairs depends on the conversion of triplet into singlet states, a process formally forbidden in non-relativistic quantum theory. Nevertheless, it is necessary to analyse the systems independently and look at the mechanisms of singlet-triplet interconversions in more detail to determine whether the transition may occur or not.

Above, it has been assumed that the radicals are formed pairwise and are surrounded or trapped by a solvent cage or cluster. Alternatively, the radical pairs can follow a path that is not spin selective, such as diffusion, and escape the solvent cage to form free radicals that would possibly re-encounter and undergo a spin-selective reaction.[9] This process, which is more likely to take place in solution, can be inhibited if the radicals are generated in environments that prevent diffusion, such as rigid cages and solids. Several elusive radical pairs, including $RS^{\bullet\cdots\bullet}ON$ (R = Me and Et)[53], suggested to occur as a singlet pair, $Ph^{\bullet\cdots\bullet}ON$[54] triplet pair, $Ph^{\bullet\cdots\bullet}CH_3$[55] and $PhCH_2{}^{\bullet\cdots\bullet}COCl$[56] have been generated upon photoinduced homolysis of their precursors, and characterized by infrared spectroscopy in solidified inert gases at low temperatures. Despite of that, the photoinduced generation and stabilization of radical pairs at low temperature remains scarce due to their rapid and often barrierless recombination. However, the recombination reaction may be prevented by constrained motion or orientation in the matrix cage, and eventually through a subsequent formation of a triplet pair *via* intersystem crossing. In this case, the recombination is a barrier mediated process. Related to this topic, the photoinduced switching between dimers linked by S-S bridges into radical pairs in the solid state has been recently reported[51], and it stimulates further investigations on similar molecular systems containing sulphur and nitrogen atoms.
In the present work, 2,2′-dipyridyldisulphide has been explored as source of the pyridyl-2-thiyl radicals upon irradiation of matrices with UV-light in different matrix environments. Flash *vacuum* pyrolysis has also been employed in combination with matrix isolation for the same purpose.

Thesis Outline

To summarise, the aim of this work is to provide new experimental reference results on hydrogen bonded clusters of nitroxides with OH-containing solvents and on sulphur and nitrogen containing radicals using infrared spectroscopy and modern quantum chemical calculations. It was triggered by the lack of experimental data and by the challenges associated with experimental detection of radicals and calculations on open-shell species.
This Thesis is organised in five Chapters. Matrix isolation and supersonic expansion methods are introduced in Chapter 2, along with the available and used methods for matrix-isolated and jet-cooled radicals' preparation and a brief description of some of the most relevant works on these subjects reported hitherto. The photoinduced generation of radicals in the matrix environment is highlighted.
Chapter 3 comprises the detailed description of the matrix and jet setups existing at the LMCB in Coimbra and in Göttingen, respectively. The jet-spectroscopy measurements

were performed at “gratin” and “filet” Jet, being the first technique based on the same principles of the latter, but with some extra experimental and advantageous features for the measurement of hydrates. The experimental conditions for matrices deposition and supersonic expansion preparation, as well as the photolysis equipment used for UV-irradiations are also described in Chapter 3. Flash *vacuum* pyrolysis conditions of the experiments performed at the University of Giessen are also briefly described. Furthermore, the modern DFT approaches, with dispersion corrections (D3BJ), and the highly accurate quantum chemical DLPNO-CCSD(T) method are also addressed in this Chapter, alongside with the software packages used to carry out the quantum chemical calculations. Local energy decomposition (LED) analysis, which allows decomposition of the interaction energy between two fragments calculated at the DLPNO-CCSD(T) level into individual contributions from several interactions, as electrostatic, dispersion, and charge transfer, is also described briefly.

Chapter 4 is one of the main chapters of this work, and it introduces the jet and matrix isolation FTIR investigations carried out on the studied nitroxide radicals and radical complexes with protic solvents. Firstly, the IR spectra of the first detected radical monohydrate (TEMPO and water) by FTIR supersonic jet spectroscopy, and the comparison with the analogue ketone TEMCO are introduced and discussed. Afterwards, the solvation of TEMPO and DTBN with a series of alcohols and phenol is presented. The IR spectra in the OH stretching range are assigned based in DFT predictions for microsolvates and the closed-shell solvents. The interpretation of jet FTIR spectroscopy is followed by the discussion of the obtained matrix isolation IR results.

Chapter 5 comprises the investigations performed on 2,2′-dipyridyldisulphide as a suitable precursor for pyridyl thiyl radicals. The experiments of the photolysis and flash *vacuum* pyrolysis carried out in Coimbra and in Giessen, respectively, are herein discussed. This Chapter comprises important findings on the topic of matrix-isolated radical pairs.

Chapter 6 describes the photoinduced reactivity of a matrix-isolated peroxide, investigated by both IR and EPR spectroscopies. The experimental IR results suggested a diradical mediate reactivity that was further supported by ESR measurements with the detection of triplet diradical species.

Appendix A includes the relevant supporting information of Chapter 4. Appendix B provides additional information of the Chapter 5. Appendix C includes a publication about additional investigations on a disulfide molecule, which go beyond the scope of this PhD project centred on the investigation of radicals, but that are also relevant to understand the structure of the selected radical precursor for the investigations presented on Chapter 4 of the Thesis. Finally, Appendix D contains further information about the study of the photoinduced reactivity of an organic peroxide.

Chapter 2

Experimental Techniques

2.1 Matrix Isolation

The general aim of this work focuses on the generation and characterization of radicals and radical complexes. As radicals typically have short lifetimes and rapidly take part in chemical reactions, suitable methods for their characterization are required. One of the most important approaches in this endeavour is the capture and isolation of radicals within a non-reactive environment at low temperature. Matrix isolation approaches the required conditions for such environment because it may prevent radicals from reacting further, providing an opportunity to investigate their intrinsic properties.

Matrix isolation was pioneered by Pimentel[39,42] and Porter[40] in 1954, and it has been a very useful technique for the characterization of molecular systems since then. It was originally developed to overcome the difficulties associated with the detection of transient species, such as radicals, but the range of chemical problems addressed has extended throughout the years.[57–61]

In essence, matrix isolation is a technique for trapping isolated molecules (or atoms) of interest in a rigid host material.[62–65] It involves the mixing of a substrate with a large excess of an inert (or occasionally reactive) gas and its condensation on a window that is sufficiently cold to ensure rapid solidification. The sample is usually quite diluted (typically 1: 500 – 1: 2000 solute : matrix ratio), and each solute molecule is in an individual cavity, surrounded by one or more layers of inert gas and isolated from the other solute molecules, in a globally rigid ‘‘matrix’’.

The rigidity of the matrix prevents diffusion of the guest species, which otherwise would react with other molecules (through recombination or other bimolecular reactions) or

undergo aggregation (e.g., formation of complexes through hydrogen bonding). The requirement of low temperature (*ca.* 30 K) to obtain the rigid environment leads also to the suppression or extreme slowdown of unimolecular thermally activated processes. Substances that can be frozen at low temperatures can be used as host gases, but the inertness of the matrix environment towards most of the guest molecules can be only attained with substances that are not able to establish strong interactions with the guest. Noble gases (Ne, Ar, Kr, and in a less extent Xe) and molecular nitrogen are not reactive (although they can interact with guest molecules), and provide the broad optical transparency needed for spectroscopic measurements. Depending on the nature of the matrix experiment, matrices can be intentionally doped with a substance that reacts or interacts with the targeted intermediate, such as, for example, the small CO, O_2 or H_2O molecules that are commonly used to this purpose.[64] O_2-doped matrix experiments are advantageous for trapping radical species and other reactive intermediates that may undergo recombination within the matrix cages. They may provide further evidence of their generation, without the inconvenience of interfering absorption bands in the infrared spectrum. In this work, the molecular systems were investigated predominantly in Ar matrices (and Ar matrices doped with H_2O), although several experiments required the preparation of N_2 and O_2 gaseous mixtures to achieve suitable O_2-doped matrices, as will described in Section 3.1 of this Thesis.

Under the above referred conditions, short-lived species or small complexes can be trapped and investigated at leisure using conventional (non-time-resolved) spectroscopic tools. Most of the investigations performed under matrix isolation conditions thus aim at direct observation and characterisation of reactive intermediates, as well as the determination of their molecular structures. The characterization of small molecular complexes and their characteristic weak interactions, as well as the investigations of molecular conformations, are also hot topics in the field. Alternatively, one can take advantage of time-resolved spectroscopy, which has paved the way for direct monitoring dynamics and molecular interactions that take place in an extremely short timeframe. The two approaches are complementary, since time-resolved techniques provide kinetic information, while the spectra of isolated molecules provide a much more detailed view into the electronic and molecular structures.

Herein, the matrix isolation technique was used in combination with FTIR spectroscopy (*Fourier-Transform InfraRed*), which is well-suited to use in combination with the matrix isolation technique due to its high sensitivity to structural changes and has been by far the most employed spectroscopic technique for detection and characterization of matrix-isolated species. In FTIR spectroscopy, the signal is acquired by collecting the interference pattern generated by the sample and reference beams in an interferometer – whose main components are a beam splitter that divides the incoming radiation in two

beams and two mirrors, one of them movable. The interferogram contains information about the whole range of frequencies absorbed and is subsequently processed by Fourier transform to produce the infrared spectrum. FTIR spectroscopy is much faster than dispersive spectroscopy, allowing to obtain much better signal-to-noise ratios and perform kinetical studies in an easier way.

Comparison of experimental matrix isolation and quantum chemical calculations results is a common technique for the verification of the spectral assignments.

When interpreting the IR spectra of matrix isolated species, it is also necessary to consider the special features of this technique and be aware of potential setbacks due to the so-called *matrix effects* caused by the host gas on the guest molecules. For instance, the vibrational levels of the guest are perturbed by the matrix and therefore the vibrational frequencies will be shifted when compared to the gas phase – known as *matrix shifts*. This effect will be pointed out further along this work, in Chapter 4, with the comparison of matrix isolation and jet spectroscopy investigations on radical complexes. On the flipside, the spectra collected under these conditions are characterized by very narrow peaks when compared to spectra obtained at room temperature and under other sampling conditions (solution or KBr pellets, for example) where bands due to different vibrations may overlap and are often not separable. Furthermore, the rotation of the guest molecules or complexes is quenched (apart from a few smaller size molecules, like water, which almost rotate freely in the matrix environment), so that pure vibrational spectra are acquired without the complications due to rotational effects.

Another well-known matrix effect results from the possibility of trapping molecules in different local environments (sites) and is referred as *site-splitting*. Molecules trapped in different matrix-sites are exposed to different external fields or may experience distinct geometrical restrictions. Thus, the vibrational bands can be shifted (most frequently the stretching or out-of-plane deformation modes) due to the perturbation of the intramolecular vibrational potential (and geometry) by the intermolecular interactions. The cages size and the intermolecular interactions depend on the type and size of the host gas and guest and, consequently, the observed band splitting is also variable, even for the same solute molecule and conformer.[63,64]

Reactivity also depends on the selected host material, as the host material can affect the barrier of a given chemical reaction when compared to the barrier existing for the considered system in the *vacuum*. This effect might be pronounced in the case of several processes, such as the torsion of bulky groups,[66] and may have influence in recombination reactions due to geometrical constrains, as in the case of the thiyl radicals recombination processes described in the Chapter 5 of this Thesis.

2.1.1 Matrix-Isolated Radicals

There are some available methods for the preparation of radicals for matrix isolation studies, but the most widespread approaches are the photolysis and the pyrolysis of suitable precursors.[62,64,67] The photogeneration *in situ* is most of times the method of choice for the preparation of reactive intermediates in matrix isolation conditions since it is the easiest to implement. It often involves the irradiation of the samples with UV light supplied by arc lamps, such as Hg, Xe, Hg(Xe) lamps, or tuneable lasers. Because it is often required to select specific reaction channels through wavelength selection to avoid competitive reactions of the precursor, narrowband irradiations undertaken with help of appropriate optical filters or monochromators, or using lasers, are often necessary. The irradiation conditions must also be optimized to avoid that the desired photoproduced intermediates are also photoexcited and undergo unwanted transformations.

As referred in Chapter 1, radicals are often formed pairwise upon the homolytic cleavage of a bond of a photoexcited precursor. The pairs would retain the multiplicity of the excited precursor, which is most of times a closed-shell molecule in the singlet state. Since the diffusion is inhibited in the matrix environment, the singlet radical pairs will be retained in the matrix cage and usually a rapid recombination takes place. Indeed, the so-called *cage effect* can be a great source of disappointment and discouragement for matrix isolation investigations regarding the photogeneration of radicals *in situ*, since radical species are often formed pairwise, and their recombination is a process that is usually barrierless or requires a small activation energy, so being in general the most probable process following dissociation. Eventually, recombination of the radical pairs can be prevented by geometrical constrains/stabilisation in the matrix cage, and/or through a subsequent formation of triplet pair *via* intersystem crossing. Therefore, the formation and the yields of generated radicals under matrix isolation conditions can be influenced by several factors, such as the structure and reactivity of the precursor, the host gas, and the temperature of the experiment. As result, the success of the experiments is quite unpredictable *a priori*, and the optimisation of the experimental conditions is an essential requirement. To overcome the inherent challenges, one can include some strategies based on experience and take some advantage of the chemical intuition provided by empirical knowledge. For instance, one can deliberately select precursors which are prone to "release" hydrogen atoms, because they may escape the matrix cages and diffuse apart.[64] This strategy is quite limited to molecules bearing a chromophore because the X-H bond cleavage requires the absorption at the energy of that bond. On the other hand, this approach is suitable for the generation of radicals stabilized by resonance effects, such as benzyl radicals.[68] Another alternative strategy consists in the

generation of radical pairs by photoelimination of a small molecule, which will afterwards prevent the recombination process.

Diacyl peroxides are precursors that satisfy this target property. When irradiated with UV-light, diacyl peroxides fragment into radical pairs and carbon dioxide.[69,70] The latter can hinder the approach of the radicals, preventing dimerisation. Eventually, the recombination takes place after the annealing of the matrix, since warming reduces the matrix rigidity thus allowing diffusion and bimolecular reactions of the trapped molecules to take place.

In addition, nitric oxide N-O$^{\bullet}$ has been shown to survive in the matrix environment without recombine with other radicals. Hence, the generation *in situ* of this radical from suitable precursors (such as nitroso compounds) is a useful strategy to investigate their reactions and interactions with other molecules. For instance, it has been reported the detection of caged radical pairs consisting of nitric oxide and thiyl radicals R-S$^{\bullet}$, bridged by O$^{\cdots}$S and H$^{\cdots}$N interactions.[53] The hydrogen-bonds stabilize the pair and an activation energy barrier must be overcome in order to the rearrangement and recombination occur in the matrix environment (ca. 5 kcal mol^{-1})[53].

In fact, an activation energy may prevent the recombination reaction between two radicals (though radical-radical recombination is often a barrierless process and more exothermic than most of the reactions between a radical and non-radical species). This activation barrier can be determined by a complex interplay of aspects, such as geometrical and steric factors, including the surrounding environment, as well as the own structure of the radicals. For instance, the environment may impose an activation barrier if it constrains the orientation of the radicals in relation to one another, making the close contact between the two radical centres unattainable. On the other hand, the interplay of intermolecular interactions between the caged radicals may also prevent their recombination. Steric factors arise when the accessibility of other molecules is hindered by the spatial environment around a group or molecule, as in the case of the studied nitroxides.[25,26] The activation energy for recombination can be expected to be higher for two radical centres surrounded by bulky substituents than for those surrounded by hydrogen atoms.

The generation of PhCH$^{\bullet\cdots\bullet}$COCl, formed upon the irradiation of oxychlorocarbene $PhCH_2OCCl$ in cryomatrices, is an example of a generated radical pair that does not recombine spontaneously.[56] It has been suggested that this is due to the unfavourable location of the unpaired electron to attack the benzyl radical. The reaction takes place upon giving the necessary energy through heating or excitation of the benzyl radical for the reorientation of the fragments inside the matrix cage.

To overcome the inherent problems of the *in situ* irradiations, radicals can be generated externally through flash *vacuum* pyrolysis (FVP) and subsequently trapped with a large

excess of inert gas onto a cold window, thus forming a matrix sample.[64,67] Such technique allows the trapping of free radicals in single cages upon their formation in the gas phase and thus, the recombination reactions are suppressed if the matrix is sufficiently diluted, which make FVP a powerful choice as a method for preparation of radicals. The main problem of this procedure is that the decomposition of the precursor frequently occurs in the walls of a hot tube, through energy transfer by collisions. The surface of the walls may trap radical species, and collisions may result in undesired reactions. Therefore, the yields of generated radicals can be quite small, and the data can be quite difficult to interpret due to the formation of side products. Furthermore, a high vacuum is required inside the tube to avoid aggregation (specially dimerization) to take place.

In principle, nearly all precursors are suitable for FVP experiments, although one should take care in choosing the appropriate ones. Among many other examples, phenyl disulphide and allyl phenyl sulphide have been successfully used to generate the phenyl thiyl radical through FVP[28] experiments, while phenyl radical has been generated from several precursors, namely azobenzene[71], benzoyl peroxide and benzoic anhydride[72], with the latter two by both FVP in an effusive thermal source and by flash pyrolysis in a hyperthermal nozzle followed by supersonic jet expansion. In this work, either the generation of radicals through photolysis of a suitable matrix-isolated precursor and by its flash vacuum pyrolysis were applied.

Another important application of matrix isolation technique is the investigation of weakly bound systems as H-bonded complexes, as these structures may easily dissociate under room temperature conditions due to the weak intermolecular forces but can remain stable under matrix isolation conditions. Within this topic, persistent radicals and their hydrate complexes were also investigated under matrix isolation environment. These experiments do not require cumbersome preparation conditions but require a series of experiments over a range of sample concentrations of water and host-gas mixtures to attain the optimum conditions for monohydrates formation. Other radical-water complexes have been studied before by matrix isolation, including HO$^{\bullet}$-water[73] and aromatic radicals such as, phenyl[20,21], phenoxy[22], benzyl and anilinyl[23] radical-water complexes. The systems were investigated by infrared spectroscopy and quantum chemical calculations mainly to identify the possible interactions between the aromatic radicals and the water molecules (microsolvation), which are relevant to further understand their reactivity. In this regard, it was observed the hydrogen-atom transfer from water to the phenyl radical upon UV-light irradiation of these complexes, and hydroxyl radical and benzene complexes were detected and characterized for the first time through FTIR matrix isolation. [20]

2.2. Supersonic Expansion

The ideal conditions of isolated molecules or molecular clusters in the gas phase at low temperatures are closely reached in a supersonic expansion. The term refers to an expansion of a gas beam beyond the speed of sound, and it is a useful experimental tool to study the structure and dynamics of molecules. The low internal temperatures attained in a supersonic jet lead to highly resolved and greatly simplified spectra of many chemical species, such as radicals, which would otherwise not be possible to investigate at such detail. It resembles a matrix isolation environment in the sense that the molecular species are isolated at low temperatures, but it offers a great advantage in relation to the latter: the perturbations with the surrounding environment - the so-called "matrix effects" - are negligible within a jet expansion. Thus, the jet spectroscopy technique fulfils the necessary requirements for high-resolution spectroscopic measurements and provide the ideal conditions for the collection of benchmark data for validation of quantum chemical methods.[74–77]

A supersonic expansion is formed when a gas is expanded through a small nozzle orifice from a high-pressure reservoir p_0 into a lower pressure region p_1[78,79], as illustrated in Figure 3. Its generation occurs when the mean free path of the particles in the reservoir is much smaller than the diameter of the orifice, a result of the increasing on stagnation pressure within the reservoir. As the molecular beam passes through the orifice, the atoms and molecules undergo numerous collisions. The collisions between particles lead to partial redistribution of the thermal energy, [79,81–83] and the random motion of the initial system in thermal equilibrium inside the reservoir is then converted into a directed flow, leading to an internal cooling of the gas beam, and creating a cold translational bath.[79] The redistribution also results in a reduction of the population of excited rotational and vibrational energy levels, as the energy is transferred to translational motion of the gas particles. As a result, the density of the flow and the collision frequency diminish with distance.

The collisions in the expanding gas tend to equalize the relative particles velocities towards a narrow velocity distribution, while the temperature characterising the distribution becomes lower. The speed of sound within the ensemble will decrease until the speed of the molecular beam exceeds it - at this stage, the expansion is defined as supersonic. The gas flow undergoes a transition between a continuum to an almost collision-free regime, termed as "zone of silence", where the collision frequency becomes negligible and the degrees of freedom fall out of equilibrium – at this point, the gas flow reaches its maximum and molecules become ultra cold.[84] At a final stage of the expansion, the beam is recompressed through collisions with the background gas and a

shock wave is formed. Across a shock wave, the pressure, the temperature, and gas density rise.

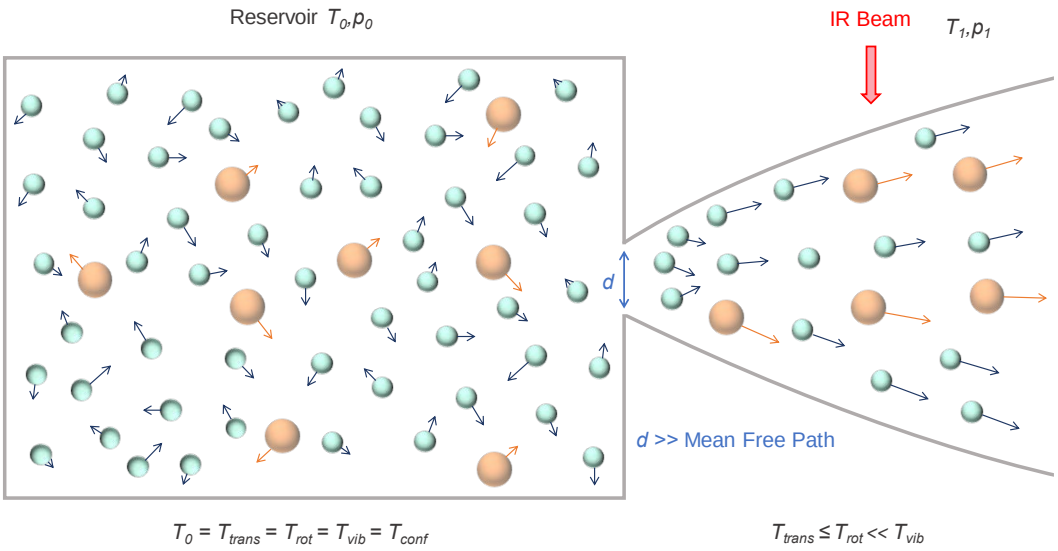

Figure 3. Representation of a supersonic jet expansion. The gas is expanded from a high-pressure region (reservoir, at T_0 and p_0) to a background lower-pressure region (T_1 and p_1). The arrows represent the magnitude and direction of the velocity of the individual atoms and molecules. The sketch is adapted from Refs.[78–80] and it is not drawn to scale.

It should be mentioned that the disruption of thermodynamic equilibrium in a supersonic expansion causes a difference in the cooling of vibrational degrees of freedom, in relation to rotational and translational degrees of freedom. The rotational cooling may slightly deviate from translational counterpart, but they may be nearly close. Consequently, the vibrational rotational T_{rot}, and translational temperatures T_{trans} of the ensemble differ significantly in the following sequence $T_{trans} \leq T_{rot} < T_{vib}$.

Supersonic molecular beams have become increasingly important for stabilization of molecules and small molecular aggregates for spectroscopic analysis. The low translational temperatures achieved in supersonic beams may favour the generation and stabilization of high concentrations of clusters and transient species difficult to prepare under other gas phase conditions.[85] The experiments involving aggregation processes and reactive species are often performed in diluted beams of gas mixtures, in which the solute is seeded in a carrier gas (typically an inert gas). The size distribution of the clusters and the concentrations may be controlled by varying several factors, including the dimension of the nozzle, the concentration of the sample, the stagnation pressure in the reservoir, and the carrier gas.

The cooling effect increases along the inert gases group, from He to Xe.[86] The inert gas effect on temperature has been ascribed to the velocity slip related to the gas, defined by the difference between average velocities of the solute molecules and the velocity of the gas.[86]

The free molecular flow region of the expansion is outstanding for spectral probing because at this stage the molecules and clusters are ultra-cold in a collision-free environment[54][81]. In this regard, Fourier transform infrared spectroscopy (FTIR) is a powerful tool elucidate the dynamic behaviour and the structure of molecules and small clusters, and it offers the accuracy and sensitivity needed for the pioneered investigations on the radical microsolvates presented along this Thesis. In fact, FTIR spectroscopy is complementary to other spectroscopic techniques, providing reference data for further investigations. For instance, FTIR and rotational spectroscopy can be used synergistically to elucidate the structural details of complex molecular structures. The combination of both is an outstanding option for gaining insight on such information.[87,88]

The interpretation of the vibrational spectra obtained in supersonic beams can be also challenging due to the complexity of the structures, and the complexity of the spectrum itself often makes difficult to extract the intended vibrational signatures. For instance, overlapping peaks whose deconvolution is not feasible can hinder the contributions of individual vibrational modes. On the other hand, as supersonic expansions closely reproduce the gas phase at a temperature of 0 K, and thus shifts broadenings of bands are greatly avoided due to the considerable translational, rotational, and eventually vibrational cooling, the interpretation of the spectra is greatly simplified by the direct comparison with theoretical data. In essence, supersonic expansions provide a unique environment to study the intermolecular interactions that govern the formation of small aggregates. The adiabatic cooling leads to the conversion of internal energy into a "translational bath", allowing intermolecular forces to hold molecules together. Measuring in detail and understanding the intra- and intermolecular forces and dynamics governing the changes from isolated monomer species in the gas phase into the liquid and solid phases is a long-standing aim in the field of clusters' research.[89]

In the context of the present work, the overall aim of the performed jet FTIR spectroscopy measurements was to gain insight into the microsolvation processes concerning nitroxide radicals. The experimental work and its interpretation are presented in Chapter 3 of this Thesis.

2.2.1 Jet-Cooled Radicals

Radicals can also be formed through several methods in jet expansions.[90] For instance, slit supersonic discharge sources have been used for generation of intense jet-cooled densities of radicals, the method being based on the combination of slit supersonic expansions with pulsed electric discharges.[36,91] Methyl radicals are an example of jet-cooled radicals studied in slit supersonic discharges by infrared spectroscopy.[36] This type of experiments require the use of special jet preparation techniques and the use of long slit jet nozzles.[36,38,91]

Radicals can also be generated through flash pyrolysis[38,92] and photolysis[93] in jet expansions. For instance, $RO^{\bullet}$ and $NO^{\bullet}$ have been successfully generated through the pyrolysis of CH_3CH_2ONO and detected within supersonic molecular beams.[38] The free jet expansion provides cooling of chemical species to very low temperatures, such as that even reactive intermediates, like organic radicals, can be identified and characterised.[90]

However, the generation and detection of jet-cooled radicals has not been reported as often as it has been in matrix isolation works. The requirement of elaborate techniques relates to the fact that radicals are highly reactive species that typically have very short lifetimes, and thus easily react upon collisions within the expansion. The own conditions of the technique, as the pressure gradient, make then challenging to study radicals under jet conditions. Furthermore, radicals are often formed in low concentrations, especially in jet expansions where the substance is highly diluted in the gas, so the requirement for higher concentrations might also be a major drawback.

As persistent and volatile radicals, TEMPO and DTBN do not require elaborate jet preparation techniques, but their difference in terms of stability required the experiments to be performed in different jet-setups, as described elsewhere in this Thesis.

Chapter 3

Experimental Set-ups and Computational Methods

3.1. Matrix Isolation Set-up

The LMCB laboratory (Laboratory for Molecular Cryospectroscopy and Biospectroscopy) is equipped with three distinct matrix isolation set-ups labelled with numbers – a practical approach to identify the different apparatuses. The experiments were performed in the so-called cryostat 2, which will be discussed in more detail in this section along with the sample's preparation procedures and experimental conditions, whereas the details of the cryostat 3 set up will be only briefly addressed. Furthermore, experimental details of flash *vacuum* pyrolysis experiments, which were performed in collaboration with the group of Prof. Peter R. Schreiner at the University of Giessen, will also be here described.

Cryostat 2 is a closed cycle cryostat (see Figure 4) that comprehends an helium compressor connected to an expander by high pressure (feed) and low pressure (return) lines.[62] It is an ARS Cryogenics closed-cycle helium refrigeration system, with a DE-202SI expander. In this refrigerator, helium is compressed and then expanded to produce a cooling effect. The attainable temperatures are about 10 K at the second stage of the expander. The results reported herein were collected at a temperature between 10-11 K, but if it is intended to use gases such as Ne and H_2, one should make use of cryostats that can attain temperatures equal or lower than 4 K.[62,64]

Experiments are not strictly conducted at the lowest temperature attained by the cryostat. The temperatures are rather dependent on the desired deposition conditions,

or if annealing experiments are necessary. During this work, annealing experiments were needed to induce the complexation between radicals and water molecules through molecular diffusion, as well as to promote radical recombination reactions, as described in Chapters 4 and 5 of this Thesis.

In cryostat 2, the variation in temperature is accomplished by fitting the cold end with a resistive heating element and a silicon diode connected to a digital temperature controller (Scientific Instruments, model 9650–1 and LakeShore 335), to monitor and control the temperature at the sample holder, which usually is only very slightly warmer than the cold end of the expander. The employed temperature controller provides an accuracy of 0.1 K.

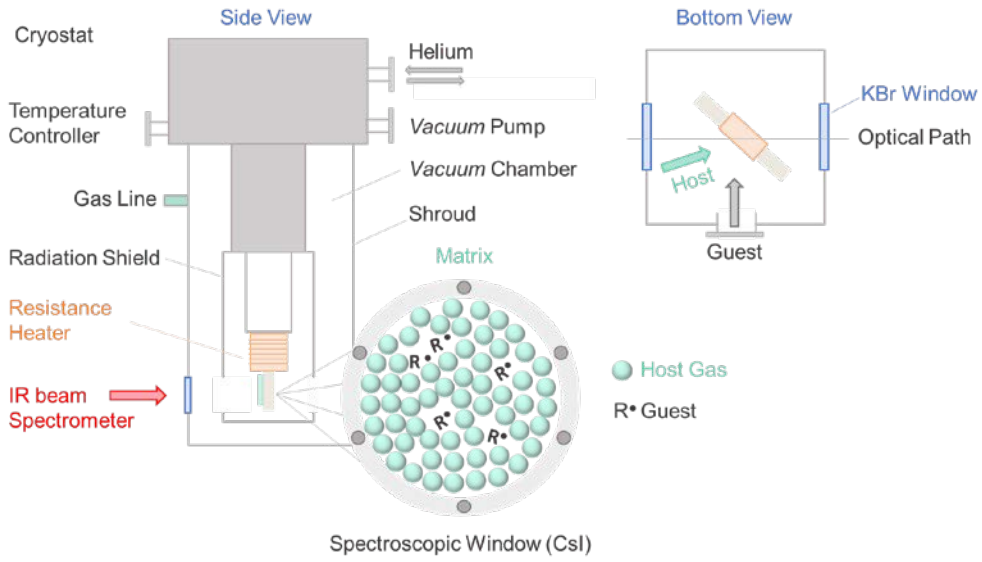

Figure 4. Schematic representation of the matrix isolation set-up used for the investigations carried out in this work. The sketch is not drawn to scale.

Another fundamental element of the cryostat is the shroud, a stainless-steel chamber that surrounds the sample holder and the expander. These must be kept under high vacuum while they are cold to prevent collisional heat transfer. The vacuum provided by high vacuum pumps not only insulates the cold sample from warming by conduction and convection, but it also prevents the contamination of the matrix from unwanted gases. It is therefore important to attain the highest vacuum possible, although pressures about 10^{-4}–10^{-5} within the sample chamber are often satisfactory and demand less expensive equipment than ultra-high vacuum (better than 10^{-9}). In cryostat 2, a turbomolecular pump has been used to attain vacuum pressures within this range. The sample holder refers to the surface on which the sample is deposited, and the connection

with the cold end of the cryostat. It is composed by a window of 25 mm diameter, which is placed between two sections of a two metal plates screwed into the bottom of the head module of the cryostat. Because it is crucial to assure a good thermal contact between all the elements - the window and the holder, as well as the holder and the cold end - the elements are made of copper and are fitted with indium O-rings (or gaskets) to maximize the contact between the pieces.

The choice of the window depends strongly on the spectroscopic measurements of interest. For IR spectra collection, it is required to choose a material that is transparent in this spectral range, and a CsI window appears as the best option due to high IR transparency as well as good mechanical resistance to temperature changes.

The sample preparation vacuum line incorporates a storage bulb for the host gas (or gas pre-mixture), inlets for the attachment of valves (or vessels), a needle valve that allows the monitored release of the gas and an inlet attached to the shroud. It allows a controlled filling of the gas in a storage bulb through a pressure controller, and the release of the gas sample through a needle valve towards the cryostat. Alternatively, the substance can be placed in a bulb, or a valve (e.g., J Young) connected through the cryostat through a stainless-steel needle valve. J. Young needle valves allow the degassing of the substrate prior to its deposition and the storage of the degassed sample to be reused later.

For matrices preparation, the substances were placed in a slightly modified J. Young needle valve and condensed simultaneously with excess of gas (or doped gas) from a storage bulb onto the cooled spectroscopic window. This requires a sufficient vapor pressure under vacuum, a condition verified for both TEMPO and DTBN radicals.

There is another set-up available for investigations on radical microhydrates at the LCMB. The quite recent cryostat 3 allows to attain lower temperatures, but the buildup of water impurities on the cold window during the deposition has been somewhat limiting its use. Interestingly, with additional improvements and optimisation of the deposition conditions, this feature might be exploited for the investigations of microsolvation processes in matrices.

The experiments on nitroxide radical aimed at the generation and vibrational characterization 1:1 complexation with water molecules. To enable the formation of the complexes, the radicals were trapped in argon doped with 0.1–1 % of water, a pre-mixture prepared in a storage bulb. After the deposition, the matrices were annealed at the temperature range of 10–25K to induce the diffusion of the molecules in solid argon, and consequently the formation of aggregates in the matrix medium. The results can be found in the Chapter 4 of this work.

Due to the insufficient vapor pressure, the investigations on the precursor of pyridyl-2-thiyl radicals 2,2′-dipyridyldisulphide required its sublimation directly from a Pyrex

small bulb upon warming with a heating tape at approximately 60 ºC. The produced gas was then investigated in both argon (99.9999 %, N60 Air Liquide) and nitrogen matrices (99.9999 %, N60 Air Liquide). To capture radicals, experiments with O_2-doped host gas were performed. The choice of the matrix gas for such experiments, was restricted to nitrogen due to the use of dry CO_2-filtered air as the source of triplet molecular oxygen (around 78 % nitrogen and 21 % oxygen). Pyridyl-2-thiyl peroxy radicals were generated through the co-deposition of the disulphide precursor and O_2 (concentrations in the range of 1-2 %) with a large excess of nitrogen, followed by in-situ photolysis and annealing experiments (10–25K), to activate the recombination reaction.

The mid-IR (4000-400 cm^{-1}) spectra were collected with 0.5 cm^{-1} resolution using a Thermo Nicolet 6700 FTIR spectrometer equipped with a mercury cadmium telluride (MCT) detector (cooled with liquid nitrogen) and a KBr beam splitter. During the experiments, the optical path of the spectrometer was continuously purged with a stream of dry CO_2-filtered air to avoid interference with atmospheric H_2O and CO_2. An overview of the experiments carried out through matrix isolation technique, the investigated substances and other relevant experimental details can be found in Table 1.

Table 1. Overview of the experiments performed with matrix isolation technique, including the substances, matrix host gas, the type of experiment and the Chapter that includes the experimental results.

Substances	**Gas**	**Experiment**	**Chapter**
TEMPO	Ar	Deposition	4
TEMPO + H_2O	H_2O-doped Ar	Annealing; Photolysis	4
DTBN	Ar	Deposition	4
DTBN + H_2O	H_2O-doped Ar	Annealing; Photolysis	4
	Ar	Photolysis; Annealing	5
2,2′-Dipyridyldisulphide	Ar	FVP, Deposition	5
	N_2	Photolysis; Annealing	5
2,2′-Dipyridyldisulphide + O_2	O_2-doped N_2	Photolysis; Annealing	6
Adamantane-2-spiro-3′-8′-oxo--1′,2′,4′-trioxaspiro[4,5]decane	Ar, N_2	Deposition, Photolysis	6
4-oxohomoadamantan-5-one	Ar	Deposition	6
1,4-cyclohexanedione	Ar	Deposition	6

3.1.2 Photolysis Experiments

Irradiations of the trapped precursors were carried out through outer KBr windows of the cryostat using two distinct UV light sources, in distinct experiments. Narrow band irradiations with a Quanta-Ray MOPO-SL optical parametric oscillator pumped with a pulsed Nd:YAG laser (pulse energy 10 mJ, duration 10 ns, repetition rate 10 Hz) and broad band irradiations were carried out by a 500 W high-pressure Hg(Xe) lamp (Newport, Oriel Instruments), with output power set to 250 W, through an additional water filter ($\lambda \geq 235$ nm, as defined by the onset of KBr transmission in the UV). After the irradiations, the cryostat was repositioned in the spectrometer and aligned with the IR beam for monitoring the induced spectral changes.

3.1.2 Flash *Vacuum* Pyrolysis Experiments

In addition to the experiments performed at the LMCB, further matrix isolation FTIR experiments combining flash vacuum pyrolysis with were undertaken at the Justus-Liebig University of Giessen (Germany), in cooperation with the group of Professor Peter R. Schreiner. Details about the matrix setup can be found in other works reported by Artur Mardyukov *et.al.*[94,95] In brief, to perform the matrix isolation experiments in combination with FVP, a home-built oven was directly connected to the shroud of the cryostat. The pyrolysis zone contains a quartz tube (inner diameter 8 mm), which can be heated by coaxial wire, over a length of 50 mm, and the temperature in this zone can be measured using a NiCr–Ni thermocouple. The substance of interest is evaporated from a storage bulb into the quartz pyrolysis tube, and the resulting pyrolysis products are deposited in the cold window at 11 K, along with and excess of argon. The travel distance from the pyrolysis zone till the cold window is ca. 5 mm. In this work, 2,2–dipyridyldisulphide was evaporated at 60 ºC and decomposed in the pyrolysis tube in several experiments, at temperatures varying from 750 ºC to 840 ºC.

3.2 Jet-FTIR Set-ups

Within the framework of this Thesis, jet spectroscopy measurements were extended to nitroxide complexes with non-radical molecules owning an OH group, being the hydrogen bond established between the two molecular entities the targeted interaction for probing. Thus, the FTIR spectra-based strategy implied the investigation of the hydride region for characterization of the OH stretching dynamics and the hydrogen bond patterns within these clusters.

The measurements presented herein were performed on two supersonic FTIR jet set-ups, the *gratin* jet[96] and *filet* jet[97], in this order. The latter is first described in the next subsection, followed by the *gratin jet,* which is an enhanced version based on the well-established jet FTIR principle of the *filet* jet. Besides the working principle and the components of the jet apparatus, the preparation and expansion of the samples are also described in that subsection.

3.2.1 Filet Jet

The *Filet* Jet is a system optimised for the measurements of FTIR-jet spectra with a high-signal-to-noise ratio, described in Figure 5. It was constructed by Nicole Borho under the scope of her PhD[98], and it was further improved by Matthias Heger[99]. The acronym "*Filet"* stands for *fine but lengthy,* a feature of the slit nozzle with 0.2 mm x 600 mm dimensions.[97]

The preparation of the samples for supersonic expansions at the *filet* can be done by seeding 1–2 substances of interest in a carrier gas, using two temperature-controlled saturators made of glass that can be cooled down to approximately –35 °C. The substances are filled in the saturators and a carrier gas stream (in this case, helium) is directed to the saturators with a pressure typically between 1.5—1.8 bar, conducting mixture to a 67 L reservoir, where the substances are homogenously mixed. The substances can be liquid or solid, but a sufficient vapour pressure at room temperature is required because the set-up is not heatable. This is a limitation of this set-up, as the choice of the molecular systems depends on its volatility.

Then the gas mixture enters a pre-expansion chamber from the reservoir by six high throughput solenoid valves connected to an oscilloscope. The gas passes through the slit nozzle into a vacuum chamber maintained at a pressure (lower than 1 mbar) by a pumping speed of 2000 m^3 h^{-1} and connected to a buffer volume of up to 23 m^3 to avoid large increases in the background pressure.

The pressure within the reservoir, also referred as stagnation pressure, is adjustable. Although a pressure of 1.25 bar had been tested for TEMPO and phenol, a pressure of 0.75 bar has revealed to be appropriate to promote at least the formation of the 1:1 cluster of all the systems under investigation in this work.

The absorption path through the filet-shape expansion zone improves the sensitivity for the IR absorption measurements.[85,100] These were performed using a FTIR Bruker spectrometer (Bruker IFS 66v/S), synchronized to gas pulses with the duration of 147 ms, with waiting times on the order of 15 to 120 s between each pulse, to ensure a background pressure no higher than 1 mbar throughout the expansions.

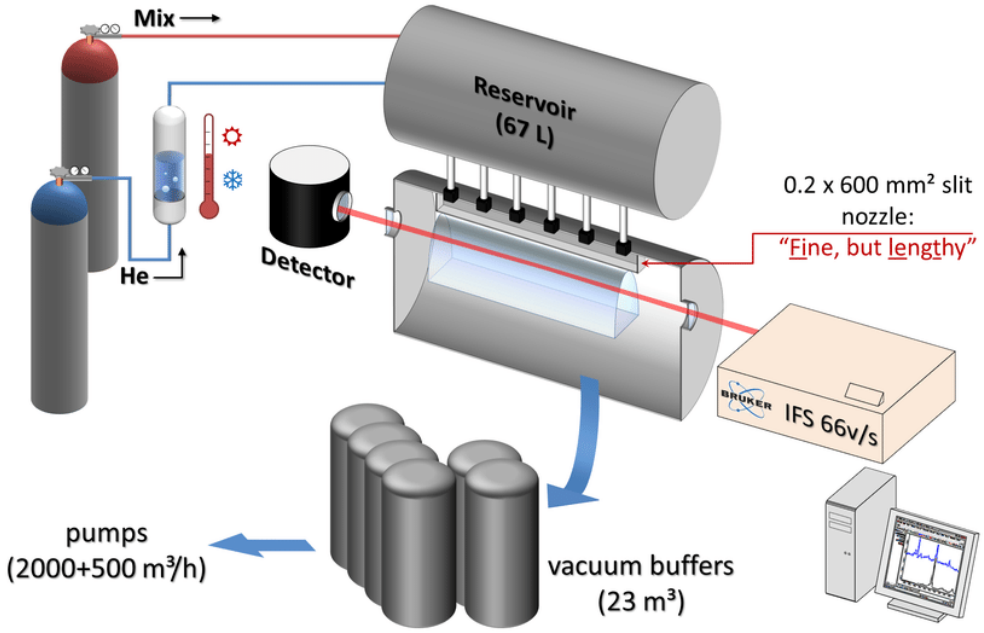

Figure 5. Schematic representation of the filet jet spectroscopy setup. Taken from Refs.[99][97], and licensed under CC BY-NC-ND 4.0.

Band pass filters and the optics can be used in combination to narrow the spectral range while improving the signal-to-noise (S/N) ratio. For these measurements, a 150 W tungsten lamp was used as a light source, along with a CaF_2 beam splitter. Since the measurements were focused on the hydride stretching range (OH and OD fundamental region) of 4000–2400 cm^{-1}, an infrared filter that is transparent in this region was intercalated in the optical pathway of the spectrometer. For probing in this region an indium antimonide (InSb) detector was used. Several of the jet slit investigations on radical microsolvates described throughout this Thesis (TEMPO and DTBN microsolvates) were performed using this experimental set-up (exception were the investigations performed on TEMPO/TEMCO hydrates). An overview of the filet jet-FTIR spectra presented in Chapter 4 of this Thesis is shown in Appendix A.

Table 2. Overview of the measurements performed at the filet jet set-up. The collected spectra shown are in Figures 15 and 16 of Chapter 4.

Spectrum	Figure
DTBN + H_2O	15
DTBN + $HOCH_3$	15
TEMPO + $HOCH_3$	15
TEMPO + $HOC(CH_3)_3$	16
DTBN + $HOC(CH_3)_3$	16
TEMPO + HOC_6H_5	16
TEMPO + HOC_6H_5	16

3.2.2 Gratin Jet

Established on the jet principle of the *filet*-jet, the gratin-jet (an acronym for gas-recycling atom-economic infrared jet spectroscopy) carries out new and innovative experimental features, with the possibility of recycling the gas mixture being the most relevant one.[96] This allows the reuse and thus reduction of substance consumption, leading to a more sustainable measurement concept. Furthermore, gratin also encodes the heat ability of the nozzle, a feature that allows to adjust the internal temperature and size distribution of the clusters. Due to the similarities with the previous described *filet* set-up, only some of the most important shared features and differences are pointed out here.

For the sample preparation, the substances are directly filled into the reservoir, followed by the gas fill in until the desired stagnation pressure is attained. Thus, the continuous refilling of the reservoir with subsequent newly gas mixtures is no longer necessary, contrary to the required for filet-jet measurements. One-time filling of the reservoir replaces the large carrier gas and substance consumption during the measurements, the most prominent drawback of the *filet*. This feature allows the use expensive carrier gases such as neon when certain experimental conditions are required.

As might be expected, the main conceptual difference comes from the fact that the gas mixture is not thrown away, but rather fed back to the reservoir from the buffer volume and subsequently re-expanded. Thus, the cycle of expansion, recompression and recirculation is repeated hundreds to thousands of times.

For the implementation of this new recycling concept, impurities that contaminate the sample compromising the measurements must be avoided. This required an efficient

evacuation procedure as well as a higher control of the leakage rate than in a conventional operation mode. Furthermore, a special pumping system to recompressing and recirculate the gas mixture was also required. Considering these constraints, a system made up of a heatable reservoir, buffer volume, and gas recirculation along with a pumping system for gas-circulation, and a turbomolecular pump for evacuation was commissioned.[101] The system represented in Figure 6 was built under the scope of Hannes Gottschalk PhD thesis[102], and it has been improved by Taija L. Fischer.

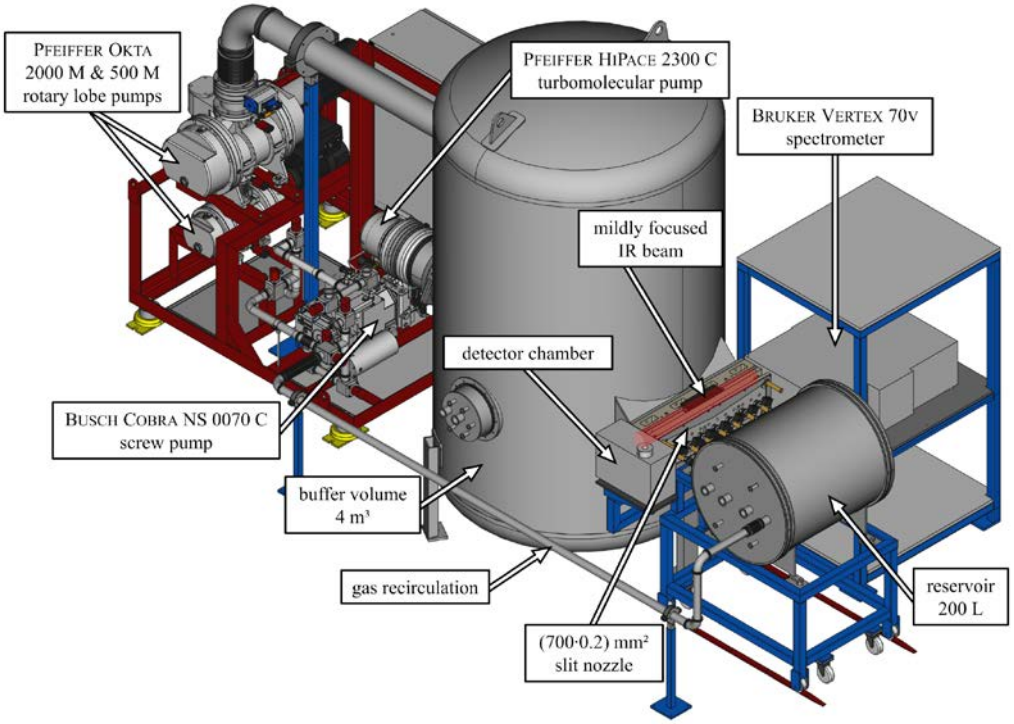

Figure 6. Schematic representation of the gratin jet spectroscopy setup. Taken from Refs.[96], and licensed under CC BY-NC-ND 4.0.

In this set-up, the gas mixture is expanded through the slit nozzle into a buffer volume (4 m^3 on the gratin, smaller than the filet jet buffer volume) and measured by the mildly focused IR beam emitted from a spectrometer Bruker IFS 66v/S spectrometer synchronized with the pulses. In addition, the absorption path is increased in comparison to the absorption path in the *filet*, being the length of the nozzle 700 nm and its geometry optimized to attain local lower pressures. The IR beam emitted by the spectrometer crosses the expansion along the slit nozzle at 10 mm (nozzle to beam center). CaF_2 optics

(beam splitter and windows) combined a 150 W tungsten filament, and an InSb/HgCdTe sandwich detector were employed for the measurements presented in this Thesis.

The expanded gas mixture is recompressed by a series of two rotary lobe pumps and eventually by a screw pump and then routed back to the reservoir. To evacuate the vacuum system between measurements, a turbomolecular pump has been used. This last process can be aided by heating the most important parts of the vacuum system (not only the nozzle can be heated, but the entire set-up is equipped with a heating system) up to 370 K. Further details of the set-up, including the pumping system can be found in the work described by Hannes Gottschalk *et al.*[96]

Despite the considerable degree of sophistication of the system, water impurities present in this quite new set-up constrain the recycling gain. But this apparently disadvantageous feature has been harnessed for the investigation of hydrate complexes of volatile molecules.[101]

The wavenumber of the hydrogen bonded OH stretching vibration (defined here as OH_b) of a water molecule locked to a hydrogen bond acceptor can be obtained from vibrational spectroscopy in a straightforward way. As the spectral position of the OH stretching vibration is quite sensitive and strongly correlated to the strength of the hydrogen bond, the value is representative of the structure and energetics of the complexes. Furthermore, the accessibility of isotopologues of water and relaxation experiments make accessible a wide variety of dynamical variations and allow for the discrimination of hydrides stretching modes.[96] Indeed, the gratin slit jet spectrometer application has allowed several investigations on microhydrates, including the recently published first systematic blind challenge initiative (HyDRA blind challenge) regarding the OH bond shifts in solvating water[74] and the investigations presented in this Thesis.[25,26]

DTBN monohydrates, which were part of the training set of the HyDRA blind challenge, were first investigated on the gratin jet and later at the filet jet set-up. The IR spectra of several experiments evidenced the decomposition of DTBN and water complexes in the gas recycling experiment, which was avoided by switching to a continuous gas flow at the *filet*-jet. In this regard, the gaseous TEMPO radical has revealed its thermal metastability under hundreds of recycling expansions. These results are provided in Chapter 3 of this Thesis.

Due of this gas recycling concept, the expensive Neon could be used as carrier gas in a He:Ne mixture (see Table 3) to attain a better cooling and enhance the relaxation processes within the jet expansion.

Table 3. Overview of the measurements performed at the gratin jet set-up. The collected spectra shown in Figures 11 and 12 are expanded in a He: Ne gas mixture.

Spectrum	He:Ne	Figure
TEMCO + H_2O	1:0	11
TEMPO + H_2O	1:0	11
TEMPO + H_2O	1:1	11
TEMPO + H_2O	1:1	11
TEMPO + $H_2{}^{18}O$ *minus* TEMPO + H_2O	1:1	11
TEMPO + D_2O	1:0	11
DTBN H_2O	1:0	12
DTBN H_2O	1:1	12

3.3 Quantum Chemical Methods

Quantum chemical calculations were extensively employed in this work, essentially to predict structures and energies, to aid the spectral assignments, and to evaluate the effectiveness of some of the most common employed methods in describing the vibrational spectra of the systems of interest through benchmarking. Because radicals have an unpaired electron that can significantly affect the structure when compared to closed-shell analogue, it is important to validate the methods applied for closed-shell systems to ensure their applicability to open-shell radicals. The employed approach and the quantum chemical methods used are described along this section.

3.3.1 Structures search

Searching for different structures of non-covalently bound complexes can be quite challenging due to the complex and dynamic nature of such interactions. Finding new low-lying complexes is more difficult than finding solely conformers, because each fragment of the complex may also adopt several different conformations.
To ensure that all the relevant structures were found during the manual structure search using B3LYP functional[103–105] with def2-TZVP basis set[106,107] (as described in the next section), the extensively used software for automated conformational search CREST was employed.[108,109] CREST (abbreviated from Conformer-Rotamer Ensemble Sampling Tool,

version 2.10.2) was developed by S. Grimme and co-workers and is available in the computer cluster of the Institute of Physical Chemistry of the University of Göttingen. The program CREST is based on GFN2-xTB[110,111] (Geometries Frequencies Non-covalent interactions extended Tight Binding) semi-empirical quantum chemical method and the iMTD-GC[109] (iterative Meta-Dynamics - Genetic Crossing) procedure to sample the conformational space. iMTD-GC is established in the idea to combine GFNn-xTB calculations with root-mean-square-deviation (RMSD) based metadynamics simulations. The given structures were then fully optimized with the B3LYP functional as described below.

3.3.2 Density Functional Theory

The Born-Oppenheimer approximation relies in the large difference between the electron mass and the mass of atomic nuclei.[112] It assumes that the motion of the electrons and nuclei are decoupled, and consequently the nuclear and electronic wavefunctions can be treated separately, which is extremely convenient for solving the Schrödinger equation. Quantum chemical calculations performed herein are based on this approximation.

Density functional theory (DFT) relies on the principle that the ground electronic state is a functional of electron density. It is by far the most applied approach for the calculation of the electronic structure of molecular systems, an accomplishment directly related to the development of further approximations for the description of the elusive exchange-correlation functional.[113] This success is manifested by the large and ever-expanding "zoo of density functional approximations"[114,115], implemented into standard quantum-chemical software packages.

The calculations presented in this Thesis were performed with ORCA 4.2.1[116–118] and 5.0.3[116,118,119] and Gaussian 16 Rev A.03[120] and B.01[121] program packages. The program employed in each case will be specified throughout the text, but in general the calculations presented in Chapter 4 were mainly performed with ORCA, while the theoretical data provided in Chapter 5 were essentially obtained with Gaussian 16 software.

In this work, three DFT functionals from the "zoo of functionals" were used for benchmarking the experimental data. To explore the ensemble of the selected monomers and dimers, an extensive manual search using the hybrid functional B3LYP[103–105] (closed-shell variant for non-radicals and unrestricted open-shell for radicals) in combination with Grimme's D3 dispersion correction[122] and Becke-Johnson damping[123–126] was performed. This manual search was complemented using CREST, to ensure that all the minimum structures of monomers, dimers and, in some cases, trimers were identified. Further reoptimisations on the starting structures were completed at B3LYP-D3BJ, with

the Ahlrichs (Karlsruhe) def2-TZVP [abbreviated TZ and def2-QZVP (abbreviated QZ) basis sets][106][107].

In addition, the non-empirical meta-GGA functional TPSS available in ORCA 4.2.1 was also explored and tested, which may provide superior results when compared to standard GGAs but less accurate results than those given by the hybrid density functionals improved with a part of exact exchange from Hartree Fock (HF) theory. For predictions in energy, properties, and spin densities the hybrid functionals, such as B3LYP, seem to be a better option. The computational cost associated with hybrid functionals is higher than for meta-GGA functionals, as the HF exchange must be computed in an exact manner.

The perturbatively corrected functional B2PLYP was also tested in this work. This is a not very expensive way of improving a DFT method by including parts of the correlation energy using second-order Møller-Plesset perturbation theory (MP2).[127] These type of functionals with parts of the MP2 correlation energy are defined as double-hybrid functionals.[128,129]

Within the framework of this Thesis, calculations at the unrestricted open shell were almost exclusively employed. The exceptions are the calculations on closed-shell systems with multiplicity 1 (singlet species), such as the precursor of thiyl radicals and 2,2,6,6-tetramethylcyclohexanone, abbreviated TEMCO, the analogous ketone of the nitroxide TEMPO, and an essential substance for the interpretation of the micro solvation driving forces and dynamics of the radical. For these systems, restricted closed-shell calculations were carried out, as it will be indicated throughout the next Chapters.

One of the major drawbacks of DFT functionals is the inability to describe London-dispersion forces appropriately.[115,130–132] London dispersion forces (or London dispersion) are an important element of structural stability but have been undervalued over the years. An emerged strategy to rectify this was the development of Grimme's three body-inclusive dispersion correction D3, which relies on the addition of a parametrised empirical dispersion correction terms to the electronic energy of the functionals.[122] These terms vary for the different functionals. Furthermore, damping functions are required to control the overlap of electron densities between adjacent atoms (short-range interactions), known as the Becke-Johnson damping (BJ).[122,123,125,126] This correction is based on a pairwise approximation, but one can account for three-body dispersion interactions using the Axilrod-Teller-Muto expression (abc).[133,134] This three-body dispersion interaction can be employed with ORCA software, but it is not included in Gaussian 16.

Ahlrichs (Karlsruhe)[106,107,135] basis sets were selected for predictions on the radical complexes and their components, namely def2-TZVP and def2-QZVP (abbreviated TZ and QZ throughout this work). As the series of hydrogen bond donors expanded over

time, starting from water, and ending in larger molecules such as *t*-butanol and phenol, the size of basis set was adapted. The def2-QZVP basis set is a better choice in terms of accuracy, as it will be shown in the section describing the TEMPO and water results, but def2-TZVP provides a better balance of accuracy and cost if the molecules under investigations are particularly large. On this account, the relative energies and spectral assignments using the results provided by QZ basis set were limited to the preliminary work on TEMPO and water clusters. The Cartesian coordinates of radical complexes obtained at the B3LYP level can be found in Appendix A.

Relative energy differences were corrected for vibrational zero-point energies and the spectral assignments were based on the computed harmonic frequencies, appropriately scaled. Since it is the first work on radical monosolvate complexes by FTIR jet spectroscopy, and the first reported work on nitroxides isolated in cryogenic matrices, a scaling strategy based on the OH vibrational stretching frequencies of well-established dimers and trimers of closed-shell molecules has proved to be essential for the correct assignment of the vibrational spectra and to validate the employed quantum chemical methods. The harmonic band positions were then scaled considering the harmonic experimental spectra of appropriated reference substances, such as TEMCO and water, methanol, *t*-butyl alcohol, and phenol dimers and trimers, depending on the experiment, as described in Chapter 4.

It is important to refer that the spectra of complexes with water isotopes were obtained considering the default atomic masses provided by ORCA program package of 18.00000 u (^{18}O) and 2.00141 u (D) for D_2O, and $H_2{}^{18}O$, respectively, and 1.00800 u (H), 12.01100 u (^{12}C), 14.00700 u (^{14}N), 15.99900 u (^{16}O), for all the remaining chemical species. Furthermore, calculations performed with ORCA software utilised a fine integration grid GRID5, and TIGHTOPT keyword, which define how tightly the energy optimisation will be performed, whereas Gaussian 16 the int=ultrafine and opt=tight setting were used for optimisations.

Computations performed on the sulphur-containing precursor and sulphur-centred radicals were mainly carried out using the Gaussian 16 software, as described in Chapter 5. The B3LYP hybrid functional (closed-shell and unrestricted open-shell variants) was employed together with Ahlrichs def2-TZVP basis set, with and without D3(BJ) dispersion correction, and with the largest Pople style basis set, 6-311++G(3df,3pd). Electronic isomerisation barriers were computed by relaxed scans (Gaussian 16 software package Rev. A03[120]), at unrestricted open-shell B3LYP/def2-TZVP from the pre-optimised structures. Except if otherwise specified, D3(BJ) correction was employed.

Table 4. Selected DFT functionals, including the multiplicity, type of dispersion correction, the basis set, and the software package. Input lines and more detailed information can be found in Appendices A and B.

Method	Multiplicity	Dispersion	Basis set	Program
B3LYP	1 and 2	D3(BJ,abc)	Def2-TZVP/QZ	ORCA 4.2.1
B2PLYP	2	D3(BJ,abc)	Def2-TZVP/QZ	ORCA 4.2.1
TPSS	2	D3(BJ,abc)	Def2-TZVP/QZ	ORCA 4.2.1
B3LYP	1 and 2	D3(BJ)/ -	Def2-TZVP	Gaussian 16
B3LYP	1 and 2	-	6-311++(3df,3pd)	Gaussian 16

3.3.3 DLPNO-CCSD(T)

Coupled-cluster theory using single and double, with perturbative triple excitations [CCSD(T)] has become the 'gold-standard' model of computational chemistry, being often used as reference for theory benchmarking purposes.[136] However, the method has an inherent drawback: the computational effort is extremely non-linear with the size O(N) of the molecules, and thus being affordable only for small systems.[137] This has motivated the development of further approximations that preserve the CCSD(T) accuracy while reduce the highly computational cost. An alternative is the DLPNO-CCSD(T) method[137–143], which stands for Density-fitted Local Pair Natural Orbital Coupled Cluster with Single and Double excitations, augmented by a perturbative treatment of Triple excitations, and can be assessed using ORCA software package. DLPNO-CCSD(T) provides a near CCSD(T) accuracy but at a significantly reduced cost and has allowed calculations of single-point energies of large systems, such as proteins.[144] To accomplish this, two main thresholds control the size of the correlation space: TCutPairs and TCutPNO. Additionally, the coupled-cluster equations are solved in a compact virtual space that is specific to each electron pair. This virtual space is spanned by a set of pair natural orbitals (PNOs).[145,146]

The calculations presented herein were limited to single-point DLPNO-CCSD(T) computations on the B3LYP computed geometries, using both closed-shell and unrestricted open-shell variants available in the ORCA software package. Dunning-basis sets[147,148], aug-cc-pVTZ, and in some cases aug-cc-pVQZ, with matching auxiliary basis sets for RI-approximation were selected.

The DLPNO-CCSD(T) method is consistent with the open-shell implementation[141–143], and thus applicable to the radical species and radical complexes studied herein. When the variable that commands the type of wavefunction to be computed was not specified in the input line, the program checked the defined multiplicity, and the computation was performed based on it by default. For the investigated closed-shell systems with multiplicity = 1, RHF/RKS (restricted Hartree-Fock and Kohn-Sham) were assumed, in both DLPNO-CCSD(T) and DFT calculations. For open-shell systems with multiplicity = 2, UHF/UKS were employed.

For weakly interacting systems, the "TightPNO" settings[149] are recommended in the ORCA manual for high accuracy calculations, and thus they were also employed here. Using these settings, TCutPairs and TCutPNO thresholds are set to 10^{-5} and 10^{-7}, respectively.

Local energy decomposition (LED)[150,151] analysis is a tool that allows for a more detailed understanding of the nature of intermolecular interactions by decomposing the DLPNO-CCSD(T) interaction energy between pairs of interacting fragments into individual contributions. Within the LED scheme, the interaction energy is decomposed into a repulsive intramolecular energy term defined as electronic preparation, along with a series of intermolecular energy terms that include electrostatic, quantum mechanical exchange, and London dispersion interactions. This approach has been reported in other contexts, but it was applied in this work using both closed- and open-shell variant of DLPNO-CCSD(T)/LED scheme to obtain further insights into the nature of the intermolecular interactions established in the studied closed-shell systems and open-shell radical complexes[25,26]. For this aim, two fragments were defined in the input file by assigning the atoms of each fragment with numbers one and two, as described in the Appendices A and B. The resulting LED output provided the electrostatics, exchange, and strong and weak pairs dispersion contributions.

Although the hydrogen bonds are primarily formed due to electrostatic interactions, these alone are often not sufficient to properly describe the energy and structure of hydrogen bonded clusters. LED analysis presented here has allowed a more detailed understanding of this type of interaction in terms of contributions to the overall stability of the investigated molecular clusters.

Dissociation energies of the weakly bound complexes presented further along this Thesis were determined by the difference between the electronic energies of the complexes E^{AB}, and the sum of the electronic energies of the 1:0 and 0:1 monomers E^{A}(radicals) and E^{B} (solvents) obtained at DLPNO-CCSD(T) level. An undesired effect commonly found on the studies of weak molecular interactions is the basis set superposition error (BSSE). It arises from the artificial stabilization of the dimer as the basis functions on monomer A help to lower the energy of monomer B, and vice versa. Therefore, the obtained energy

is biased in favour of dimer formation because of basis set effects. One usual solution is to correct this deficiency using the counterpoise correction introduced by Boys and Bernardi, where the calculation of the interaction energy between the two monomers with a basis set that includes both basis functions for each fragment as well as those for the dimer. However, counterpoise corrections tend to overestimate BSSE.[152,153] Indeed, for local correlation methods, such as DLPNO, the counterpoise correction is often negligible and, in some cases, disadvantageous since it can lead to less accurate results compared to the non-corrected ones.[154] Counterpoise corrections were not considered in the present study.

Chapter 4

Vibrational Spectroscopy and Dynamics of Solvates of Nitroxide Radicals[25,26,155]

The Introduction and the subsection 4.1 of this Chapter are based on the previously published and submitted articles:

E. M. Brás, T. L. Fischer, M. A. Suhm, The Hydrates of TEMPO: Water Vibrations Reveal Radical Microsolvation, *Angew. Chemie Int. Ed.* **2021**, *60*, 19013–19017.

E. M. Brás, C. Zimmermann, R. Fausto, M. A. Suhm, Benchmarking the Anisotropy of Nitroxyl Radical Solvation with IR Spectroscopy, *Phys. Chem. Chem. Phys.* **2023** (submitted).

Nitroxide radicals[156] display a remarkable reactivity towards different environments due to their molecular and electronic structures. These molecules have multiple uses in the fields of organic synthesis[10], oxidation catalysis[157], polymerization reactions [7,10,158], solvation dynamics[159,160], proton-coupled electron transfer energetics[161,162], or biomolecular structure determination[163], being used as spin traps[13] for probing molecular structures. 2,2,6,6-Tetramethylpiperidinyloxyl (TEMPO) has been extensively

investigated[164,165], in particular in solution[160]. Nitroxide radicals can be quite stable in protic solvents, which are likely to coordinate the N-O• radical centre[166], leading to non-reactive metastable complexes. This stability is defined by sterically shielding substituents (bulky *tert*-butyl groups) at the nitrogen-bound α-carbon atoms, which supress dimerisation and offer secondary hydrogen bond interactions with the solvent. Hence, a systematic investigation of the coordination geometry between the protic solvents and the N-O• centre in the gas phase is essential for the understanding of the microsolvation driving forces between radical and non-reactive closed-shell molecules, and to disentangle global solvent effects (macrosolvation) from local solvent effects. This microsolvation method fits itself very well to the testing of quantum chemical methods, in comparison to macrosolvation processes, which require further approximations. As soon as the solvation by hydrogen bridges between solvents and radicals is well-known and characterized, reactive processes such as hydrogen atom transfer[167] may be explored and modelled and described more accurately using quantum chemical methods. In the lack of microwave structure investigation of monomers and solvates, infrared spectroscopy appears a powerful technique that can contribute for a better understanding of the intermolecular forces and dynamics, if low temperatures and an inert environment with the reduction of further solvent molecules are attained. These conditions can be achieved by both matrix isolation[39] and supersonic jet expansions,[168] although the latter is the preferred method for small molecular clusters preparation. It provides a better connection with theory because there is no need to model the environment, while the matrix environment is not neglectable. However, there are disadvantages in relation to the first one: the detection sensitivity suffers from the transient observation of the species, and it thus requires the use of long slit nozzles and pulsed operations[97] when combined to FTIR spectroscopy, while matrix isolation is a powerful tool for metastable complexes of reactive species[20,169,170]. This Chapter comprises the investigations on an exceptionally stable radical, the persistent TEMPO,[25,26] and one of the simplest bulky di-*tert*-butyl-nitroxide radical DTBN (see Figure 7), and their coordination to different solvents through both FTIR jet and matrix isolation spectroscopies.

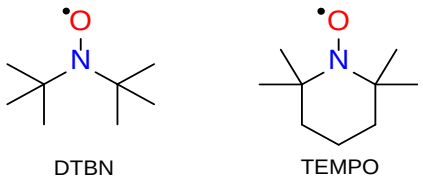

Figure 7. Persistent TEMPO (2,2,6,6 Tetramethylpiperidinyloxyl) and DTBN (di-*tert*-butyl-nitroxide) radicals investigated in this work.

These investigations have started by vibrationally characterizing the mono- and di-hydrate of TEMPO in vacuum isolation by jet FTIR spectroscopy[171]. The direct comparison with the experimental results for the closed-shell analogue 2,2,6,6-tetramethylcyclohexanone (abbreviated TEMCO; see Figure 8) has been proved to be crucial for the interpretation of the vibrational dynamics and of the microsolvation driving forces and the vibrational dynamics in TEMPO-water complexes, due to the remarkable universality across several ketone hydrates.[101]

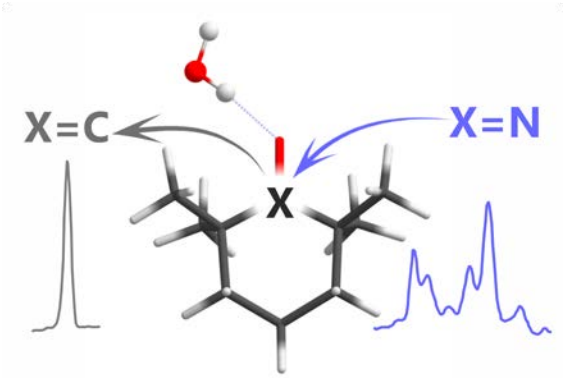

Figure 8.The mono-solvates of the persistent open-shell TEMPO compared by analogy to the closed-shell ketone analogue TEMCO are vibrationally characterized at low temperature by jet and matrix isolation FTIR spectroscopies and quantum chemical calculations. Taken from Refs.[25,26], and licensed under CC BY.

After the interpretation of TEMPO and water spectra, the following strategy went through the variation of the protic solvent for a better understanding and support of the previous results, and for testing the electronic structure calculations, which has proven to be useful for other case studies[172]. It comprised not only water and its isotopologues (D_2O, $H_2{}^{18}O$ and HOD), but the coordination with other four hydroxyl containing solvents, namely methanol ($HOCH_3$), *t*-butanol ($HOC(CH_3)_3$), and phenol (HOC_6H_5), in comparison to the less stable radical DTBN.

The substituents flanking the N-O$^\bullet$ radical centre surrounded by two tertiary carbon atoms in both TEMPO and DTBN may offer a similar environment for the solvent coordination, but the closing into a six-membered ring in the least strained chair conformation by an additional carbon atom in TEMPO has significant effects. Furthermore, the methyl groups attached to the α-carbons are hindered regarding their relative torsion, leading to an increase in stability and the room temperature phase appears a volatile solid, while the DTBN is a liquid. Despite of the increased radical stability in comparison to DTBN, the solvent coordination with the radical centre of TEMPO and DTBN share a common pattern, as it will be discussed throughout this Chapter. This common descriptor has been introduced for TEMPO radical[25,26] and

distinguishes three coordination positions: a tightly embedded top position (t), an opposite and more open coordination (o) exposing the N atom and making it more accessible to coordination, and the close to the ring plane (p) position (see Figure 9), which experiences most steric hindrance and/or offer secondary interaction with the methyl groups of DTBN radical.

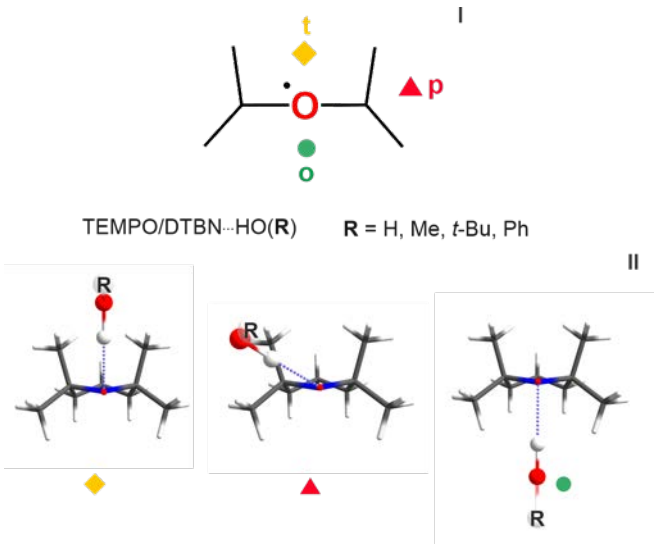

Figure 9. The clusters of TEMPO and DTBN with solvent molecules ROH share an up to three-fold isomerism (I) with the OH group docking close to the nitroxide plane p (▲, red), on the tighter site t (◆, orange) or on the open side o (●, green), of the α-alkyl groups. The coordinating sites are illustrated in the structures of TEMPO monosolvates (II).

In the present Chapter, the close analogies between the complexes TEMPO and DTBN, but also distinguishing differences between the favoured mono-and di-solvation docking sites of the two radicals as a function of the OH-containing solvent are presented.
The experimental findings reported herein were based on theory-assisted assignments and based on non-radical reference computations for a careful and common interpretation of the experimental IR spectra, which was necessary due to the lack of available gas phase spectroscopy investigations of radical solvent complexes. As described herein, theoretical calculations in the harmonic approximation allow the description of the vibrational spectra of these solvated radical species rather consistently, at a variety of density functionals, with the use of non-radical complexes as bridge. The reason for this is related to the related anharmonic effects in both radical and non-radical complexes, that causes a systematic cancellation of errors.

4.1 Radical Hydrates

TEMPO radical monohydrates and dihydrates have been investigated and characterized by FTIR supersonic jet spectroscopy for the first time, in collaboration with Dr. Taija L. Fischer. The experiments revealed that TEMPO radical is stable enough to be measured for several hours of compression and expansion cycles in the new gratin jet setup[96]. This confirmed TEMPO remarkable metastability, even when exposed to humid conditions for many hours. The comparison with the closed-shell analogue has revealed a less directional hydrogen bond with the water molecule, whereas the OH stretching vibration of the bonded water is found to be strongly downshifted due to the stronger formed bond. The dihydrated TEMPO structure reveals that the second water solvates the oxygen of the first water, taken the advantage of further interactions with the nitrogen centre of the nitroxide N-O$^{\bullet}$ and the ring centre.

4.1.1 TEMPO Monohydrates and Dihydrates: Comparison with a Closed-Shell Analogue

Closed and open-shell quantum chemical calculations at B3LYP/def2-QZVP[103,104,106,128] with D3 three-body inclusive dispersion corrections[122] and Becke-Johnson damping,[123–126] (using the ORCA[117] software package; see Chapter 3 and Appendix A for computational details) in the double harmonic approximation predict up to three types docking sites between the first water with the N-O$^{\bullet}$ or C=O centers (see Figure 10). The oxygen of the water molecule may be embedded by the two geminal methyl groups on one half of the puckered ring, optimizing C-H$\cdots$O dispersive interactions close to the ring plane (p for planar or parallel position). Instead, it can be in or near the symmetry plane of the TEMPO/TEMCO molecule and either align with the two axial methyl groups on one face of the ring (t for tight or top) or otherwise point to the open side (or opposite side) of the ring framed by the two equatorial methyl groups (o for open or opposite or orthogonal). These three docking sites to probe the anisotropy of the X-O (where X correspond to C/N atoms) bond along with nonbonded interactions with the molecular scaffold. The bond anisotropy is certainly different for the sp^2 hybridized C=O oxygen and the nearly planarized N-O bond,[173] whereas the nonbonded interactions should be similar for both species. Thus, the difference between the N-O and C=O bonds towards hydrogen bonding can be probed by the relative abundance of 1:1p, 1:1t and 1:1o monohydrate isomers. Indeed, the calculations predict that the three structures (p, t, and o) are closely spaced minima for the TEMPO monohydrate, whereas the p

conformation is the most attractive for the TEMCO monohydrate because it is compatible with oxygen lone pair hydrogen bonding (Figure 10).

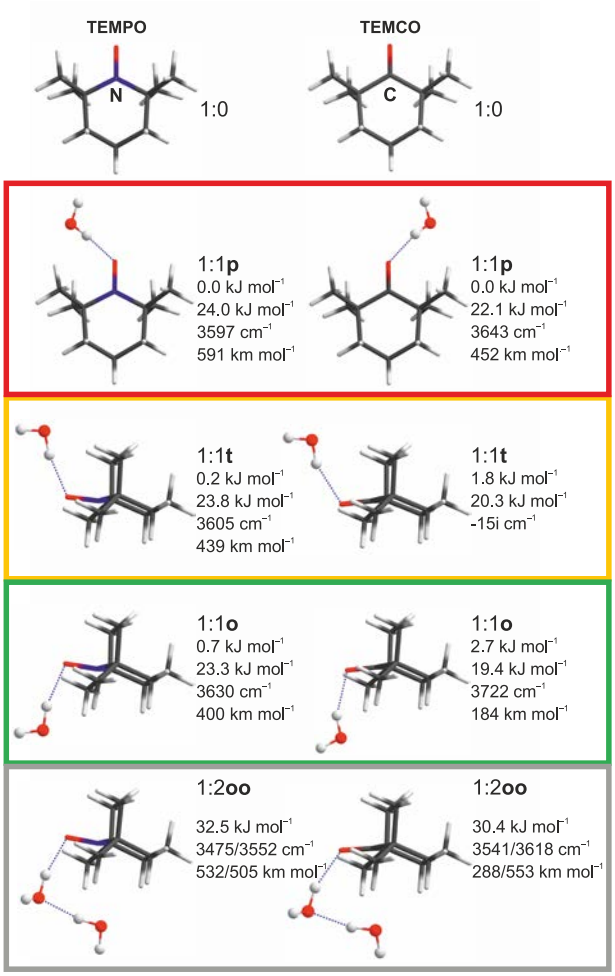

Figure 10. Monomers, 1:1 and 1:2 hydrates of TEMPO nitroxide and TEMCO ketone along with the harmonically zero-point corrected relative energies (in kJ mol^{-1}), dissociation energies (in kJ mol^{-1}), unscaled harmonic p···HOH, t···HOH, o···HOH, and oo···HOH wavenumbers (in cm^{-1}) and intensities (km mol^{-1}) were obtained at (U)B3LYP and B3LYP-D3(BJ, ABC)/def2-QZVP level. The hydrate conformations are framed in colours which are used in Figure 11 to encode the spectral predictions. Taken from Refs.[25,26], and licensed under CC BY.

For TEMPO, all the three structures are minima in the potential energy surface. For TEMCO, the t conformation becomes a saddle point, whereas the o conformation a high-energy lying minimum. For the nitroxide, the torsional p/t/o energetics around the N-O$^\bullet$ moiety is so delicate that replacement of the (U)B3LYP electronic structure level by unrestricted open-shell DLPNO-CCSD(T)[137–139,143] reverts the order of the zero-point corrected energies of the t and o isomers (see Table 5), while p persists as the global minimum. Indeed, the interconversion barriers are shallow, as represented in Figure A1

of Appendix A. On the other hand, the collapse of the population of TEMCO hydrates into the p conformation is more likely to occur according to the calculations. For both analogue compounds, the second water is predicted to coordinate with the first water by cooperative hydrogen bonding and reorientates the first water into the o structure, which is favoured because it makes possible the interaction with the positively polarized C or N and the entire open ring face. This 1:2oo cluster is therefore predicted to be by far the most stable arrangement for both TEMPO and TEMCO. This computational prediction of the o structure for both TEMPO and TEMCO dihydrates and a very different monohydrate binding situation for TEMPO and TEMCO had to be tested by vibrational spectroscopy.

Table 5. Relative energies (ΔE_0 kJ mol^{-1}) of the 1:1 TEMPO hydrates, showing the subtle balance between different coordination directions.

TEMPO	$\Delta E_{0\ (U)B3LYP}$ [a]	$\Delta E_{0\ DLPNO\text{-}CCSD(T)}$ [b]
p···HOH	0.0	0.0
t···HOH	0.2	0.7
o···HOH	0.7	0.2

[a] Harmonically zero-point corrected (U)B3LYP-D3(BJ,ABC)/def2-QZVP relative energies. [b] Harmonically zero-point corrected closed[137] and unrestricted open-shell[143] DLPNO-CCSD(T)/aug-cc-pVQZ//(U)B3LYP-D3(BJ,ABC)/def2-QZVP relative energies (in kJ mol^{-1}).

4.1.2 Gratin-Jet Spectra of TEMCO/TEMPO

The experimental spectrum in the OH stretching region of TEMCO (trace A of Figure 11) fits well into what one would expect from other ketone hydrate clusters.[101] It was collected by the compound-economic FTIR slit jet cluster spectrometer with gas recycling referred in Section 3 of this Thesis (see section 3.2.2 for the gratin jet principle, and the Appendix A for experimental details and scaling factors).[96] In the IR spectrum, one can observe a dominant peak (p···HOH) as a result of the water docking to one of the equivalent lone electron pairs of the oxygen atom of TEMCO, embedded into the two α-methyl groups which shield the lone pair, roughly in the ring plane. Interestingly, there is a little satellite peak (b2lib) which we attribute to a recently discovered universal Darling-Dennison resonance involving the bending overtone of the water molecule (b2) and a hydrogen bond librational motion (lib).[101] Because of its small intensity and large separation, is possible to derive an anharmonic coupling constant between the two vibrational states of 11±2 cm^{-1} for TEMCO (see the Appendix A, subsections 3.3 and

3.4), in acceptable agreement with other ketone and water clusters. The free OH counterpart of the solvating water molecule gives rise to a weaker peak at much higher wavenumber (···HOH; see figure 11), near the water rovibrational lines (H_2O). Furthermore, one of two predicted hydrogen-bonded OH absorptions of the 1:2 complex (oo···HOH, see the Appendix A, subsection 3.5, for experimental cluster size discrimination), is observed, while the other one appears to be broadened and overlapped with other resonances. It is also of note that the observed OH stretch is actually predicted to be the more IR-intense of the two bands (see Figure 10 and trace B of Figure 11), although it is less downshifted from water monomer. This is not typically observed for hydrogen-bonded complexes with weakly coupled oscillators and different from TEMPO, because the more strongly shifted water is forced into an orthogonal position relative to the carbonyl lone pairs. The computed harmonic predictions (trace B of Figure 11) fit fairly well the experimental spectrum, once reasonably scaled ($\times$0.959 for the free and $\times$0.975 for the hydrogen-bonded OH fundamentals, the latter also supported by a close water dimer match calculated with the same method), with the typical deficiency of DFT methods, specifically the relative overestimation of the shifts in cooperative hydrogen bonding. As expected, there is no experimental evidence for the higher-lying (o) or transition state (t) structures for the TEMCO monohydrate predicted by computations, in agreement with the expectation that a carbonyl group is highly anisotropic regarding solvation, which evidently favours the lone pair solvation as an alternative of orthogonal π solvation. Thus, the first water is pointed into the effective ring plane by the anisotropic C=O bond, whereas the second water likely enforces π-type docking of the keto group of the first water to solvate the carbonyl group.

The two uppermost traces of Figure 11 afford a helpful setting for the interpretation of the much more complex spectrum of the hydrates of the structurally analogous TEMPO nitroxide, where the closed shell carbonyl C is replaced by an open shell nitrogen center. Instead of a distinct prominent (p···HOH) peak, there is a more complex spectrum of at least 5 bands (trace C, Figure 11), downshifted by approximately the theoretically predicted amount from TEMCO (note that same scaling factors were used; see trace E), due to stronger hydrogen bond interaction. For the 1:2 complexes (oo···HOH, Figure 11), which can be surely discriminated from the monohydrates by concentration variation (see the Appendix A, section 3.5 regarding the size discrimination), the pattern seems to be actually less complicated than for TEMCO, with the two expected hydrogen-bonded OH stretching modes observed as single peaks of similar intensity, somewhat downshifted from the scaled predicted frequencies. Once more, the downshift compared to TEMCO confirms stronger hydrogen bonding to the nitroxide centre. Additionally, the free OH vibration (···HOH, Figure 11) is predicted very consistently in both TEMPO and TEMCO.

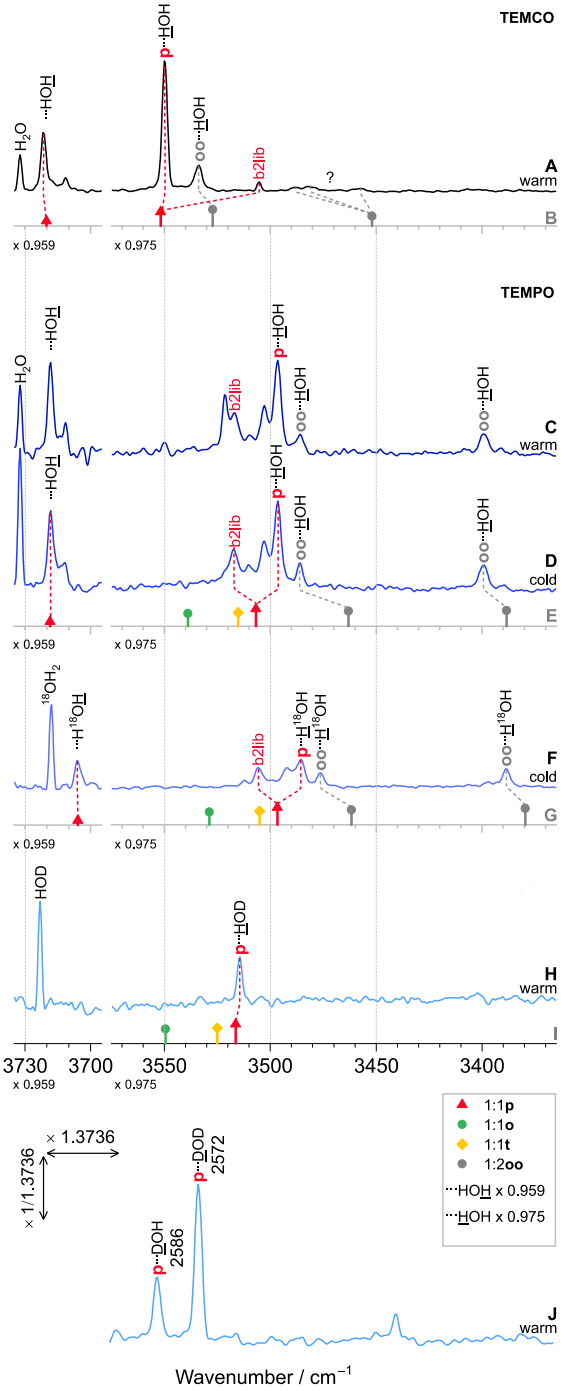

Figure 11. Jet FTIR spectra of TEMCO (A) and TEMPO (C and D) with H_2O, and TEMPO with different isotopologues of water: $H_2{}^{18}O$ (F), HOD (H), DOH and D_2O (J, same spectrum as H), in warm (0.75 bar of He) and cold (0.375 bar of He and 0.375 bar of Ne mixture) expansions, revealing the dominance of p over t and o complexes (from top to bottom, see text for further discussion). Scaled harmonic spectra of TEMCO (B) and TEMPO (E,G,I) from closed- and open-shell B3LYP-D3(BJ,ABC)/def2-QZVP computations for p (▲, red), o (●, green), and t (◆, orange) 1:1, and for oo (●, gray) 1:2 hydrates are shown. Taken from Refs.[25,26], and licensed under CC BY.

Table 6. Experimental wavenumbers of TEMCO and TEMPO hydrates (in cm^{-1}), unscaled computed wavenumbers (in cm^{-1}) and absolute intensities (in km mol^{-1}) at unrestricted open-shell B3LYP-D3(BJ,ABC)/def2-QZVP level.

Structure	Experiment	Computed	
	Jet-FTIR	$\tilde{\mathcal{V}}$	I
TEMCO···HOH			
p···HOH	3550	3643	452
o···HOH	-	3722	184
b2lib	3505		
oo···HOH	3534 / 3488? / 3482? /3457	3618 / 3541	553 / 288
p···HOH	3722	3879	91
TEMPO···HOH			
p···HOH	3497	3597	591
t···HOH	-	3605	439
o···HOH	3521? (He)	3630	400
b2lib	3517		
oo···HOH	3486 / 3399	3552 / 3475	505 / 532
p···HOH	3718	3878	85
p···H^{18}OH	3486	3586	592
t···H^{18}OH	-	3595	441
o···H^{18}OH	3512? (He)	3619	402
b2lib	3506		
oo···H^{18}OH	3476 / 3389	3550 / 3466	490 / 547
p···H^{18}OH	3706	3864	77
p···HOD	3514	3607	659
t···HOD	-	3616	505
o···HOD	-	3641	469
p···HOD	-	2819	10
p···DOD	2572	2615	291
t···DOD	-	2621	213
o···DOD	-	2638	191
p···DOD	2751	2836	79
p···DOH	2586	2629	337
t···DOH	-	2635	256
o···DOH	-	2653	237
p···DOH	-	3871	40

Indeed, the main faced spectroscopic challenge is to understand the complexity of the IR spectra of the TEMPO monohydrate around 3500 cm^{-1}. There are several possible reasons for the observed complexity: the radical character favours three local minima (p, t, o) into close energetic vicinity (Figure 10), and each of them could additionally undergo a b2lib-like resonance, which has been reported in this spectral range for monohydrates.[101] Thus, 6 peaks would be explainable based on TEMCO IR spectrum and the different torsional potential for a water molecule around the hydrogen bond acceptor. Using neon as carrier gas (trace D, Figure 11), affordable due to the recycling concept of the jet spectrometer (as previously explained in section 3),[96] removes a single peak from the manifold, but leaves the other 4 more or less unaffected. This indicates that the vanishing peak must belong to a metastable isomer of TEMPO monohydrates (scaled harmonic predictions indicate o···HOH as the most likely, and also the electronic energies, as this isomer is the second-lowest energetic structure after CCSD(T) correction and separated by moderate barriers from its torsional isomers). The assignment of o isomer also indicates that it does not undergo a strong b2lib resonance, which might be reasonably explained by the very floppy nature of the o docking site. The assignment of the 4 left peaks requires thus further efforts. It is plausible to assign the dominant peak to the most stable isomer (p···HOH), but its position and intensity is somewhat low, compared to the harmonic prediction in trace E and the TEMCO case. Considering a similar dark vibrational state and anharmonic coupling constant as in TEMCO, it is reasonable to consider the second-strongest peak (labelled b2lib, Figure 11) as the most likely candidate for an assumed coupling partner. With this assignment, there are still two remaining and weaker than the previously referred, peaks left. They might be due to the isomer t, which may not be observed within the supersonic expansion, or due to other vibrational resonances. The dominant p/b2lib assignment of the complex spectrum is confirmed by its centre of gravity, which fits the scaled harmonic prediction (trace E, Figure 11) and has a better correspondence of each individual transition. Considering all these uncertainties, an anharmonic coupling constant of $9\pm2\ cm^{-1}$ can be derived (see the Appendix A), which is of the same order of magnitude as for TEMCO and other ketone hydrates.

Additional support is given by ^{18}O-substituted water (trace F, Figure 11), which induced an almost uniform downshift of the 4-peak pattern (and also the 1:2 cluster signals), as a result of the mass increase, and as predicted by harmonic calculations (trace G, Figure 11).

The strongest evidence for the dominant p 1:1 hydrate of TEMPO complexes is provided with partial deuteration of the water. This substitution of regular water by D_2O enormously simplifies the spectrum in the OH stretching range (trace H, Figure 11), even without neon as a cooling enhancer. In this case, the b2lib resonance is below the

detection limit for p···HOD, since its dark state is shifted far away. The t and o isomers are no longer observed in the spectrum, maybe due to slightly different zero-point energy destabilization in the isotopologue and more quantitative relaxation. Thus, a single peak remains and matches reasonably well the scaled harmonic prediction for p···HOD (trace I, Figure 11). For completeness, trace J also displays the OD window for the same expansion with a reduced-mass scaling of the wavenumber axis (and inverse scaling of the absorbance to preserve the peak area). It demonstrates the high degree of deuteration and explains why no undeuterated signals are left in trace H. Consequently, the final interpretation of the TEMPO monohydrate spectrum is less complex than appeared, as it essentially consists of a dominant in-plane docking of the first water (isomer p). In the main isotopologue, this interpretation is more complex due to the anharmonic resonance and because of the presence of at least another isomer. Furthermore, the 1:2 hydrate of TEMPO exchange the in-plane coordination p to orthogonal coordination of the nitroxyl group, because it favours the coordination of the second water molecules with the nitrogen atom of the NO• bond. The comparison with the analogous ketone TEMCO indicates that for low temperature and suitable isotope substitution, the dominant species are analogous (p for monohydrates), although the larger anisotropy of the C=O bond shifts competing isomers significantly higher in energy or converts them to transition states. The second water molecule recovers the similarity between the two cyclic species, because its heterocyclic interaction controls any anisotropy advantage of the first in plane water and imposes orthogonal direction to the open side of the ring o.
The effective bright state position of the hydrogen-bonded OH stretch, which would be observed if the perturber state were far away, was also of interest. This position is encoded in the relative intensity of the two observed bands (OH stretching and b2lib), assuming that the perturber holds no intrinsic intensity but takes all its infrared activity from the bright stretching state. For TEMCO, the intensity ration is (10 – 20) : 1, which means that the bright state is very close to the OH stretching vibration near 3547±1 cm^{-1}. For TEMPO, the uncertain assignment of the weak signals lead to an intensity ratio between 1:3 and 1:2 in favour of the more downshifted signal. This leads to a bright state localization near 3503±2 cm^{-1} and somewhat less guidance from experiment for theoretical predictions.
In addition to TEMPO, the related di-*tert*-butylnitroxide (DTBN) was also investigated in the gratin jet spectrometer. Whereas TEMPO was found to survive several hours of gas recycling in the presence of water, DTBN decays significantly during the first hour of measurements, but it was already possible to assign a dominant hydrogen-bonded OH stretching at 3484 cm^{-1} (see the Appendix A, subsections 3.3 and 3.4).
The radical character of the radical-water hydrogen bond stimulated the inclusion of a radical hydrate (DTBN) monohydrate into the training set for the blind challenge, called

HyDRA, (for Hydrate Donor Redshift Anticipation). For the blind challenge on the predictability of hydrogen bonded water stretching wavenumbers, the experimental values for the OH stretching mode and the b2lib perturber state were of interest, as well as the effective bright state position of the hydrogen-bonded OH stretch. The inclusion of radicals was encouraged with the aim of of increasing the molecular diversity in the planned competition and generalizing the importance of anharmonic resonances for weak hydrogen bonds of monohydrates.

4.1.3 Gratin-Jet Spectra of DTBN

Analogous jet expansion experiments were carried out with di-*tert*-butyl nitroxide (DTBN) mixed with water and He (warm) or He/Ne (cold) carrier gas (Figure 12).
Depending on the carrier gas and water content, more or less rapid decomposition in the gas cycling experiment was monitored, with estimated half-life of 1 h or less, as determined by the decay of the dominant hydrate signal at 3484 cm^{-1}. This should be compared to a half-life well above 24 h for TEMPO under similar conditions. The decay products could not be identified, although the spectrum suggests that the product form weaker and stronger hydrogen bonds with the co-expanded water than DTBN, as shown by the appearance of absorption signals in the region of 3600 and 2800 cm^{-1}. Due to the complexity of the surfaces to which the recirculating gas flow is exposed under different pressure and temperature conditions, a more quantitative analysis of the decay kinetics is not indicated.
For the purpose of quantum-chemical benchmarking, the strong signal at 3484 cm^{-1} directly observed after mixing must be due to the most stable monohydrate of DTBN. The measured spectra in He/Ne suggest that there are neither significant resonance signals nor significantly populated competing isomers in this case. Such evidence makes DTBN monohydrate more suitable for performance assessments of scaled harmonic calculations of radical hydrate band positions than the spectrally complex case of TEMPO monohydrate. However, the faster decay of the radical in the gratin jet prevented a reliable statement on weaker spectral contributions, and further investigations in another jet set-up are required.

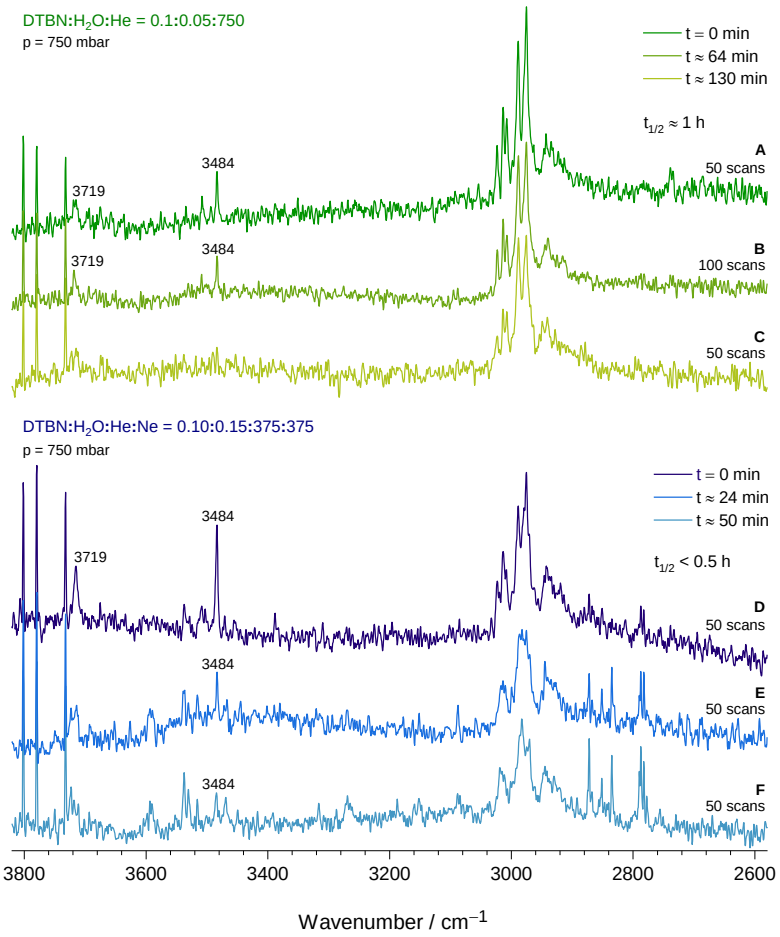

Figure 12. Monohydrate and spectral decomposition evidence for DTBN-water co-expansions in the gas recycling experiment. The upper three traces (green) refer to sub-stoichiometric amounts of water in a He expansion, the lower three traces (blue) to an excess of water in a colder He:Ne expansion. The signal at 3484 cm^{-1} corresponds to the OH_b vibration of the most stable monohydrate of DTBN, the signal at 3719 cm^{-1} may include OH_f contributions from the monohydrate. Any secondary peak due to a resonance or other conformation of the 1:1 complex is at least 4 times weaker in a cold expansion. The half-life of DTBN in the cycling gas and thus its monohydrate in the jet expansion decreases from about 1 h in the warm expansion to < 0.5 h in the colder, more water-rich expansion. In the warm expansion, the decomposition products are not spectrally prominent, but in the cold expansion, they are revealed by water complexation and the spectral spread (2700 – 3600 cm^{-1}) indicates weak and strong hydrogen bonds involved. For TEMPO and its monohydrate, no significant decomposition could be observed for a day of continuous operation, placing its half-life well above 24 h. Taken from Refs.[25,26], and licensed under CC BY.

4.2 Benchmarking the Anisotropy of the Radical Solvates

As referred above in this Chapter, di-*tert*-butylnitroxide (DTBN) and 2,2,6,6-tetramethylpiperidinyloxyl (TEMPO) solvated by one or two water, methanol, *t*-butyl alcohol, or phenol molecules, were detected for the first time in by FTIR-jet spectroscopy. The IR experimental findings presented herein were based on theory-assisted assignments, using non-radical reference calculations for the interpretation of the vibrational data of DTBN and TEMPO solvates, as will be described in the next subsection. Systematic structural preferences are adopted, depending on the conformational rigidity of the nitroxide. The assignment of the organic radical solvates are collected into an experimental benchmark data set and used to evaluate the spectral predicting ability of several DFT methods, as previously performed for other chemical systems.[174] One of the main aims of these investigations was to find methods which offer reliable spectral predictions for these recently detected radical microsolvates at an inexpensive computational cost.

4.2.1 Computational Details

The structures of radical solvates and the non-radical fragments were computed at the at the B3LYP-D3BJ/def2-TZVP level [103,104,128] (unrestricted open-shell and closed-shell, respectively), using Becke-Johnson-damped [123–125] Grimme D3 dispersion correction with three-body inclusive correction term[126]. To find all the energy minimum structures a procedure described in Chapter 3 and in section 4 of Appendix A (see also additional detail of the computations listed herein). Further reoptimisations were performed at unrestricted open-shell B3LYP-D3BJ/def2-TZVP (triple, abbreviated TZ) and def2-QZVP (quadruple zeta, abbreviated QZ) levels[103,104,106,128]. The robustness of some predictions was tested with other DFT functionals (including TPSS and B2PLYP) [175,176] and additionally by computed single point energies to stationary points at unrestricted open-shell DLPNO-CCSD(T) level [137–139,143], using aug-cc-pVTZ[177] basis set. The isomerisation barriers were determined by relaxed one dimensional scans along different coordinates to evaluate the interconvertibility between the computed isomers (t, o, p) under jet expansion environment. The interconvertibility is less prone to occur in a supersonic expansion for isomerisation barriers significantly surpassing 5 kJ mol^{-1}[178].

4.2.2 Scaling Strategy

To take advantage from the analogy between the different nitroxide radicals and solvents, a detailed scaling strategy of (U)B3LYP-D3BJ harmonic normal modes prediction for spectral assignments was required. This adopted scaling method is explained prior to the discussion of the experimental results, to clarify and to reduce the explanations in the next subsections. The established harmonic theory scaling factor of 0.975 for the hydrogen-bonded OH stretching in the previously reported TEMPO and water complexes[26] was adopted to all the radical solvates studied in this work. Using the 0.975 scaling factor, computed wavenumbers for the p and o isomers of DTBN-HOH are 3504 cm^{-1} and 3010 cm^{-1}, respectively, while the experimental IR value is 3509 cm^{-1}. Theory matches the o isomer and is thus accurate. For the more stable t complex, the more intense band at 3483 cm^{-1} has a good correspondence with the predicted band at 3488 cm^{-1}. In this case, theory is marginally too high. These deviations between harmonic calculations and experiment are in the expected range and depend on a large amount of error compensation due to similar anharmonicity and an apparently more than qualitative description of the significant intermolecular interactions by the used density functional (experimental and computed spectra can be found Table 9 in page 61 of this subchapter and in Appendix A).

To extend some of the error cancellation to all the chemical systems investigated in this work, such as radical-alcohol 1:1 solvates, radical-phenol and also radical disolvates, we used harmonic reference calculations for the most IR-active OH stretching vibrations in water dimer, water trimer, methanol dimer, methanol trimer, *t*-butanol dimer and phenol dimer, which all do not possess a radical character and are thus impartial reference systems (see the OH stretching vibrations are presented in Table A42 in Appendix A). The computed TZ harmonic wavenumbers of these homodimers and trimers have to be shifted by a certain value to match the experiment without using scaling factors. For methanol dimer, the shift has to surpass that of water dimer [179–181] by 8 cm^{-1} (in this case, a downshift). For the *t*-butanol dimer, the required downshift correction is 48 cm^{-1} and for phenol dimer, it is 53 cm^{-1}. For methanol trimer, it is required an extra downshift of 9 cm^{-1}, while for water trimer the upshift by 28 cm^{-1} is necessary. These values also indicate that the bulky dimers are described quite differently by DFT theory than the reference system (water dimer). Thus, the correction shifts varying from $+28$ cm^{-1} to -53 cm^{-1} in relation to water dimer predictions assure that any harmonic (U)B3LYP/TZ predictions of the related homocluster spectra would parallel the one for water dimer. We carried out the homocluster corrections and applied them to the radical solvates, in which one solvent unit is replaced by the nitroxide radical (DTBN or TEMPO), taking into account that the DFT error including anharmonicity effects is qualitatively

transportable in those cases from a closed shell solvent cluster to the radical solvent cluster with the same number of units. These harmonic shifts that take into account the solvent changes were applied, and were followed by a uniform scaling factor of 0.975, previously determined for TEMPO hydrates.[26] This scale factor was employed to make a minimally biased prediction of the experimental band value for other radical-solvent complexes.

This is exemplified as follows: after switching from water to methanol ($HOCH_3$), as single solvent molecule coordinated to the radical, we first corrected the harmonic OH stretching estimation for this radical-methanol cluster by the difference (8 cm^{-1}) between the experiment and theory gap for both $(HOH)_2$ and for $(HOCH_3)_2$[179–181]. Concretely, the experimental OH stretching of $(HOH)_2$ is observed at the 3602 cm^{-1} and harmonical computed value is predicted at 3666 cm^{-1}, i.e. 64 cm^{-1} too high. The $(HOCH_3)_2$ signal is observed at 3575 cm^{-1} and harmonically predicted at 3647 cm^{-1}, 72 cm^{-1} too high. Consequently, the estimation at 3601 cm^{-1} of DTBN-$HOCH_3$ (o) is first downshifted by (72−64) cm^{-1} = 8 cm^{-1} to correct for the switch in the OH solvent and then scaled by 0.975 to give 3503 cm^{-1}, while this method applied to (p) yields 3496 cm^{-1}. This is to be compared to 3496 cm^{-1} and 3470 cm^{-1} experimental values. The same procedure applied to the more stable (t) complex of DTBN-$HOCH_3$ (harmonically predicted at 3575 cm^{-1}) yields 3478 cm^{-1}, which resembles more closely (although overestimated) to the stronger signal at 3470 cm^{-1}. Despite of the closest proximity of the predicted value for the p isomer and the weaker band at 3496 cm^{-1}, a consistent assignment picture emerges for the t and o isomers of DTBN-$HOCH_3$. The theory overestimation for t structures is consistent across the two solvents HOH and $HOCH_3$, as well as it is the overestimation for the o isomer of DTBN and TEMPO (as will be described in more detail later in this section 4.2). The noted underestimation of the computed frequencies for the p isomer of TEMPO-HOH and $HOCH_3$ may assist a future assignment of the o isomer in combination with DTBN, instead of p. This shows the utility of scaled and shifted harmonic calculations bridging the spectra of two related systems, by taking into account the spectra of pure solvent clusters.

4.2.3 DTBN and TEMPO Monosolvates

DTBN structures are predicted to be two enantiomers with C_1 symmetry, which are easily interconvertible due to the twisting of the *t*-butyl groups. The global minimum of TEMPO has a chair-like conformation and is to a good approximation C_s symmetric.

Regarding the electronic structure, the NO moiety is evidently more isotropic than that of ketones concerning the angle of solvation, as confirmed in the previous work on TEMPO/TEMCO hydrates.[26] Whereas the preferential in plane coordination (p) of the oxygen by the first hydrogen-bonding is found for ketones, the N-O radical centre offers

the option of coordinating close to the plane (p) or on the tighter (t) or more open (o) positions (Figure 13). DTBN and TEMPO share this common pattern, but the chair puckering of the ring in TEMPO and the facile torsion of the *t*-butyl groups of DTBN lead to different solvent docking preferences.

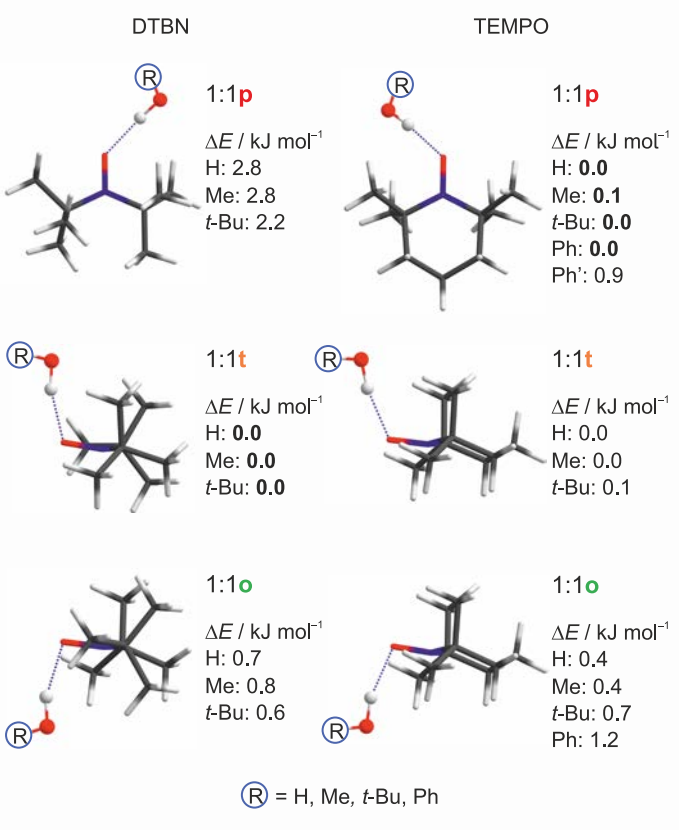

Figure 13. Structures of DTBN and TEMPO monosolvates as a function of OH-containing solvent. Relative zero-point corrected energies (ΔE in kJ mol^{-1}) of the docking sites are given. Reproduced from Ref.[155] with permission from the PCCP Owner Societies.

For DTBN, all explored solvents are predicted to prefer the t docking site. The open and opposite coordination site o is slightly less stable, but it becomes the most favourable structure for the second water coordination, as it allows a direct interaction with the nitrogen atom of the N-O bond, which is more accessible in o than in p or t. The same is observed in TEMPO dihydrates[26] (see Figures A3, A4 and A5 in Appendix A). The in-plane position of DTBN clusters is considerably less stable for the herein investigated solvents. For TEMPO solvates, the latter is predicted to be preferred, which is closely followed by t, and o docking is also slightly higher in energy. This indicates a very close competition between the three coordination sites that resembles the results for water[26], and which appears to be largely preserved when the nonbonded hydrogen in water is replaced by an organic rest R. Seemingly, the torsional flexibility of DTBN renders the

t and o docking structures more attractive (Figure 13). Indeed, while the electronic dissociation energies (see Table 7) of the solvated complexes with TEMPO and DTBN in the p structure are within 1 kJ mol^{-1} for a particular R, the dissociation energies of t and o clusters are predicted to be systematically lower for DTBN than for TEMPO by 1-2 kJ/mol. This flexibility advantage is observed with the increasing in R from -H to -C(CH$_3$)$_3$, whereas the absolute dissociation energy increases by up to 7 kJ mol^{-1}.

Table 7. Relative electronic energies and dissociation energies (both in kJ mol^{-1}) of DTBN and TEMPO solvates.

Structure	$E_{0\ (U)B3LYP-D3BJ}$ [a]]	$E_{0\ DLPNO-CCSD(T)}$ [b]]	$E_{diss\ DLPNO-CCSD(T)}$ [c]]
TEMPO···HOH			
t···HOH	0.0	0.5	30.7
o···HOH	0.4	0.1	31.1
p···HOH	0.0	0.0	31.7
TEMPO···HOCH$_3$			
t···HOCH$_3$	0.0	0.7	32.7
o···HOCH$_3$	0.4	0.1	33.8
p···HOCH$_3$	0.1	0.0	33.9
TEMPO···HOC(CH$_3$)$_3$			
t···HOC(CH$_3$)$_3$	0.4	0.7	37.4
o···HOC(CH$_3$)$_3$	0.7	0.5	37.4
p···HOC(CH$_3$)$_3$	0.0	0.0	38.6
TEMPO···HOC$_6$H$_5$			
o···HOC$_6$H$_5$	0.9	1.4	47.5
p'···HOC$_6$H$_5$	1.2	1.7	46.0
p···HOC$_6$H$_5$	0.0	0.0	45.3
DTBN···HOH			
t···HOH	0.0	0.0	33.1
o···HOH	0.7	0.3	32.5
p···HOH	2.8	2.0	31.0
DTBN···HOCH$_3$			
t···HOCH$_3$	0.0	0.0	35.7
o···HOCH$_3$	0.8	0.7	35.0
p···HOCH$_3$	2.8	2.7	32.9
DTBN···HOC(CH$_3$)$_3$			
t···HOC(CH$_3$)$_3$	0.0	0.0	40.3
o···HOC(CH$_3$)$_3$	0.7	0.9	39.1
p···HOC(CH$_3$)$_3$	2.2	2.4	38.1

[a] Harmonically zero-point corrected (U)B3LYP-D3(BJ,ABC)/def2-TZVP relative energies. [b] Harmonically zero-point unrestricted open-shell[143] DLPNO-CCSD(T)/aug-cc-pVTZ//(U)B3LYP-D3(BJ,ABC)/def2-TZVP relative energies (in kJ mol^{-1}) relative energies and [c] dissociation energies.

In the two nitroxide radicals, the p,t,o docking sites are described by a common pattern of the hydrogen bond angle N-O•···H (α), which is close to 90° for o structures, close to tetrahedral for t, and in excess of 120° (sp^2-like) for p (see Figure 14 and Appendix A). Such correlation increases mnemonic value to the previously defined abbreviations t, that also states for tetrahedral, and o, for orthogonal. It has been observed a tendency for the t wavenumbers being lower than p, and o conformations to have a higher predicted OH stretching vibration than those of p. In structures t, this is because the solvent is not so much pushed away from ideal (roughly tetrahedral) coordination by the shielding methyl groups, whereas in the latter this be explained by the distortion of the hydrogen bond by interaction of the solvent molecular with the N atom in the o clusters (see Figure 13 and Figure 17 in page 60). For spectral assignments purpose, it is relevant to verify whether the predicted correlation is robust among other theoretical methods, and it is also necessary to check its consistency with the experimental results. For the last-mentioned aim, information regarding the relaxation paths between the different conformations is pivotal.

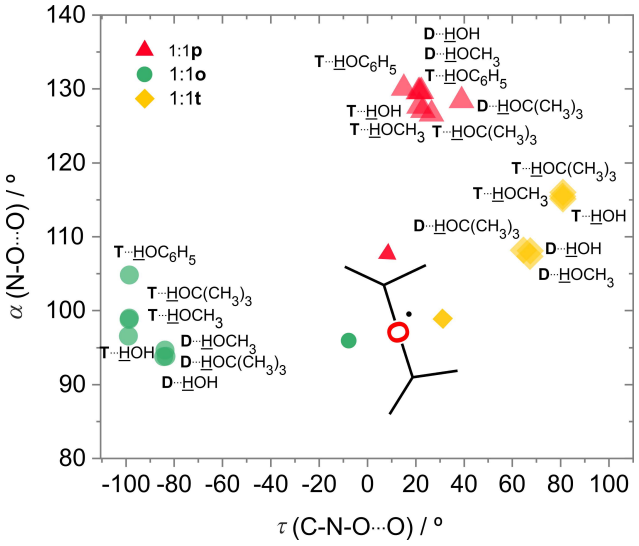

Figure 14. Correlation graph of the N-O···O angle (α) of the solvent relative to the nitroxide bond as a function of the dihedral C-N-O···O angle (τ) of the solvent relative to the approximate nitroxide radical plane, defining the coordination topologies o, p and t for DTBN (D) and TEMPO (T) clusters with the different solvents. Reproduced from Ref.[155] with permission from the PCCP Owner Societies.

4.2.4 Conformational Interconversion

Collisions can induce conformational changes [182]. Thus, the barriers that separate the conformations are crucial for the survival of excited isomers [183].Within this framework, a relevant difference between the two bulky radicals TEMPO and DTBN is depicted in relaxation barriers between the different isomers in the Figure A6 in the Appendix A. In DTBN, intermolecular torsion around a C-N-O$^{\bullet}$···O dihedral angle can easily lead to the relaxation of the p isomer (red triangles) into the o or t isomers (green circles and yellow diamonds) of DTBN-HOH/DTBN-$HOCH_3$, and DTBN-$HO(CH_3)_3$ complexes, respectively, across a low barrier. The intramolecular torsion around the C-C-N-C angle is not hindered as in TEMPO due to the ring closure, but apparently the o/t conversion in DTBN has an associated higher barrier than the p/o (or t, in DTBN-$HO(CH_3)_3$ complexes) conversion. Thus, the lowest energy isomers are expected to be detected (t and o; Figure A6), whereas the higher energy conformation p is expected to relax. In TEMPO, it is easier for a t isomer to relax to a p isomer through the intermolecular torsion around the C-N-O$^{\bullet}$···H dihedral angle, whenever this offers an energy gain. On the other hand, the o docking site is hidden behind a higher energy barrier. Therefore, up to two conformations for the monosolvates of both nitroxide radicals are expected in supersonic jets, but not the same for DTBN (t and perhaps o) and TEMPO (p and perhaps o).

4.2.5 Theory-assisted Spectral Assignments

The harmonic scaling strategy successfully applied for DTBN and TEMPO complexes was described in the subsection 4.2.2. This is depicted in Figure 15, which shows the comparison between the scaled spectra with the experimental obtained jet-FTIR results in the 3550-3250 cm^{-1} range, which is relevant for hydrogen-bonded OH groups of water and methanol in the complexes with the nitroxides (see also the assignments Table 8). As described in the TEMPO hydrates section, the TEMPO-HOH spectrum is far more complicated due to the harmonic resonance splitting (b2lib resonance[101] described in Appendix A). The comparison shows a still slightly underestimation by scaled theory for the p complex, and overestimation by theory for the o complex. The p isomer remains unobserved in DTBN experiments, due to the relaxation into o/t through the C-N-O$^{\bullet}$···O torsion, while the t isomer easily relaxes to the p structure, at least in colder expansions, and thus remains undetected. Hence, TEMPO yields mostly p and trapped o complexes, while DTBN yields mainly t and trapped o complexes. A very analogous behaviour to HOH is observed for $HOCH_3$ radical complexes.

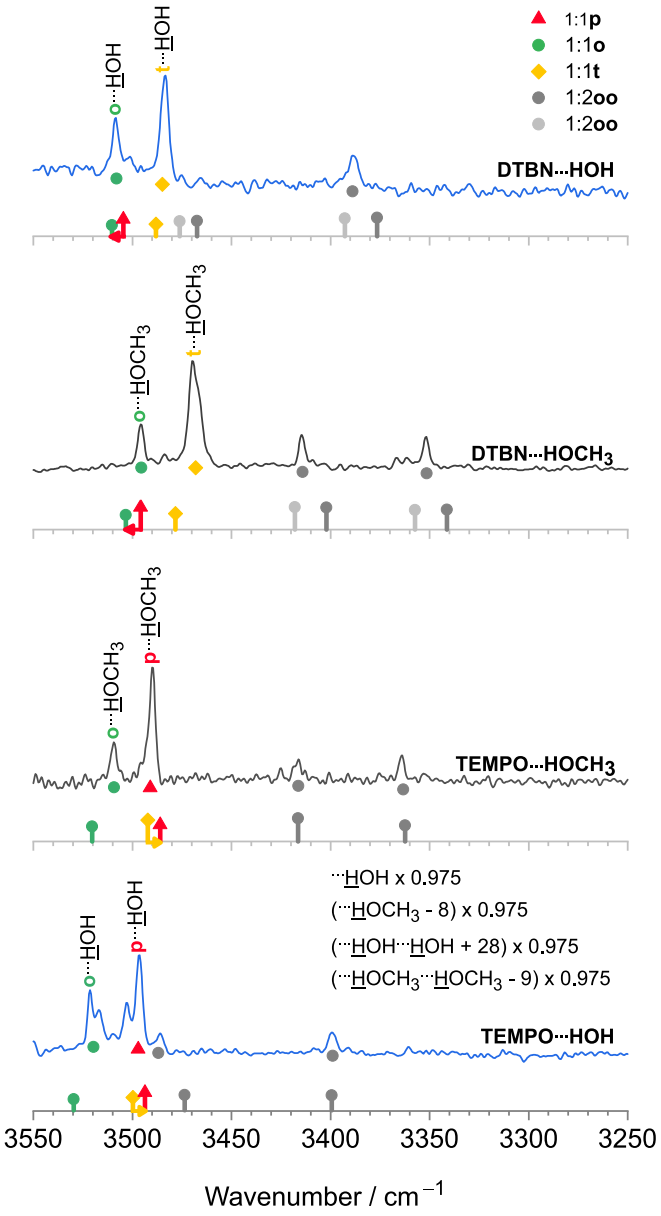

Figure 15. IR spectra of water (outer, blue) and of methanol (inner, black) solvates of DTBN (upper) and TEMPO (lower half). The computed stick spectra are uniformly scaled after correcting for pure solvent dimer and trimer deficiencies according to the scaling strategy described in section 4.2.2. Colour and symbol-coded isomers that are predicted to relax into other conformers across small and shallow barriers are connected to the more stable ones through horizontal arrows representing the relaxation path. There is a straightforward correspondence of the two preferred isomers for each solvate with signal strength, indicating that the scaling model is effective. Scaled harmonic spectra of DTBN and TEMPO from unrestricted open-shell B3LYP-D3(BJ, ABC)/def2-TZVP computations for p (▲, red), o (●, green), and t (◆, yellow) 1:1, and for oo (●●, grey) 1:2 hydrates are shown. Reproduced from Ref.[155] with permission from the PCCP Owner Societies.

Apart from the monosolvates contributions, one can also observe spectral contributions from disolvates (represented by oo) in Figure 15. In nitroxide disolvates, the second solvent unit forces the first solvent unit to adopt an o conformation so that it can coordinate to the nitrogen atom of the N-O$^{\bullet}$ moiety of the radical. The radical-unbiased scaling approach highlighted in section 4.2.2 demonstrates to be quite successful for the solvate trimers spectral predictions as well. In contrast to TEMPO-water trimers, where the overlap between the trimers and dimers band is narrowly avoided by a small margin[26], in DTBN-water disolvates the less shifted OH stretching vibration overlaps with the mixed dimer. Although two competing structures of DTBN water disolvates with slightly different spectra are predicted by theory, the experiment itself cannot decide between them.

4.2.6 Interactions with Bulky Solvents

The accomplishment of the detailed understanding of the interaction between the two nitroxides and the water and methanol solvents was followed by the extension of the investigations to more bulky and aromatic solvents, in particular *t*-butanol[184] and phenol[185]. In the case of complexes with *t*-butanol and phenol, there is a greater preference for a single mixed dimer (Figure 16), possibly due to secondary intermolecular interactions between the nitroxide and the solvent molecules illustrated in Figure 16 for TEMPO solvents (see Figure 17 and the supplementary information in Appendix A). Despite of the possibly offered secondary interactions and the change between aliphatic and aromatic hydroxy compounds, the scaling approach described in section 4.2.2 worked notably well. At this stage of the investigations on nitroxides through jet spectroscopy, we refrain from speculating about the structures that lead to the minor IR signals observed in the spectra. Despite of that, the theory predictions are in total agreement with the smaller OH-containing solvents, specifically with the preference for p docking sites in TEMPO, and for t docking sites in DTBN.

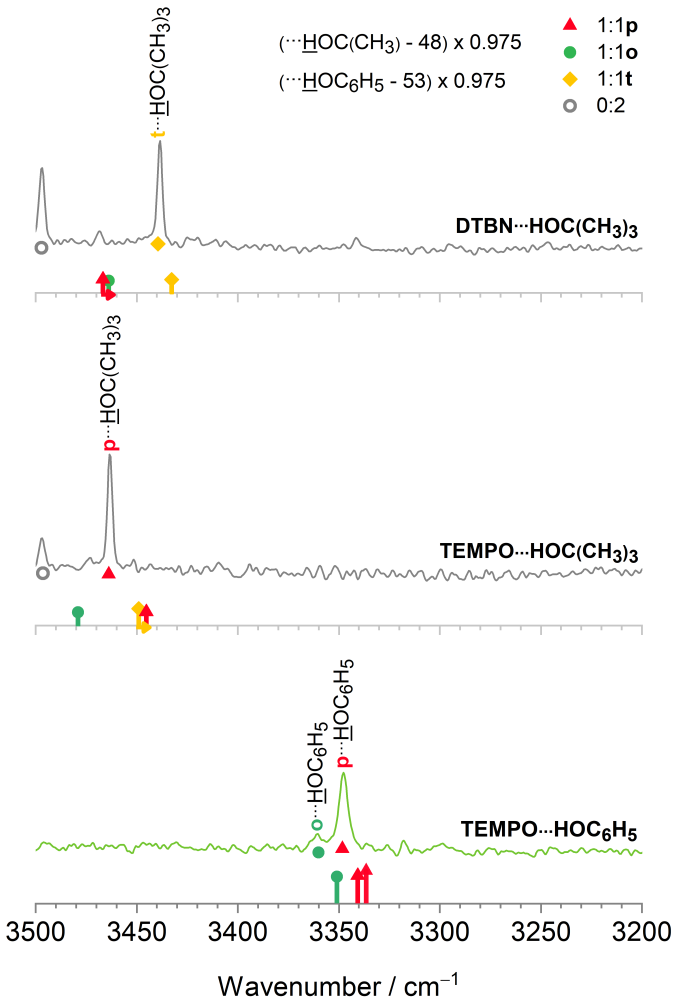

Figure 16. Jet-FTIR spectra of tert-butyl alcohol complexes with DTBN (top) and TEMPO (center) radicals, along with the IR spectrum of phenol and TEMPO complexes (bottom). The computed stick spectra are uniformly scaled after correcting for pure solvent dimer and trimer deficiencies according to the scaling strategy described in section 4.2.2, as described before. Colour and symbol-coded isomers that are predicted to relax into other conformers across small and shallow barriers are connected to the more stable ones through horizontal arrows representing the relaxation path. There is an unequivocal correlation of the most stable structure for each complex (the bottom spectrum shows two energetically similar complexes) with signal strength, indicating that the scaling model is effective for bulky solvents. Scaled harmonic spectra of DTBN and TEMPO from unrestricted open-shell B3LYP-D3(BJ, ABC)/def2-TZVP computations for p (▲, red), o (●, green), and t (◆, yellow) 1:1, are shown. Reproduced from Ref.[155] with permission from the PCCP Owner Societies.

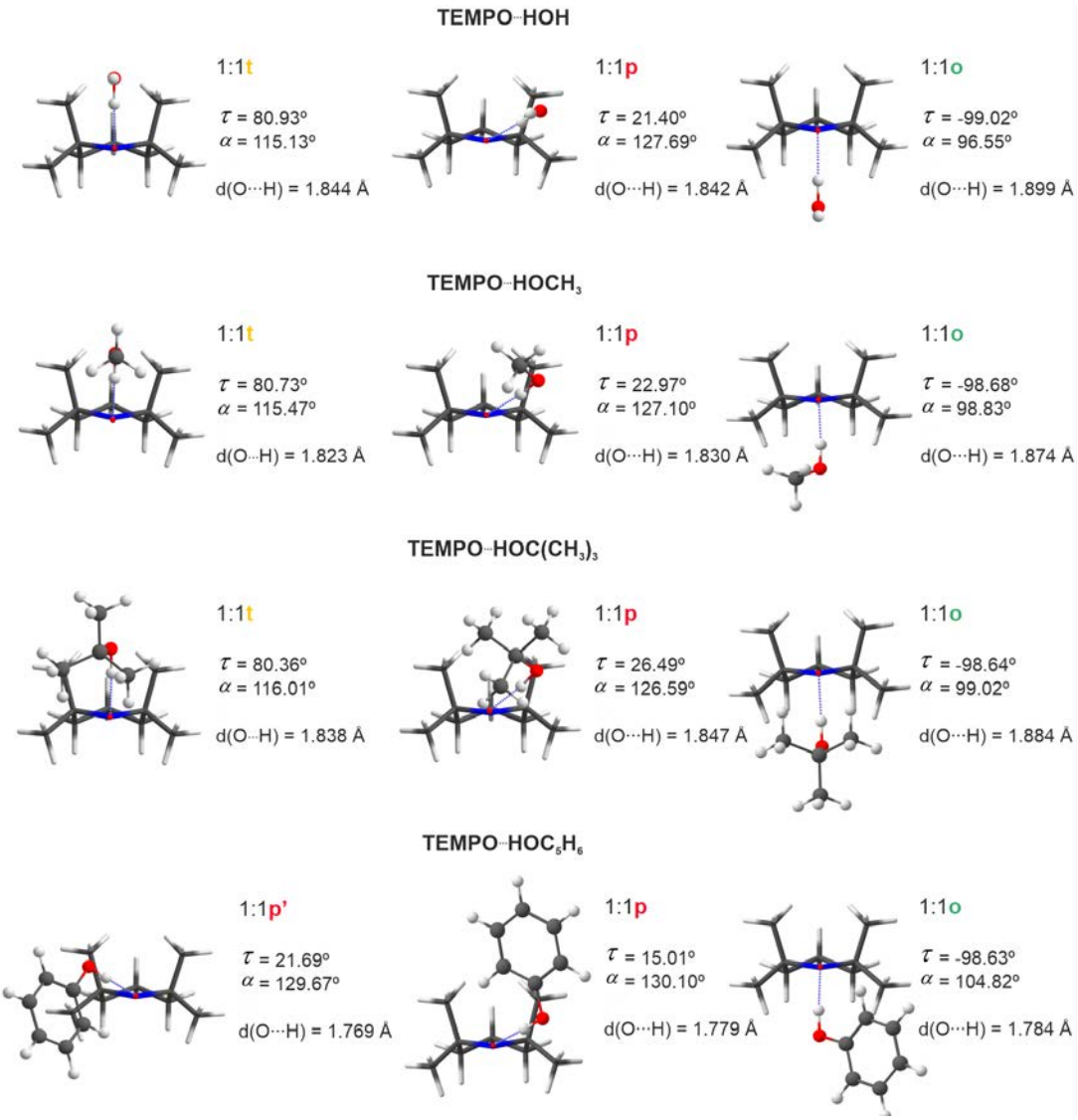

Figure 17. Structures of TEMPO monosolvates with the four OH-containing solvents in a different perspective. The N-O···O angle (α) of the solvent relative to the nitroxide bond as a function of the dihedral C-N-O···O angle and (τ) of the solvent relative to the approximate nitroxide radical plane are also given. This figure is also representative of DTBN-water, methanol, and *t*-butanol 1:1 solvates.

Table 8. Experimental wavenumbers of TEMPO solvates (in cm^{-1}) together with the unscaled computed wavenumbers (in cm^{-1}) and absolute intensities (in km mol^{-1}) at unrestricted open-shell B3LYP-D3(BJ,ABC)/def2-TZVP level.

Structure	Experiment Jet-FTIR	Computed $\tilde{\nu}$	I
DTBN···HOH			
t···HOH	3483	3578	382
o···HOH	3509	3600	339
p···HOH	–	3594	556
oo···HOH	–/3389	3528/3435	489/613
oo···HOH	–/3389	3537/3452	484/579
DTBN···$HOCH_3$			
t···$HOCH_3$	3470	3575	523
o···$HOCH_3$	3496	3601	471
p···$HOCH_3$	–	3593	750
oo···$HOCH_3$	3415/3352	3498/3436	731/664
oo···$HOCH_3$	3415/3352	3452/3515	751/645
DTBN···$HOC(CH_3)_3$			
t···$HOC(CH_3)_3$	3439	3569	503
o···$HOC(CH_3)_3$	–	3601	462
p···$HOC(CH_3)_3$	–	3604	522
TEMPO···HOH			
t···HOH	–	3589	405
o···HOH	3521	3620	347
p···HOH	3497	3583	587
oo···HOH	3486/3399	3535/3459	497/483
TEMPO···$HOCH_3$			
t···HOH	–	3583	549
o···HOH	3509	3619	481
p···HOH	3490	3590	710
oo···HOH	3417/3365	3513/3458	769/513
TEMPO···$HOC(CH_3)_3$			
t···HOH	–	3582	496
o···HOH	–	3490	1059
p···HOH	3348	3478	1101

4.2.7 Benchmarking

With the assignment of mono- and disolvates of the two nitroxide radicals firmly established and systematic over the investigated OH-containing solvents, one can proceed to a first benchmarking step, specifically the comparison to other harmonic predictions at the unrestricted open-shell level. To avoid complexity of the employed scaling approach, this is done considering the spectral shifts relative to the o conformation that is observed in most solvates (both DTBN and TEMPO).
Because the t isomer is observed to occur with o for DTBN complexes, whereas the p conformation is observed in TEMPO monosolvates, Figure 18 plots both as a function of HOR substitution. It is possible to observe that B3LYP describes the experimentally secured substitution trends (green symbols) fairly well, with B2PLYP approaching at least as close.

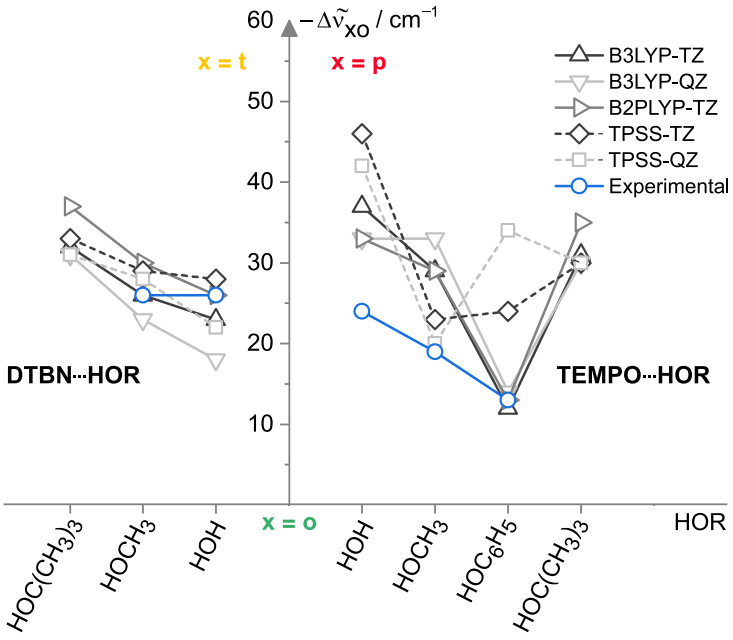

Figure 18. Experimental OH stretching shifts (green) and computed (with grey TZVP and black QZVP basis set) for o isomers in DTBN solvates and t isomers in TEMPO solvates in relation to o as a function of the ROH substituent for three different DFT functionals. TPSS (dashed) is proven to be less systematic than the LYP-based functionals in capturing the trends and therefore of reduced predictive value for IR spectroscopy investigations. Reproduced from Ref.[155] with permission from the PCCP Owner Societies.

On the other hand, TPSS seems to be somewhat less systematic and consequently of low predictive value for spectroscopy. Most of the employed approaches predicted a larger

o-t splitting for $HOC(CH_3)_3$ than for $HOCH_3$ solvents, which may support a future assignment of the t docking site of DTBN. For TEMPO-HOC_6H_5, the weak experimental signal in the IR spectrum was upshifted from the dominant p conformation instead of p' in the bottom of the spectrum in Figure 14. We can attempt to apply the correlations in the Figure 16 shown above to assign the peak. B3LYP computations suggest that the o conformation is now notably (≈15 cm^{-1}) less shifted from p than in HOH or $HOCH_3$. The same trend is observed for open-shell B2PLYP. Thus, the prediction is a ≈10 cm^{-1} upshift from the IR experimental p position. One can also observe that TPSS predicts a larger upshift in this case than in $HOCH_3$, but a smaller upshift than for HOH, being the prediction *ca.* 20 cm^{-1} higher than the experimental IR p position. The weak IR signal stays in between these DFT-assisted extrapolations, rather closer to the HOH and $HOCH_3$ adjusted B3LYP and B2PLYP computed values. If a more accurate method is found in future investigations, these theory-assisted assignments would be more straightforward with no requirement for the employed scaling strategies.

4.3 Matrix-Isolated Nitroxide Microhydrates

Matrix isolation is a very powerful technique to isolate transient species or weakly bound molecular complexes, and a very sensitive tool to probe their structure and dynamics through spectroscopy. It offers the possibility to investigate controlled aggregation processes through hydrogen bonds, such as radical-water complexes,[73,186][20–22,71][169] and eventually the photoinduced reactivity of these metastable complexes.[21]

Furthermore, the matrix environment allow the isolation whilst simultaneously establishes weak van der Waals interactions with the caged species. Such interactions between the matrix media and the guest species often lead to spectral shifts and matrix splitting when compared to the unperturbed gas phase values.[187] The values of the matrix shifts are not predictable in terms of chemical intuition. It is only predictable that they depend on the properties of the host-guest system,[188] and that they should be less pronounced in Ne matrices, in which the deviations to the gas phase should be minimized. Indeed, an improved understanding of matrix effects would provide advantages in terms of the rigorous comparison with predicted spectra. For instance, one can address the question whether matrix isolation effects are systematic or not for a class of molecular systems. In this regard, the comparison between results from matrix isolation and jet spectroscopy experiments on a molecular system may eventually provide information about the effect of the matrix host. Furthermore, jet-FTIR and matrix isolation results may offer complementary information about the system under investigation, not only regarding the matrix host effects, but also about its conformational preferences in the two environments.

In matrix isolation, the population distribution of conformers in the sample resembles the equilibrium ratio of the gas phase prior to deposition.[63][189,190] By this means that if different conformational isomers exist in the gas phase, the conformational population in this phase is then trapped onto the matrix. Because an inert cryogenic matrix is a non-equilibrium system, where the internal rotation is typically hindered due to the solid environment, the population prior to deposition is usually kept. Molecules/molecular complexes with low energy isomerisation barriers can occasionally undergo conformational cooling[63][189,190] immediately upon the contact with the cold window, or upon annealing experiments, although it is not always possible to depopulate the higher energy populations through this method.

The preparation of molecular complexes in the matrix environment usually requires adding two species to the matrix gas followed by their subsequent deposition, or alternatively the annealing of the matrix after deposition to thermally mobilise the molecules. Upon the annealing, the molecular complexes may eventually undergo isomerisation.

In jet cooled molecular beam spectroscopy, the conformational cooling induced by gas-phase collisions is expected to occur for isomerisation barriers not significantly surpassing 5 kJ mol^{-1}[178]. The relaxation occurs prior to molecules enter the collision-free region, and conclusions about the interconversion barrier can be taken from the observed conformers/complexes present in it.

It may be argued that the interconversion can be more facilitated in supersonic beams than in the matrix isolation environment, as the rotational barriers should be higher in the latter, especially in large molecular systems. Eventually, the study of relaxation in both environments may provide information about the interconversion barriers.

Herein, TEMPO and DTBN hydrates were investigated in matrix isolation environment and the results are described in this subchapter. The vibrational spectra and the interactions between water and the radicals, along with the comparison of the previously obtained jet FTIR spectroscopy results are addressed herein. As matrix isolation offers a favourable environment to study metastable and unstable species some preliminary studies on the photochemistry of such species are also reported.

4.3.1 Preparation of Radical-water Complexes

The formation of weakly bonded complexes in the matrix isolation environment can be quite challenging and it is a process that depends strongly on the concentration of the sample, the matrix temperature during the deposition and the annealing temperature. Upon matrices annealing, small molecules can diffuse in the inert medium, which favours the formation of aggregates, a process that can be monitored through IR spectroscopy. TEMPO and DTBN radical–water complex were generated by co-deposition of the

radicals and a large excess of argon doped with 0.1 %–1 % H_2O at 10 K, followed by annealing of the matrices at temperatures up to 25 K. For the preparation of TEMPO complexes, a storage bulb was filled with argon doped with water and was deposited simultaneously with the TEMPO from a solid sample placed in a valve container connected to the cryostat. The preparation of DTBN water complexes was also performed using the same strategy.

The changes in the spectra by varying the concentration of water were carefully analysed and compared with the spectra of matrix isolated water, and the spectra of the isolated TEMPO (chair conformation) and DTBN radicals, previously dried with the vacuum to avoid complexation. All the samples (except those with monomeric radicals) contain not only isolated water, but also water dimers, trimers, and oligomers of water, depending on the water concentration as well as temperature.[191,192] As the concentration of water increases, the complexity of the formed complexes increases, as anticipated.

Annealing of argon matrices containing both nitroxide and water gives rise to the formation of a new set of IR absorptions which are not observed when argon is doped with solely TEMPO/DTBN or exclusively water. The observed new absorptions resemble the vibrations of the isolated monomers, although they are shifted (red or blue-shifted) from the corresponding monomer absorptions.

For TEMPO in argon with water concentration of 0.1 %, IR absorptions in the OH stretching region were observed upon matrices annealing, although it was not possible to assign the new bands due to their weak intensities. For a higher concentration of water (0.5 %), new observed IR absorptions were already observed upon deposition at 10 K, prior to annealing. Annealing the matrices at temperatures up to 25 K led to the increasing of in intensity of these pre-existing observed IR bands, as the increasing in temperature enhanced further formation of radical complexes with water molecules.

DTBN and water complexes were similarly generated in argon cryogenic matrices. As DTBN have a higher tendency for aggregation, the deposition conditions were optimised to prepare a more diluted matrix and avoid the aggregates formation. In this case, the rate of gas deposition was slightly increased, and the concentration of water was optimised to 0.2 %. For higher concentrations of water (1 %), it is observed the formation of a higher concentration of the radical-water dimers, but also of water complexes.

4.3.2 Matrix Isolation and Jet-FTIR Experiments

The FTIR spectra of H_2O doped argon matrices in the 3580−3220 cm^{-1} range in Figure 19 shows the formation of water and radical-water complexes in the matrix environment, and the distinct peaks from the absorptions of monomeric TEMPO, and water dimers, trimers, tetramers and oligomers.[191–194] The upper trace (A) of Figure 19 shows the

experimental OH stretching spectrum of matrix isolated water, at the concentration of 0.5 % in argon, after the annealing at higher temperatures (25 K) and recooling to 10 K.

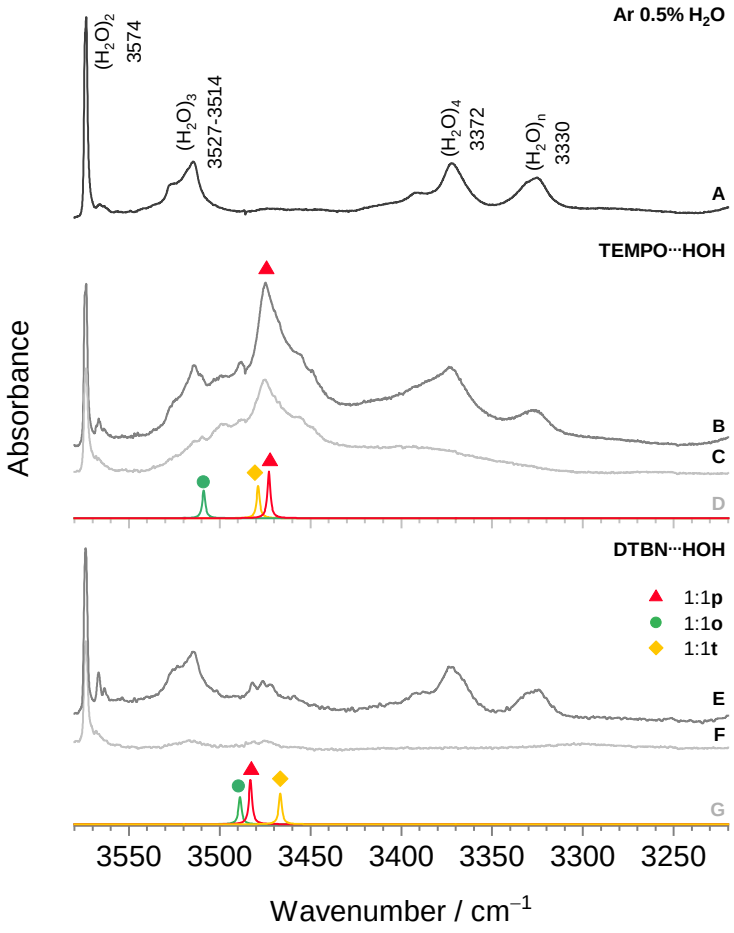

Figure 19. FTIR spectra (3580-3220 cm^{-1}) of argon matrices doped with 0.5 % of water after annealing up to 25 K and, recooling down to 10 K (A). The spectrum shows the vibrational frequencies of water dimer, trimer, tetramer, and polymers. IR spectrum of matrix-isolated TEMPO with H_2O (B,C). TEMPO-water complexes were trapped in argon matrices doped with 0.5 % of water before (C, light grey) and after (B, dark grey) 25–10 K annealing and recooling to 10 K. IR spectrum of matrix-isolated DTBN hydrates (E, F). DTBN-water complexes were trapped in argon matrices doped with 0.2 % of water before (F, light grey) and after (E, dark grey) 25-10K annealing and recooling to 10 K. Harmonic scaled spectra of TEMPO (D) and DTBN (G) 1:1 hydrates from unrestricted open-shell B3LYP-D3(BJ,ABC)/def2-TZVP computations for p (▲, red) o (●, green), and t (◆, yellow) complexes are shown. The scaled wavenumbers and computed IR intensities (in km mol^{-1}) were convoluted with Lorentzian functions with a full width at half-maximum (fwhm) of 2 cm^{-1}.

This spectrum provides a helpful background for the interpretation of the much more complex spectra of radical hydrates (middle B and lower E traces of Figure 19), due to the concomitant formation of water complexes in the matrix environment. The absorptions of water dimers (3574 cm^{-1}), trimers (3527−3514 cm^{-1}), tetramers

(3527−3514 cm^{-1}), and oligomers (3527−3514 cm^{-1}) in the upper trace A, occur mainly due to diffusion of water molecules upon matrices warming and are a result of a complex aggregation processes. [186–189] For TEMPO-water (middle traces: B, after the annealing and C, before the annealing), it is possible to observe at least 3 overlapped peaks in the spectra (besides the bands of water monomers and complexes), with the most prominent peak centred at 3474 cm^{-1}. This reveals a stronger red shift of the OH stretching vibration in the matrix environment in relation to the value observed for the most intense peak in the previously collected jet-FTIR spectra (p-HOH in He expansions: 3497 cm^{-1}). As previously referred, p-HOH is the preferred conformation for TEMPO water complexes, closely followed by t and o isomers in terms of relative electronic energies. Thus, the most prominent band in the OH stretching region of TEMPO-water spectrum is preferably assigned to the most stable isomer p, meaning that there is a shift in 22 cm^{-1} from the value observed in the jet-FTIR spectrum with helium as carrier gas (TEMPO hydrates in helium expansions) and the observed value for the matrix-isolated p isomer in argon.

If the most prominent band observed for the matrix isolated complexes belongs to isomer p, then the adopted scaling strategy of the (U)B3LYP/TZ harmonic predictions for spectral assignments described in the previous subsection in this Chapter is no longer advantageous for the assignment of matrix-isolated complexes. Instead, we adopted another strategy that takes into account the shift between the most prominent peaks (both assigned to p-HOH) in the different environments (22 cm^{-1}) and subtracted it to the harmonic predictions and multiply it also by 0.975 factor (see the previous subchapter for more detail about the adopted scaling strategies).

As referred in the Introduction, the degree to which the IR bands are shifted upon the change from a free beam to the matrix environment depends on the host-guest interactions[195], which varies with the polarizability of the matrix host. Modelling the bulk matrix shift can be highly demanding, and it adds to the fact that the multiple weak interactions between guest and host can influence the frequently challenging electronic structure of molecular complexes, and thus it goes beyond the scope of this work. So, we focused on find analogies and patterns in an attempt to correctly assign the spectra of TEMPO and DTBN in the different environments, which could be eventually extended to another nitroxides. With the scaling strategy referred above, the downshift correction to the (U)B3LYP estimated value for TEMPO p-HOH 3583 cm^{-1} yields 3472 cm^{-1}, and the experimental OH signal is observed at 3474 cm^{-1}. The main spectroscopic challenge is to assign the remaining peaks, centred at 3499 cm^{-1} and 3489 cm^{-1}. Because of the broad shape and spectral overlap, and because it is plausible to attribute the remaining peaks to matrix effects (once the occupancy of different trapping sites may lead to site splitting) we could only speculate about their assignments. These

remaining peaks might be due to o and t structures, respectively, as their predicted OH stretching vibrations at 3620 and 3589 cm^{-1} (unscaled), which yielded 3508 and 3478 cm^{-1} after applying the scale factor, fit reasonably well the experimental values at 3499 cm^{-1} and 3489 cm^{-1}, as well as the IR intensities. Furthermore, matrices annealing at temperatures up to 25 K induce the increasing of the peaks at 3472 cm^{-1} 3489 cm^{-1}, whereas the peak 3499 cm^{-1} at cm^{-1} is not altered. Thus, this may indicate that the peak at 3499 cm^{-1} must belong to a metastable structure that is formed immediately upon deposition (or prior to deposition), and which eventually does not undergo relaxation in the matrix environment upon warming, because the associated isomerisation barrier is sufficiently high to be overcome (approximately 1.7 kJ mol^{-1} at (U)B3LYP/QZ without zero-point correction, for the gas-phase. For further information about the torsional scans see Figure A6 in Appendix A).

Besides, (U)B3LYP/TZ OH harmonic computations indicate an overestimation of the predicted value of the OH stretching vibration for isomer o in relation to the experimental value, as it was also observed in the jet-FTIR spectra. Otherwise, if the harmonic prediction matched the experiment in this case, an overlapping with the OH band from the water trimer would prevent the correct assignment of the matrix isolated o isomer. The second peak at 3478 cm^{-1}, might be due to t isomer, although the isomerisation barrier associated with the torsion around the C-N-O$^{\bullet}$O dihedral that converts t into p is quite small (less than 1 kJ mol^{-1} at (U)B3LYP/QZ without zero-point correction; see Figure A6 in Appendix A). Indeed, the interconversion barriers are generally higher in the matrix environment than in the gas phase, especially for larger species, such that torsions and rearrangements are often hindered in this case. Nevertheless, the matrix-site splitting cannot be disregarded in this case. Distinct matrix sites may lead to different intermolecular potentials that eventually will affect the vibrational potential of the guest molecules. Thus, the observed multiple bands can be a consequence of such effect.

The complexity of the IR spectra around 3500 cm^{-1} further increases when switching from TEMPO to DTBN hydrates (lower traces: E, after the annealing and F, before the annealing in Figure 19). In DTBN-water spectrum (lower trace E), there are also at least 3 peaks, at 3482 cm^{-1}, 3476 cm^{-1} and 3472 cm^{-1} to assign, which emerge after the annealing (trace E, Figure 19). The intensities of these absorption bands in the IR spectrum resemble the predictions for t, p, o DTBN-water complexes.

The scaling strategy used for matrix-isolated TEMPO-water clusters was applied to DTBN-water, as an attempt to take advantage of the analogy between nitroxides and water in the matrix environment. The scaling strategy applied predicted OH stretching vibrations for t, p, o at 3578 cm^{-1}, 3594 cm^{-1}, 3600 cm^{-1} yielded 3467 cm^{-1}, 3483 cm^{-1}, 3489 cm^{-1}, respectively. For the most stable complex t, the deviation between the

experiment and the scaled harmonic calculations is slightly more significant than for TEMPO p isomer, with a shift of 5 cm^{-1}, showing that the adopted scaling for TEMPO hydrates yields a better agreement between predicted and experimental vibrations for TEMPO hydrates than for DTBN hydrates. The OH stretching vibration of the matrix-isolated t isomer is shifted in 11 cm^{-1} from the gas phase value, a smaller shift than for TEMPO p···HOH (see Table 10).

Table 9. Experimental OH stretching vibration (in cm^{-1}) of radical-water complexes in argon matrices and in helium jet expansions. The shift between the two values is also shown.

Structure	Experiment		
	Argon-matrix	Jet-FTIR	Shift [a]
TEMPO···HOH			
p···HOH	3475	3497	22
DTBN···HOH			
t···HOH	3472	3483	11

One can suggest the assignment for p, t, o isomers of TEMPO and DTBN hydrates in the matrix environment. However, matrix site-splitting and overlapped bands may lead to a misleading interpretation of the data, and thus more spectral information is required for an assured assignment of the peaks. In addition to the red-shift observed of the OH stretching vibration of water, which is the largest found band shift, several shifts of other IR bands in the 1480—500 cm^{-1} region were observed in both IR spectra of TEMPO and DTBN. Such observation firmly supports the intermolecular interaction between TEMPO/DTBN with water, but the broadness of the other observed bands does not allow to discriminate the isomers (see Figure 20 with fragment of the IR spectra of TEMPO and DTBN hydrates and isolated monomers. The Mid-IR spectra of DTBN and TEMPO monomers are shown in Figures A7 and A8 in Appendix A). The new bands shifted from those of the monomeric species are mainly observed in the N-$O^{\bullet}$ stretching region between 1400-1330 cm^{-1} (see figures 20 and 21, some of the new observed bands are marked with an asterisk over the top of the radical-water spectra). We can list a shift of approximately 3 cm^{-1} to a higher wavenumber from the TEMPO monomer band at 1367 cm^{-1}, and shift of 1 cm^{-1} from the bands at 1359 cm^{-1} and 1342 cm^{-1}. Furthermore, the absorption at 1381 cm^{-1} increases in intensity in the hydrates' spectra, while the 1377 cm^{-1} band decreases in intensity. For DTBN, the absorption band at 1390 cm^{-1} of the monomer spectrum is shifted by approximately 3 cm^{-1} to a higher wavenumber, and the same is observed for the bands at 1373, 1366 and 1356 cm^{-1}.

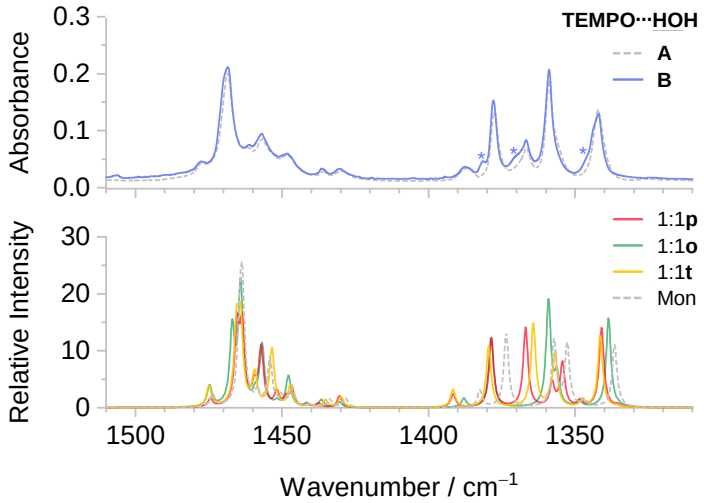

Figure 20. FTIR spectra (1510−1310 cm^{-1}) of TEMPO monomer (upper trace A, dashed grey) and TEMPO-water complexes trapped in argon matrices doped with 0.5 per cent of water (upper trace B, —, blue). (U)B3LYP/def2-TZVP harmonic spectra for p (—, red), o (—, green), and t (—, yellow) complexes and for TEMPO monomer are shown (Mon, ---, dashed grey). The harmonic frequencies below the OH stretching region were scaled by 0.97 factor. The scaled wavenumbers and computed IR intensities (in km mol^{-1}) were convoluted with Lorentzian functions with a full width at half-maximum (fwhm) of 2 cm^{-1}. The new observed bands in the TEMPO-water spectrum (upper trace B, —, blue) are depicted with asterisks (*).

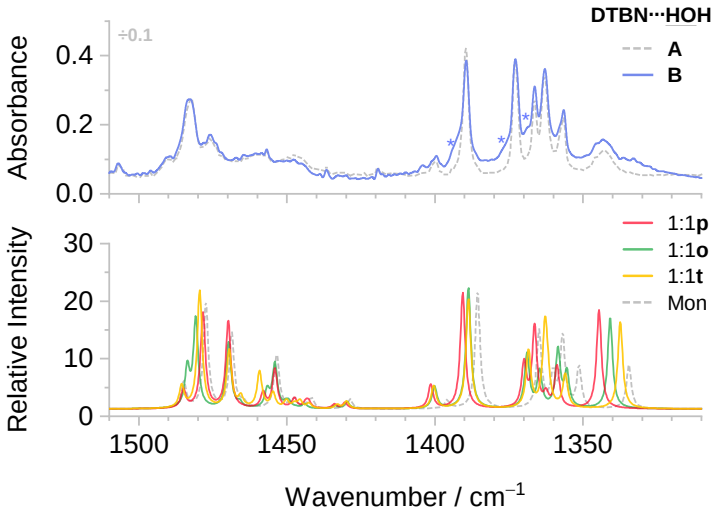

Figure 21. FTIR spectra (1510−1310 cm^{-1}) of DTBN monomer (upper trace A, dashed grey and TEMPO-water complexes trapped in argon matrices doped with 0.5 per cent of water (upper trace B, —, blue). (U)B3LYP/def2-TZVP harmonic spectra for p (—, red), o (—, green), and t (—, yellow) complexes and for TEMPO monomer are shown (Mon, ---, dashed grey). The harmonic frequencies below the OH stretching region were scaled by 0.97 factor. The scaled wavenumbers and computed IR intensities (in km mol^{-1}) were convoluted with Lorentzian functions with a full width at half-maximum (fwhm) of 2 cm^{-1}. The new observed bands in the DTBN-water spectrum (upper trace, —, blue) are depicted with asterisks (*).

4.3.3 Comparison with Other Matrix-Isolated Radicals

Previous investigations show that radicals can act as hydrogen bond acceptors.[1,15,21,22,26,73,196,197] On the few examples, one can refer the phenoxy radical interacting with water under matrix isolation conditions. Resembling TEMPO and DTBN hydrates, the most stable dimer of the former radical complex can also establish an hydrogen bond between the hydrogen atom of water and the oxygen atom ($PhO^{\bullet}\cdots\underline{HO}H$), being the predicted $O^{\bullet}\cdots H$ distance of 1.917 Å (at UM05-2X/6-311++G(2d,2p) level of theory).[22] The structure is further stabilized by a secondary interaction between the O atom of water and one ortho hydrogen atom of the radical.

For the phenoxy radical and in water-doped matrices, a blue-shift of the CO stretching vibration by 15 cm^{-1} (C-$O^{\bullet}\cdots$H-O-H) was found. Such observation is unusual, as the establishment of hydrogen bonds with oxygen atoms from a carbonyl typically results in a strong red shift of the CO stretching vibration.

The OH stretching vibration observed for the radical complexes decreases with the following order $TEMPO^{\bullet}\cdots\underline{H}OH$>$DTBN^{\bullet}\cdots\underline{H}OH$>$PhO^{\bullet}\cdots\underline{H}OH$. The lower absorption at 3470.5 cm^{-1} of phenoxy-water complex[22] indicates a stronger hydrogen bond in comparison with the strength of hydrogen bond formed between water and TEMPO/DTBN.

The hydrogen abstraction from water by the phenoxy radicals was also investigated in the matrix isolation medium. The authors reported that such reaction does not occur at low temperatures, as it is strongly endothermic. No evidence was also found for the photochemical hydrogen abstraction either, contrarily to the previously reported investigations for the phenyl radical.[22]

For phenyl radical and water, the most stable complex is stabilized by $OH\cdots\pi$ interactions, which has proved to be photolabile upon irradiation with near-UV light. The irradiation of the matrix-isolated complex in argon for several minutes with a wavelength of $\lambda >$ 350 nm led to the formation of the benzene$\cdots{}^{\bullet}$OH complex.[21]

4.3.4 UV-irradiation of Matrix-Isolated Radical Hydrates

The matrix-isolated DTBN and TEMPO hydrates were also irradiated in the investigations reported herein. Irradiation of complexes with the tunable laser (wavelength of $\lambda =$ 280 nm) for approximately 30 minutes induced changes in the spectrum of the radical hydrates. While the nitroxide radicals were partially consumed, several other absorptions appeared in the infrared spectrum. For TEMPO, the most

pronounced bands appear at 3612, 1282, 1075, 963, 931, 890, 684, 604 and 543 cm^{-1}. A small absorption band at 1871 cm^{-1} assigned to free nitric oxide N=O• stretching vibration[53,198,199] was also observed upon the irradiation of both TEMPO and DTBN, indicating that the one of the channels involve the cleavage of the C-N bonds (see Figure 22 and Figure 23 with the suggested mechanism, and the stretching vibration of nitric oxide). For DTBN, the most prominent absorption bands are observed at 3701, 1568, 1463, 1368, 1361, 1234, 1211, 888, 801 cm^{-1} (see Figures 24 and 25 showing the difference spectra covering the MID IR range and showing the generation of the new photoproducts upon the irradiation of matrix-isolated TEMPO and DTBN hydrates).

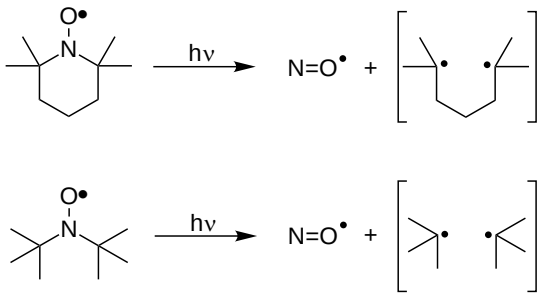

Figure 22. Proposed mechanism for the generation of nitric oxide upon TEMPO and DTBN UV-irradiation under matrix isolation conditions.

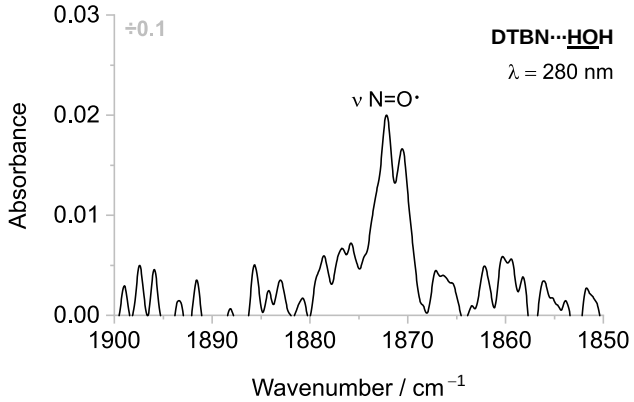

Figure 23. Fragment of IR spectra showing the formation of N=O• (ν N=O• 1871 cm^{-1}) upon irradiation of matrix isolated DTBN hydrates (λ = 280 nm; 30 min) in argon matrices.

There are several reports about the photoinduced reactivity of nitroxides.[200–206] For instance, Keana and co-workers reported the photoreduction of 4-hydroxy-2,2,6,6-tetramethylpiperidinyl-1-oxy, with toluene as solvent, upon the at 350 nm.[200] The products were 1,4-dihydroxy-2,2,6,6-tetramethylpiperidine and 1-(benzyloxy)-4-hydroxy-2,2,6,6-tetramethylpiperidine. An intramolecular hydrogen atom abstraction was also observed upon the irradiation of a *tert*-butyl-substituted cyclic nitroxide in a protic

solvent[203] and from the irradiation of a doxyl.[205] The photoelimination of nitric oxide has also been observed for other nitroxides, upon excitations at higher energy wavelengths.[206] Furthermore, irradiation of DTBN in the UV region yielded 2-methyl-2-nitrosopropane and di-*tert*-butyl-butoxyamine as photoproducts.[201,202,207] Nor the latter, nor the *tert*-butyl radical,[208] were observed in the preliminary investigations of matrix-isolated DTBN reported in this Thesis.

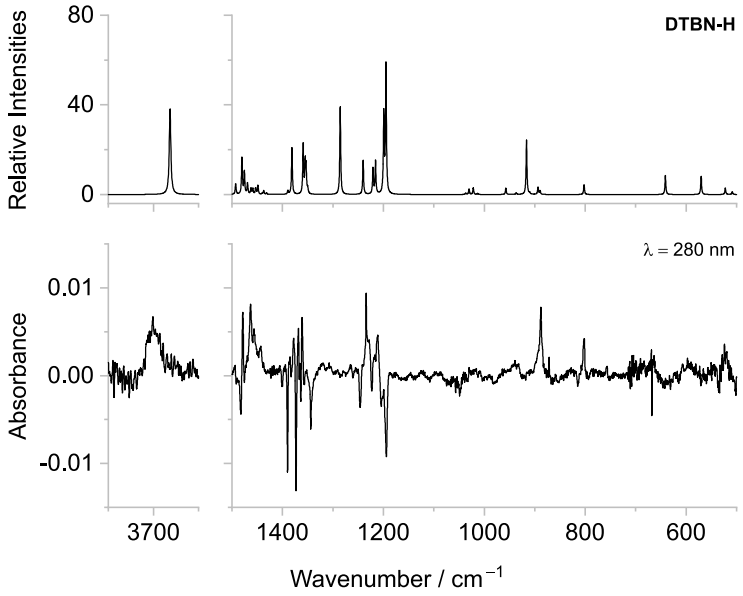

Figure 24. IR difference spectra (on the bottom) showing the generation of new photoproducts and the consumption of DTBN-water complexes (Ar, 10 K) upon the irradiation with UV-light (λ = 280 nm). The B3LYP-D3BJ/def2-TZVP harmonic spectra (top) of the DTBN correspondent hydroxylamine (DTB-H) was compared with the irradiated spectrum. The latter was scaled according to the previously adopted scaling strategy for matrix isolated TEMPO and DTBN hydrates.

Another considered reactional pathway was the abstraction of a hydrogen from water by DTBN and TEMPO upon UV-irradiation. The irradiated spectra of matrix-isolated DTBN and TEMPO hydrates were further compared with the computed spectra of the correspondent hydroxylamine's, DTBN-H and TEMPO-H. The predictions closely resemble the experiment, in particular in the OH stretching region and regarding the N-O stretching vibration at 888/890 cm^{-1}, for DTBN and TEMPO, respectively. However, there is also a mismatch with the predicted (unscaled) N-O-H bending at 1325 cm^{-1} (DTBN-H) and at 1332 cm^{-1} (TEMPO-H).

This suggest that the hydroxylamine's might not be observed in the IR spectrum of the irradiated nitroxides, but the similarities between the predicted and experimental spectra suggest the formation of a related structure.

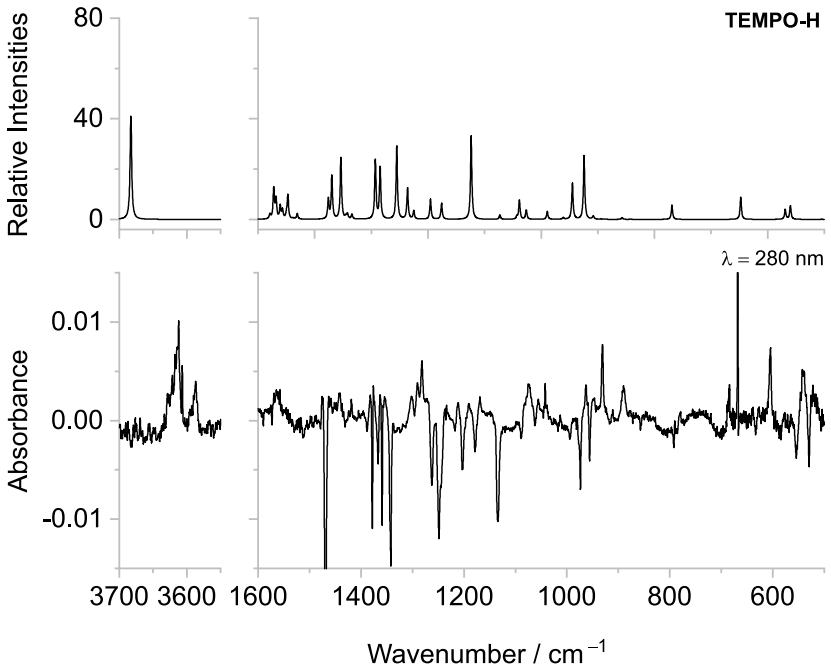

Figure 25. IR difference spectra (on the bottom) showing the generation of new photoproducts and the consumption of TEMPO-water complexes (Ar, 10 K) upon the irradiation with UV-light (λ = 280 nm). The B3LYP-D3BJ/def2-TZVP harmonic spectra (top) of the TEMPO correspondent hydroxylamine (TEMPO-H) was compared with the irradiated spectrum. The latter was scaled according to the previously adopted scaling strategy for matrix isolated TEMPO and DTBN hydrates.

4.4 Conclusions

To conclude, the OH stretching region of vacuum-isolated mono- and dihydrates of TEMPO is described reasonably well by an unrestricted B3LYP approach with dispersion correction, while some details profit from unrestricted DLPNO-CCSD(T) electronic structure refinement.[25,26] Similar to other open-shell systems,[202,203] TEMPO has showed to be sensitive to solvation effects, without further decomposition.

The complexity of the IR spectrum of TEMPO microhydrates was brought down to the low complexity of the analogous ketone TEMCO microhydrates by selected experimental tricks, namely the deuteration of the dangling hydrogen and the decreasing of the temperature using Ne as carrier gas. The 1:1 hydrates of TEMPO shown to exhibit a freer rotation of the hydrogen bond attached to the N-O$^{\bullet}$ moiety than for the ketones. Furthermore, it was revealed a more pronounced anharmonic resonance with bend-librational states due to the stronger hydrogen bond with water in the first case.

Still, under the experimental conditions attained in the present study, the structural similarities between the radical TEMPO and the ketone TEMCO dominate over the differences, and the radical character of TEMPO does not affect the predictive power of density functional in a significant way.
The finding of the first jet-FTIR-detected organic radical hydrate encouraged further investigations on other radical-complexes by supersonic jet vibrational spectroscopy. Since radicals play key role in several chemical processes, including processes that occur in atmosphere,[2] and radical-solvent mechanisms are crucial in several processes,[209,210] their inclusion into quantum chemical methods training is pivotal.

Further investigations of radical-solvates at low temperatures revealed that the HO group of a hydroxy compound attaches the nitroxide radical through the coordination with the oxygen atom of the N-O$^{\bullet}$ moiety, similarly to the case of TEMPO microhydrates. For DTBN, the OH group preferably attaches at on the most hindered side (t from tight) of the radical plane. The in-plane coordination (p) is found in some cases, while the higher opposite and more open side (o) coordination is avoided. When a second solvent molecules coordinates the first unit, the docking site becomes the favoured site due to the established secondary interaction with the N atom of the N-O$^{\bullet}$ bond. The p docking site becomes the predominant isomer when the torsion around the NO bond is quenched by closing the substituents to a ring in the cyclic nitroxide TEMPO. The coordination o can be trapped and further stabilised with the attachment of a second solvent molecule, while the docking site t relaxes by overcoming the barrier. This docking pattern for nitroxide microsolvates was observed through IR spectroscopy in supersonic jet expansions, and it was probed and modelled by harmonic functional density calculations. A scaling strategy considering related closed-shell species was successfully applied. Thus, radical solvation is not a challenge to overcome in terms of DFT calculations, although one can refer that the meta-GGA functional TPSS performs not systematically as hybrid and double hybrid functionals from the LYP family. Nevertheless, anharmonic[211] benchmark calculations would be welcome, as they can be expected predict accurately electronic energies, relaxation and spectral patterns, although this task is considerably more complex for open-shell systems than non-hydrogen-bonded alcohol monomers[212], which have been successfully tackled by this approach.

Furthermore, the investigations were extended to matrix isolation studies to probe the low-temperature structure of TEMPO and DTBN hydrates and their photochemisty, as matrix isolation could enable longer interaction times and allow for more reactive species to be investigated. Switching from jet spectroscopy to matrix isolation (Ar, at 10 K) environment led a shift in the OH stretching vibration of radical hydrates, due to the perturbative effects of the host gas. Such host effects hampered the assignment of the

radical-water complexes. Nevertheless, the p complex of TEMPO and the t complex of DTBN were successfully assigned based on the jet spectroscopy results. Rotational spectroscopy measurements would be welcome for more accurate structural assignments, which do not depend on the sensorial potential of the $OH^{\cdots}O^{\bullet}$ intermolecular bond.
Moreover, DTBN radical was found to survive for several hours in the water-doped Ar environment, while it significantly decomposes when exposed to cyclic gas recycling expansions. This further proves the advantages of matrix isolation over jet spectroscopy for radical species investigations.
Preliminary investigations about the photoinduced reactivity revealed that both TEMPO and DTBN react upon UV excitation. Further investigations are required to understand whether the complexation with water and the formation of pre-reactive complexes influences the photoinduced reactivity of such radicals. It is crucial to determine whether the H-atom abstraction is an intramolecular process, or if the abstraction comes from water by TEMPO and DTBN radicals.

Chapter 5

Generation and Characterisation of Sulphur-Centred Radicals

Sulphur-centred radicals are highly reactive and key intermediates in several chemical reactions in atmosphere[213–216], in biological chemistry[216] and in organic synthesis[217,218]. For instance, thiyl radicals are known to be mediators of several thiol-disulphide conversions, initiated by the oxidation of thiols in the presence of oxygen in the biological environment[219,220] This easy induced exchange is a very important process in enzyme machineries, and it has been quite explored for the design of stimulus-responsive switches.[221]

In addition, thiyl radicals' generation is easily and commonly initiated by heat or through light-induced homolytic bond cleavages of thiols and disulphides. In this framework, aromatic disulphides have been proven to be suitable precursors for the generation of thiyl fragments, not only in solution, but also as matrix-isolated species.[29,94] In the case of matrix isolation experiments, the simplest aromatic phenyl thiyl radical has been generated through flash *vacuum* pyrolysis (FVP) of diphenyl disulphide and characterized by IR spectroscopy quite recently, alongside with the corresponding phenylthiyl peroxy radicals.[94]

Despite of several and some quite recently reports on the generation of thiyl radicals, many remain elusive, or their structures remain still uncharacterised. For instance, the pyridyl-2-thiyl radical (**2**) has never been characterised by matrix isolation spectroscopy, despite of the importance of pyridine as a scaffold with an ever-expanding role in drug design,[222] and the applications of the radical itself in organic synthesis.[223] This Chapter describes our effort to fill this gap.

In these investigations, the selected strategies for radicals preparation included the *in-situ* photolysis and FVP (detailed in Chapters 2 and 3 of this Thesis) of the 2'2-

dipyridyldisulphide as precursor (**1**; Figure 26), in combination with the matrix isolation technique. The *in-situ* irradiation of matrix isolated **1** (performed in the matrix isolation set-up established in Coimbra) led to the generation of caged pyridyl-2-thiyl radical pairs (**2a**) through the homolytic cleavage of the S–S bond. The elusive radical pairs **2a**, bridged by intermolecular interactions, were trapped in the matrix cages initially occupied by the precursor **1** and identified through IR spectroscopy. Upon matrix annealing, the caged radical pairs **2a** undergo recombination to reform the precursor **1**, proving that the disulphide bond of **1** can be photochemically cleaved and restored upon matrices warming. Additional photolysis experiments using O_2-doped matrices have also been carried out to confirm the generation of the pyridyl-2-thiyl radicals upon photolysis of **1**. In these experiments, O_2 acted as radical trapping species by generation of the pyridyl-2-thiyl peroxy radicals (**5**) which could be successfully identified spectroscopically.

The FVP experiments were performed (at the University of Giessen) with the purpose to generate the pyridyl-2-thiyl radical (**2**) in the gas phase, followed by their trapping in cryogenic matrices as isolated species. However, the IR spectrum obtained after pyrolysis of **1** at 750 and 850 ºC revealed a high degree of complexity that indicated formation of several products and precluded the firm identification of the radical **2**. Among the products, pyridine-2-thiol (**3**) and the pyridyl radical (**4**) were identified through the comparison with reference data from previous matrix isolation experiments[224,225], while the presence in the matrices of the thiyl radical **2** remains uncertain, due to the similarity of the IR spectrum of the isolated radical **2** and that of the thiol **3**.

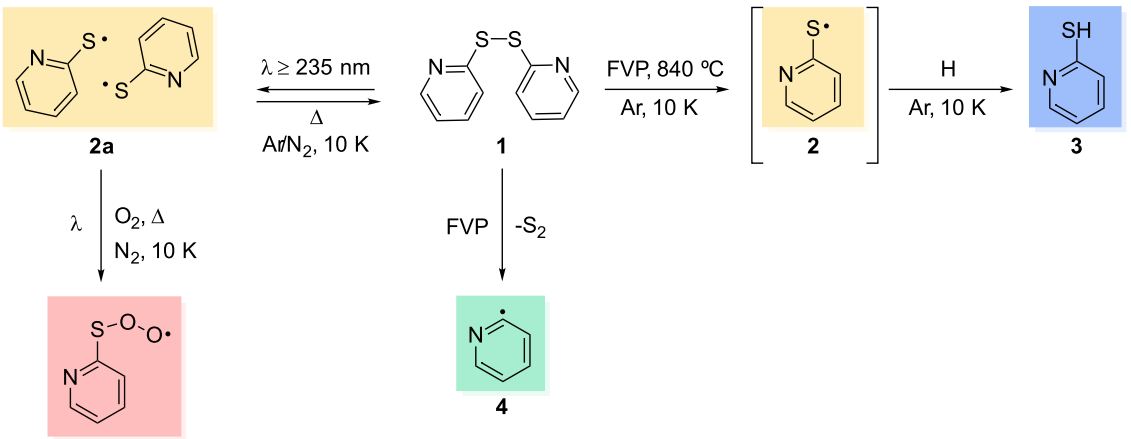

Figure 26. Radical pairs **2a** formed upon the *in-situ* photolysis of **1** in argon and nitrogen matrices. The formation of **2** (isolated) was demonstrated through the detection of **3** in the matrix environment upon FVP of **1.** Radical **4** was also detected. Photolysis of **1** in O_2-doped matrices led to the formation of pyridyl-2-thiyl peroxy **5** radicals.

5.1 Structure of 2,2′-Dipyridyldisulphide

The conformational properties often exhibited by disulphide molecules are bestowed by the flexibility of the S–S moiety, which is a feature of extremely importance in the structure and function of proteins. These conformational changes can be triggered by the cleavage and reformation of the disulphide bridge, and through the rotation around this bond/or adjacent bonds. Because of this inherent flexibility of disulphides, the ensemble of different conformers of **1** was investigated at first.

Although the structures of many disulfides have been determined by X-ray crystallography (including that of the imidazole disulphide,[226] which is presented in Appendix C), investigations on their isolated molecules remain scarce. To explore the conformational landscape of **1**, an exhaustive conformational search was performed using quantum chemical electronic structure calculations. In this search, both manual and automated procedures were applied. The latter was achieved through the evaluation of the potential energy surface around the relevant dihedral angles, performed at the B3LYP/def2-TZVP level with and without three-body dispersion term and using the CREST tool.

The conformational degrees of freedom of **1** are defined by the C–S–S–C and N–C–S–S dihedral angles (*i.e.*, are associated with the internal rotation around the S–S and C–S bonds of the molecule), as shown in the two-dimensional relaxed scans given in Figure 27. The torsions around the S–S and C–S bonds give rise to four possible different conformers, whose optimized geometries at B3LYP-D3BJ/def2-TZVP level are provided in Figure 28 along with their relative zero-point corrected electronic energies, and conformation-defining dihedral angles.

Disulphide **1** may occur as *gauche* and *anti* conformers around the S–S bond. The three *gauche* conformers (with C–S–S–C dihedrals around 79–83°) differ in the orientation of the two pyridine rings, which can be distinguished through the position of the nitrogen atoms. When the nitrogen points towards the "outside" of the reference point – the second ring moiety – the N–C–S–S dihedral angle is 178.2°, while when it points "in" (or to "inside") the reference point, the N-C-S-S dihedral angle is *ca.* 20°. The global minimum (*gauche* out-out; C_2 symmetry) has the pyridine rings oriented in such a way that the two nitrogen atoms point towards opposite directions, mostly to avoid the destabilizing N/N interactions, which are the main interactions responsible for the higher relative energy of 10.4 kJ mol^{-1} the *gauche* in-in conformer (C_2 symmetry). The *gauche* out-in (C_1 symmetry) conformer has an intermediate relative energy of 5.2 kJ mol^{-1}. The *anti* conformer is predicted to be the energetically less stable (with a relative energy of 26.4 kJ mol^{-1}), in agreement with the expected increased repulsion caused by the lone pairs of the sulphur atoms. The isomerisation barriers associated with the conversion

between the highest energy *gauche* conformer (in-in) and the second most stable form (out-in) is slightly higher (8.2, without ZPE correction) than the barrier associated with the conversion of the out-in structure into the global minimum (6.7 kJ mol^{-1}; see Figure 27). Furthermore, the rotational barrier for *anti*→*gauche* isomerisation is considerably small (*ca.* 1.9 kJ mol^{-1}).

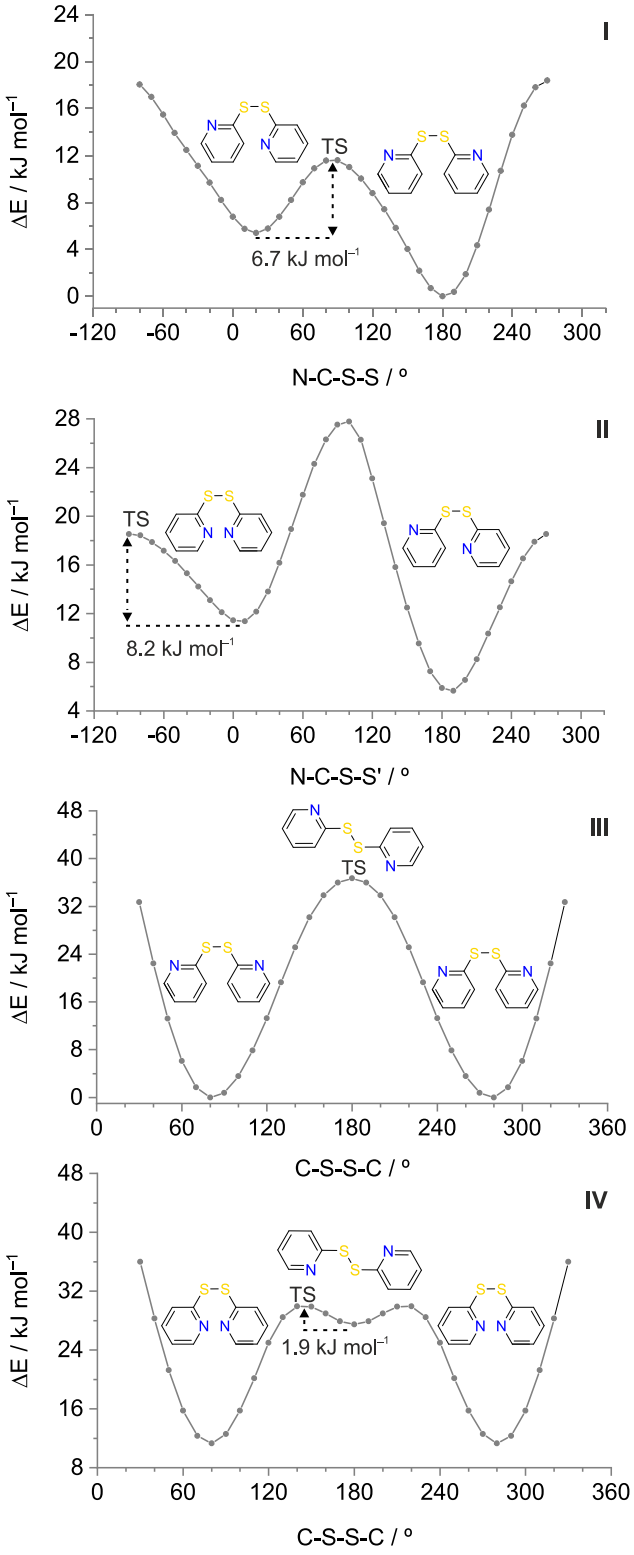

Figure 27. B3LYP-D3BJ/def2-TZVP relaxed torsional scans around the two C–S and S–S bonds of the precursor 1, showing the interconversion between gauche conformers in-out→out-out (I), in-in→in-out (II), out-out→out-out (III), and out-out→anti (IV), respectively. The barriers associated with the interconversions (in kJ mol^{-1}) are shown.

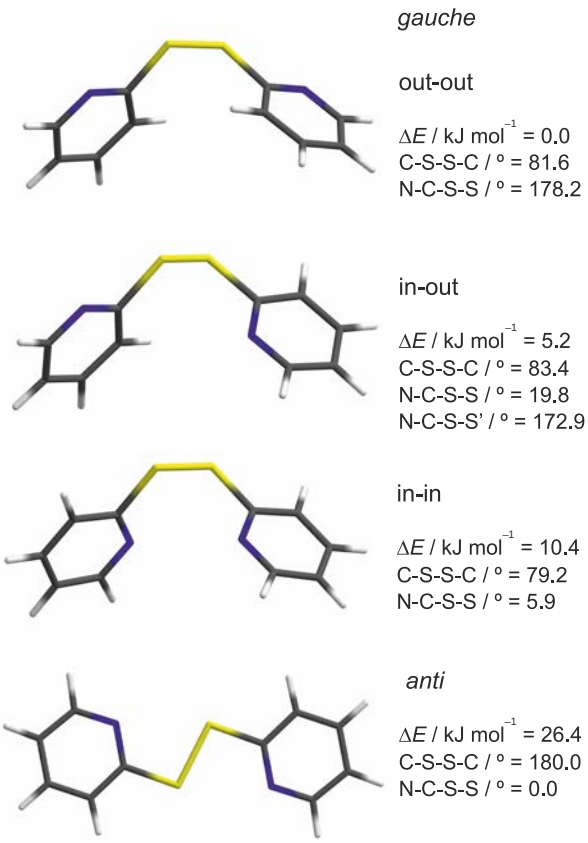

Figure 28. B3LYP-D3BJ/def2-TZVP optimized geometries of gauche (out-out, in-out, and in-in) and anti conformers of **1**, together with the zero-point corrected relative energies (in kJ mol^{-1}), and the C-S-S-C and N-C-S-C angles. The four distinct conformers can be interconverted by the rotation about the C-S and/or S-S bonds.

The effect of Grimme's dispersion correction with Becke-Johnson damping (D3BJ) on the relative zero-point corrected energies was evaluated through the comparison with the B3LYP non-corrected values. As shown in Figure 29, the same trend is found for both corrected and non-corrected values. The same is observed for the single point energies computed with DLPNO-CCSD(T) method (see Figure 29).

Monomers of precursor **1** were isolated in argon and nitrogen matrices at 10 K. The experimental IR and predicted spectra confirm the presence of the most stable conformer out-out in the matrices (see Figure 30). There is no experimental evidence of the presence of other isomers of **1**, contrary to the determined gas-phase equilibrium populations based on the computed Gibbs energies (predicted 48:49 ratio of out-out: in-out), considering the deposition temperature of 333 K (the Gibbs energy values, and Boltzmann populations are given in Table B12 Appendix B). Such preference indicates that the barrier associated with the in-out→out-out interconversion is sufficiently small to be overcome during matrix deposition.

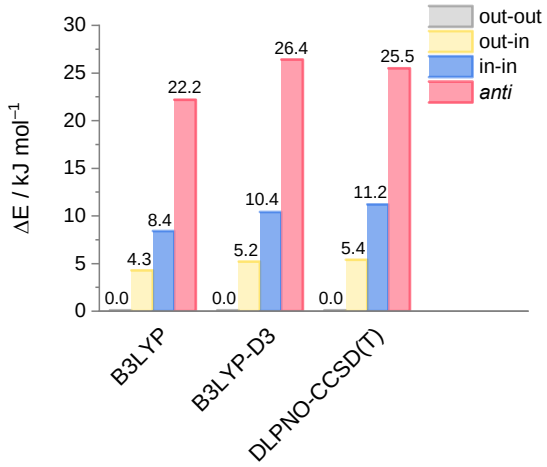

Figure 29. Zero-point corrected B3LYP/def2-TZVP with and without dispersion corrections, and DLPNO-CCSD(T)/aug-cc-pVTZ//B3LYP-D3BJ/def2-TZVP relative energies of the conformers of **1** (in kJ mol^{-1}). The computed absolute energies structures in Hartree are given in Appendix B in Table B12.

The choice of the quantum chemical model was based on the good compromise between accuracy and computational efficiency of the B3LYP functional in predicting vibrational frequencies of other disulphides and other sulphur molecules together with Ahlrichs basis sets.[227,228] Nevertheless, as the extended basis sets containing polarization and diffuse functions have been required for reliable structural and vibrational analysis of sulphur-containing molecules[229], the 6-311++G(3df,3pd) Pople-type basis set was also tested (see Figure 30). Both B3LYP/def2-TZVP and B3LYP/6-311++G(3df,3pd) methods provide a reasonable accuracy in the calculation of the wavenumbers of most of the vibrational modes with the typically deficiency of DFT methods, in this case in terms of overestimation of the vibrational frequencies (see the determination of the used scale factors in Figure B2 in Appendix B), while the intensities were found to show only a fair agreement with the experimental data. The calculations were performed with and without Grimme dispersion correction, which was found not to alter the general quality of the vibrational calculations in the case of the disulphide **1**.

Because London dispersion interactions have been found to play a key role in the structure of π-systems, the closed-shell B3LYP and unrestricted open-shell (U)B3LYP with three body dispersion term corrections D3BJ were the preferred and selected approaches. However, the non-corrected B3LYP results were compared throughout this work with the dispersion corrected results to evaluate the ability of both approaches in predicting the structures of the investigated species.

Vibrational characterisation of **1**, and the assignments can be found in Table 11. The spectra consist of several bands with splitting into subsites that result from site-splitting,

namely in the case of the bands associated with stretching vibrations and CH out-of-plane deformations.

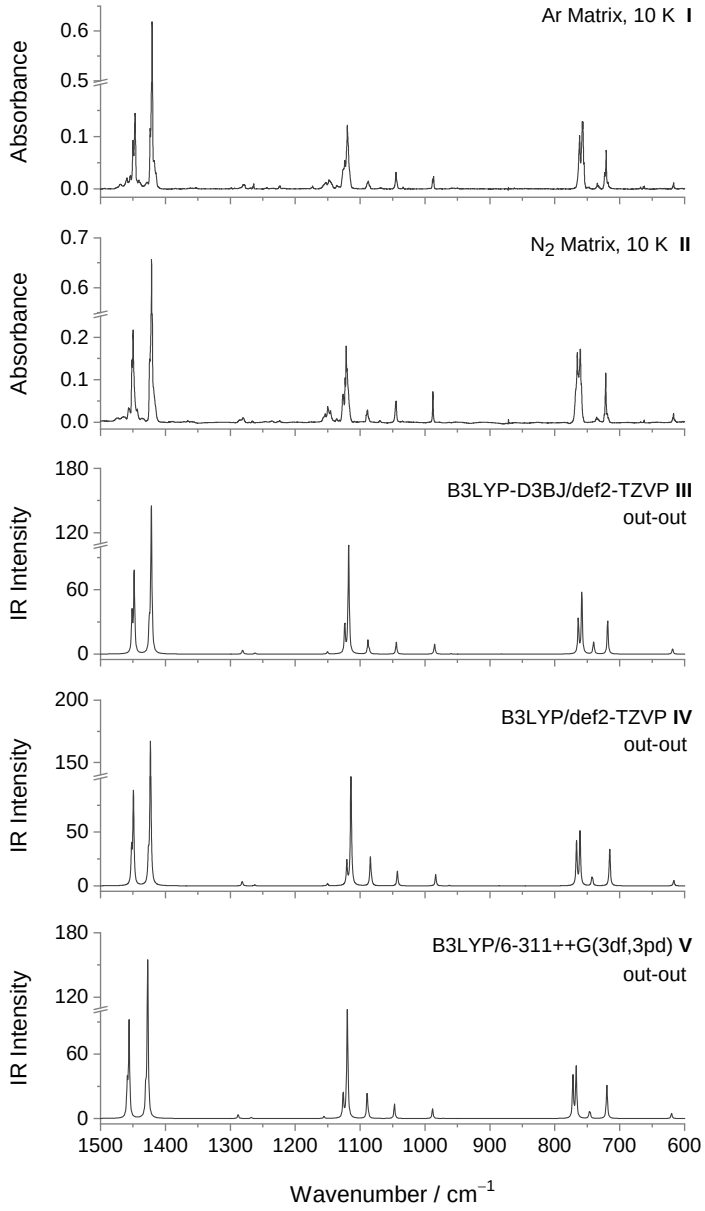

Figure 30. FTIR spectra (1510–600 cm^{-1}) of the precursor **1** trapped in argon (I) and nitrogen (II) matrices at 10 K. Harmonic scaled spectra of the global minimum (out-out) of **1** computed at B3LYP-D3BJ/def2-TZVP with and without three-body D3 dispersion corrections (III and IV, respectively), and at B3LYP/6-311++(3df,3pd) level (V) and are shown. The frequencies were scaled by 0.976, 0.978, and 0.984 factors, respectively.

Table 10. Experimental and computed IR spectra (cm^{-1}) of disulphide **1**.

Experimental[a]		Computed[b]		Approximated
Ar matrix	N_2 matrix		out-out	Assignment[c]
1577.7/1581.1	1580.1	52	1580.7 (73.4)	ring str. + CH bend.
1576.2	1576.8/1573.5	51	1576.3 (95.6)	ring str.+ CH bend.
1566.6	1566.2/1563.1	50	1570.1 (0.1)	ring str. + CH bend.
		49	1570.0 (88.4)	ring str. + CH bend.
1459.3/1450.2	1456.8/1451.6	48	1451.5 (35.7)	CH bend. + ring str.
1446.8	1449.8	47	1448.2 (78.0)	CH bend. + ring str.
1423.6	1424.4	46	1424.9 (24.5)	CH bend. + ring str.
1420.5	1421.4	45	1421.7 (150.2)	CH bend. + ring str.
1284.3	1285.3	44	1281.3 (3.3)	CH bend.
1280.3	1278.6/1280.2	43	1280.1 (1.1)	CH bend.
1266.0	1266.3	42	1262.2 (0.7)	ring str. + CH bend.
1263.9	1264.9	41	1261.6 (0.5)	ring str. + CH bend.
-	-	40	1150.6 (0.1)	CH bend.
1152.9	1153.7	39	1150.3 (2.3)	CH bend.
1148.0/1146.4	1149.9/1145.6	38	1123.7 (26.8)	CS str + ring dist.
1123.7/1119.7	1123.1/1121.5/1120.2	37	1117.7 (109.4)	CS str + ring dist.
1087.5/1084.7	1090.6/1088.5/1086.2	36	1088.0 (12.5)	ring dist. + CH bend
-	-	35	1085.7 (3.4)	ring dist. + CH bend
1044.8	1044.6	34	1044.4 (4.0)	ring dist. + CH bend
		33	1044.2 (7.6)	ring dist. + CH bend
-	-	32	986.0 (0.8)	CH o.o. def.
-	-	31	985.6 (0.2)	CH o.o. def.
988.3/986.7	987.9	30	985.2 (8.1)	ring breathing
		29	984.8 (1.2)	ring breathing
962.8/954.7/951.3	958.2/955.8/950.8	28	959.9 (0.2)	CH o.o. def
		27	959.7 (0.3)	CH o.o. def.
-	-	26	883.9 (0.0)	CH o.o. def.
-	-	25	881.9 (0.2)	CH o.o. def.
761.9	765.3/763.9	24	763.9 (32.4)	CH o.o. def.
757.6/756.6/755.1	760.8/759.1	23	758.4 (57.3)	CH o.o. def.
734.5/732.3	735.5/732.8	22	740.7 (6.3)	CH o.o. def.
		21	739.8 (7.0)	CH o.o. def.
722.6/720.7/717.9	723.0/721.5/719.1	20	718.8 (6.3)	CS str. + ring dist.
		19	718.4 (25.4)	CS str. + ring dist.
617.0	618.3/617.0/615.4	18	619.3 (1.5)	ring dist. + SS str.
		17	618.2 (4.1)	ring dist.
-	-	16	522.5 (0.6)	SS str.
481.1	482.0	15	483.7 (3.4)	ring tors.

[a] Experimental frequencies (1600–480 cm^{-1}) of **1** in Ar and N_2 matrices at 10 K. [b] Computed B3LYP-D3BJ/def2-TZVP harmonic frequencies (cm^{-1}) of out-out conformer of **1** (scaled by 0.976) and intensities (in km mol^{-1}). [c] Approximate description: str. (stretching), bend. (bending), dist. (distortion), tors. (torsion), o.o. def. (out-of-plane deformation).

5.2 Photoinduced Reactions

In this subchapter, it is reported the observation of caged pyridyl-2-thiyl radical pairs **2a** generated upon the photoinduced homolytic cleavage of the S–S bond of **1** in argon and nitrogen matrices, under the selected irradiation conditions.

Aromatic disulphide molecules display absorptions in the UV/Vis-region and there are several reports of the UV-induced disulphide-bond cleavage.[230–237] In agreement, the computed UV/Vis spectrum of the disulphide **1** using time-dependent density functional theory (TD-DFT(B3LYP-D3BJ)/def-TZVP) predicts five transitions at 272 nm (f = 0.0626), 263 nm (f = 0.0391), 262 nm (f = 0.0024), 257 nm (f = 0.0056), 243 nm (f = 0.0059). In the experiments reported below, UV light irradiations at of the matrix isolated **1** were performed considering these results.

In line with theory, irradiations performed at $\lambda = 310$ nm did not induce significative changes in the IR spectrum of the precursor **1**, whereas irradiations at $\lambda = 250$ nm (with a narrow band light source) and at ≥ 235 nm (with a broad-band light source with a cut-off filter) led to the partial consumption of **1**, and to the appearance of a set of new bands in the IR spectrum. In Figure 31, some fragments of the spectra and the changes upon 60 min of irradiation (≥ 235 nm) are shown.

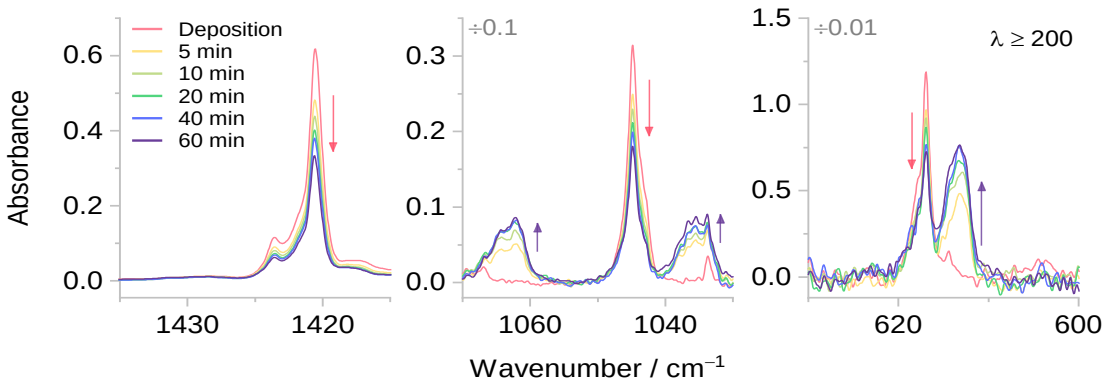

Figure 31. Selected regions of the IR spectra of matrix isolated **1** (red, deposition spectrum) and after UV-light irradiations at ≥ 235 nm for 60 minutes (yellow to violet-coloured spectra). Downward arrows (red, ↓) indicate the consumption of **1** over the time, while the upward arrows (violet, ↑) indicate the increase in intensity of some selected bands of the generated photoproducts.

Upon annealing experiments up to 25 K (performed at an approximate rate of 1 K/min, as described in Chapter 3 of this Thesis) the precursor was reformed, whereas the bands of the photoproducts were depleted from the IR spectra. Such observation is totally consistent with the generation of caged radical pairs after *in-situ* irradiation of the

matrix-isolated precursor **1** with UV-light. Given a sufficient thermal energy to overcome the activation barrier, the radicals recombination takes place (see Figure 32).

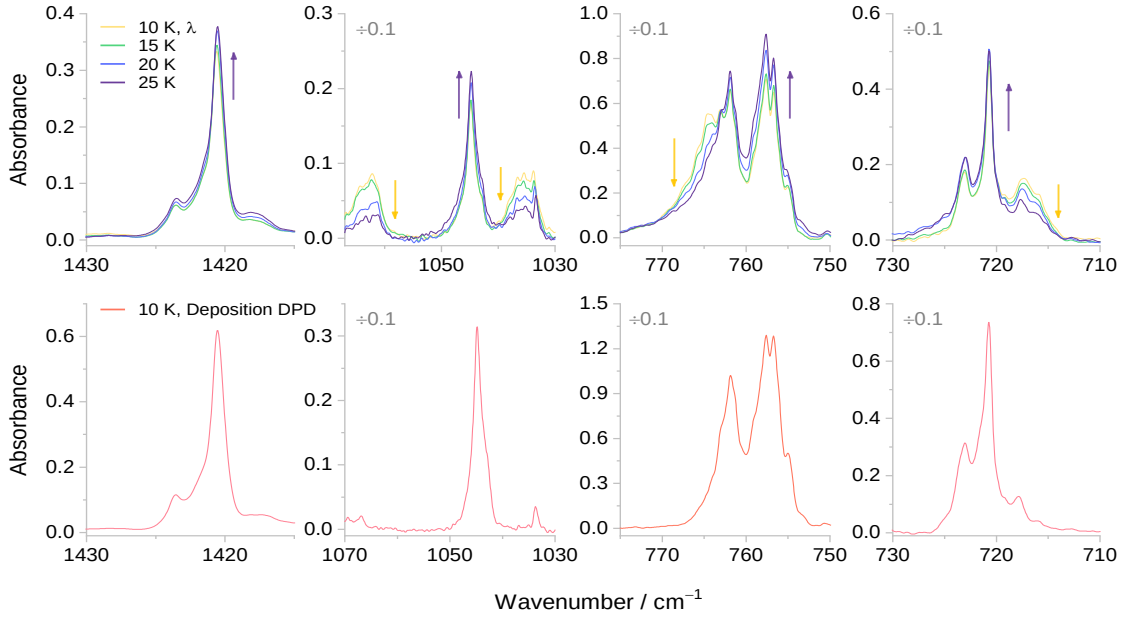

Figure 32. Fragments of the IR spectra collected upon the annealing of the irradiated Ar matrices showing the consumption of the photoproducts and the reformation of **1**. Top: IR spectrum collected after the irradiations (yellow; 10 K, **l**), together with the spectra collected upon the gradual increase in temperature (green, 15 K; blue, 20 K; purple, 25 K). Bottom: Deposition spectrum of **1** at 10 K.

5.2.1 Caged Radical Pairs

Clearly, the spectral assignment of the radical pairs was the main encountered challenge. Considering the structure of other radical caged pairs and the structure of the out-out conformation of **1**, chemical intuition was considered to construct the starting structures and to explore the configurational landscape of the radical dimers. The optimisations started from both C–H···•S–C bonded and π–π stacked pairs and were extended to several other arrangements, using (U)B3LYP with and without three-body dispersion corrections D3BJ. Following this procedure, several triplet and singlet structures (the latter using OPT=STABLE keyword and through fragment-based computations) were predicted as minimum structures on the potential energy surface, as indicated by the non-existence of imaginary frequencies.

Regarding the starting point structures, it was found that one of the pairs is stabilised by two C-H···•S-C contacts in a planar structure **2a-p** (p stands for planar), whereas the

other unveiled a stacked arrangement **2a-s** (stacked displacement), as illustrated in Figure 33.

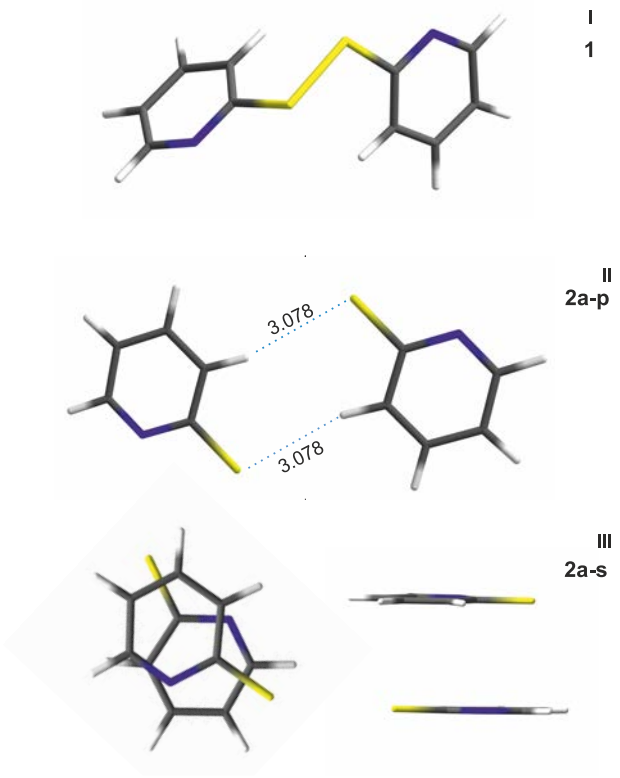

Figure 33. Predicted structures of the generated pyridyl-2-thiyl **2a** radical pairs consistent with the starting point structure of **1** (I). The established C–H···•S–C contacts (3.078 Å) in the planar structure **2a-p** (**p**: planar) evidence two stabilizing contacts between the radical pairs (II). This structure was optimized at (U)B3LYP/def2-TZVP level with and without three-body Grimme dispersion corrections (D3BJ). Alternatively, π–π stacking intermolecular interactions energetically overcome the C–H···•S–C contacts at (U)B3LYP-D3BJ approach, favouring the structure **2a-s** (**s**: stacked) illustrated on the bottom of the figure (III). The latter has been predicted as a triplet specie, and when three-body dispersion correction is added to the (U)B3LYP approach.

The latter is only predicted when the three-body inclusive dispersion term is added to the (U)B3LYP functional indicating that is favoured by London dispersion interactions, while the planar structure is predicted by both (U)B3LYP-D3BJ and (U)B3LYP approaches. These two starting-point structures provided the best spectral-structure correlations, as revealed by the accuracy of the predicted IR frequencies (see Figure 34) when compared with the experimental values, while simultaneously represent the most suitable molecular arrangements when compared with the observed out-out conformation of **1**.

The π–π stacking intermolecular interactions energetically overcome the C-H···•S-C contacts at (U)B3LYP-D3BJ, favouring the **2a-s** (stacked) dimer over the **2a-p** (planar) dimer in 14.5 kJ mol^{-1} (17.9 kJ mol^{-1} at DLPNO-CCSD(T) without ZPVE correction), with the relative electronic energy difference of 50.3 kcal mol^{-1} and of 53.8 kcal mol^{-1}, respectively, between the observed out-out conformation of **1** (see Tables B12, B13 and B14 with energy values in Hartree in Appendix B). To make the interpretation even more challenging, the **2a-p** geometry is predicted as both singlet **2a-^{1}p** (fragment-based calculation with the keyword OPT=STABLE) and triplet and **2a-^{3}p**, with very close harmonic vibrational frequencies, also as **2a-s** (see the computed (U)B3LYP-D3BJ spectra in Figure 34 and in Tables 12, B15 and B16 of the Appendix B), when dispersion corrections are not added to the B3LYP approach.

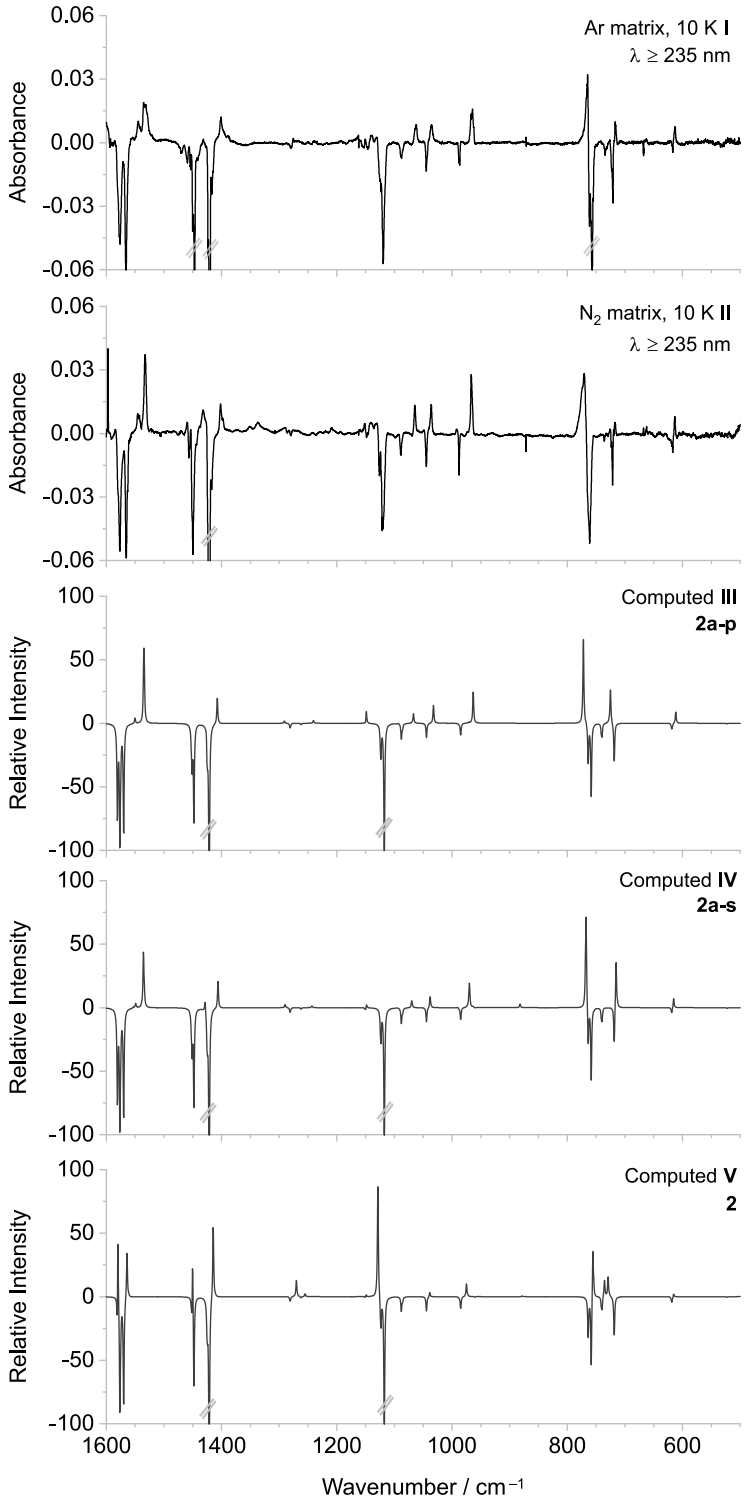

Figure 34. IR difference spectra showing the generation of radical pairs **2a** in Ar (I) and N_2 (II) matrices upon UV-light irradiation ($\lambda \geq 235$ nm) of matrix-isolated disulphide **1** (10 K), and the predicted spectra of **2a-^{3}p** (planar) and **2a-^{3}s** (stacked) radical pairs. Harmonic spectra radical dimers and precursor 1 were obtained using the unrestricted open-shell and (U)B3LYP-D3BJ and closed-shell B3LYP-D3BJ/def2-TZVP approaches and were uniformly scaled by 0.976 factor.

The singlet-triplet splitting gives an energy (ΔE_{S-T}) separation of 0.07 kJ mol^{-1}, with the singlet state being lower in energy than the triplet state. The replacement by DLPNO-CCSD(T) single point energies on the (U)B3LYP geometries reverses this energetic order (−1289.892231 Hartree for singlet and −1289.905134 Hartree for triplet, with an energy difference of 8.1 kcal mol^{-1}), revealing that the DFT method reproduces the harmonic spectra of the radical pairs very well, but the most robust DLPNO-CCSD(T) approach is more accurate in terms of electronic energies of the singlet and triplet **2a-p** states.

Indeed, is known that sulphur is an 'heavy atom' that can enhance the intersystem crossing through spin-orbit coupling in excited states and there are several reports of the formation of triplet pairs upon the photo-excitation of disulphide molecules.[238–241][242] Therefore, the generation of a triplet state followed by bond scission, would be foreseeable sequence of events upon the photoexcitation of **1**, and it would be in line with the prediction of a triplet ground state structure for the caged pairs **2a**.

It should be noted that the theoretical methods succeeded at predicting the relative stability, as the radical pairs were predicted to be lower in energy than the sum of the energy the two free radicals **2** at DLPNO-CCSD(T) level (−1289.91194624 Hartree for **2a-^{3}s,** −1289.90513415 Hartree for **2a-^{3}p** and −1289.89502573 Hartree for 2**x2**). Thus, the dissociation energies are, respectively for **2a-s** and **2a-p** at DLPNO-CCSD(T), and 10.6 kcal mol^{-1} and 6.3 kcal mol^{-1} at DLPNO-CCSD(T). The results indicate that a significantly higher amount of energy it is required to dissociate the **2a-s** structure.

Heteroaromatic radical pairs tend to prefer π–π stacked arrangements,[243–246] but non-covalent and non-stacked dimers have also been reported in crystalline structures.[51] Indeed, another crucial factor that can influence the arrangement of the radical pairs generated in these investigations is not considered by the theory predictions: the surrounding environment. Considering the matrix environment, the **2a-p** geometry appears to be more favoured as it requires the fragments displacement into a planar structure, whereas **2a-s** demands an apparently more complex reorganization of both radicals into a parallel displacement between the rings and further translation, which is probably less likely to dissociate once formed. Indeed, the electronic dissociation energy is considerably higher in the latter, which would prevent the recombination of the two fragments upon the annealing experiments. Moreover, the closeness between the stacked structures also favours the formation of other covalent bonds in addition to the S-S bond upon the fragment's recombination, whereas the recombination between sulphur atoms is more likely in **2a-p**, in line with the observed results.

As the matrix cage may play a significant role in the radical pairs structure, it is difficult to make a straightforward assignment in this case. The observed splitting patterns indicate different matrix sites, especially in argon matrices. Also, the IR experiment itself

does not provide the multiplicity of the observed species, which are only estimated as triplets based on predictions and on reported experiments for other disulphides. Nevertheless, the interplay of results points to a preference for the planar structure **2a-^{3}p**, which is tentatively assigned to the experimental observed IR bands (see Table 12 and Figure 34). Indeed, the experimental spectrum is rather well reproduced by scaled theory for radical pairs. Furthermore, the comparison between the experiment and the computed spectrum of pyridyl-2-thiyl **2** shows that there is no match between the observed and the predicted bands for the isolated radical. This indicates that initially generated radicals **2** can hardly diffuse apart and escape the matrix cages. Instead, the generated pairs snuggle up in the cold cavities.

Table 11. Experimental IR spectra of matrix isolated radicals in argon and N_2 matrices along with the unscaled harmonic (U)B3LYP-D3BJ/def2-TZVP spectrum of radical pairs **2a-^{3}p**.

Experiment[a]			Computed[b]	Approximate
Ar matrix	N_2 matrix		(U)B3LYP	Description [c]
-	-	52	1550.1 (0.0)	ring str. + CH bend.
1544.8	1545.5/1542.6	51	1550.1 (4.3)	ring str.+ CH bend.
-	-	50	1535.2 (0.0)	ring str. + CH bend.
1535.3/1531.7/1529.6	1532.6	49	1534.8 (62.0)	ring str. + CH bend.
1431.6	1431.9	48	1426.3 (5.6)	CH bend. + ring str.
-	-	47	1426.0 (0.0)	CH bend. + ring str.
-	-	46	1408.7 (0.0)	CH bend. + ring str.
1401.0	1401.9	45	1407.6 (21.8)	CH bend. + ring str.
1275.6	-	44	1290.9 (1.9)	CH bend. + CN str.
-	-	43	1290.7 (0.0)	CH bend. + CN str.
-	-	42	1241.9 (0.0)	ring str. + CH bend.
-	-	41	1240.6 (2.4)	ring str. + CH bend.
-	-	40	1150.4 (0.0)	CH bend.
1150.7	1152.1	39	1149.0 (10.2)	CH bend.
-	-	38	1093.1 (0.5)	ring dist. + CH bend. + CS str.
-	-	37	1093.0 (0.0)	ring dist. + CH bend. + CS str.
-	-	36	1069.8 (0.0)	ring dist.
1064.4/1063.4/1062.2	1064.6	35	1067.2 (8.0)	ring dist.
-	-	34	1032.3 (0.0)	ring breathing
1036.6/1035.5/1034.6	1036.1	33	1032.2 (14.5)	ring breathing
-	992.4	32	999.9 (0.1)	CH o.o. def.
-	-	31	998.2 (0.0)	CH o.o. def.
-	973.8	30	970.8 (0.8)	CH o.o. def.
-	-	29	970.4 (0.0)	CH o.o. def.
966.9/964.6/962.3	966.7	28	963.2 (25.3)	ring breathing + CS str.
-	-	27	962.7 (0.0)	ring breathing + CS str.
-	-	26	896.7 (0.0)	CH o.o. def.
-	-	25	895.6 (0.2)	CH o.o. def.
-	-	24	772.7 (0.0)	CH o.o. def.
765.8/765.8/764.7	770.6	23	772.0 (67.9)	CH o.o. def.
-	-	22	733.0 (0.1)	CH o.o. def.
-	-	21	732.9 (0.0)	CS str. + ring dist.
717.8/716.9	716.9/715.9	20	725.3 (28.7)	ring tors.
-	-	19	723.7 (0.0)	ring tors.
-	-	18	612.2 (0.0)	ring dist.
613.1	613.3	17	611.8 (9.0)	ring dist.

[a] Experimental frequencies (1600–600 cm^{-1}) of the radical caged pairs in Ar and N_2 matrices at 10 K. [b] Computed (U)B3LYP-D3BJ/def2-TZVP harmonic frequencies (cm^{-1}) of triplet **2a-^{3}p** (scaled by 0.976) and intensities (in km mol^{-1}). [c] Approximate description: str. (stretching), bend. (bending), dist. (distortion), tors. (torsion), o.o. def. (out-of-plane deformation).

5.2.2 Reactions with Molecular Oxygen

To gain additional support for the assignment, molecular oxygen was used as a trapping agent to capture pyridyl-2-thiyl radicals **2**. Fully in line with the preceding experimental results of the photolysis of **1**, pyridyl-2-thiyl peroxy radical **5** was formed upon the generation of **2** through the *in-situ* irradiation of **1** in O_2-doped N_2 matrices (see reaction scheme in Figure 29). These experimental findings are supported by theory, as described below.

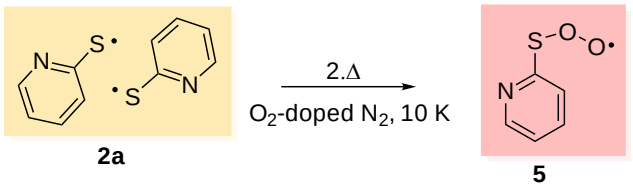

Figure 35. Generation of pyridyl-2-thiyl peroxy radical **5** upon the recombination reaction of triplet molecular oxygen with pyridyl-2-thiyl **2a** radicals in N_2 cryogenic matrices.

(U)B3LYP/def2-TZVP computations with and without dispersion corrections (D3BJ) predicted three different possible isomers for the pyridyl-2-thiyl peroxy radical **5** (see the three-dimensional potential energy surface obtained from the rotation of both C-S-O-O• and N-C-S-O• dihedral angles in Appendix B, and further details of the structural search). Two approximately *trans* structures, (**5a** and **5b**) and a *gauche* form (**5c**), as depicted in Table 13 with relevant structural parameters.

Table 12. (U)B3LYP-D3BJ/def2-TZVP computed structures of the pyridyl-2-thiyl peroxy radical **5** conformers with the N-C-S-O• and C-S-O-O• dihedral angles. The electronic energy values (in Hartree), ZPE (in Hartree), Gibbs energies (in kJ mol^{-1}), and relative zero-point electronic energies (in kJ mol^{-1}) are also shown.

	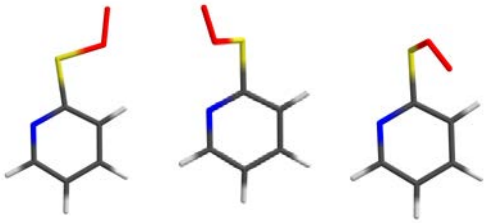		
Structure	**5a**	**5b**	**5c**
∡N-C-S-O•	180.0 °	55.2	109.5 °
∡C-S-O-O•	179.0 °	171..0	18.5 °
$E_{\text{B3LYP-D3}}$ (Hartree)	−796.379763	−796.376681	−796.377943
ZPVE (Hartree)	0.08439	0.08425	0.084316
$\Delta G_{298\ \text{B3LYP-D3}}$ (kJ mol^{-1})	0.0	7.5	5.4
$\Delta E_{0\ \text{B3LYP-D3}}$ (kJ mol^{-1})	0.0	7.7	4.6
$\Delta E_{0\ \text{B3LYP}}$ (kJ mol^{-1})	0.0	7.2	6.7

The global minimum (**5a**) displays C_s symmetry, whereas the other two structures display no symmetry. According to B3LYP-D3BJ computations, the first is separated from the highest energy minimum **5b** and from the second local minimum **5c** through small barriers (*ca.* 1 and 2 kJ mol^{-1}, respectively, as shown in Figure B1 in Appendix B).

Upon irradiation of **1** in nitrogen matrices with molecular oxygen, it was observed its partial consumption and the generation of new photoproducts. The IR bands of the radical pairs **2a** emerged in the spectrum together with a set of new IR bands (see figure 36).

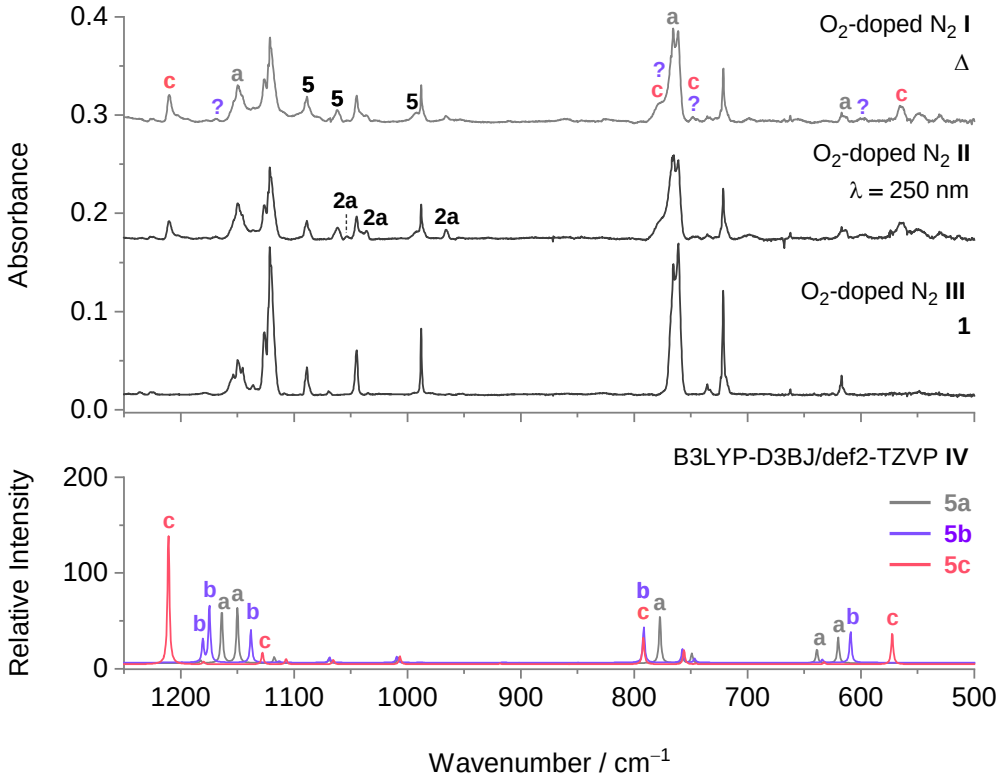

Figure 36. IR spectra showing the generation of peroxy radical **5** collected upon matrix annealing, revealing the presence of 5a and 5c conformers (I). IR spectrum collected upon the irradiation of **1** in O_2-doped nitrogen matrices showing the formation of **2a** and **5** (II). IR spectrum of **1** O_2-doped nitrogen matrices (III). Unscaled harmonic spectra peroxy radical **5** from open-shell (U)B3LYP-D3BJ/def2-TZVP computations of peroxy radical conformers 5a, 5b, and 5c are shown.

While some of the IR bands assigned to **2a** were almost depleted upon matrices warming (from 10-25 K), the new set of IR bands increased in intensity. From the IR spectrum, stands out the vibrational frequency at 1210 cm^{-1} (see Figure 36) that was fairly assigned to the νO–O stretching mode due to the fully agreement with the unscaled harmonic computed IR spectrum for **5c** and with the experimental values of the O–O$^{\bullet}$ stretching vibration of other matrix-isolated peroxy radicals, as PhSOO$^{\bullet}$ (at 1173

cm^{-1})[247], $CH_3(O)OO^{\bullet}$ (at 1100.3/1081.3 cm^{-1} syn/anti)[30], and $CH_3SOO^{\bullet}$ (at 1102.2 cm^{-1})[32]. Another prominent band appears at 566 cm^{-1} corresponding to the S–O–O$^{\bullet}$ bending vibration, and at *ca.* 777 cm^{-1}. The presence of the **5a** structure in the matrices is evidenced by the IR bands at 1327 cm^{-1} (medium intensity) and at 613 cm^{-1} (weak), whereas the assignment of the remaining IR bands is not straightforward due to the superimposed spectra of **1**, and of **5c**. One can highlight the bands at 1434 cm^{-1}, that match both **5a** and **5c** (ring str. + CH bend.), at *ca.* 1150 cm^{-1} (O-O$^{\bullet}$ Str.), which is superimposed with **1**, and also at 1065, 992 (possibly from both **5a** and **5c**) and 749 cm^{-1} (to **5a** and **1**). The latter locates the CS str. mode (see Tables B17 and B18 in Appendix B with the detailed assignment).

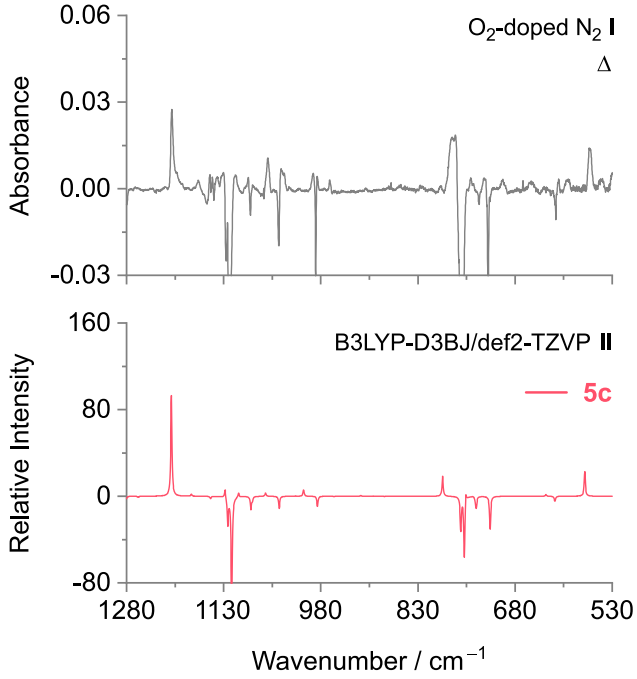

Figure 37. Top: Experimental difference spectrum: Bands pointing upwards showing the formation of pyridyl-2-thiyl peroxy radical, and bands downwards showing the consumption of the precursor **1** upon photolysis and subsequent annealing experiments (10-25 K) in O_2-doped N_2 matrices (I). Bottom: Computed difference spectrum: harmonic (U)B3LYP-D3BJ/def2-TZVP spectrum of pyridyl-2-thiyl peroxy radical **5c** *minus* the B3LYP-D3BJ spectrum of out-out conformer of **1** (II). The correlation between the experimental and theoretical spectral supported the identification of the pyridyl-2-thiyl peroxy radical **5c** in the matrix environment.

The conformation **5b** remains undetected, either due to overlapping or because it is not present in the O_2-doped matrices. The overlapping of vibrational spectra, and possibly the concentration of molecular oxygen in the matrix (*ca.* 2 %), can be accountable to some spectral broadening. According the described O_2 trapping experiments, and theory at B3LYP-D3BJ/def2-TZVP level, the formation of **5** is an exothermic process. The

reaction of **2** with triplet molecular oxygen is predicted to be − 6.5 kcal mol^{-1} (ΔH; **5c**) at (U)B3LYP, in line with the results obtained for phenylthiyl peroxy radical[247]. The generation of **5** at lower temperatures during the irradiation of **1** suggests that the reaction may proceed across a very small barrier, or through a barrierless process.

5.3 Flash Vacuum Pyrolysis

Herein, we describe the flash vacuum pyrolysis (FVP) of **1** at 750 and 840 ºC and the subsequent trapping of the FVP products with an excess of argon, as the host matrix gas (see figure 38). Identical experimental procedures and conditions were adopted for the FVP experiments performed on diphenyl disulphide, which have allowed the generation and detection of the phenyl thiyl radical.[247]

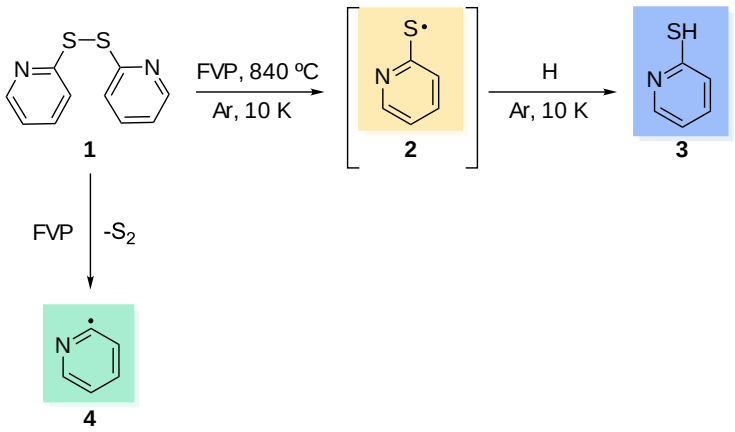

Figure 38. FVP of disulphide **1** and subsequent trapping of the products with an excess of argon at 10 K produces pyridine-2-thiol **3** and pyridyl **4** radicals. The evidence of the formation of the radical **2** is given by the detection of **3** under matrix conditions.

Based on the comparison with experimental data provided by Dr. Leszek Lapinski (see Figure 39), the pyridyl-2-thiol **3** was undoubtedly identified in the measured IR spectra of the FVP of **1**, whereas the radical **2** remains elusive. Indeed, a set of bands in the measured spectra perfectly matched the IR bands of the authentic sample of **3** (see the detailed assignment of the IR spectrum in the two previously reported studies dealing with hydrogen-atom-transfer reactions in pyridyl-2-thiol/pyridine-2-thione[224,225]), including the band at 2609.1 cm^{-1} of the S–H stretching vibrational mode. Thus, the indication of the generation of **2** through the FVP **1** was otherwise accomplished by the detection of **3**. Nevertheless, the thiol **3** and the isolated thiyl radical **2** are expected to give rise to very similar IR spectra with the probability of spectral overlapping, according to the B3LYP-D3 computational spectra of **2** and **3**, and therefore the presence of **2** in the matrices as a minor species cannot be undoubtedly excluded.

The presence of the thiol derivative in the experiment can be justified by the result of the recombination of the initially formed thiyl radical with mobile hydrogen atoms in the matrix. The complexity of the spectra indicates that multiple reaction channels take place upon FVP of **1** at both 750 and 840 º C, so that hydrogen atoms can be expected to be readily available for recombination in the matrix. At the highest temperature of 840 º C, the concentration of the generated fragments increases, and several additional bands are found.

Also note that, as referred in Chapter 2, unwanted reactions may occur in the pyrolizer tube, thus leading to additional reactions that can generate products that are also present in the matrix and were not identified, since this work goes beyond the objectives of the present study.

The thermal decomposition of **1** occurs at both at 750º and 840º. However, the final product mixture contains the undecomposed precursor **1** even at the highest FVP employed temperature of 840 ºC, as depicted in the spectral Figure 39.

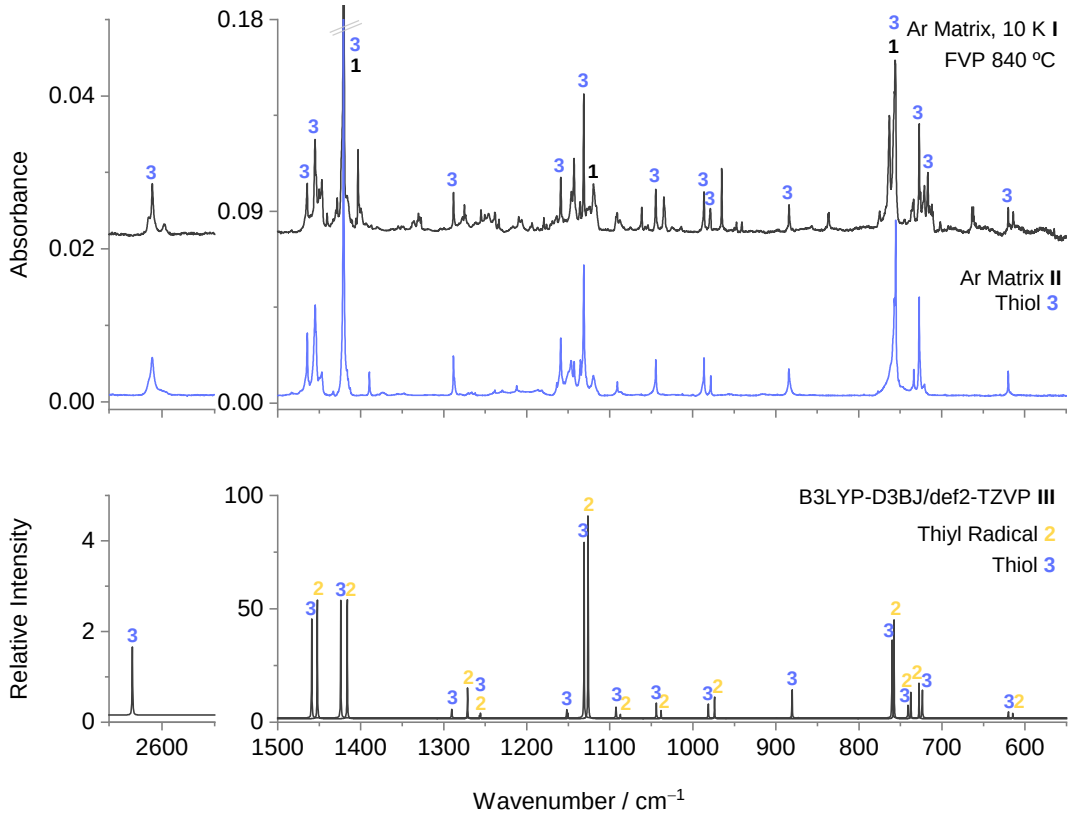

Figure 39. IR spectrum of an Ar matrix (10 K) containing the FVP (840 ºC) products (I). IR spectrum of authentic **3**[224,225] in argon matrices (II). Computed harmonic spectra of thiol **3** and of radical **2** at closed-shell and unrestricted open-shell B3LYP-D3BJ/def2-TZVP level of theory, multiplied by 0.976 scale factor (III). The absorptions of **3** are labelled with the respective number; the stronger absorptions of the undecomposed precursor are labelled with **1**. The complexity of the spectra indicates that multiple reaction channels take place.

Besides the homolytic cleavage of the S–S bond, other reactional paths were considered and deserve a brief comment. These included the fragmentation of the C–S bonds of **1** and the formation of pyridyl **4** radicals *via* S_2 elimination, or alternatively, the simultaneous generation of the pyridyl and perthiyl (R-S-S•) radicals through the cleavage of a sole C–S bond. Whereas no experimental bands could be assigned to the perthiyl radical, a set of three IR bands, observed at 940.9, 735.1, and 564.5 cm^{-1} (see Figure 40) indicates the presence in the matrix of the pyridyl **4** radical, which have been reported previously to be formed *via* FVP of pyridine by trapping in an argon matrix of the resulting products.[31]

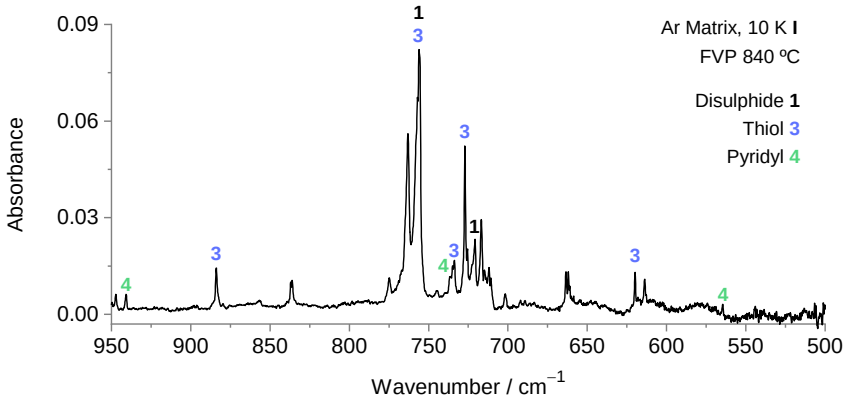

Figure 40. Fragment of the FTIR spectrum (950–500 cm^{-1}) of matrix-isolated products of FVP of **1**. Spectral assignments disulphide **1**, thiol **3** and radical **4** are indicated.

5.4 Conclusions

The elusive radical pairs **2a** have been trapped in cryogenic matrices (Ar, and N_2 at 10 K) upon the irradiation (with both broad band $\lambda \geq 235$ nm and narrow band source $\lambda = 250$ nm) of disulphide **1**. The conclusions were drawn based on the reformation of the precursor after matrices annealing (10–25 K), and through the comparison between the observed IR bands and the computed spectra of the radical pairs predicted within the harmonic approximation (U)B3LYP-D3BJ/def2-TZVP level.

To further support the results, radicals **2a** were captured by chemical trapping experiments with molecular oxygen in O_2-doped N_2 matrices. In line with the formation of sulphur centred radicals upon the excitation of **1**, the peroxy radical **5** was generated and detected in the matrix environment.

To identify the structure of the caged pairs, an extensive search was performed. Quantum chemical calculations predicted two structures with equivalent spectra that rather well

reproduce the experimental observed IR bands. One of the caged pairs is bridged by two C–H···•S–C contacts (3.078 Å), in a planar structure **2a-p** (p: planar), while the second structure a π–π stacked pair. The latter is predicted to be lower in energy, but the experimental and theoretical data point towards the preference of the **2a-p** (p: planar) structure, which was tentatively assigned in this work. Calculations predicted the triplet structures to be lower in energy then the sum of the energy of the two doublets.

Indeed, a spin forbidden reaction would prevent a fast reformation of **1** after the S–S bond homolytic cleavage. To support our suggestion, EPR spectroscopists were encouraged to perform matrix- isolation investigations under the same experimental conditions.

Looking at the overall picture, the structure and stabilization of the caged radical pairs is a result of an interplay of several factors: the radicals resonance stabilization by neighbouring atoms, the spin forbidden recombination through triplet pairs formation due to the presence of the heavy atom sulphur, the intermolecular stabilization, the geometrical constrains provided by matrix isolation that prevented the escape of the doublets due to the cage confinement, and the low temperatures attained.

It is also worth to mentioning that several other reaction pathways and products were considered during these investigations, besides the generation of the thiyl radicals above described.

Chapter 6

Photoinduced Reactivity of an Endoperoxide: Detection of Triplet Diradical Intermediates[248]

This Chapter is based on the previously published article:
E. M. Brás, L. I. L. Cabral, P. S. M. Amado, M. Abe, R. Fausto, M. L. S. Cristiano, Photoinduced Reactivity in a Dispiro-1,2,4-trioxolane: Adamantane Ring Expansion and First Direct Observation of the Long-Lived Triplet Diradical Intermediates., *J. Phys. Chem. A*, **2020**, 124, 21, 4202-4210.

Organic dispiro-endoperoxides, in particular dispiro 1,2,4-trioxanes and trioxolanes (endoperoxides), have been attracting much attention since the discovery of artemisinin more than 40 years ago[249–251]. The mechanism of bioactivation and action of the artemisinins and related endoperoxide based drugs has been discussed thoroughly[252–259][260–262]. The activation is known to require iron(II)-induced reductive cleavage of the peroxide bond to form oxygen-centred radicals, followed by rearrangement to generate carbon-centred radical species. From a synthetic point of view, endoperoxides are useful for preparation of different types of molecules *via* ring expansion reactions[263], and also for the synthesis of α-keto acids[264], *cis*-diols,[265] 1,2-diol monoesters,[266][267] benzofurans

and benzopyrans[268] *via* selective ring cleavage.

In all the above chemical processes, radical or diradical species have been assumed to be the key reactive intermediates, following the initial homolytic cleavage step. For asymmetrically substituted dispiro-1,2,4-trioxolanes, represented by **1**, and also for their dispiro-1,2,4-trioxane analogues, it has been postulated, based on the final reaction products obtained, that after the cleavage of the peroxide bond generating the dioxygen-centred diradical **2** a regioselective β-scission occurs concomitantly with the rearrangement, leading to the carbon-centred/oxygen-centred diradical species **3** (see Figure 41).[269–271]

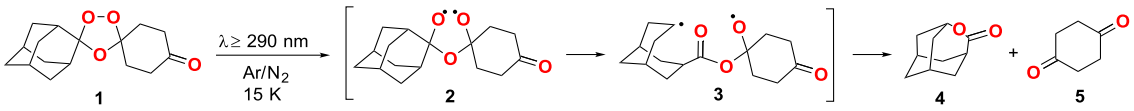

Figure 41. Proposed mechanistic scheme for the reaction of peroxide **1** upon the homolytic cleavage of the O–O bond.[272] The reaction takes place in matrix environment (Ar and N_2 at 15 K), upon UV light irradiation (λ ≥ 290 nm).

In the presence of Fe(II), the metal ion binds to the radical species and induces the cleavage of the peroxide bond.[252–259][260–262] Despite of accumulated evidence of the formation of radicals or diradicals in such reactions, and the successful detection of some of these species for reactions involving cyclic peroxides,[272,273,273] the experimental detection and characterisation of the diradical species following the homolytic peroxide bond cleavage of dispiro-1,2,4-trioxolanes has not been reported hitherto.

Herein, we report the first direct observation of the two proposed diradical intermediates for this reaction. The strategy used to achieve this goal started with the identification of the final products of the UV-induced unimolecular photolysis of adamantane-2-spiro-3'-8'-oxo-1',2',4'-trioxaspiro[4,5]decane (**1**) isolated in low temperature matrices (argon and N_2), and their vibrational characterisation. To further prove the mechanism, EPR spectroscopy measurements were performed to detect diradical species, which was performed upon the UV-photolysis of isolated **1** in a low temperature MeTHF matrix. The choice for the low temperature solid state media to perform this investigation was motivated by three main reasons: (**1**) the molecules of the precursor are cage-confined and diffusion can be prevented[62,63,65,274,275] under these conditions. This considerably simplifies the accessible chemistry, thus allowing to focus on the main features of the mechanism of the reaction; (**2**) due to the low temperature (of a few K) the attainable spectral resolution is much higher compared to what can be obtained in solution[62,63,65,274,275]; together with absence of significant interactions with the host material, this feature allowed to obtain detailed spectral information for structural elucidation that could be directly compared with results of quantum chemical

computational predictions for the isolated molecules in vacuo; (3) finally, reactive species can eventually be stabilized under these conditions, (low temperature; inhibited molecular diffusion; relative inertness of the medium), and thus, their lifetimes can be extended enough to allow their detection.

As described in detail below, the obtained IR and EPR experimental results provide evidence that the UV-induced photolysis of the investigated dispiro-1,2,4-trioxolane proceeds with the formation of the two proposed diradical triplet previously suggested[270]. As it could be expected, the measured lifetimes of the two diradicals differ considerably, with the carbon-centred/oxygen-centred diradical being considerably more stable than its oxygen centred diradical precursor.

6.1 Structure of the Diradicals Precursor

Quantum-chemical calculations (at both B3LYP and M06-2X with 6-311++G(3df,3pd) basis set; see Appendix D) in the double harmonic approximation predicted two conformations for the investigated dispiro-1,2,4-trioxolane (adamantane-2-spiro-3'-8'-oxo-1',2',4'-trioxaspiro[4,5]decane; **1**). Both methods predicted two isomers closer in energy (see Table 14), which are represented in Figure 42. The two conformers differ in the orientation of the spiro-*p*-cyclohenanonyl moiety, which in the most stable form (A) is turned to the peroxide group and in the less stable one (B) is oriented towards the ring ether fragment. Their population ratio (A:B) in the room temperature (298.15 K) gas phase equilibrium is expected to stay between 1.1 and 1.5 (from the relative energies obtained in the B3LYP and M06-2X calculations, respectively), i.e., both forms are predicted to be significantly populated in these experimental conditions, and can then be expected to be present in the cryogenic matrices investigated in this work (see below).

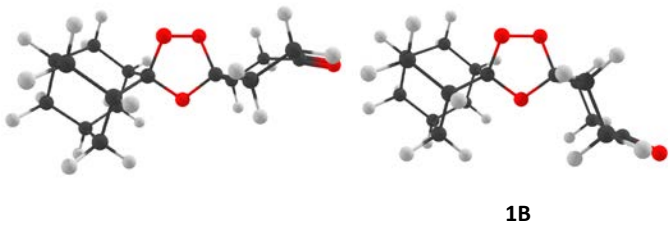

Figure 42. B3LYP/6-311++G(3df,3pd) optimized structures of the two conformers of **1** in the electronic ground state (S_0).Reprinted and adapted from Ref.[248]. Copyright 2020 American Chemical Society.

Table 13. B3LYP/6-311++G(3df,3pd) and M06-2X/6-311++G(3df,3pd) predicted energies for conformers 1A and 1B, zero-point energies (ZPE) and estimated Boltzmann populations in the gas phase equilibrium at room temperature (298.15 K).

Method	B3LYP		M06-2X	
Structure	1A	1B	1A	1B
$E_{\text{B3LYP-D3}}$ (E_h)	-924.09807272	-923.73639952	-924.09807272	-923.73639952
ZPVE (E_h)	954.8331	966.6227	954.8331	966.6227
$\Delta E_{0\,\text{B3LYP-D3}}$ (kJ mol^{-1})	0.00	0.99	0.00	0.16
Population (298.15 K)	59.8 %	40.2 %	51.7 %	48.3 %

6.2 Matrix-Isolation IR Experiments

The dispiro-1,2,4-trioxolane **1** was sublimed under high-vacuum at room temperature and co-deposited with large excess of Ar or N_2 onto the cold (15 K) CsI substrate of the cryostat. The IR spectrum obtained argon matrix is shown in Figure 43, while that obtained in the N_2 matrix is provided in the Appendix D (Figure D1). The experiments in different matrices demonstrated that the conformational population of **1** existing in the gas phase prior to deposition was efficiently trapped in both matrices. Thus, the peroxide **1** was found not to undergo thermal decomposition upon sublimation under the experimental conditions for matrix deposition.

The spectroscopic data (both experimental and predicted data) are given in Appendix D (see Tables D1, D2 and D3). Despite the similarity of the spectra of the two conformers of **1**, several bands observed in the experimental spectra could be assigned to the individual forms, thus confirming the presence of both conformers in the matrices. The comparison of the spectrum obtained in the argon matrix with the predicted spectra (see Figure 43), shows that the B3LYP functional reproduces better the experimental data throughout the spectrum than the M06-2X functional. Thus, B3LYP was the chosen functional for the interpretation of the experimental IR spectra.

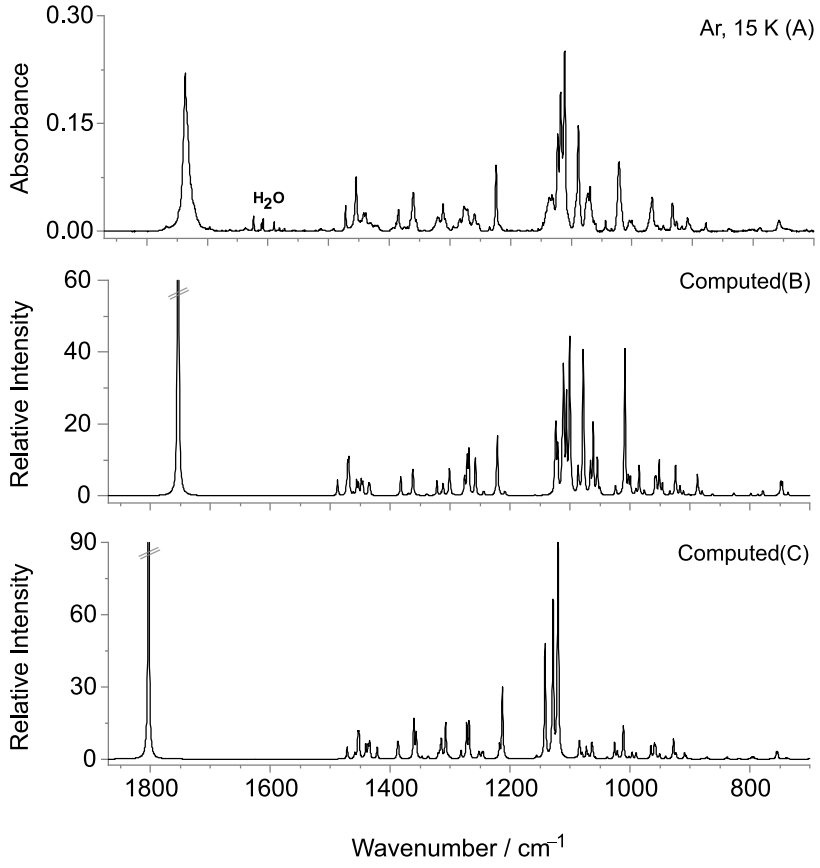

Figure 43. Infrared spectra of peroxide **1**: (A) isolated in an Ar matrix (15 K); (B), (C) computed using the B3LYP and M06-2X functionals with 6-311+G(3df,3pd) basis set. The calculated spectra are shown as the 1:1 sum of the spectra of both conformers of **1**, and the frequencies were scaled following the scaling strategy described in the text. The spectrum observed in the N_2 matrix is very similar to that obtained in argon and is provided in Figure D1 in Appendix B. Reprinted and adapted from Ref.[248]. Copyright 2020 American Chemical Society.

The UV-induced reactivity of **1** was investigated using both Ar and N_2 as matrix gases. Argon matrix was used as standard work medium, while N_2 matrix, which is known to stabilize high-energy species by establishing specific interactions with the guest species[276,277], was chosen to capture putative reaction intermediates. Both broadband ($\lambda \geq 290$ nm) and narrowband ($\lambda = 290$ nm) excitations were applied. The irradiations were performed at wavelengths within the observed band in the UV-vis spectra of **1** in ethanol solution (Figure D2). The results were found to be qualitatively identical in both matrices and for the two excitation procedures followed. Upon excitation, the IR bands of the precursor were consumed, while new bands started to emerge due to the formation of photoproducts. One can refer new spectral features were observed in the ν(C=O), (between 1720-1750 cm^{-1}) and ν(C-O), (1080-1120 cm^{-1}) regions. The intensities of the

bands of **1** decreased with the irradiation time, until almost complete conversion of the reactant **1** (after ~30 min. of broadband irradiation of the peroxide in an argon matrix). Detailed analysis of the spectra allowed the identification of 4-oxahomoadamantan-5-one **4** and 1,4-cyclohexanedione **5**, as the photoproducts obtained from the photolysis of the peroxide **1**, initiated by homolytic cleavage of the labile peroxide bond. This is shown in Figure 44 through the direct comparison between the experimental difference IR spectrum (spectrum obtained after 30 min. of irradiation at $\lambda \geq 290$ nm minus spectrum of the as-deposited argon matrix) with the predicted B3LYP/6-311++G(3df,3pd) difference IR spectrum obtained upon subtracting the spectrum of **1** from the sum of the spectra of **4** and **5** {in a ratio (0.5[**4**]+0.5[**5**]):1[**1**]}.

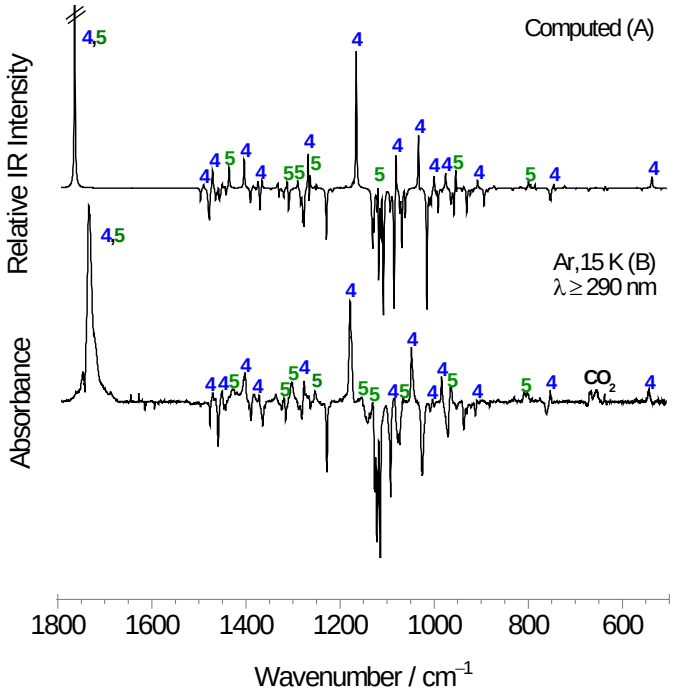

Figure 44. Computed B3LYP/6-311++G(3df,3pd) difference spectrum of 4-oxahomoadamantan-5-one **4** and 1,4-cyclohexanedione **5** *minus* the spectrum of **1** [in a ratio (0.5+0.5):1] (A). Experimental difference IR spectrum showing the formation of 4-oxohomoadamantan-5-one **4** and 1,4-cyclohexanedione **5** (upward bands) after and the consumption of matrix isolated 1 (downward bands) upon UV-light irradiation ($\lambda \geq 290$ min) at 15 K. Reprinted and adapted from Ref.[248]. Copyright 2020 American Chemical Society.

The identification of the photoproducts was further confirmed by measuring the IR spectra of the authentic samples of **4** and **5** deposited in argon matrices. The spectra of the photoproducts of **1** (Figure 44) resemble the IR experimental spectra of the isolated authentic samples deposited in argon matrices, as depicted in Figures 45 and 46. For a clearer comparison with the difference experimental IR spectrum shown in Figure 44

(irradiated minus as-deposited matrix spectra of **1**), the spectra of the authentic samples 4 and 5 (in Figure 46) were summed and subtracted from the experimental spectrum of **1** (irradiated minus as-deposited matrix spectra of **1**).

The structural computed data obtained with the B3LYP and M06-2X functionals for **4** and **5** (graphical representation of the optimized minimum energy structures, and summary of calculated energy data), as well as the spectroscopic data obtained both theoretically and experimentally for these authentic samples (graphical comparison of the calculated and matrix isolation experimental infrared data, and tables with calculated and experimental frequencies and intensities, those latter including the bands of 4 and 5 both in the photolyzed matrices of **1** and as isolated species) are given in the Appendix B (Tables D6-D14 and Figures D4 and D5). The B3LYP computed vibrational frequencies of **4** and **5** were scaled by 0.983 and 0.982, respectively.

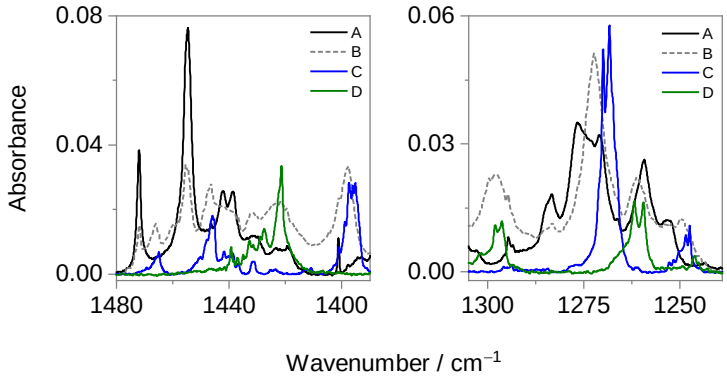

Figure 45. Selected regions of the experimental IR spectrum collected before irradiation of the matrix isolated **1** (Ar matrix at 15 K) (solid black line; A) with the spectrum collected after 30 min of ($\lambda \geq 290$ nm) irradiation (dashed gray line; B) and with the IR spectra of matrix-isolated authentic samples of 4-oxahomoadamantan-5-one **4** (solid blue line; C) and 1,4-cyclohexanedione **5** (solid green line; D) at 15 K. Reprinted and adapted from Ref.[248]. Copyright 2020 American Chemical Society.

According to the obtained results, the diradical rearrangement is regioselective, with no evidence of formation of the alternative species, such as 2-adamantanone and oxocane-2,7-dione, or other decomposition products. This can be clearly seen when one compares the infrared spectra of the photoproduced species, generated after UV irradiation of the matrix-isolated **1**, with those of 2-adamantanone and oxocane-2,7-dione (see Figure 44; the experimental and predicted IR spectra of these chemical was also considered and is shown in Appendix B, Figure B6 and Tables B15 and B16). The observed regioselectivity can be explained by the expected greater stability of the (secondary carbon-centred)/oxygen-centred diradical species **3**, in comparison with the putative alternative (primary carbon-centred)/oxygen-centred diradical that would lead to the non-observed

final products. In addition, spin density calculations (performed at the (U)B3LYP/6-311++G(3df,3dp) level) on the triplet state dioxygen-centred diradical result in a considerable larger electron spin density in the tertiary β-carbon of the spiroadamantyl substituent as compared to that of the secondary β-carbon of the spiro-*p*-cyclohexanonyl substituent, which can also be considered an indication of a most favourable rearrangement of the initially generated dioxygen-centred diradical into the (secondary carbon-centred)/oxygen-centred diradical species **3**, leading to the observed final products.

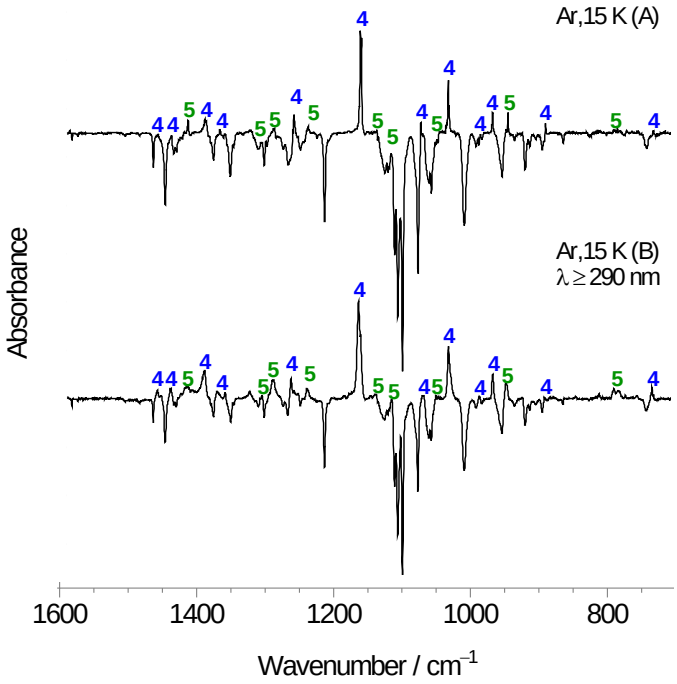

Figure 46. Experimental difference IR spectrum of authentic matrix-isolated 4-oxohomoadamantan-5-one **4** and authentic 1,4-cyclohexanedione **5** *minus* spectrum of **1** Ar matrix at 15 K (A). Experimental difference IR spectrum showing the formation of 4-oxohomoadamantan-5-one **4** and 1,4-cyclohexanedion **5** after and the consumption of matrix isolated 1 upon UV-light irradiation (λ ≥ 290 min) at 15 K. Reprinted and adapted from Ref.[248].Copyright 2020 American Chemical Society.

6.3 EPR Spin-Trapping Experiments

The *in situ* EPR measurements in the photolysis of 1 in MeTHF matrix were conducted using nm laser light (5 mJ) at 10-50 K. The X-band EPR signals were measured at a resonance frequency of 9.40 GHz (Figure 47). During the photolysis at 10 K (Figure 47 Ib), a half-field signal at ~1550 G (triplet species A) was observed after 120 seconds, which is a typical triplet species of diradicals, and another half-field signal at 1670 G

(triplet species B) was detected after 420 seconds, together with the 1550 G signal (Figure 47 Ic). Both resonance frequencies (1550 and 1670 GHz) are typical for triplet diradicals. Under dark conditions, only the half-field signal at 1670 G was detected (Figure 47 Id), indicating that the disappeared triplet species A is short-lived, while the triplet species B is persistent, under the MeTHF matrix conditions, at 10 K.

To gather further insight regarding the reactivity of the triplet species B, the photolyzed at 10 K was warmed to 50 K under dark conditions (Figure 47 IIb). The typical triplet signal disappeared and did not recover to the original one in Figure 47 Ic after re-cooling the sample to 10 K, indicating that the triplet species B was also thermally labile at ~50 K. The triplet signal of B was obtained by the difference spectrum of Figure 47 IIa–b (Figure 47 IIc). The zero-field splitting parameters D/hc and E/hc of the triplet species B were determined to be 0.160 cm^{-1} and 0.001 cm^{-1} after the simulation (Figure 47 IId). From the D/hc value, the distance between two spins was estimated to be ~5 Å.

The EPR results demonstrate that two triplet species (A and B) are formed during the photolysis of the investigated endoperoxide **1**. One of the triplet species (A) is thermally quite labile, while the other (B) is persistent at 10 K. Considering the results obtained in the photolysis of **1** in argon matrix, in particular the obtained final products, the theoretical data described in the previous sections, and the literature evidence, diradicals **2** and **3** are tentatively assigned to the intermediates A and B, respectively, detected by EPR. This is the first experimental detection of these diradical intermediates.

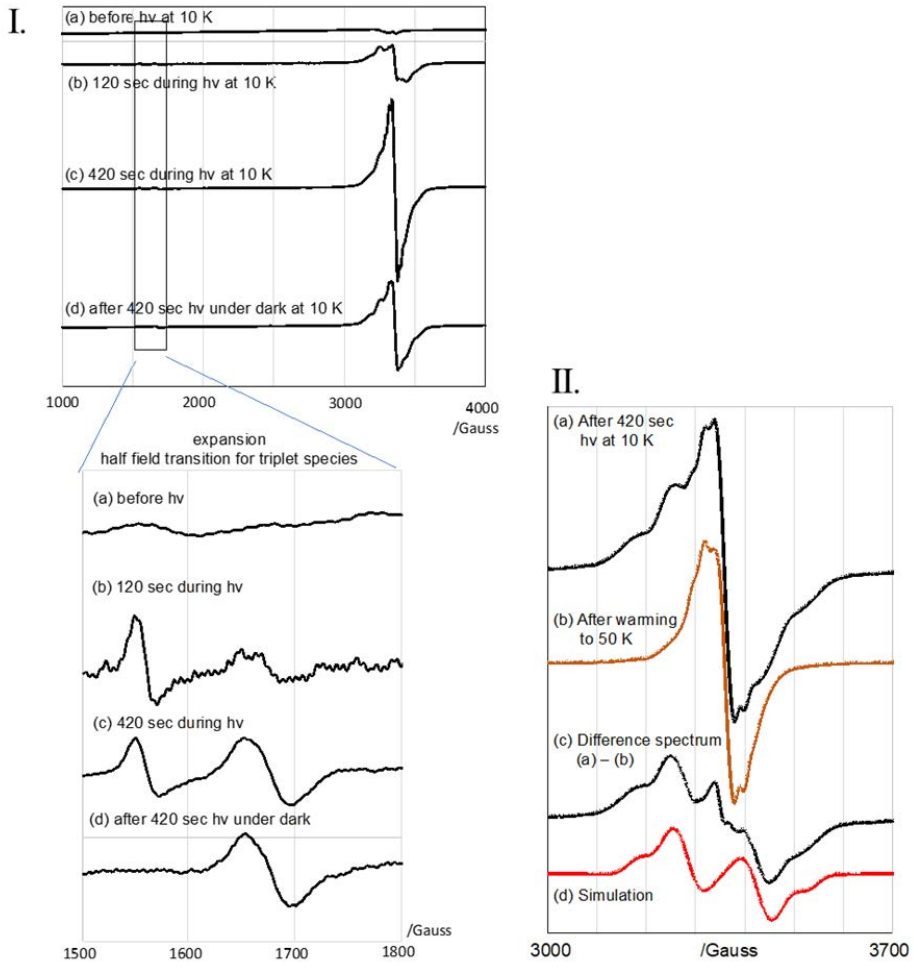

Figure 47. (I) X-band EPR spectra (9.40 GHz, 1000-4000 G) obtained from photolysis studies of peroxide **1** (100 mM) in MeTHF-matrix, at 266 nm; (a) before irradiation at 10 K; (b) after irradiation for 120 seconds at 10 K; (c) after irradiation for 420 seconds, at 10 K; (d) after irradiation for 420 seconds, under dark, at 10 K; II: X-band EPR signals (9.40 GHz, 3000-4000 G) from photolysis of peroxide 1 (100 mM) in MeTHF-matrix at 266 nm; (a) after 420 seconds photolysis, under dark, at 10 K; (b) after warming the sample to 50 K, and subsequent re-cooling to 10K; (c) difference spectrum between (a)–(b); (d) simulated spectrum with D/hc = 0.160 cm^{-1} E/hc = 0.001 cm^{-1} at g value of 2.003. Reprinted and adapted from Ref.[248].Copyright 2020 American Chemical Society.

6.4 Conclusions

The endoperoxide **1** has been investigated using matrix isolation techniques coupled to FTIR and EPR spectroscopies. All experimental results have been supported by quantum chemical calculations using two levels of theory [B3LYP/6-311++G(3df,3dp) and M06-2X/6-311++G(3df,3dp)]. The comparison of the spectrum obtained in the argon matrix with those theoretically predicted shown that the B3LYP functional reproduces better the experimental data throughout the spectrum than the M06-2X functional. Both methods predict two conformers for the dispiro-1,2,4-trioxolane **1** with very close energies, differing in the orientation of the spiro-*p*-cyclohexanonyl moiety, which in the most stable form is directed to the peroxide group, while it is oriented towards the ring ether fragment in the less stable conformer. Both conformers were identified and assigned.

The UV-induced reactivity of **1** was investigated in both Ar, N_2, using broadband ($\lambda \geq 290$ nm) and narrowband ($\lambda = 290$ nm) irradiation sources. The obtained results were proved to be qualitatively identical in both matrices and for the two followed excitation procedures. Irradiation of matrix-isolated **1** at $\lambda \geq 290$ nm led to the photocleavage of the endoperoxide with the formation of other chemical species, as evidenced by the observation of new spectral features in the ν(C=O), (between 1720-1750 cm^{-1}) and ν(C-O), (1080-1120 cm^{-1}) regions. Detailed analysis of the spectra of the photolyzed matrices allowed identification of 4-oxahomoadamantan-5-one **4** and 1,4-cyclohexanedione **5** as the sole final products from photolysis of the trioxolane **1**. This identification was further confirmed through the comparison with the matrix spectra of the authentic samples. Such observation indicates that the dioxygen-centred diradical **2**, formed upon homolytic cleavage of the labile peroxide bond, undergoes a regioselective radical isomerisation to form the more stable (secondary carbon-centred)/oxygen-centred diradical **3**. In fact, no evidence was observed for the formation of 2-adamantanone and oxocane-2,7-dione, the products that would arise from the putative alternative (primary carbon-centred)/oxygen-centred diradical. The observed regioselectivity can be explained by the expected greater stability of the (secondary carbon-centred)/oxygen-centred diradical species **3** in comparison to its primary counterpart. These results are in keeping with information gathered from studies on the mechanisms of bioactivation of trioxolane based antimalarial candidates, where heme-adducts of the secondary carbon-centred)/oxygen-centred diradical species analogues of **3** were detected[278].

In situ EPR measurements during photolysis of the endoperoxide **1** deposited in a MeTHF-matrix led to the detection of signals at 1550 and 1670 GHz, corresponding to resonances of two triplet diradicals. The diradical with the signal at 1550 GHz has

revealed to be thermally labile, while the other specie (at 1670 GHz) proved persistent at 10 K. The observation of signals with resonance frequencies that are typical for triplet diradicals, combined with the product characterisations achieved through the matrix isolation FTIR studies, indicate that the postulated diradicals **2** and **3** shall correspond to the intermediates detected by the experiment. In conclusion, our results support the proposal of a regioselective radical isomerisation and provide evidence for the presence of both intermediate diradicals after photolysis of **1** in a MeTHF-matrix. This work deepens the knowledge concerning the photoreactivity of endoperoxides.

Aknowledgments

The Coimbra Chemistry Centre (CQC) and the Center of Marine Sciences (CCMar) are supported by the Portuguese Science Foundation (FCT; Projects UID/ QUI/0313/2019 and UID/MULTI/04326/2019) and COMPETE-EU. E.M.B. thanks FCT for both the Research Grants CCMAR/BI/0013/2017, awarded within the Project PTDC/MAR-BIO/4132/2014, and SFRH/BD/136246/2018.

Bibliography

[1] S. Aloisio, J. S. Francisco, *Acc. Chem. Res.* **2000**, *33*, 825–830.

[2] E. Vöhringer-Martinez, B. Hansmann, H. Hernandez, J. S. Francisco, J. Troe, B. Abel, *Science,* **2007**, *315*, 497–501.

[3] T. Trabelsi, J. M. Anglada, M. F. Ruiz-López, J. S. Francisco, *J. Chem. Phys.* **2019**, *151*, 111103.

[4] G. Porter, *Nature* **1948**, *162*, 390–390.

[5] D. Griller, K. U. Ingold, *Acc. Chem. Res.* **1976**, *9*, 13–19.

[6] O. Ouari, D. Gigmes, in *Nitroxides*, Royal Society Of Chemistry, Cambridge, **2021**, pp. 1–6.

[7] H. Fischer, *Chem. Rev.* **2001**, *101*, 3581–3610.

[8] D. Leifert, A. Studer, *Angew. Chemie Int. Ed.* **2020**, *59*, 74–108.

[9] A. R. Forrester, R. H. Thomson, *Nature* **1964**, *203*, 74–75.

[10] L. Tebben, A. Studer, *Angew. Chemie Int. Ed.* **2011**, *50*, 5034–5068.

[11] A. De Mico, R. Margarita, L. Parlanti, A. Vescovi, G. Piancatelli, *J. Org. Chem.* **1997**, *62*, 6974–6977.

[12] A. Studer, T. Schulte, *Chem. Rec.* **2005**, *5*, 27–35.

[13] L. G. Arnaut, M. M. Pereira, J. M. Dąbrowski, E. F. F. Silva, F. A. Schaberle, A. R. Abreu, L. B. Rocha, M. M. Barsan, K. Urbańska, G. Stochel, C. M. A. Brett, *Chem. - A Eur. J.* **2014**, *20*, 5346–5357.

[14] P. J. Wright, A. M. English, *J. Am. Chem. Soc.* **2003**, *125*, 8655–8665.

[15] J. R. Alvarez-Idaboy, N. Mora-Diez, R. J. Boyd, A. Vivier-Bunge, *J. Am. Chem. Soc.* **2001**, *123*, 2018–2024.

[16] S. Du, J. S. Francisco, S. Kais, *J. Chem. Phys.* **2009**, *130*, 124312.

[17] R. Crespo-Otero, E. Sánchez-García, R. Suardíaz, L. A. Montero, W. Sander, *Chem. Phys.* **2008**, *353*, 193–201.

[18] S. Jørgensen, C. Jensen, H. G. Kjaergaard, J. M. Anglada, *Phys. Chem. Chem. Phys.* **2013**, *15*, 5140.

[19] M. Lucarini, V. Mugnaini, G. F. Pedulli, M. Guerra, *J. Am. Chem. Soc.* **2003**, *125*, 8318–8329.

[20] A. Mardyukov, E. Sanchez-Garcia, R. Crespo-Otero, W. Sander, *Angew. Chemie - Int. Ed.* **2009**, *48*, 4804–4807.

[21] A. Mardyukov, R. Crespo-Otero, E. Sanchez-Garcia, W. Sander, *Chem. - A Eur. J.* **2010**, *16*, 8679–8689.

[22] W. Sander, S. Roy, I. Polyak, J. M. Ramirez-Anguita, E. Sanchez-Garcia, *J. Am. Chem. Soc.* **2012**, *134*, 8222–8230.

[23] R. Crespo-Otero, K. Bravo-Rodriguez, S. Roy, T. Benighaus, W. Thiel, W. Sander, E. Sánchez-García, *ChemPhysChem* **2013**, *14*, 805–811.

[24] J. C. Hansen, J. S. Francisco, *ChemPhysChem* **2002**, *3*, 833–840.

[25] E. M. Brás, T. L. Fischer, M. A. Suhm, *Angew. Chemie* **2021**, *133*, 19161–19165.

[26] E. M. Brás, T. L. Fischer, M. A. Suhm, *Angew. Chemie Int. Ed.* **2021**, *60*, 19013–19017.

[27] A. J. Barnes, *J. Mol. Struct.* **2018**, *1163*, 77–85.

[28] A. Mardyukov, F. Keul, P. R. Schreiner, *J. Phys. Chem. A* **2019**, *123*, 4937–4941.

[29] J. Xu, Z. Wu, H. Wan, G. Deng, B. Lu, A. K. Eckhardt, P. R. Schreiner, T. Trabelsi, J. S. Francisco, X. Zeng, *J. Am. Chem. Soc.* **2018**, *140*, 9972–9978.

[30] H. P. Reisenauer, J. Romański, G. Mlostoń, P. R. Schreiner, *Chem. Commun.* **2013**, *49*, 9467.

[31] A. Korte, A. Mardyukov, W. Sander, *Aust. J. Chem.* **2014**, *67*, 1324.

[32] Z. Wu, X. Shao, B. Zhu, L. Wang, B. Lu, T. Trabelsi, J. S. Francisco, X. Zeng, *Commun. Chem.* **2022**, *5*, 1–8.

[33] M. J. Nowak, I. Reva, A. J. Lopes Jesus, L. Lapinski, R. Fausto, *Phys. Chem. Chem. Phys.* **2019**, *21*, 22857–22868.

[34] A. J. Lopes Jesus, M. T. S. Rosado, R. Fausto, I. Reva, *Phys. Chem. Chem. Phys.* **2020**, *22*, 22943–22955.

[35] Z. Wu, L. Wang, B. Lu, A. K. Eckhardt, P. R. Schreiner, X. Zeng, *Phys. Chem. Chem. Phys.* **2021**, *23*, 16307–16315.

[36] S. Davis, D. T. Anderson, G. Duxbury, D. J. Nesbitt, *J. Chem. Phys.* **1997**, *107*, 5661–5675.

[37] M. Snels, V. Horká-Zelenková, H. Hollenstein, M. Quack, in *Handb. High-Resolution Spectrosc.*, John Wiley & Sons, Ltd, Chichester, UK, **2011**.

[38] H. W. Rohrs, C. T. Wickham-Jones, G. B. Ellison, D. Berry, B. M. Argrow, *Rev. Sci. Instrum.* **1995**, *66*, 2430–2441.

[39] E. Whittle, D. A. Dows, G. C. Pimentel, *J. Chem. Phys.* **1954**, *22*, 1943–1943.

[40] I. Norman, G. Porter, *Nature* **1954**, *174*, 508–509.

[41] *Proc. R. Soc. London. Ser. A. Math. Phys. Sci.* **1955**, *230*, 399–414.

[42] E. D. Becker, G. C. Pimentel, *J. Chem. Phys.* **1956**, *25*, 224–228.

[43] G. Porter, *Spectrochim. Acta* **1959**, *14*, 261–270.

[44] G. E. Ewing, W. E. Thompson, G. C. Pimentel, *J. Chem. Phys.* **1960**, *32*, 927–932.

[45] W. Lubitz, F. Lendzian, R. Bittl, *Acc. Chem. Res.* **2002**, *35*, 313–320.

[46] C. T. Rodgers, P. J. Hore, *Proc. Natl. Acad. Sci.* **2009**, *106*, 353–360.

[47] P. J. Hore, H. Mouritsen, *Annu. Rev. Biophys.* **2016**, *45*, 299–344.

[48] Z. Yang, D. Ng, M. A. Garcia-Garibay, *J. Org. Chem.* **2001**, *66*, 4468–4475.

[49] J. M. Rawson, A. Alberola, A. Whalley, *J. Mater. Chem.* **2006**, *16*, 2560.

[50] D. Bates, C. M. Robertson, A. A. Leitch, P. A. Dube, R. T. Oakley, *J. Am. Chem. Soc.* **2018**, *140*, 3846–3849.

[51] H. Phan, K. Lekin, S. M. Winter, R. T. Oakley, M. Shatruk, *J. Am. Chem. Soc.* **2013**, *135*, 15674–15677.

[52] M. Sakurai, R. Kabe, M. Fuki, Z. Lin, K. Jinnai, Y. Kobori, C. Adachi, T. Tachikawa, *Commun. Mater.* **2021**, *2*, 74.

[53] Z. Wu, C. Chen, J. Liu, Y. Lu, J. Xu, X. Liu, G. Cui, T. Trabelsi, J. S. Francisco, A. Mardyukov, A. K. Eckhardt, P. R. Schreiner, X. Zeng, *J. Am. Chem. Soc.* **2019**, *141*, 3361–3365.

[54] W. G. Hatton, N. P. Hacker, P. H. Kasai, *J. Chem. Soc., Chem. Commun.* **1990**,

227–229.

[55] J. Pacansky, J. Bargon, *J. Am. Chem. Soc.* **1975**, *97*, 6896–6897.

[56] R. A. Moss, Y. Ma, F. Zheng, R. R. Sauers, T. Bally, A. Maltsev, J. P. Toscano, B. M. Showalter, *J. Phys. Chem. A* **2002**, *106*, 12280–12291.

[57] M. Pettersson, E. M. S. Maçôas, L. Khriachtchev, J. Lundell, R. Fausto, M. Räsänen, *J. Chem. Phys.* **2002**, *117*, 9095–9098.

[58] A. K. Eckhardt, F. R. Erb, P. R. Schreiner, *Chem. Sci.* **2019**, *10*, 802–808.

[59] B. Bernhardt, F. Dressler, A. K. Eckhardt, J. Becker, P. R. Schreiner, *Chem. – A Eur. J.* **2021**, *27*, 6732–6739.

[60] R. Fausto, T. Nikitin, E. M. Brás, in *Light Induc. React. Cryog. Matrices*, **2019**, pp. 28–69.

[61] R. Fausto, T. Nikitin, E. M. Brás, in *Light Induc. React. Cryog. Matrices*, **2021**, pp. 53–108.

[62] I. R. Dunkin, *Matrix Isolation Techniques: A Practical Approach*, Oxford, **1998**.

[63] A. J. Barnes, in *Low-Temperature Chem. Atmos.*, Springer Berlin Heidelberg, Berlin, Heidelberg, **1994**, pp. 351–372.

[64] T. Bally, in *React. Intermed. Chem.*, John Wiley & Sons, Inc., Hoboken, NJ, USA, **2005**, pp. 795–845.

[65] R. Fausto, *Low Temperature Molecular Spectroscopy*, Kluwer, Amsterdam (Holland), **1996**.

[66] L. Duarte, R. Fausto, I. Reva, *Phys. Chem. Chem. Phys.* **2014**, *16*, 16919.

[67] A. Mardyukov, W. Sander, in *Encycl. Radicals Chem. Biol. Mater.*, John Wiley & Sons, Ltd, Chichester, UK, **2012**.

[68] L. Andrews, J. H. Miller, B. W. Keelan, *Chem. Phys. Lett.* **1980**, *71*, 207–210.

[69] J. Pacansky, M. Dupuis, *J. Am. Chem. Soc.* **1982**, *104*, 415–421.

[70] J. Pacansky, W. Koch, M. D. Miller, *J. Am. Chem. Soc.* **1991**, *113*, 317–328.

[71] A. Mardyukov, W. Sander, *Chem. - A Eur. J.* **2009**, *15*, 1462–1467.

[72] A. V. Friderichsen, J. G. Radziszewski, M. R. Nimlos, P. R. Winter, D. C. Dayton, D. E. David, G. B. Ellison, *J. Am. Chem. Soc.* **2001**, *123*, 1977–1988.

[73] A. Engdahl, G. Karlström, B. Nelander, *J. Chem. Phys.* **2003**, *118*, 7797–7802.

[74] T. L. Fischer, M. Bödecker, A. Zehnacker-Rentien, R. A. Mata, M. A. Suhm, *Phys. Chem. Chem. Phys.* **2022**, *24*, 11442–11454.

[75] H. C. Gottschalk, A. Poblotzki, M. Fatima, D. A. Obenchain, C. Pérez, J. Antony, A. A. Auer, L. Baptista, D. M. Benoit, G. Bistoni, F. Bohle, R. Dahmani, D. Firaha, S. Grimme, A. Hansen, M. E. Harding, M. Hochlaf, C. Holzer, G. Jansen, W. Klopper, W. A. Kopp, M. Krasowska, L. C. Kröger, K. Leonhard, M. Mogren Al-Mogren, H. Mouhib, F. Neese, M. N. Pereira, M. Prakash, I. S. Ulusoy, R. A. Mata, M. A. Suhm, M. Schnell, *J. Chem. Phys.* **2020**, *152*, 164303.

[76] C. Zimmermann, T. L. Fischer, M. A. Suhm, *Molecules* **2020**, *25*, 5095.

[77] K. A. E. Meyer, M. A. Suhm, *Chem. Sci.* **2019**, *10*, 6285–6294.

[78] M. D. Morse, in *Exp. Methods Phys. Sci.*, **1996**, pp. 21–47.

[79] D. H. Levy, *Science,* **1981**, *214*, 263–269.

[80] B. Hartwig, *Diols under Investigation: Benchmarking Their Monomers; Dimers and Chirality Recognition, PhD Thesis,* Georg-August-Universität Göttingen,Göttingen, Germany, **2022**.

[81] J. M. Hayes, *Chem. Rev.* **1987**, *87*, 745–760.

[82] D. R. Miller, *Atomic and Molecular Beam Methods*, Oxford University Press, New York, **1988**.

[83] P. C. Engelking, *Chem. Rev.* **1991**, *91*, 399–414.

[84] M. Herman, R. Georges, M. Hepp, D. Hurtmans, *Int. Rev. Phys. Chem.* **2000**, *19*, 277–325.

[85] J. Arnó, J. W. Bevan, in *Jet Spectrosc. Mol. Dyn.*, Springer Netherlands, Dordrecht, **1995**, pp. 29–73.

[86] A. Amirav, U. Even, J. Jortner, *Chem. Phys.* **1980**, *51*, 31–42.

[87] R. Medel, J. R. Springborn, D. L. Crittenden, M. A. Suhm, *Molecules*, **2021**, *27*, 101.

[88] M. M. Quesada-Moreno, M. Fatima, R. Medel, C. Pérez, M. Schnell, *Phys. Chem. Chem. Phys.* **2022**, *24*, 12849–12859.

[89] D. J. Nesbitt, *Annu. Rev. Phys. Chem.* **1994**, *45*, 367–399.

[90] T. A. Miller, *Science,* **1984**, *223*, 545–553.

[91] D. T. Anderson, S. Davis, T. S. Zwier, D. J. Nesbitt, *Chem. Phys. Lett.* **1996**,

258, 207–212.

[92] D. W. Kohn, H. Clauberg, P. Chen, *Rev. Sci. Instrum.* **1992**, *63*, 4003–4005.

[93] D. E. Powers, J. B. Hopkins, R. E. Smalley, *J. Phys. Chem.* **1981**, *85*, 2711–2713.

[94] A. Mardyukov, P. R. Schreiner, *Phys. Chem. Chem. Phys.* **2016**, *18*, 26161–26165.

[95] A. Mardyukov, Y. A. Tsegaw, W. Sander, P. R. Schreiner, *Phys. Chem. Chem. Phys.* **2017**, *19*, 27384–27388.

[96] H. C. Gottschalk, T. L. Fischer, V. Meyer, R. Hildebrandt, U. Schmitt, M. A. Suhm, *Instruments* **2021**, *5*, 12.

[97] M. A. Suhm, F. Kollipost, *Phys. Chem. Chem. Phys.* **2013**, *15*, 10702–10721.

[98] N. Borho, *Chirale Erkennung in Molekülclustern: Maßgeschneiderte Aggregation von Alpha-Hydroxyestern, PhD Thesis,* Cuvillier Verlag, Göttingen, Germany, **2005**.

[99] M. Heger, *Diagonal and Off-Diagonal Anharmonicity in Hydrogen-Bonded Systems*, Georg-August-Universität Göttingen, Göttingen, **2015**.

[100] K. A. E. Meyer, *Carboxylic Acids Under Vibrational Scrutiny: Experimental Reference Data to Benchmark Quantum Chemical Calculations, PhD Thesis,* Eorg-August-Universität Göttingen, Göttingen, Germany, **2019**.

[101] T. L. Fischer, T. Wagner, H. C. Gottschalk, A. Nejad, M. A. Suhm, *J. Phys. Chem. Lett.* **2021**, *12*, 138–144.

[102] H. C. Gottschalk, *IR Investigation of Weakly Bound Molecular Clusters in the Supersonic Jet, PhD Thesis,* Georg-August- Universität Göttingen, Göttingen, Germany, **2020**.

[103] A. D. Becke, *Phys. Rev. A* **1988**, *38*, 3098–3100.

[104] A. D. Becke, *J. Chem. Phys.* **1993**, *98*, 5648–5652.

[105] C. Lee, W. Yang, R. G. Parr, *Phys. Rev. B* **1988**, *37*, 785–789.

[106] F. Weigend, R. Ahlrichs, *Phys. Chem. Chem. Phys.* **2005**, *7*, 3297–3305.

[107] J. Zheng, X. Xu, D. G. Truhlar, *Theor. Chem. Acc.* **2011**, *128*, 295–305.

[108] S. Grimme, **2019**, *15*, 2847–2862.

[109] P. Pracht, F. Bohle, S. Grimme, **2020**, *22*, 7169–7192.

[110] C. Bannwarth, S. Ehlert, S. Grimme, **2019**, *15*, 1652–1671.

[111] S. Grimme, C. Bannwarth, P. Shushkov, *J. Chem. Theory Comput.* **2017**, *13*, 1989–2009.

[112] M. Born, R. Oppenheimer, *Ann. Phys.* **1927**, *389*, 457–484.

[113] A. D. Becke, *J. Chem. Phys.* **2014**, *140*, 18A301.

[114] L. Goerigk, A. Hansen, C. Bauer, S. Ehrlich, A. Najibi, S. Grimme, *Phys. Chem. Chem. Phys.* **2017**, *19*, 32184–32215.

[115] L. Goerigk, N. Mehta, *Aust. J. Chem.* **2019**, *72*, 563.

[116] F. Neese, *WIREs Comput. Mol. Sci.* **2012**, *2*, 73–78.

[117] F. Neese, *WIREs Comput. Mol. Sci.* **2018**, *8*, e1327.

[118] F. Neese, F. Wennmohs, U. Becker, C. Riplinger, *J. Chem. Phys.* **2020**, *152*, 224108.

[119] F. Neese, *WIREs Comput. Mol. Sci.* **2022**, *12*, e1606.

[120] M. J. Frisch, G. W. Trucks, H. B. Schlegel, G. E. Scuseria, M. A. Robb, J. R. Cheeseman, G. Scalmani, V. Barone, G. A. Petersson, H. Nakatsuji, X. Li, M. Caricato, A. V Marenich, J. Bloino, B. G. Janesko, R. Gomperts, B. Mennucci, H. P. Hratchian, J. V Ortiz, A. F. Izmaylov, J. L. Sonnenberg, D. Williams-Young, F. Ding, F. Lipparini, F. Egidi, J. Goings, B. Peng, A. Petrone, T. Henderson, D. Ranasinghe, V. G. Zakrzewski, J. Gao, N. Rega, G. Zheng, W. Liang, M. Hada, M. Ehara, K. Toyota, R. Fukuda, J. Hasegawa, M. Ishida, T. Nakajima, Y. Honda, O. Kitao, H. Nakai, T. Vreven, K. Throssell, J. A. Montgomery Jr., J. E. Peralta, F. Ogliaro, M. J. Bearpark, J. J. Heyd, E. N. Brothers, K. N. Kudin, V. N. Staroverov, T. A. Keith, R. Kobayashi, J. Normand, K. Raghavachari, A. P. Rendell, J. C. Burant, S. S. Iyengar, J. Tomasi, M. Cossi, J. M. Millam, M. Klene, C. Adamo, R. Cammi, J. W. Ochterski, R. L. Martin, K. Morokuma, O. Farkas, J. B. Foresman, D. J. Fox, *Gaussian 16 Revision A.03*, Gaussian Inc. Wallingford CT, **2016**.

[121] M. J. Frisch, G. W. Trucks, H. B. Schlegel, G. E. Scuseria, M. A. Robb, J. R. Cheeseman, G. Scalmani, V. Barone, G. A. Petersson, H. Nakatsuji, X. Li, M. Caricato, A. V Marenich, J. Bloino, B. G. Janesko, R. Gomperts, B. Mennucci, H. P. Hratchian, J. V Ortiz, A. F. Izmaylov, J. L. Sonnenberg, D. Williams-Young, F. Ding, F. Lipparini, F. Egidi, J. Goings, B. Peng, A. Petrone, T. Henderson, D. Ranasinghe, V. G. Zakrzewski, J. Gao, N. Rega, G. Zheng, W. Liang, M. Hada, M. Ehara, K. Toyota, R. Fukuda, J. Hasegawa, M. Ishida, T. Nakajima, Y. Honda, O. Kitao, H. Nakai, T. Vreven, K. Throssell, J. A. Montgomery Jr., J. E. Peralta, F. Ogliaro, M. J. Bearpark, J. J. Heyd, E. N. Brothers, K. N. Kudin, V. N. Staroverov, T. A. Keith, R. Kobayashi, J. Normand,

K. Raghavachari, A. P. Rendell, J. C. Burant, S. S. Iyengar, J. Tomasi, M. Cossi, J. M. Millam, M. Klene, C. Adamo, R. Cammi, J. W. Ochterski, R. L. Martin, K. Morokuma, O. Farkas, J. B. Foresman, D. J. Fox, *Gaussian 16 Revision B.01*, Gaussian Inc. Wallingford CT, **2016**.

[122] S. Grimme, J. Antony, S. Ehrlich, H. Krieg, *J. Chem. Phys.* **2010**, *132*, 154104.

[123] A. D. Becke, E. R. Johnson, *J. Chem. Phys.* **2005**, *123*, 154101.

[124] E. R. Johnson, A. D. Becke, *J. Chem. Phys.* **2005**, *123*, 024101.

[125] E. R. Johnson, A. D. Becke, *J. Chem. Phys.* **2006**, *124*, 174104.

[126] S. Grimme, S. Ehrlich, L. Goerigk, *J. Comput. Chem.* **2011**, *32*, 1456–1465.

[127] C. Møller, M. S. Plesset, *Phys. Rev.* **1934**, *46*, 618–622.

[128] C. Lee, W. Yang, R. G. Parr, *Phys. Rev. B* **1988**, *37*, 785–789.

[129] T. Schwabe, S. Grimme, *Phys. Chem. Chem. Phys.* **2007**, *9*, 3397.

[130] S. Kristyán, P. Pulay, *Chem. Phys. Lett.* **1994**, *229*, 175–180.

[131] J. Pérez-Jordá, A. D. Becke, *Chem. Phys. Lett.* **1995**, *233*, 134–137.

[132] P. Hobza, Š. Jiří, R. Tomáš, *J. Comput. Chem.* **1995**, *16*, 1315–1325.

[133] B. M. Axilrod, E. Teller, *J. Chem. Phys.* **1943**, *11*, 299–300.

[134] Y. Muto, *J. Phys. Math. Soc. Jpn* **1943**, *17*, 629.

[135] D. Rappoport, F. Furche, *J. Chem. Phys.* **2010**, *133*, 134105.

[136] R. A. Mata, M. A. Suhm, *Angew. Chemie Int. Ed.* **2017**, *56*, 11011–11018.

[137] C. Riplinger, B. Sandhoefer, A. Hansen, F. Neese, *J. Chem. Phys.* **2013**, *139*, 134101.

[138] C. Riplinger, F. Neese, *J. Chem. Phys.* **2013**, *138*, 034106.

[139] C. Riplinger, P. Pinski, U. Becker, E. F. Valeev, F. Neese, *J. Chem. Phys.* **2016**, *144*, 024109.

[140] Y. Guo, C. Riplinger, U. Becker, D. G. Liakos, Y. Minenkov, L. Cavallo, F. Neese, *J. Chem. Phys.* **2018**, *148*, 011101.

[141] M. Saitow, U. Becker, C. Riplinger, E. F. Valeev, F. Neese, *J. Chem. Phys.* **2017**, *146*, 164105.

[142] D. G. Liakos, Y. Guo, F. Neese, *J. Phys. Chem. A* **2020**, *124*, 90–100.

[143] Y. Guo, C. Riplinger, D. G. Liakos, U. Becker, M. Saitow, F. Neese, *J. Chem. Phys.* **2020**, *152*, 024116.

[144] J. Calbo, J. C. Sancho-García, E. Ortí, J. Aragó, *J. Comput. Chem.* **2017**, *38*, 1869–1878.

[145] C. Edmiston, M. Krauss, *J. Chem. Phys.* **1965**, *42*, 1119–1120.

[146] F. Neese, F. Wennmohs, A. Hansen, *J. Chem. Phys.* **2009**, *130*, 114108.

[147] T. H. Dunning, *J. Chem. Phys.* **1989**, *90*, 1007–1023.

[148] R. A. Kendall, T. H. Dunning, R. J. Harrison, *J. Chem. Phys.* **1992**, *96*, 6796–6806.

[149] D. G. Liakos, M. Sparta, M. K. Kesharwani, J. M. L. Martin, F. Neese, *J. Chem. Theory Comput.* **2015**, *11*, 1525–1539.

[150] W. B. Schneider, G. Bistoni, M. Sparta, M. Saitow, C. Riplinger, A. A. Auer, F. Neese, *J. Chem. Theory Comput.* **2016**, *12*, 4778–4792.

[151] A. Altun, M. Saitow, F. Neese, G. Bistoni, *J. Chem. Theory Comput.* **2019**, *15*, 1616–1632.

[152] K. E. Riley, P. Hobza, *J. Phys. Chem. A* **2007**, *111*, 8257–8263.

[153] A. Altun, S. Ghosh, C. Riplinger, F. Neese, G. Bistoni, *J. Phys. Chem. A* **2021**, *125*, 9932–9939.

[154] J. R. Alvarez-Idaboy, A. Galano, *Theor. Chem. Acc.* **2010**, *126*, 75–85.

[155] E. M. Brás, C. Zimmermann, M. A. Suhm, *Phys. Chem. Chem. Phys.* **2023** **(submitted)**.

[156] J. F. W. Keana, *Chem. Rev.* **1978**, *78*, 37–64.

[157] J. Guin, S. De Sarkar, S. Grimme, A. Studer, *Angew. Chemie - Int. Ed.* **2008**, *47*, 8727–8730.

[158] B. Keoshkerian, M. K. Georges, D. Boils-Boissier, *Macromolecules* **1995**, *28*, 6381–6382.

[159] I. Kaminker, R. Barnes, S. Han, *Methods Enzymol.* **2015**, *564*, 457–483.

[160] J. Hunold, J. Eisermann, M. Brehm, D. Hinderberger, *J. Phys. Chem. B* **2020**, *124*, 8601–8609.

[161] A. Wilting, M. Kügler, I. Siewert, *Inorg. Chem.* **2016**, *55*, 1061–1068.

[162] J. J. Warren, T. A. Tronic, J. M. Mayer, *Chem. Rev.* **2010**, *110*, 6961–7001.

[163] K. Halbmair, J. Seikowski, I. Tkach, C. Höbartner, D. Sezer, M. Bennati, *Chem. Sci.* **2016**, *7*, 3172–3180.

[164] O. H. Griffith, A. S. Waggoner, *Acc. Chem. Res.* **1969**, *2*, 17–24.

[165] A. K. Hoffmann, W. G. Hodgson, W. H. Jura, *J. Am. Chem. Soc.* **1961**, *83*, 4675–4676.

[166] F. Hecker, L. Fries, M. Hiller, M. Chiesa, M. Bennati, *Angew. Chemie Int. Ed.* **2023**, *62*, e202213700.

[167] A. Baschieri, L. Valgimigli, S. Gabbanini, G. A. DiLabio, E. Romero-Montalvo, R. Amorati, *J. Am. Chem. Soc.* **2018**, *140*, 10354–10362.

[168] R. Campargue, *J. Phys. Chem.* **1984**, *88*, 4466–4474.

[169] R. Crespo-Otero, K. Bravo-Rodriguez, S. Roy, T. Benighaus, W. Thiel, W. Sander, E. Sánchez-García, *ChemPhysChem* **2013**, *14*, 805–811.

[170] I. Reva, M. J. Nowak, L. Lapinski, R. Fausto, *Phys. Chem. Chem. Phys.* **2015**, *17*, 4888–4898.

[171] A. Amrein, M. Quack, U. Schmitt, *J. Phys. Chem.* **1988**, *92*, 5455–5466.

[172] D. Bernhard, M. Fatima, A. Poblotzki, A. L. Steber, C. Pérez, M. A. Suhm, M. Schnell, M. Gerhards, *Phys. Chem. Chem. Phys.* **2019**, *21*, 16032–16046.

[173] L. Horný, F. Mariotti, M. Quack, *Chim. Int. J. Chem.* **2008**, *62*, 256–259.

[174] C. Zimmermann, *Investigation of Intermolecular Ketone-Alcohol Balances via FTIR Spectroscopy , PhD Thesis,* Georg-August-Universität Göttingen, Göttingen, **2022**.

[175] J. Tao, J. P. Perdew, V. N. Staroverov, G. E. Scuseria, *Phys. Rev. Lett.* **2003**, *91*, 146401.

[176] S. Grimme, *J. Chem. Phys.* **2006**, *124*, 34108.

[177] R. A. Kendall, T. H. Dunning, R. J. Harrison, *J. Chem. Phys.* **1992**, *96*, 6796–6806.

[178] R. S. Ruoff, T. D. Klots, T. Emilsson, H. S. Gutowsky, *J. Chem. Phys.* **1990**, *93*, 3142–3150.

[179] U. Buck, F. Huisken, *Chem. Rev.* **2000**, *100*, 3863–3890.

[180] R. W. Larsen, P. Zielke, M. A. Suhm, *J. Chem. Phys.* **2007**, *126*, 194307.

[181] K. E. Otto, Z. Xue, P. Zielke, M. A. Suhm, **2014**, *16*, 9849.

[182] U. Erlekam, M. Frankowski, G. von Helden, G. Meijer, *Phys. Chem. Chem. Phys.* **2007**, *9*, 3786.

[183] S. L. Sherman, K. A. Nickson, E. Garand, *J. Phys. Chem. Lett.* **2022**, *13*, 2046–2050.

[184] D. Zimmermann, T. Häber, H. Schaal, M. A. Suhm, *Mol. Phys.* **2001**, *99*, 413–425.

[185] T. Ebata, T. Watanabe, N. Mikami, *J. Phys. Chem.* **1995**, *99*, 5761–5764.

[186] B. Nelander, *J. Phys. Chem. A* **1997**, *101*, 9092–9096.

[187] S. Oswald, M. A. Suhm, S. Coussan, *Phys. Chem. Chem. Phys.* **2019**, *21*, 1277–1284.

[188] G. C. Pimental, S. W. Charles, *Pure Appl. Chem.* **1963**, *7*, 111–124.

[189] V. Vidya, K. Sankaran, K. S. Viswanathan, *Chem. Phys. Lett.* **1996**, *258*, 113–117.

[190] I. . Reva, S. . Stepanian, L. Adamowicz, R. Fausto, *Chem. Phys. Lett.* **2003**, *374*, 631–638.

[191] G. P. Ayers, A. D. E. Pullin, *Spectrochim. Acta Part A Mol. Spectrosc.* **1976**, *32*, 1629–1639.

[192] G. P. Ayers, A. D. E. Pullin, *Spectrochim. Acta Part A Mol. Spectrosc.* **1976**, *32*, 1641–1650.

[193] J. E. Desnoyers, R. Francescon, **1971**, 1236–1241.

[194] G. P. Ayers, A. D. E. Pullin, *Spectrochim. Acta Part A Mol. Spectrosc.* **1976**, *32*, 1695–1704.

[195] G. T. Pullen, P. R. Franke, Y.-P. Lee, G. E. Douberly, *J. Mol. Spectrosc.* **2018**, *354*, 7–14.

[196] Q. Shi, S. D. Belair, J. S. Francisco, S. Kais, *Proc. Natl. Acad. Sci.* **2003**, *100*, 9686–9690.

[197] D. Leicht, M. Kaufmann, R. Schwan, J. Schäfer, G. Schwaab, M. Havenith, *J. Chem. Phys.* **2016**, *145*, 204305.

[198] G. Maier, H. P. Reisenauer, M. De Marco, *Chem. - A Eur. J.* **2000**, *6*, 800–808.

[199] A. Givan, A. Loewenschuss, C. J. Nielsen, *Phys. Chem. Chem. Phys.* **1999**, *1*,

37–43.

[200] J. F. W. Keana, R. J. Dinerstein, F. Baitis, *J. Org. Chem.* **1971**, *36*, 209–211.

[201] D. R. Anderson, T. H. Koch, *Tetrahedron Lett.* **1977**, *18*, 3015–3018.

[202] J. M. Coxon, E. Patsalides, *Aust. J. Chem.* **1982**, *35*, 509–515.

[203] L. Call, E. F. Ullman, *Tetrahedron Lett.* **1973**, *14*, 961–964.

[204] E. F. Ullman, L. Call, S. S. Tseng, *J. Am. Chem. Soc.* **1973**, *95*, 1677–1679.

[205] J. A. Nelson, S. Chou, T. A. Spencer, *J. Am. Chem. Soc.* **1975**, *97*, 648–649.

[206] J. F. W. Keana, F. Baitis, *Tetrahedron Lett.* **1968**, *9*, 365–368.

[207] J. S. Keute, D. R. Anderson, T. H. Koch, *J. Am. Chem. Soc.* **1981**, *103*, 5434–5439.

[208] J. Pacansky, J. S. Chang, *J. Chem. Phys.* **1981**, *74*, 5539–5546.

[209] K. Oum, K. Luther, J. Troe, *J. Phys. Chem. A* **2004**, *108*, 2690–2699.

[210] F. Hecker, J. Stubbe, M. Bennati, *J. Am. Chem. Soc.* **2021**, *143*, 7237–7241.

[211] V. Barone, *J. Chem. Phys.* **2005**, *122*, 14108.

[212] R. Medel, M. A. Suhm, *Phys. Chem. Chem. Phys.* **2021**, *23*, 5629–5643.

[213] H. P. Reisenauer, J. Romański, G. Mlostoń, P. R. Schreiner, *Chem. Commun.* **2015**, *51*, 10022–10025.

[214] J. D. Cope, K. H. Bates, L. N. Tran, K. A. Abellar, T. B. Nguyen, *Proc. Natl. Acad. Sci.* **2022**, *119*, e2202857119.

[215] A. Mardyukov, P. R. Schreiner, *Acc. Chem. Res.* **2018**, *51*, 475–483.

[216] C. Chen, B. Lu, X. Zhao, W. Qian, J. Liu, T. Trabelsi, J. S. Francisco, J. Qin, J. Li, L. Wang, X. Zeng, *J. Am. Chem. Soc.* **2020**, *142*, 2175–2179.

[217] Q. Zhang, D.-H. Qu, B. L. Feringa, H. Tian, *J. Am. Chem. Soc.* **2022**, *144*, 2022–2033.

[218] J. H. Kuhlmann, J. H. Dickoff, O. G. Mancheño, *Chem. – A Eur. J.* **2023**, *29*, e202203347.

[219] P. Nagy, *Antioxid. Redox Signal.* **2013**, *18*, 1623–1641.

[220] L. B. Poole, *Free Radic. Biol. Med.* **2015**, *80*, 148–157.

[221] W. Szymański, J. M. Beierle, H. A. V. Kistemaker, W. A. Velema, B. L. Feringa, *Chem. Rev.* **2013**, *113*, 6114–6178.

[222] Y. Ling, Z.-Y. Hao, D. Liang, C.-L. Zhang, Y.-F. Liu, Y. Wang, *Drug Des. Devel. Ther.* **2021**, *Volume 15*, 4289–4338.

[223] D. H. R. Barton, J. Boivin, J. Sarma, E. da Silva, S. Z. Zard, *Tetrahedron Lett.* **1989**, *30*, 4237–4240.

[224] M. J. Nowak, L. Lapinski, H. Rostkowska, A. Les, L. Adamowicz, *J. Phys. Chem.* **1990**, *94*, 7406–7414.

[225] H. Rostkowska, L. Lapinski, I. Reva, B. J. A. N. Almeida, M. J. Nowak, R. Fausto, *J. Phys. Chem. A* **2011**, *115*, 12142–12149.

[226] E. M. Brás, M. S. C. Henriques, J. A. Paixão, R. Fausto, *Cryst. Growth Des.* **2018**, *18*, 4167–4173.

[227] N. Herrmann, N. Heinz, M. Dolg, X. Cao, *J. Comput. Chem.* **2016**, *37*, 1914–1923.

[228] W. M. C. Sameera, F. Maseras, *Phys. Chem. Chem. Phys.* **2011**, *13*, 10520.

[229] L. Duarte, I. Reva, M. L. S. Cristiano, R. Fausto, *J. Org. Chem.* **2013**, *78*, 3271–3275.

[230] W. E. Lyons, *Nature* **1948**, *162*, 1004–1004.

[231] N. P. Ernsting, *Chem. Phys. Lett.* **1990**, *166*, 221–226.

[232] M. Ochmann, A. Hussain, I. von Ahnen, A. A. Cordones, K. Hong, J. H. Lee, R. Ma, K. Adamczyk, T. K. Kim, R. W. Schoenlein, O. Vendrell, N. Huse, *J. Am. Chem. Soc.* **2018**, *140*, 6554–6561.

[233] I. Barnes, K. H. Becker, N. Mihalopoulos, *J. Atmos. Chem.* **1994**, *18*, 267–289.

[234] R. M. Abaskharon, F. Gai, *Phys. Chem. Chem. Phys.* **2016**, *18*, 9602–9607.

[235] M. A. B. Larsen, A. B. Skov, C. M. Clausen, J. Ruddock, B. Stankus, P. M. Weber, T. I. Sølling, *ChemPhysChem* **2018**, *19*, 2829–2834.

[236] M. T. Neves-Petersen, Z. Gryczynski, J. Lakowicz, P. Fojan, S. Pedersen, E. Petersen, S. Bjørn Petersen, *Protein Sci.* **2002**, *11*, 588–600.

[237] C. Kolano, J. Helbing, G. Bucher, W. Sander, P. Hamm, *J. Phys. Chem. B* **2007**, *111*, 11297–11302.

[238] D. Creed, *Photochem. Photobiol.* **2008**, *39*, 577–583.

[239] T. Autrey, C. Devadoss, B. Sauerwein, J. A. Franz, G. B. Schuster, *J. Phys. Chem.* **1995**, *99*, 869–871.

[240] M. Wakasa, Y. Sakaguchi, H. Hayashi, *J. Phys. Chem.* **1993**, *97*, 1733–1735.

[241] J. Cao, D.-C. Chen, *Phys. Chem. Chem. Phys.* **2019**, *21*, 4176–4183.

[242] E. Sagstuen, J.-P. Jørgensen, T. Henriksen, J.-P. Jorgensen, *Radiat. Res.* **1982**, *89*, 453.

[243] D. Small, V. Zaitsev, Y. Jung, S. V. Rosokha, M. Head-Gordon, J. K. Kochi, *J. Am. Chem. Soc.* **2004**, *126*, 13850–13858.

[244] C. P. Constantinides, D. B. Lawson, G. A. Zissimou, A. A. Berezin, A. Mailman, M. Manoli, A. Kourtellaris, G. M. Leitus, R. Clérac, H. M. Tuononen, P. A. Koutentis, *CrystEngComm* **2020**, *22*, 5453–5463.

[245] Y. Ikabata, Q. Wang, T. Yoshikawa, A. Ueda, T. Murata, K. Kariyazono, M. Moriguchi, H. Okamoto, Y. Morita, H. Nakai, *npj Quantum Mater.* **2017**, *2*, 27.

[246] H. Oshita, Y. Shimazaki, *Molecules* **2022**, *27*, 1135.

[247] A. Mardyukov, P. R. Schreiner, *Phys. Chem. Chem. Phys.* **2016**, *18*, 26161–26265.

[248] E. M. Brás, L. I. L. Cabral, P. S. M. Amado, M. Abe, R. Fausto, M. L. S. Cristiano, *J. Phys. Chem. A* **2020**, *124*, 4202–4210.

[249] Y. Tu, *Nat. Med.* **2011**, *17*, 1217–1220.

[250] Y. Tu, *Angew. Chemie Int. Ed.* **2016**, *55*, 10210–10226.

[251] C. Liu, *Chinese Herb. Med.* **2017**, *9*, 101–114.

[252] C. Jefford, *Curr. Med. Chem.* **2001**, *8*, 1803–1826.

[253] J. N. Cumming, P. Ploypradith, G. H. Posner, **1996**, pp. 253–297.

[254] Y. Wu, *Acc. Chem. Res.* **2002**, *35*, 255–259.

[255] A. Robert, Y. Coppel, B. Meunier, *Chem. Commun.* **2002**, 414–415.

[256] S. R. Meshnick, *Int. J. Parasitol.* **2002**, *32*, 1655–1660.

[257] J. Krieger, T. Smeilus, M. Kaiser, E. Seo, T. Efferth, A. Giannis, *Angew. Chemie Int. Ed.* **2018**, *57*, 8293–8296.

[258] L. Tilley, J. Straimer, N. F. Gnädig, S. A. Ralph, D. A. Fidock, *Trends Parasitol.* **2016**, *32*, 682–696.

[259] E. A. Winzeler, M. J. Manary, *Genome Biol.* **2014**, *15*, 544.

[260] P. Cravo, H. Napolitano, R. Culleton, *Acta Trop.* **2015**, *148*, 1–7.

[261] J. Wang, C.-J. Zhang, W. N. Chia, C. C. Y. Loh, Z. Li, Y. M. Lee, Y. He, L.-X. Yuan, T. K. Lim, M. Liu, C. X. Liew, Y. Q. Lee, J. Zhang, N. Lu, C. T. Lim, Z.-C. Hua, B. Liu, H.-M. Shen, K. S. W. Tan, Q. Lin, *Nat. Commun.* **2015**, *6*, 10111.

[262] F. T. Aweeka, P. I. German, *Clin. Pharmacokinet.* **2008**, *47*, 91–102.

[263] P. S. Horspool, W. M.; Song, *Handbook of Organic Photochemistry and Photobiology*, CRC Press, London, **1994**.

[264] C. W. Jefford, J.-C. Rossier, J. Boukouvalas, *J. Chem. Soc., Chem. Commun.* **1986**, 1701–1702.

[265] C. W. Jefford, J.-C. Rossier, J. Boukouvalas, *J. Chem. Soc. Chem. Commun.* **1987**, 1593.

[266] C. W. Jefford, S. Kohmoto, J.-C. Rossier, J. Boukouvalas, *J. Chem. Soc. Chem. Commun.* **1985**, 1783.

[267] C. W. Jefford, J.-C. Rossier, J. Boukouvalas, *Heterocycles* **1989**, *28*, 673.

[268] C. W. Jefford, J.-C. Rossier, J. Boukouvalas, *J. Chem. Soc. Chem. Commun.* **1987**, 713.

[269] S. Erhardt, S. A. Macgregor, K. J. McCullough, K. Savill, B. J. Taylor, *Org. Lett.* **2007**, *9*, 5569–5572.

[270] X. W. K. S. J. K. W. and J. L. V. Yuanqing Tang; Yuxiang Dong, *J. Org. Chem* **2005**, *70*, 5103–5110.

[271] A. Haq, B. Kerr, K. J. McCullough, *J. Chem. Soc. Chem. Commun.* **1993**, 1076.

[272] M. Abe, T. Inakazu, J. Munakata, M. Nojima, *J. Am. Chem. Soc.* **1999**, *121*, 6556–6562.

[273] M. Abe, W. Adam, T. Heidenfelder, W. M. Nau, X. Zhang, *J. Am. Chem. Soc.* **2000**, *122*, 2019–2026.

[274] B. Meyer, *Low Temperature Spectroscopy*, American Elsevier Publishers Company, New York (USA), **1971**.

[275] M. Andrews L.; Moskovits, *Chemistry and Physics of Matrix Isolated Species*, Elsevier, Amsterdam (Holland), **1989**.

[276] S. Lopes, A. V. Domanskaya, R. Fausto, M. Räsänen, L. Khriachtchev, *J. Chem.*

Phys. **2010**, *133*, 144507.

[277] N. Kuş, R. Fausto, *J. Chem. Phys.* **2017**, *146*, 124305.

[278] P. Gibbons, E. Verissimo, N. C. Araujo, V. Barton, G. L. Nixon, R. K. Amewu, J. Chadwick, P. A. Stocks, G. A. Biagini, A. Srivastava, P. J. Rosenthal, J. Gut, R. C. Guedes, R. Moreira, R. Sharma, N. Berry, M. L. S. Cristiano, A. E. Shone, S. A. Ward, P. M. O'Neill, *J. Med. Chem.* **2010**, *53*, 8202–8206.

Appendix A

Jet-Cooled and Matrix-Isolated Radical Microsolvates

Contents

List of Tables

List of Figures

The Appendix A is based on the previously published and submitted articles:

E. M. Brás, T. L. Fischer, M. A. Suhm, The Hydrates of TEMPO: Water Vibrations Reveal Radical Microsolvation, Angew. Chemie Int. Ed. 2021, 60, 19013-19017.

E. M. Brás, C. Zimmermann, R. Fausto, M. A. Suhm, Benchmarking the Anisotropy of Nitroxyl Radical Solvation with IR Spectroscopy, Phys. Chem. Chem. Phys. 2023 (submitted).

1 Chemicals

Tab. A1 contains details on the investigated compounds and introduces abbreviations for their referencing in this supplement.

Table A1: List of the investigated substances of Chapter 3 and their abbreviation, along with the CAS number, supplier and purity.

Name	Abbreviation	CAS No.	Supplier	Purity
(2,2,6,6-Tetramethylpiperidin-1-yl)oxyl	TEMPO	2564-83-2	Sigma Aldrich	98%
2,2,6,6-Tetramethylcyclohexanone	TEMCO	1195-93-3	Abcr	95%
Di-*t*-butyl nitroxide	DTBN	2406-25-9	Sigma Aldrich	90%
			Santa Cruz	90%
Deuterium oxide	D_2O	7789-20-0	Abcr	99.85%
Water-^{18}O	$H_2{}^{18}O$	14314-42-2	Sigma Aldrich	97%, 97% ^{18}O
Methanol	$HOCH_3$	67-56-1	Roth	$\geq$ 99.9%
tert-Butanol	$HO(CH_3)_3$	75-65-0	Alfa Aesar	$\geq$ 99%
Phenol	HOC_6H_5	108-95-2	Alfa Aesar	$\geq$ 99%
Helium	He	7440-59-7	Linde	99.996%
Neon	Ne	7440-01-9	Linde	99.995%
Ar	Ar	7440-37-1	N60 Air Liquide	99.9999%

2 Computations of Subsection 4.1[1]

2.1 Methods and keywords

The structures of monomers, 1:1 and 1:2 hydrates of TEMPO and TEMCO were obtained from manual starting structures and through the CREST[2, 3] program at GFN2-xTB level[4, 5], and reoptimized at closed- and open-shell B3LYP/def2-TZVP and QZVP[6–9] levels with Grimme's three-body term dispersion correction D3[10]. and Becke-Johnson (BJ) damping[11–14], using the ORCA[15] software package. The structures were also confirmed *via* relaxed potential surface energy scans around the C−X−O···O dihedral angle of both 1:1 TEMPO and TEMCO hydrates. Further single point calculations on the B3LYP geometries were carried out with the DPLNO-CCSD(T)[16–19] method using aug-cc-pVTZ and aug-cc-pVQZ[20], and

matching auxiliary basis sets, in both closed- and unrestricted open-shell[19] variants, using the same software package (see Table A2).[15] Local energy decomposition (LED) was also carried out.[21, 22] For this purpose, two fragments were defined in the input file. The atoms which define TEMPO and TEMCO were assigned to fragment (1), and the atoms of water were assigned to fragment (2) (see Tables A3-A8).
When the basic variable that commands the type of wavefunction to be computed (HFTyp in the %scf block) is not specified, the program checks the multiplicity given in the input file, and performs the calculation based on it.[15] In the case of the closed-shell systems with multiplicity = 1 (TEMCO and TEMCO hydrates), RKS/RHF were assumed in B3LYP and DPLNO-CCSD(T) computations. For open-shell systems with multiplicity = 2 (TEMPO and TEMPO hydrates), UKS/UHF were employed. RHF (Restricted Hartree-Fock) and UHF (Unrestricted Hartree-Fock) are replaced by RKS (Restricted Kohn-Sham) und UKS (Unrestricted Kohn-Sham) in DFT computations.[15] By program default, quasi-restricted orbitals (QRO [23]) were used to avoid spin contamination[24].

The atomic masses used in the calculations are: 1.00800 u (H), 2.00141 u (D) and 18.00000 u (^{18}O).

Table A2: Methods and keywords applied for closed- and open-shell quantum chemical calculations of TEMCO and TEMPO monomers and hydrates shown in Subsection 4.1 of this Thesis. The calculations were performed using ORCA[15] 4.2.1 software package.

Method	Basis set	Keywords
B3LYP-D3(BJ)	def2-TZVP	`B3LYP D3BJ ABC def2-TZVP GRID5 NOFINALGRID VERYTIGHTSCF TIGHTOPT FREQ` (multiplicity = 2 for unrestricted open-shell)
B3LYP-D3(BJ)	def2-QZVP	`B3LYP D3BJ ABC def2-QZVP GRID5 NOFINALGRID VERYTIGHTSCF TIGHTOPT FREQ` (multiplicity = 2 for unrestricted open-shell)
DLPNO-CCSD(T)	aug-cc-pVTZ	`DLPNO-CCSD(T) TightPNO aug-cc-pVTZ aug-cc-pVTZ/C TightSCF LED` (multiplicity = 2 for unrestricted open-shell)
DLPNO-CCSD(T)	aug-cc-pVQZ	`DLPNO-CCSD(T) TightPNO aug-cc-pVQZ aug-cc-pVQZ/C TightSCF LED` (multiplicity = 2 for unrestricted open-shell)

2.2 Cartesian Coordinates

Cartesian coordinates (in Å) of B3LYP- and (U)B3LYP-D3(BJ)/def2-QZVP computed structures (in Å) of TEMPO and TEMCO 1:1 hydrates (shown in the Subsection 4.1 of the Thesis) are given in the Tables A3,A4,A5,A6,A7 and A8.

Table A3: Cartesian coordinates of TEMPO p···HOH hydrate computed at (U)B3LYP-D3(BJ)/def2-QZVP level of theory.

Atom	Fragment	X	Y	Z
C	(1)	-2.28465640584835	0.01044594152491	0.44557749517313
C	(1)	-2.01932830843495	1.39655304273183	-0.12292783492939
C	(1)	-0.73418547983058	1.94132470274457	0.48246817539850
H	(1)	-2.41672804274740	0.09671645288386	1.52689435857296
H	(1)	-2.85216672905950	2.05982719195668	0.11372926548109
H	(1)	-0.52266068575246	2.94763750219336	0.11960942960722
C	(1)	0.49945104815570	1.07418712320341	0.19347918187413
C	(1)	1.62860881974330	1.47649355050469	1.14552796880966
H	(1)	2.55869297325413	0.96875826571320	0.91090591444914
H	(1)	1.35736127219279	1.25290864703821	2.17658225339266
H	(1)	1.79300344176027	2.55030978347054	1.05809866624057
C	(1)	0.96696326925785	1.24208369933482	-1.26122764042971
H	(1)	0.16045116353916	1.07600349459189	-1.97148771863626
H	(1)	1.77855944460671	0.55473338190754	-1.48594418377838
H	(1)	1.33453874085454	2.25831726053425	-1.40237650594669
C	(1)	-1.15715355262349	-0.99285618565330	0.16915722761033
C	(1)	-1.30879597365151	-2.19448006019791	1.10418483579914
H	(1)	-2.30123507731164	-2.62461582704885	0.97163766807130
H	(1)	-1.20046644642217	-1.88769574680391	2.14364713991386
H	(1)	-0.56367372384924	-2.95494034677504	0.89141495775773
C	(1)	-1.18039751926075	-1.47588730275935	-1.28978810574603
H	(1)	-2.06977152912186	-2.08284678990618	-1.45778953508642
H	(1)	-0.30142274255090	-2.08458517770250	-1.49093369307169
H	(1)	-1.19733232309299	-0.65061036981913	-1.99725906205532
H	(1)	-1.95221429982119	1.36432402019059	-1.21142882603211
H	(1)	-3.20941054181056	-0.41019608562136	0.04862686864140
H	(1)	-0.86240741300093	2.01688084693727	1.56512207272261
N	(1)	0.17321076881894	-0.36548179808003	0.44965140139465
O	(1)	1.15682926744719	-1.17814179129452	0.52465341061660
O	(2)	3.72317797776796	-0.81391558305872	-0.56345612918491
H	(2)	4.22898637725147	-1.62436962665417	-0.47840959677208
H	(2)	2.86752222954052	-0.99482221608663	-0.13749945985768

Table A4: Cartesian coordinates of TEMPO t···HOH hydrate computed at (U)B3LYP-D3(BJ)/def2-QZVP level of theory.

Atom	Fragment	X	Y	Z
C	(1)	1.83755264819499	1.23918033483223	-0.03256554615273
C	(1)	2.33119764737013	-0.00036570077473	0.70008440921515
C	(1)	1.83691145389515	-1.24175351717135	-0.02900504172940
H	(1)	2.18783483388296	2.15013218850663	0.45423179591607
H	(1)	1.99054498732644	0.00118583498871	1.73655420208684
H	(1)	2.25593328834112	-1.24465083676204	-1.03832597782285
C	(1)	0.30765171843112	-1.32386151387323	-0.13375776318084
C	(1)	-0.32654799314130	-1.71420656045302	1.21107720437242
H	(1)	-0.05541694730307	-2.74274408941375	1.44925155155631
H	(1)	-1.41057185793108	-1.64494109537118	1.15764733842022
H	(1)	0.01429146252729	-1.08106079485439	2.02602181267542
C	(1)	-0.07406762913164	-2.35857798843324	-1.19362524063962
H	(1)	0.28172659697559	-2.05288073890812	-2.17661818539223
H	(1)	-1.15046127554888	-2.49113702724577	-1.24421716557903
H	(1)	0.38702811550550	-3.31244755095642	-0.93885404093977
C	(1)	0.30832996787320	1.32187516642412	-0.13758362579878
C	(1)	-0.32567076767349	1.71687516126191	1.20600141721594
H	(1)	-1.40967703198865	1.64727356709023	1.15307048665819
H	(1)	-0.05471046569852	2.74633947341273	1.44031769347028
H	(1)	0.01565324731530	1.08687414310712	2.02319918794056
C	(1)	-0.07280925859174	2.35354404546537	-1.20064865708136
H	(1)	0.38928100018312	3.30779325377686	-0.94912638969142
H	(1)	-1.14910458659773	2.48695615159336	-1.25120871931885
H	(1)	0.28228214849019	2.04433035704720	-2.18279800319730
H	(1)	3.42131866835961	-0.00058898437305	0.73522199070975
H	(1)	2.25663519334804	1.23899077455170	-1.04186935411078
H	(1)	2.18673980088420	-2.15149191195861	0.46038180134237
N	(1)	-0.23902165704222	-0.00150048793972	-0.57542959387789
O	(1)	-1.43417229290506	-0.00192642032187	-1.02620060702456
O	(2)	-3.48036304592258	0.00518551728130	0.89535548108199
H	(2)	-4.35689005556510	0.00869085585359	0.50540555650735
H	(2)	-2.86414791386290	0.00155839361746	0.14344198236849

Table A5: Cartesian coordinates of TEMPO o···HOH hydrate computed at (U)B3LYP-D3(BJ)/def2-QZVP level of theory.

Atom	Fragment	X	Y	Z
C	(1)	-1.24838477021347	-1.23494338372010	-1.09024637272876
C	(1)	-2.12751618166390	0.00741239497491	-1.08195570258474
C	(1)	-1.23977739031243	1.24364196684907	-1.08978021632309
H	(1)	-1.85009470537477	-2.14449631929766	-1.10782766099165
H	(1)	-2.78842866833789	0.00954625895535	-0.21354819249913
H	(1)	-0.64146485540580	1.23895764799023	-2.00372391903560
C	(1)	-0.29089129896954	1.32534552216027	0.11345364382656
C	(1)	-1.03976451240467	1.73320308851229	1.39215018436208
H	(1)	-1.90943887268487	1.10771655810835	1.57844314665534
H	(1)	-1.37929396041742	2.76463641808831	1.29991816931150
H	(1)	-0.37226489568590	1.66343391524342	2.24857395974445
C	(1)	0.81263695978269	2.34424409651185	-0.17851471727515
H	(1)	1.44895255248745	2.49350086103038	0.68891473041306
H	(1)	0.35265860386082	3.29588541800256	-0.44407358786809
H	(1)	1.43692059503962	2.01196186261580	-1.00587450299625
C	(1)	-0.30022417289167	-1.32370326328467	0.11305332325331
C	(1)	-1.05217018645765	-1.72651224754516	1.39154975726170
H	(1)	-0.38433734097280	-1.66165175295713	2.24809736355131
H	(1)	-1.39906587365160	-2.75546761709439	1.29905776095009
H	(1)	-1.91734558165459	-1.09478959670577	1.57773791950616
C	(1)	0.79612709641554	-2.35026413362570	-0.17910115013815
H	(1)	1.42260042209509	-2.02220118967655	-1.00649144238987
H	(1)	0.32947267182799	-3.29861301910363	-0.44478074647157
H	(1)	1.43144706495710	-2.50405207107457	0.68826160188639
H	(1)	-2.77434422797070	0.00983282982136	-1.96006544546460
H	(1)	-0.64995882380886	-1.23400578404989	-2.00413055302234
H	(1)	-1.83515730817840	2.15735453381379	-1.10689099284742
N	(1)	0.36346543141313	-0.00153293970906	0.33801645868318
O	(1)	1.38542482955706	-0.00526481003524	1.10620317263495
O	(2)	3.44568330882401	-0.00964648666740	-0.85033226763596
H	(2)	2.86834291155380	-0.00849270579456	-0.06961416756555
H	(2)	4.34064117924265	-0.01589605233647	-0.50524955420215

Table A6: Cartesian coordinates of TEMCO p···HOH hydrate computed at (U)B3LYP-D3(BJ)/def2-QZVP level of theory.

Atom	Fragment	X	Y	Z
C	(1)	-0.17713905181091	-0.42279617004166	0.33258918097676
C	(1)	-0.58990297953165	1.04302572069763	0.12021188190030
C	(1)	0.58794105495614	2.01353553965280	0.33334768468762
H	(1)	0.75995865378619	2.12310705104649	1.40805024718181
C	(1)	1.88809529768304	1.56139728494186	-0.31710776010738
H	(1)	1.77688016004688	1.50267893746007	-1.40128115641259
H	(1)	2.67086268241880	2.29827322794535	-0.13083664644407
C	(1)	2.30160028552132	0.21268960051396	0.25616687915852
H	(1)	3.25178323702143	-0.12045316222166	-0.16659729515735
H	(1)	2.46683742462312	0.33031094354896	1.33092228672998
C	(1)	1.25766767152970	-0.89731918376297	0.03704534181493
H	(1)	0.28784808784693	2.99780535158171	-0.03153485616702
O	(1)	-1.00544992976596	-1.24412417481849	0.67328786252015
C	(1)	1.27863692103022	-1.37060419771523	-1.43385422578599
C	(1)	1.58856299996191	-2.09495297377752	0.93539407336796
C	(1)	-1.71956115581769	1.40501814025812	1.09440561139372
C	(1)	-1.13134102447215	1.16134517351441	-1.32289901535050
H	(1)	-1.95836701160404	2.46347714834908	0.98443889010461
H	(1)	-2.62130868647453	0.83158976993174	0.90131119960299
H	(1)	-1.41579768133527	1.23193272702068	2.12693019788850
H	(1)	-0.35914439531093	1.00486049016197	-2.07252178728792
H	(1)	-1.53341838152835	2.16538895479159	-1.46256073166154
H	(1)	-1.93413569183161	0.44696880492091	-1.49544513956154
H	(1)	1.13730137377696	-0.55570118754621	-2.13935272375602
H	(1)	2.24517990145907	-1.83038421570254	-1.64279947980441
H	(1)	0.50082897687712	-2.11202370487549	-1.60955484537193
H	(1)	0.90558826057546	-2.92181617421736	0.75984333016000
H	(1)	2.60564047998233	-2.43133349559217	0.73136911778741
H	(1)	1.52491517218461	-1.82424914966295	1.98925478280655
H	(2)	-2.81553346114703	-1.29943372481064	0.17418757492527
O	(2)	-3.68156261173633	-1.18083940272019	-0.24763691194772
H	(2)	-4.17390657891476	-1.98186394887225	-0.05801356819107

Table A7: Cartesian coordinates of TEMCO t···HOH hydrate computed at (U)B3LYP-D3(BJ)/def2-QZVP level of theory.

Atom	Fragment	X	Y	Z
C	(1)	-0.00126527659480	0.03912379877011	0.72602553318211
C	(1)	-1.32842602570615	0.41800937406405	0.04858153733373
C	(1)	-1.20408037583577	1.72178974461793	-0.76296191071681
H	(1)	-1.18885066947513	2.56571703816099	-0.06705315002359
C	(1)	0.04650653792824	1.78847447703538	-1.63037647508120
H	(1)	0.02742600795825	1.00769358457608	-2.39243870628799
H	(1)	0.07182082476189	2.73732027667087	-2.16850698492738
C	(1)	1.28993049640438	1.65670110688225	-0.75997982259997
H	(1)	2.19821324875801	1.72675648135918	-1.36223952369287
H	(1)	1.31637050290608	2.49924083499305	-0.06275598431858
C	(1)	1.34482474996398	0.34712323820680	0.05002026281781
H	(1)	-2.10617679607957	1.83778648201805	-1.36744891917005
O	(1)	-0.01805025539370	-0.56341333901131	1.78119230800569
C	(1)	1.68698178154175	-0.84678158196832	-0.87076786593866
C	(1)	2.43430226619135	0.45438251419304	1.12289061881545
C	(1)	-2.41166374015362	0.58386984186200	1.12024623962137
C	(1)	-1.73179374158138	-0.75716314673508	-0.87149093482318
H	(1)	-2.57403440972809	-0.34262584623781	1.66478570905689
H	(1)	-2.13783588951166	1.35335652250238	1.84184612615253
H	(1)	-3.34839986238111	0.87803083275856	0.64575653529187
H	(1)	-1.08030703559088	-0.85639399785603	-1.73540651774959
H	(1)	-2.74469354439098	-0.58198678848688	-1.23595922977076
H	(1)	-1.71789658820009	-1.70078441960897	-0.32863798953309
H	(1)	1.03241848227783	-0.91130909287540	-1.73569146880545
H	(1)	2.70801250443744	-0.72434299190149	-1.23408664523991
H	(1)	1.62336197669261	-1.78893526713952	-0.32895709814392
H	(1)	3.38585739147065	0.69847225362556	0.64948846298253
H	(1)	2.20114633599281	1.23688092117990	1.84477630064344
H	(1)	2.54655889500856	-0.47987380893414	1.66679929839959
H	(2)	-0.09727519270203	-3.98887183087742	1.94023700268526
O	(2)	-0.06921708320907	-3.35380529140447	1.22169043407680
H	(2)	-0.05204551575981	-2.48392192043936	1.64475285775797

Table A8: Cartesian coordinates of TEMCO o···HOH hydrate computed at (U)B3LYP-D3(BJ)/def2-QZVP level of theory.

Atom	Fragment	X	Y	Z
C	(1)	-1.14702305800423	-1.24245741360606	-1.08579473702630
C	(1)	-2.01614578806123	0.00715459838716	-1.14286116356365
C	(1)	-1.13860978318353	1.25084940862817	-1.08534348693788
H	(1)	-1.75608114338206	-2.14652724468745	-1.15233282886184
H	(1)	-2.74290773247244	0.00943899343225	-0.32832232537061
H	(1)	-0.47984114233843	1.25159602805501	-1.95766418166162
C	(1)	-0.26647313232091	1.33955522627986	0.18233365604327
C	(1)	-1.12942648832351	1.71757567339492	1.40619945134035
H	(1)	-1.97980656580528	1.05554136575154	1.54529173814295
H	(1)	-1.51319583561727	2.72869553303891	1.26646383103296
H	(1)	-0.53308079771318	1.70373910940418	2.31763258345031
C	(1)	0.80027596336401	2.42360127383347	-0.01102072626799
H	(1)	1.38768319728183	2.56590341536474	0.89283944464299
H	(1)	0.31381370367148	3.36717532292234	-0.26084543781067
H	(1)	1.48360492509158	2.16305040936152	-0.81798434247414
C	(1)	-0.27547093001353	-1.33747939813047	0.18182069676906
C	(1)	-1.14083881797851	-1.71024131905355	1.40557205983676
H	(1)	-0.54440923579712	-1.70052735927370	2.31700392088608
H	(1)	-1.53113030516175	-2.71882542367548	1.26555957480749
H	(1)	-1.98695613397308	-1.04281631812754	1.54492838959543
C	(1)	0.78397703823269	-2.42859162189497	-0.01197397477140
H	(1)	1.46903425402960	-2.17234366615343	-0.81885574680684
H	(1)	0.29116137853249	-3.36877804059529	-0.26211117612640
H	(1)	1.37042780452734	-2.57515835367464	0.89182839931580
H	(1)	-2.59711135383233	0.00927959712847	-2.06641087470775
H	(1)	-0.48829693266500	-1.24734398668674	-1.95813121046960
H	(1)	-1.74150903134208	2.15905664024240	-1.15159268725136
C	(1)	0.42403216891438	-0.00135109279929	0.48828624883485
O	(1)	1.51999100653758	-0.00513031871027	1.01245518046146
O	(2)	3.26372305262334	-0.01098303412003	-1.28617234595806
H	(2)	2.91630619328458	-0.00988180558498	-0.38423169680209
H	(2)	4.21873352189461	-0.01863619845101	-1.19533623229150

2.3 Hydrate energies

Absolute and relative computed energies are given in Table A34 for checking purposes and using a smaller basis set for the DFT calculations also in Table A10. The comparison shows that the conformational energy differences are robust for TEMCO monohydrates, but not perfectly robust for the subtle sub-kJ/mol energy differences in TEMPO monohydrates. Still, the DFT basis set effects are smaller than the DLPNO-CCSD(T) corrections and therefore we consider our quadruple zeta approach sufficiently robust for the conclusions drawn in the main text. The use of a smaller basis set for the DLPNO-CCSD(T) calculations confirms that the results are also converged for this parameter.

Table A9: Electronic energies E_{el} (in E_{h}), zero-point vibrational energies (in E_{h}), and relative zero-point corrected relative energies ΔE_0 (in kJ mol^{-1}) of the TEMCO and TEMPO 1:1 and 1:2 hydrates obtained at closed- and unrestricted open-shell B3LYP-D3(BJ,ABC)/def2-QZVP and DLPNO-CCSD(T)/aug-cc-pVQZ//B3LYP-D3(BJ,ABC)/def2-QZVP and DLPNO-CCSD(T)/aug-cc-pVTZ//B3LYP-D3(BJ,ABC)/def2-QZVP levels. The relative energy values in kJ mol^{-1} were obtained by the multiplication of the E_{h} computed energies with 2625.49963948 kJ mol^{-1}. Imaginary frequencies (i freq) at saddle points are not included into the zero point energy.

TEMCO	$E_{\mathrm{el}}^{\mathrm{B3LYP}}$ def2-QZVP (E_{h})	ZPVE def2-QZVP (E_{h})	$\Delta E_0^{\mathrm{B3LYP}}$ def2-QZVP (kJ mol^{-1})	$E_{\mathrm{el}}^{\mathrm{DLPNO}}$ aug-cc-pVQZ (E_{h})	$\Delta E_0^{\mathrm{DLPNO}}$ aug-cc-pVQZ (kJ mol^{-1})	$E_{\mathrm{el}}^{\mathrm{DLPNO}}$ aug-cc-pVTZ (E_{h})
p···HOH	-543.54007045	0.28625092	0.0	-542.84359493	0.0	-542.70835034
t···HOH(i freq)	-543.53892619	0.28579141	1.8	-542.84244600	1.8	-542.70716099
o···HOH	-543.53850618	0.28572746	2.7	-542.84212334	2.5	-542.70690458
oo···HOH	-619.99170089	0.31123588	-	-	-	
TEMPO						
p···HOH	-560.12178012	0.28555835	0	-559.40976057	0.0	-559.27075553
t···HOH	-560.12146712	0.28532208	0.2	-559.40925312	0.7	-559.27022149
o···HOH	-560.12115512	0.28518405	0.7	-559.40931199	0.2	-559.27033194
oo···HOH	-636.57424264	0.31058756	-	-	-	-
p···HOD	-560.12178012	0.28257120	0.9	-559.40976057	0.9	
t···HOD	-560.12146712	0.28233453	1.1	-559.40925312	1.6	
o···HOD	-560.12115512	0.28222654	1.6	-559.40931199	1.1	
p···DOH	-560.12178012	0.28224638	0.0	-559.40976057	0.0	
t···DOH	-560.12146712	0.28205922	0.3	-559.40925312	0.8	
o···DOH	-560.12115512	0.28191964	0.8	-559.40931199	0.3	
p···DOD	-560.12178012	0.27922186	0.0	-559.40976057	0.0	
t···DOD	-560.12146712	0.27903269	0.3	-559.40925312	0.8	
o···DOD	-560.12115512	0.27892359	0.9	-559.40931199	0.4	

Table A10: Electronic energies E_{el} (in E_h), zero-point vibrational energies (in E_h), and relative zero-point corrected relative energies ΔE_0 (in kJ mol^{-1}) of the TEMCO and TEMPO 1:1 and 1:2 hydrates obtained at closed- and unrestricted open-shell B3LYP-D3(BJ,ABC)/def2-TZVP level. The relative energy values in kJ mol^{-1} were obtained by the multiplication of the E_h computed energies with 2625.49963948 kJ mol^{-1}.

TEMCO	E_{el}^{B3LYP} def2-TZVP (E_h)	ZPVE def2-TZVP (E_h)	ΔE_0^{B3LYP} def2-TZVP (kJ mol^{-1})
p···HOH	-543.49514991	0.28621102	0.0
t···HOH(i freq)	-543.49407767	0.28586775	1.9
o···HOH(i freq)	-543.49378717	0.28577684	2.4
oo···HOH	-619.93926590	0.31131285	-
TEMPO			
p···HOH	-560.07594089	0.28554610	0.0
t···HOH	-560.07574018	0.28533849	0.0
o···HOH	-560.07558957	0.28532752	0.4
oo···HOH	-636.520971	0.31065605	-

2.4 Fragment energies

Table A11: Electronic energies E_{el} (in E_h), zero-point vibrational energies (in E_h) of the TEMCO, TEMPO and water monomers (and the water dimer) obtained at closed- and unrestricted open-shell B3LYP-D3(BJ,ABC)/def2-QZVP levels.

	E_{el}^{B3LYP} (E_h)	ZPVE (E_h)
TEMCO monomer	-467.09233161	0.26199887
TEMPO monomer	-483.67326754	0.26124430
H_2O monomer	-76.436343590	0.02128720
H_2O dimer	-152.88133598	0.04600359

2.5 Scans

A major difference between TEMPO and TEMCO is the anisotropy of the water hydrogen bond to the oxygen, which is considerably more pronounced for the C=O bond than for the N-O bond. This is revealed by relaxed potential scans varying the C−X−O···H torsional angle, see Figure A1.

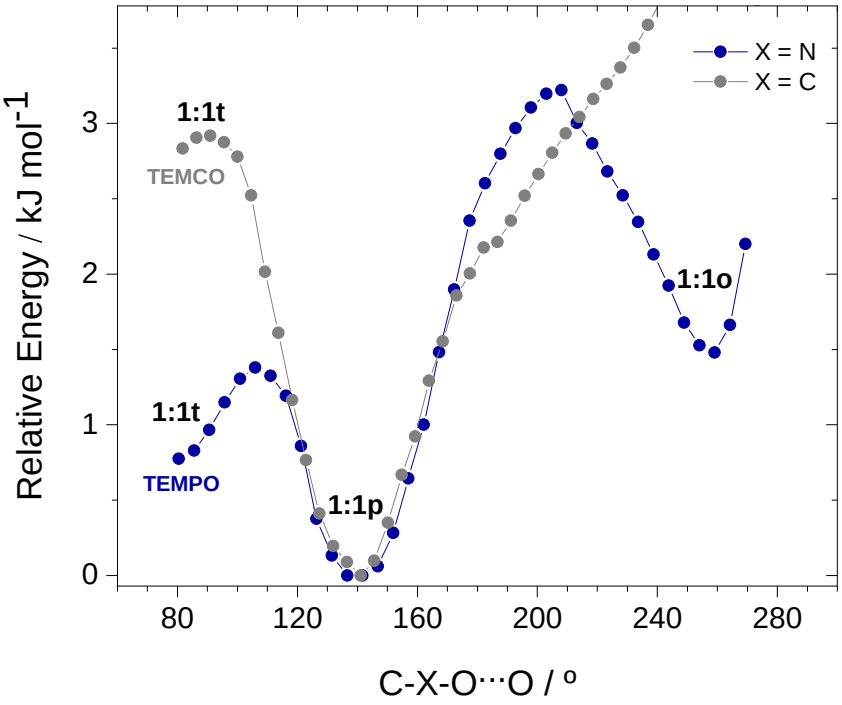

Figure A1: B3LYP and (U)B3LYP relaxed torsional scans of a single water molecule (O) around the N-O / C=O bond for TEMPO (blue) and TEMCO (grey), showing that the oxygen end of the C=O bond has a stronger hydrogen bond accepting anisotropy and preference for p-coordination than the oxygen end of the N-O bond. The barriers for TEMPO, which may be further lowered by zero-point energy of the relaxed modes, are low enough to allow for relaxation into the 1:1p global minimum, at least in colder neon expansions. Taken from Ref.[1], and licensed under CC BY.

2.6 LED analysis

To further analyze how intermolecular interactions contribute to the different torsional potentials of water around the X-O bonds in TEMPO and TEMCO, a LED-analysis [25] was carried out for the 1:1 p, t and o structures (Table A12). The analysis shows that dispersion contributions are of minor influence on the torsional potentials for TEMCO and TEMPO, contributing less than 1 kJ mol^{-1} to the relative energy of the conformations, with a tendency to favour 1:1p for TEMCO and 1:1t for TEMPO. The dominant contributions to the pronounced stability of 1:1p for TEMCO are electrostatic, as expected. Electrostatics is much less anisotropic for TEMPO and therefore leads to a more balanced energy of the water torsional isomers.

Table A12: Selected results (in E_h) of the LED analysis carried out at the stationary points of the 1:1 hydrates

TEMCO	1:1 p···HOH	1:1 t···HOH	1:1 o···HOH
Intra fragment 1 (REF.)	-464.195088394	-464.200399235	-464.202024657
Intra fragment 2 (REF.)	-76.041271655	-76.047953986	-76.049767880
Interaction of fragments 2 and 1:			
Electrostatics (REF.)	-0.051665662	-0.040669786	-0.037577255
Exchange (REF.)	-0.009134363	-0.007401572	-0.006862364
Dispersion (strong pairs)	-0.004380070	-0.004301885	-0.004159205
Dispersion (weak pairs)	-0.000479538	-0.000457589	-0.000473456
Sum of Dispersion			
(strong pairs and weak pairs)	-0.004859608	-0.004759474	-0.004632661
Sum of non dispersive correlation terms:			
Non dispersion (strong pairs)	-2.435468108	-2.435232531	-2.435278171
Non dispersion (weak pairs)	-0.005379379	-0.005356063	-0.005341783
TEMPO	1:1 p···HOH	1:1 t···HOH	1:1 o···HOH
Intra fragment 1(REF.)	-480.696940623	-480.687331791	-480.695383798
Intra fragment 2 (REF.)	-76.038458728	-76.044677184	-76.047134623
Interaction of fragments 2 and 1:			
Electrostatics (REF.)	-0.059238896	-0.059732050	-0.051828248
Exchange (REF.)	-0.011443963	-0.013680506	-0.011438618
Dispersion (strong pairs)	-0.004762392	-0.004796771	-0.004495928
Dispersion (weak pairs)	-0.000537190	-0.000620676	-0.000635520
Sum of Dispersion			
(strong pairs and weak pairs)	-0.005299582	-0.005417447	-0.005131448
Sum of non dispersive correlation terms:			
Non dispersion (strong pairs)	-2.488585219	-2.488584095	-2.488637854
Non dispersion (weak pairs)	-0.007615959	-0.007614628	-0.007604974

3 Jet-FTIR Experiments (subsection 4.1)[1]

3.1 Measurement details

The hydrate complexes were prepared in supersonic jet expansions through a 0.2 mm × 700 mm slit nozzle at a stagnation pressure of 750 mbar. CaF_2 optics, an optical filter (F20: wavenumber range <4000 cm^{-1}), an InSb/HgCdTe detector, a 150 W tungsten lamp and a VERTEX 70v FTIR spectrometer (scanning speed 140 kHz, double sided mode) were used to probe the gas pulses. A more detailed description of the experimental setup can be found in [26]. In Tab. A45 information on the number of averaged gas pulses (#) of the spectra shown in Fig. 2 of the main document and Figure S2 in the supplement, as well as the date of the measurement are provided.

Table A13: The spectra shown in subsection 4.1 are the average of # gas pulses recorded on the dates dd/mm/yyyy and expanded in a He:Ne gas mixture.

Spectrum	He:Ne	#	dd/mm/yyyy	Figure
TEMCO + H_2O	1:0	900	14/09/2020	S2
TEMCO + H_2O	1:0	800	17/09/2020	2 A; S2
TEMPO + H_2O	1:0	900	23/09/2020	S2
TEMPO + H_2O	1:0	900	24/09/2020	2 C; S2
TEMPO + H_2O	1:1	1200	20/10/2020	2 D
TEMPO + $H_2^{18}O$	1:1	750	03/11/2020	2 F
minus TEMPO + H_2O (20/10/2020)				
TEMPO + D_2O	1:0	800	10/11/2020	2 H, 2 J
450 scans (10/11/2020) *plus* 350 scans (11/11/2020)			11/11/2020	

Table A14: Relative scales of spectra shown in subsection 4.1.

Figure	Scale factor
TEMCO (light blue) S2	$\frac{29}{5}$ * 14/09/2020
TEMCO 2A	$\frac{2}{5}$ * 17/09/2020
TEMPO (light blue) S2	$\frac{5}{2}$ * 23/09/2020
TEMPO 2C	24/09/2020
TEMPO 2D	20/10/2020
TEMPO 2F	$\frac{3}{10}$ * (03/11/2020 - $\frac{1}{2}$ * 20/10/2020)
TEMPO 2 H, 2 J	10/11/2020 + 11/11/2020

3.2 Scaling factors

The harmonic spectra of TEMCO and TEMPO hydrates in Figure 2 were uniformly scaled by 0.975 for the hydrogen-bonded OH stretching transition. This scaling factor is consistent with factors which reproduce the experimental OH_b of water dimer (Matrix-Ne[27, 28] and He-Jet[29] experiments), 0.974-0.977, and the scaling factor which reproduces the 1:1p···HOH stretching vibration (0.975, 0.974 after deperturbation of the b2lib resonance) of the TEMCO monohydrate (Table A42).

Table A15: Experimental OH_b stretching wavenumbers of water dimer and of the TEMCO 1:1p···HOH transition, along with the harmonic B3LYP-D3(BJ)/def2-QZVP computed values.

	Ne-Matrix [27, 28] $\tilde{\nu}$	He-jet [29] $\tilde{\nu}$	B3LYP-D3(BJ,ABC)/def2-QZVP $\tilde{\nu}$
OH_b (H_2O dimer)	3590.5	3602	3686
TEMCO 1:1p···HOH	-	3550	3643

3.3 2-state resonance model

Water shows a rather universal resonance when the OH-stretching vibration is shifted to approximately 3500 cm^{-1}.[30] We believe that this particular resonance of the OH stretching vibration of the bonded hydrogen of the water molecule (OH_b) with the combination of the water bending overtone (b2) and the libration motions (in plane and out of plane) of the bonded hydrogen (lib) can be observed in the molecular systems studied in this publication.

Due to the coupling of the zeroth order bright OH_b and dark b2lib states, the observed signals are shifted. To reconstruct the unperturbed signal positions ($\tilde{\nu}(OH_b^0)$ and $\tilde{\nu}(b2lib^0)$) the equations Eqs. A1 and A2 were applied where I is the intensity of the signal and $\tilde{\nu}(OH_b^{exp})$ and $\tilde{\nu}(b2lib^{exp})$ are the experimentally observed signal positions. The signal with the higher intensity is defined as $\tilde{\nu}(OH_b^{exp})$.

To compare the the results to the findings in [30] the effective coupling element W_{ij} is calculated with Eq. A3 where I is the intensity of the signal, r the intensity ratio of the two observed signals (I_{OH_b}/I_{b2lib}) and $\Delta\tilde{\nu}_{ij}$ the difference between the two perturbed wavenumbers ($\tilde{\nu}(OH_b^{exp})$, $\tilde{\nu}(b2lib^{exp})$).

The experimental and unperturbed wavenumbers can be found in the main text while the intensity ratios and the coupling element can be found in Tab A16.

The determination of the intensity ratios is described in section 3.4.

$$\tilde{\nu}(OH_b^0) = \frac{I_{OH_b} \cdot \tilde{\nu}(OH_b^{exp}) + I_{b2lib} \cdot \tilde{\nu}(b2lib^{exp})}{I_{OH_b} + I_{b2lib}} \tag{A1}$$

$$\tilde{\nu}(b2lib^0) = \frac{I_{b2lib} \cdot \tilde{\nu}(OH_b^{exp}) + I_{OH_b} \cdot \tilde{\nu}(b2lib^{exp})}{I_{OH_b} + I_{b2lib}} \tag{A2}$$

$$W_{ij} = \Delta\tilde{\nu}_{ij}\sqrt{\frac{r}{(r+1)^2}} \tag{A3}$$

3.4 Experimental intensity ratios for the resonances

To calculate the unperturbed states and the coupling element W_{ij} the intensities and the intensity ratio r of the two perturbed states (observable in experiment) is needed. Since the signal-to-noise and overlap limits the precision, two different methods for the determination are applied. They are described in the following and the results are summarized in the table A16. It is assumed that the larger signal corresponds to the OH_b vibration and the signal with lower intensity to the b2lib resonance. The ratio was obtained by dividing the intensity of b2lib by the one of OH_b, so it is always < 1.

3.4.1 Method A

In method A the peak height (signal maximum) is determined relative to a horizontal baseline defined by the mean value of a signal-free spectral range (approximately 200 cm^{-1}) close to the signal region. The results are shown in table A16.

3.4.2 Method B

The signals were integrated as implemented in the spectrometer (Bruker Vertex 70v) software (OPUS 7.8, Integration Method B). The area between the connection line of two limiting points on the spectral curve and the curve itself is determined. The limiting points on the signal are determined by visual judgement. The results are shown in table A16 and converted into rounded coupling matrix elements and deperturbed band positions.

Table A16: Intensity ratios for the deperturbation analysis for the 1:1 monohydrates of TEMCO and TEMPO

System	r_A	r_B	$\bar{r}$	W_{ij} /cm^{-1}	$\tilde{\nu}(OH_b^0)$ /cm^{-1}	$\tilde{\nu}$(b2lib^0) /cm^{-1}
TEMCO	0.076	0.058	0.067	11	3547	3508
TEMPO	0.446	0.405	0.426	9	3503	3511

3.5 Size discrimination

The distinction between 1:1 and 1:2 complexes is supported by the comparison of TEMCO (A) and TEMPO (C) spectra recorded at different concentrations in warm (0.75 bar of He) jet expansions. (Figure A2).

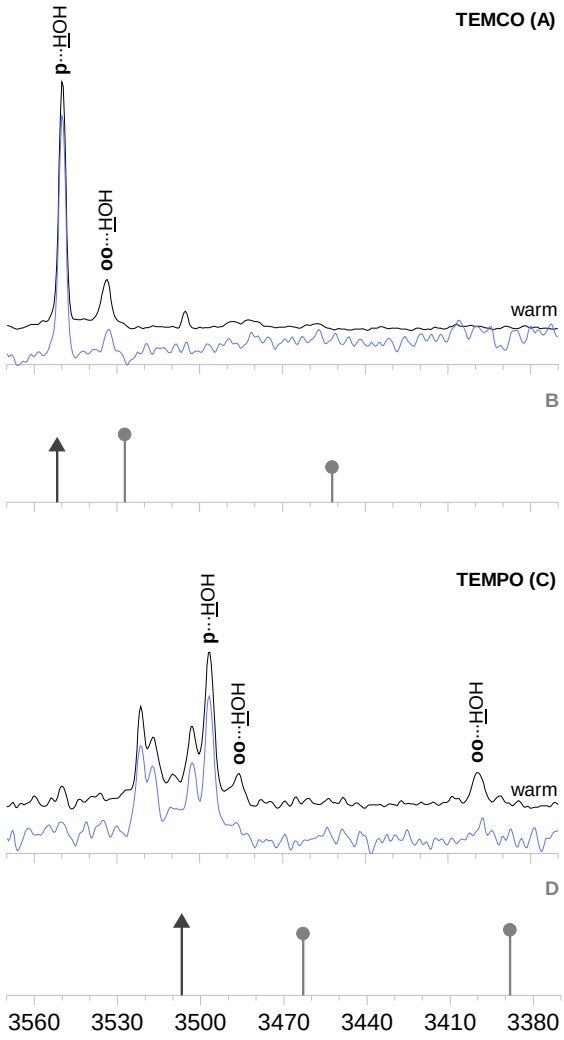

Figure A2: Spectra at different concentrations scaled to similar 1:1p peaks to support the mono- and dihydrate assignment (black spectra are also shown in the main text).Taken from Ref.[1], and licensed under CC BY.

Table A17: Relative scaling of spectra shown in Fig. 5 and Fig. 6 of the manuscript.

Spectrum	Figure	Scaling factor
DTBN + H_2O	5	$\frac{7}{10}$ (21/10/2021)
DTBN + $HOCH_3$	5	$\frac{3}{10}$ (21/09/2021)
TEMPO + H_2O [1]	5	(19/01/2021)
TEMPO + $HOCH_3$	5	$\frac{1}{2}$ (23/04/2021)
DTBN + $HOC(CH_3)_3$	6	$\frac{7}{10}$ (14/12/2021 + 15/12/2021)
TEMPO + $HOC(CH_3)_3$	6	$\frac{3}{5}$ (19/05/2021)
TEMPO + HOC_6H_5	6	$\frac{3}{5}$ (11/05/2021)

4 Computations of Subsection 4.2[31]

4.1 Methods and keywords

Monomers, 1:1 and 1:2 complexes of DTBN and TEMPO were obtained from manual starting structures computed at the unrestricted open-shell B3LYP-D3BJ/def2-TZVP level[6–9] using ORCA 4.2.1[15] and through the CREST[2, 3] program at GFN2-xTB level[4, 5], as described in Section 3 of this Thesis. Reoptimizations were then carried out using DFT functionals (open-shell B3LYP[6–8], B2PLYP[32] and TPSS[33]) with def2-TZVP and QZVP[9] basis sets, including Grimme's three-body term dispersion correction D3[10] and Becke-Johnson (BJ) damping[11–14]. These calculations performed using the ORCA[15] software package. Relaxed potential energy surface scans around the C−C−N−C, C−C−N−O, C−C···C−C dihedral angles of monomer and 1:1 solvates, and C−N−O···O of 1:1 structures were carried out at UB3LYP/def2-TZVP level of theory using Gaussian16 Rev A.03[34] software. Further single point calculations on the B3LYP geometries were carried out with the DPLNO-CCSD(T)[16–19] approach with aug-cc-pVTZ[20], and matching auxiliary basis sets, at the unrestricted open-shell[19] variant, with the ORCA software.[15] Local energy decomposition (LED) was also performed.[21, 22] As LED analysis decomposes the interaction energy between two fragments, these must be defined in the input file. Herein, the atoms which define DTBN were assigned to fragment (1), while the atoms of small OH containing solvents were assigned to fragment (2) (see Tables A19 - A33). The basic variable that commands the type of wavefunction to be computed (HFTyp in the %scf block) was not specified, and in this case, the program checked the multiplicity specified in the input file, and performs the calculation considering it.[15]. Regarding open-shell systems with multiplicity = 2 (DTBN and DTBN complexes), UKS/UHF were employed. UHF (Unrestricted Hartree-Fock) is replaced by UKS (Unrestricted Kohn-Sham) in DFT computations.[15] By program default, quasi-restricted orbitals (QRO[23]) were employed to avoid spin contamination[24].

Table A18: Computational methods, programs and and keywords used for unrestricted open-shell quantum chemical calculations of DTBN and TEMPO monomers and complexes with OH contaning solvents shown in Subsection 4.2 of this Thesis. The calculations were performed using ORCA[15] and Gaussian 16[34] software packages.

Method	Program	Basis set	Keywords
B3LYP-D3(BJ)	Gaussian 16 Rev.A.03	def2-TZVP	`# opt ub3lyp def2tzvp empiricaldispersion=gd3bj int=ultrafine freq` (multiplicity = 2)
B3LYP-D3(BJ)	ORCA 4.2.1	def2-TZVP	`B3LYP D3BJ ABC def2-TZVP GRID5 NOFINALGRID VERYTIGHTSCF TIGHTOPT FREQ` (multiplicity = 2)
B3LYP-D3(BJ)	ORCA 4.2.1	def2-QZVP	`B3LYP D3BJ ABC def2-QZVP GRID5 NOFINALGRID VERYTIGHTSCF TIGHTOPT FREQ` (multiplicity = 2)
B2PLYP-D3(BJ)	ORCA 4.2.1	def2-TZVP	`B2PLYP D3 def2-TZVP GRID5 NOFINALGRID VERYTIGHTSCF TIGHTOPT NumFreq` (multiplicity = 2)
TPSS-D3(BJ)	ORCA 4.2.1	def2-TZVP	`TPSS D3BJ def2-TZVP ABC GRID5 NOFINALGRID VERYTIGHTSCF TIGHTOPT NumFreq` (multiplicity = 2)
DLPNO-CCSD(T)	ORCA 4.2.1	aug-cc-pVTZ	`DLPNO-CCSD(T) TightPNO aug-cc-pVTZ aug-cc-pVTZ/C TightSCF LED` (multiplicity = 2)

4.2 Cartesian Coordinates

Cartesian coordinates (in Å) of DTBN and TEMPO complexes computed at (U)B3LYP-D3(BJ)/def2-TZVP (shown in the Subsection 4.2 of the Thesis) are given in the Tables A19, A20 A21, A22,A23 A24, A25, A26, A27, A28, A29, A30, A31, A32, A33

Table A19: Cartesian coordinates of 1:1 DTBN t···HOH computed at UB3LYP-D3(BJ)/def2-TZVP level of theory.

Atom	Fragment	X	Y	Z
O	(1)	-0.53247525809028	1.19645606619857	-0.90457129344892
C	(1)	-1.17576202268707	-0.89664198471922	-0.09311010966260
C	(1)	-2.14486224728637	-0.95704593113227	-1.28101551191418
C	(1)	-0.67869075038164	-2.31331963542261	0.19066164407326
C	(1)	-1.89745784853815	-0.33776187519741	1.14242503548568
H	(1)	-2.56049068822159	0.02407800133320	-1.49374393424113
H	(1)	-1.63413827427472	-1.31871961188057	-2.17519464178305
H	(1)	-2.95812770812340	-1.64515616064096	-1.04601893406426
H	(1)	0.01749153744213	-2.36323913495688	1.02454997971430
H	(1)	-1.54608863195043	-2.91847819578340	0.45760681080145
H	(1)	-0.21865647612903	-2.76610407036673	-0.68622529386096
H	(1)	-1.25102690652534	-0.34054933635187	2.01919896766279
H	(1)	-2.22476053303254	0.68453307139368	0.96336092293387
H	(1)	-2.77269103522197	-0.95218008536047	1.36111117554009
C	(1)	1.37088305639188	0.03214083148208	-0.07534184370153
C	(1)	2.07111756309778	-1.19077403402748	-0.68659498819283
C	(1)	2.04252078139191	1.28953979874648	-0.63668825793842
C	(1)	1.50119442455090	0.04744226052165	1.45470409506753
H	(1)	1.80626620944141	-2.12462258153796	-0.20120163746219
H	(1)	1.84509968738603	-1.27153322608974	-1.75085778466513
H	(1)	3.14933029608854	-1.06279759239848	-0.58116961429901
H	(1)	1.92489458243808	1.35166631280124	-1.71777863864890
H	(1)	1.63831197691474	2.19451173370708	-0.19161884447584
H	(1)	3.10668388679081	1.23377898623048	-0.40322773776527
H	(1)	1.08220000746342	-0.84450401224032	1.91707207236703
H	(1)	2.55974065798183	0.08892176189567	1.71918283851288
H	(1)	1.01011721260973	0.92723050619767	1.87006370720683
N	(1)	-0.08573669278700	0.07504896249126	-0.47702022110060
O	(2)	-0.50386228985968	2.98602277913587	1.25602216630103
H	(2)	-0.69957187065074	3.89874240123692	1.02339561483983
H	(2)	-0.57898264622925	2.48387399473456	0.42349425671825

Table A20: Cartesian coordinates of 1:1 DTBN o···HOH computed at UB3LYP-D3(BJ)/def2-TZVP level of theory.

Atom	Fragment	X	Y	Z
O	(1)	0.41567117298258	-1.42020424987360	-0.63144026970744
C	(1)	1.27099120622909	0.69388754340038	-0.09251935584857
C	(1)	1.65663664841111	1.15570184219707	-1.50603247152449
C	(1)	0.99857434254054	1.89837954590040	0.80977205700574
C	(1)	2.42868025200800	-0.10281212938397	0.52509783097452
H	(1)	0.89690272300582	1.80545642800899	-1.93964362125725
H	(1)	2.59647771386852	1.70970362994228	-1.46897239308447
H	(1)	1.79037257770667	0.29006815513801	-2.15441302234975
H	(1)	0.79899922873605	1.59012887567704	1.83486176531354
H	(1)	1.89762259612261	2.51618209506579	0.81762665677259
H	(1)	0.18080834109913	2.52499751650549	0.46367392483009
H	(1)	3.27124760982164	0.57028302003468	0.69103842759261
H	(1)	2.13010101893747	-0.53356572998329	1.48141093359179
H	(1)	2.74583307380200	-0.90952356449016	-0.13012373554562
C	(1)	-1.36582361803467	0.08348713703955	-0.13046518624085
C	(1)	-2.15217014194207	-1.16778352027193	-0.53249948111866
C	(1)	-1.75018493384255	0.44298628105332	1.31351444894082
C	(1)	-1.72065649262555	1.21156759076890	-1.10942857230714
H	(1)	-1.97068598956774	-1.98849599656516	0.15828827110536
H	(1)	-3.21416166595455	-0.91884771756881	-0.50498264740159
H	(1)	-1.89364828044040	-1.49785717893917	-1.53630796097325
H	(1)	-1.37511355892891	-0.31640782367521	2.00008113607944
H	(1)	-1.37956220113729	1.41646765046688	1.62150272755114
H	(1)	-2.83874122757579	0.46606342461191	1.39098322428124
H	(1)	-1.22149403857735	2.14970725759504	-0.87865028789385
H	(1)	-1.46785879722272	0.92645745427706	-2.13131093356351
H	(1)	-2.79595338138628	1.39261739086114	-1.06443686423816
N	(1)	0.10387169989351	-0.24995961449702	-0.21418401506929
O	(2)	0.08467343846170	-2.61644659870416	1.90097009519162
H	(2)	0.26682561131019	-2.39345277334389	0.97044375818955
H	(2)	0.37441507229918	-3.52708594124760	2.01045556070383

Table A21: Cartesian coordinates of 1:1 DTBN p···HOH computed at UB3LYP-D3(BJ)/def2-TZVP level of theory.

Atom	Fragment	X	Y	Z
O	(1)	-0.61928012751018	-1.21575037302829	-0.50869349528988
C	(1)	-0.64221298547621	1.08342186823928	-0.02318433829677
C	(1)	0.23426778262754	2.33587993072099	-0.06306947111475
C	(1)	-1.69805829851507	1.21233868563791	-1.13032097224564
C	(1)	-1.32931536087169	0.96902587604286	1.34668671548680
H	(1)	1.01918670307701	2.33745942063871	0.68958508877685
H	(1)	0.68139660303907	2.48572736003073	-1.04472453988908
H	(1)	-0.40869059217051	3.19278485812956	0.14109802363973
H	(1)	-2.42552418100982	0.40673364825497	-1.09432236618861
H	(1)	-2.22718530663620	2.15804113494468	-1.00407460266028
H	(1)	-1.22223761197151	1.21309764228756	-2.11249574651523
H	(1)	-1.93686206802855	0.06785872075287	1.40354139965014
H	(1)	-0.60173770785933	0.95893597376815	2.15814019436752
H	(1)	-1.98602351505550	1.82839905653595	1.49316668965403
C	(1)	1.56953873175181	-0.47798763715863	0.01862820477315
C	(1)	2.49657771000485	0.36521548125527	-0.87012532508654
C	(1)	1.85900750838940	-0.24119963284883	1.50781379592764
C	(1)	1.82777489365808	-1.95405615790104	-0.29795405856419
H	(1)	2.18877519620636	0.29755013795681	-1.91439148895706
H	(1)	2.52988604323567	1.41159664213980	-0.58364939872693
H	(1)	3.51106343638897	-0.02881231668547	-0.79188916594863
H	(1)	1.73870104569326	0.79983529369778	1.79945199665153
H	(1)	1.20155909345652	-0.85281490730181	2.12624713091842
H	(1)	2.89071057647449	-0.52713250604280	1.72110280400814
H	(1)	1.61915320923403	-2.17743925855902	-1.34311227677135
H	(1)	2.87951740740857	-2.16401717845909	-0.09783997790832
H	(1)	1.21422915687414	-2.60961996340360	0.31479507799697
N	(1)	0.11841493202290	-0.19303276492788	-0.28830079422812
O	(2)	-3.31549089177392	-1.66883391687779	0.18042092361442
H	(2)	-3.54371245506324	-2.57621185361810	-0.04241049727808
H	(2)	-2.38697092760094	-1.55963726422153	-0.09489652979590

Table A22: Cartesian coordinates of 1:1 DTBN t···$HOCH_3$ computed at UB3LYP-D3(BJ)/def2-TZVP level of theory.

Atom	Fragment	X	Y	Z
O	(1)	0.59295641625733	0.45259467377100	-1.17254945084802
C	(1)	-1.25939812028856	1.21531154036220	0.02804962794556
C	(1)	-2.60406851470312	0.79056922962370	0.61613940686717
C	(1)	-0.43294652440404	1.95508110163992	1.09119408244934
C	(1)	-1.52848379625993	2.14486123994194	-1.16243322093635
H	(1)	-2.50695704866786	0.12955561266402	1.47430421089260
H	(1)	-3.11209578886269	1.69253818748304	0.96005124790766
H	(1)	-3.24175942616305	0.31695726186284	-0.12866916900224
H	(1)	0.54276699175699	2.22957477261738	0.69468958219976
H	(1)	-0.95682526682350	2.86504270761079	1.38909131525734
H	(1)	-0.28177303151046	1.34271295061698	1.97927949926411
H	(1)	-2.12348683682872	2.99525822081235	-0.82627805760658
H	(1)	-0.59817287314189	2.50943781805941	-1.58917164704831
H	(1)	-2.08526702595404	1.62064070126930	-1.94116025213401
C	(1)	-0.43058056546684	-1.36455355022494	-0.02716525539332
C	(1)	-1.77711019145183	-2.03888012252051	-0.32891023814053
C	(1)	0.65550553016724	-2.11034643349442	-0.80885946676909
C	(1)	-0.09078852842463	-1.43024828133611	1.46901474406204
H	(1)	-2.07530178936691	-1.85656689169052	-1.36239516441855
H	(1)	-1.66442889390115	-3.11583628122560	-0.19663506934326
H	(1)	-2.57713542278169	-1.71313118754613	0.32799741616268
H	(1)	0.49017762581796	-2.03975128957571	-1.88307196454424
H	(1)	1.64628919272562	-1.72490149170221	-0.58609029763791
H	(1)	0.61887571711050	-3.16078450598833	-0.51711604819005
H	(1)	0.87423026424142	-0.96056040154368	1.66006401030649
H	(1)	-0.84682042307877	-0.95195093385455	2.08915732804772
H	(1)	-0.02955957530095	-2.47728361590685	1.77261404828706
N	(1)	-0.42853607664913	0.07074548874193	-0.50084739665895
O	(2)	2.80156650507555	0.46383189913251	0.53689475621957
H	(2)	2.10706294691201	0.51556203075016	-0.14394188612298
C	(2)	4.05443527099546	0.31815434862798	-0.10507974902617
H	(2)	4.81685875604908	0.25397190630645	0.67211903167673
H	(2)	4.10514045288768	-0.59466411328237	-0.71191899119248
H	(2)	4.29019005003292	1.17408740799802	-0.74849698253280

Table A23: Cartesian coordinates of 1:1 DTBN o···$HOCH_3$ computed at UB3LYP-D3(BJ)/def2-TZVP level of theory.

Atom	Fragment	X	Y	Z
O	(1)	0.65472430631493	-0.28446656600048	-1.20770983029700
C	(1)	-0.51417298928488	1.44461250082922	-0.14710283968077
C	(1)	-1.16122223505076	2.04877708883339	-1.40234581121459
C	(1)	-1.35987002918191	1.74955441900046	1.08976003423531
C	(1)	0.87467803278187	2.06137749281800	0.07082889883454
H	(1)	-1.18731380548181	3.13671423819627	-1.31759304853558
H	(1)	-0.57791453150657	1.78293458310764	-2.28337474358878
H	(1)	-2.18293225396096	1.69412706310076	-1.53761587666924
H	(1)	-0.87641306924180	1.39926735518558	2.00020966552707
H	(1)	-1.45874019972258	2.83348368439677	1.16302044567430
H	(1)	-2.36451076851158	1.33774505079756	1.04175242818383
H	(1)	1.49482015441443	1.95616423383947	-0.81511417068881
H	(1)	0.76087259259568	3.12194192852306	0.29987434763648
H	(1)	1.37923814959483	1.57575210290419	0.90695947261307
C	(1)	-1.20844755577555	-1.16971082191402	-0.01266147016959
C	(1)	-0.64618049301599	-2.44460734592659	-0.64859927151904
C	(1)	-1.20800036342548	-1.35948765234288	1.51231854894331
C	(1)	-2.62570120291515	-0.94153911320446	-0.55687867789138
H	(1)	0.34503272894612	-2.67758452828301	-0.26453175820384
H	(1)	-1.31701194145429	-3.26748077844761	-0.39703226970350
H	(1)	-0.58420074133728	-2.35906830933071	-1.73111456154069
H	(1)	-0.18381330351119	-1.37376719795344	1.88633622741415
H	(1)	-1.76827843003358	-0.59061627009472	2.03642304396828
H	(1)	-1.67023825074323	-2.31997955444737	1.74661508454504
H	(1)	-3.10851388621109	-0.06467584331658	-0.13175366558151
H	(1)	-2.60640539531534	-0.83504319941508	-1.64213088191287
H	(1)	-3.24279147418390	-1.80769229238972	-0.31174842453996
N	(1)	-0.30474422627388	-0.02507915180961	-0.39956548043520
O	(2)	2.39943276317495	-1.20047041616519	0.79382770711224
H	(2)	1.93274796834127	-0.92597314895169	-0.01434782236912
C	(2)	3.75289743566033	-0.79908123385943	0.69696859680887
H	(2)	3.85489294268292	0.28928352342407	0.60246997336727
H	(2)	4.25515415785049	-1.11097924543364	1.61345204568265
H	(2)	4.26341591378098	-1.26940259567022	-0.15183591600495

Table A24: Cartesian coordinates of 1:1 DTBN p···$HOCH_3$ computed at UB3LYP-D3(BJ)/def2-TZVP level of theory.

Atom	Fragment	X	Y	Z
O	(1)	-0.69173486555471	-0.74391979025288	-0.48403700654533
C	(1)	0.23808521088093	1.36626417606461	-0.02932249939500
C	(1)	1.55025679129497	2.14773874453083	-0.10693941589599
C	(1)	-0.69580814692248	1.90382330538131	-1.12302052624978
C	(1)	-0.40632321106480	1.56114241582467	1.35242610686462
H	(1)	2.28161802558865	1.83778039038848	0.63567008286769
H	(1)	1.99956110806031	2.08576512058199	-1.09706614055631
H	(1)	1.32014317120704	3.19606046282780	0.08643779482942
H	(1)	-1.68956654625616	1.47040656021717	-1.05803052453317
H	(1)	-0.78534046193181	2.98511560367464	-1.00922784254257
H	(1)	-0.28518211649336	1.69467561390505	-2.11222284848535
H	(1)	-1.33027879692198	0.99168459669882	1.43604209704263
H	(1)	0.26932989511768	1.26153839569291	2.15326558631497
H	(1)	-0.64736789932821	2.61650782424119	1.49172615531562
C	(1)	1.61266582935118	-0.96617841313443	0.01945523712767
C	(1)	2.78994989786445	-0.59211012911873	-0.89381190617824
C	(1)	1.99809330949948	-0.84881154248693	1.50100945550635
C	(1)	1.23506577916179	-2.42187902475155	-0.27055118165566
H	(1)	2.46442665499820	-0.54121089903042	-1.93362398348894
H	(1)	3.25615969709751	0.35133333937379	-0.62797379989973
H	(1)	3.55330222945296	-1.36799434424357	-0.81756064852906
H	(1)	2.32188750236511	0.15329224159197	1.77361749923535
H	(1)	1.15742913054391	-1.12672193595817	2.13721823434768
H	(1)	2.82384658891337	-1.53140439744358	1.71017005676143
H	(1)	0.93780942802977	-2.55475885399078	-1.30958531612200
H	(1)	2.10981714667952	-3.04343068081874	-0.07382288264848
H	(1)	0.41488576867396	-2.75756260297765	0.35897831571351
N	(1)	0.40318451755457	-0.11273439528594	-0.28038333749636
O	(2)	-3.30816099601599	-0.06971379393214	0.25640481492098
H	(2)	-2.41177081064704	-0.32309458666400	-0.02619504954427
C	(2)	-4.19514801247697	-1.12936121685343	-0.04520537399833
H	(2)	-3.92874399591930	-2.05436859442760	0.48115162783215
H	(2)	-5.19217499586156	-0.82783909693414	0.27903331747997
H	(2)	-4.23429582694099	-1.34324849269052	-1.12044509839548

Table A25: Cartesian coordinates of 1:1 DTBN t···$HOC(CH_3)_3$ computed at UB3LYP-D3(BJ)/def2-TZVP level of theory.

Atom	Fragment	X	Y	Z
O	(1)	0.09533782814065	-0.26727294601942	-1.15326414182886
C	(1)	1.64179570573856	-1.35173612276303	0.29360903326476
C	(1)	3.06558325282587	-1.83912262412881	-0.01385764110002
C	(1)	1.49580477809231	-0.93305575403756	1.76396861172739
C	(1)	0.67731405113892	-2.50910726488072	0.01338746725314
H	(1)	3.21511957378967	-2.80418572603763	0.47206720331616
H	(1)	3.20098449936055	-1.97957814730698	-1.08728472477612
H	(1)	3.83753544322510	-1.16948593222876	0.35135171509304
H	(1)	0.47841254795251	-0.59863725118865	1.96684929987452
H	(1)	1.70630582236684	-1.79487407763610	2.40047388132152
H	(1)	2.19089939813664	-0.14221389728199	2.04106443297798
H	(1)	-0.34488564609934	-2.26052837658191	0.28447803645372
H	(1)	0.69741678536213	-2.79442957347752	-1.03772973217350
H	(1)	0.99524416069698	-3.36306727900703	0.61312116869577
C	(1)	1.86699566005448	1.17300328377707	-0.67030437980650
C	(1)	3.32587755866194	1.23115504784148	-0.22077677569851
C	(1)	1.79665339801955	1.62155654742644	-2.13575971867866
C	(1)	1.01437106526076	2.10575997249473	0.20298463363363
H	(1)	3.65305513438753	2.26871132754138	-0.30030768616798
H	(1)	3.46621911086553	0.92796694414396	0.81423519216737
H	(1)	3.97317618979250	0.63233606874809	-0.85927700694177
H	(1)	2.21244871382628	2.62621767538435	-2.22514414617004
H	(1)	2.37701765751383	0.95033223371007	-2.77127625675837
H	(1)	0.76939706659280	1.63047312473915	-2.49000887260068
H	(1)	1.36448780170101	3.13296763421554	0.08666754767957
H	(1)	-0.03020792860552	2.05722438158103	-0.09672356689412
H	(1)	1.08101334640533	1.83914798875469	1.25711802665357
N	(1)	1.25594213847933	-0.20647940239933	-0.61442828843673
O	(2)	-1.82648884606674	-0.12911451915880	0.88886052299399
H	(2)	-1.24112741848644	-0.19593779041408	0.11266795770185
C	(2)	-3.15103393134671	0.16413081742132	0.42737279255126
C	(2)	-4.01242821693803	0.25618068275089	1.68108114183619
H	(2)	-5.04986995945547	0.47910219574339	1.42511469333086
H	(2)	-3.98334567047379	-0.68779147360342	2.22769777221029
H	(2)	-3.63833901327243	1.04347836989296	2.33763052688579
C	(2)	-3.14530663696555	1.49640689006972	-0.32727320073201
H	(2)	-2.49180616803891	1.43561659993603	-1.20064227040735
H	(2)	-4.14784635397941	1.76143978122319	-0.67070769828784
H	(2)	-2.77945440884687	2.29372030981071	0.32205364201966
C	(2)	-3.63467759735426	-0.96615457944922	-0.48461455290495
H	(2)	-2.98488210766122	-1.05486643929531	-1.35827933535699
H	(2)	-3.61677971165594	-1.91550774213174	0.05323791281019
H	(2)	-4.65333907314095	-0.78420095817815	-0.83485321673127

Table A26: Cartesian coordinates of 1:1 DTBN o···$HOC(CH_3)_3$ computed at UB3LYP-D3(BJ)/def2-TZVP level of theory.

Atom	Fragment	X	Y	Z
O	(1)	0.39877071573462	-0.65971193037477	-1.03983675660335
C	(1)	1.73577097509368	-1.24404445065739	0.79280577227533
C	(1)	2.75593806808957	-2.11400414547978	0.04327452915641
C	(1)	2.35983875697780	-0.65865875864647	2.06014553814647
C	(1)	0.53237517774646	-2.09932133971434	1.21300998293076
H	(1)	2.31860409319208	-2.47961793518184	-0.88541162207030
H	(1)	3.66384051341123	-1.55850319851701	-0.19090019754925
H	(1)	3.03218151240008	-2.97238315066144	0.65841948152244
H	(1)	1.62771279311372	-0.10440321068028	2.64523814931538
H	(1)	2.71107737490951	-1.49145790461566	2.67095020155546
H	(1)	3.21633184423867	-0.01822999240331	1.86622888081273
H	(1)	-0.24748817926489	-1.47452243774725	1.64933813105215
H	(1)	0.10987547855622	-2.62943787577106	0.36398356161190
H	(1)	0.85800388930781	-2.82681896755823	1.95799874361676
C	(1)	1.72505497025621	1.20336906945413	-0.36730746091913
C	(1)	1.00612018227583	1.78962664020260	-1.58597674912153
C	(1)	1.37876925842081	2.07339712137842	0.85130800375220
C	(1)	3.23368078708767	1.19882712578583	-0.65101392747202
H	(1)	-0.06710243431050	1.85509489193929	-1.41942889658374
H	(1)	1.39362114528186	2.79617866305690	-1.75066422751995
H	(1)	1.18015632574803	1.19453634387837	-2.47961459407710
H	(1)	0.32529734050715	1.95668867087755	1.10732251816771
H	(1)	1.98482348582567	1.84371929605967	1.72281438271902
H	(1)	1.55375368587568	3.12000014167114	0.59573477535505
H	(1)	3.45552697838645	0.59863845878710	-1.53415963954752
H	(1)	3.56072475334755	2.22179017726727	-0.84516558044130
H	(1)	3.82191912146735	0.81964733450781	0.18130843521605
N	(1)	1.22063007045290	-0.20508551372928	-0.16837861770335
O	(2)	-1.86099682228902	0.50056703931006	0.21112167949016
H	(2)	-1.18238650194394	0.05159335039160	-0.32248057497947
C	(2)	-3.14832660555503	0.08817186415333	-0.26512842373109
C	(2)	-3.26420550524192	-1.43480240875942	-0.16445533105164
H	(2)	-2.50390815966042	-1.91539768837243	-0.78432811275385
H	(2)	-3.11672043815665	-1.75554588482996	0.86809295738675
H	(2)	-4.24503821750929	-1.77993670030623	-0.49920834357994
C	(2)	-4.16232368327669	0.77123747373408	0.64447825239885
H	(2)	-4.00954856258480	0.46033054870506	1.67926837582719
H	(2)	-4.04506467132493	1.85488266900448	0.59171431967302
H	(2)	-5.18216285693261	0.51634910325039	0.35061746809229
C	(2)	-3.32454160965509	0.54487728416532	-1.71578053837874
H	(2)	-2.56671176869190	0.08533653144558	-2.35449284232163
H	(2)	-4.30826514315361	0.26769246094647	-2.10160305721310
H	(2)	-3.21797813815329	1.62889123403369	-1.78309864645611

Table A27: Cartesian coordinates of 1:1 DTBN p···$HOC(CH_3)_3$ computed at UB3LYP-D3(BJ)/def2-TZVP level of theory.

Atom	Fragment	X	Y	Z
O	(1)	0.01333058138695	0.03474422447572	1.01463699623354
C	(1)	1.58204840212531	-1.33219827167279	-0.08174972377413
C	(1)	3.08976748633624	-1.49503874902610	-0.27787421075831
C	(1)	1.10896856551371	-2.42892962744831	0.88195142742796
C	(1)	0.85650914665206	-1.47926042716126	-1.42852157333683
H	(1)	3.62695474062893	-1.45591292071990	0.66883927103175
H	(1)	3.26195617330969	-2.47895279915435	-0.71563462879121
H	(1)	3.51637349141401	-0.76226994261945	-0.95872293933124
H	(1)	1.41584453506274	-3.39940381180152	0.48959332193341
H	(1)	1.56023672237468	-2.29567318052873	1.86639338355866
H	(1)	0.02865515103362	-2.42784882141231	0.99401599350215
H	(1)	1.03737231378417	-2.48005527608674	-1.82530107180655
H	(1)	-0.21772341330619	-1.35433553026798	-1.30546432211354
H	(1)	1.21764631231541	-0.75738101290892	-2.16018607356698
C	(1)	1.90479083594032	1.31604783981448	0.37731401705917
C	(1)	2.05899904668953	1.67019813299583	-1.10846696844147
C	(1)	1.03573887079415	2.38679892987861	1.04332035137456
C	(1)	3.26648037508605	1.30183435006447	1.08913313033181
H	(1)	1.08626183677050	1.69579313000527	-1.60022223255903
H	(1)	2.50824992063705	2.66143464095301	-1.19260028996265
H	(1)	2.69935160566017	0.97244574303039	-1.64360129120858
H	(1)	0.05836234010576	2.46245548070977	0.57335949346993
H	(1)	0.88459825769821	2.17473676039393	2.10027810225193
H	(1)	1.54734213932119	3.34547867628134	0.94694843466181
H	(1)	3.16099747496996	0.91899877494400	2.10501037465755
H	(1)	4.01432670731410	0.71086534380799	0.56976110740841
H	(1)	3.64158787949573	2.32456431460812	1.15141617756639
N	(1)	1.20033898631217	-0.01013544740140	0.53792231547482
O	(2)	-2.34795709123579	-1.09597294065493	-0.04487217286288
H	(2)	-1.55146018734285	-0.75867281161624	0.40134931344398
C	(2)	-3.17038967508917	0.02194104370515	-0.39817381846649
C	(2)	-2.43164321834285	0.90672160077945	-1.40810519691785
H	(2)	-3.04992220695029	1.75076453072050	-1.72251921688036
H	(2)	-1.51579683117240	1.30149600095166	-0.96389543568871
H	(2)	-2.16327063388953	0.32537802173444	-2.29199399702028
C	(2)	-4.42553690939176	-0.57444517964715	-1.02425986932878
H	(2)	-5.11977325832756	0.21034087017851	-1.33064333581247
H	(2)	-4.16250077351284	-1.16905572802261	-1.90076294668478
H	(2)	-4.92840345057801	-1.22602447478616	-0.30807624700394
C	(2)	-3.51585231100999	0.82305247399523	0.85953989646855
H	(2)	-4.02520417013327	0.18367957753493	1.58233485733546
H	(2)	-2.60637528663952	1.20969119697456	1.32475684538968
H	(2)	-4.16629048181046	1.66864529439948	0.62363275173555

Table A28: Cartesian coordinates of 1:1 TEMPO p···$HOCH_3$ computed at UB3LYP-D3(BJ)/def2-TZVP level of theory.

Atom	Fragment	X	Y	Z
C	(1)	2.63417702252661	-0.53637455452458	0.00335068213640
C	(1)	2.63941524995298	0.80020812981734	-0.72323995183042
C	(1)	1.69579587861952	1.75535067349238	-0.00763318754117
H	(1)	3.31579977586428	-1.24716131627998	-0.46923393690497
H	(1)	2.34713919924590	0.67594217955717	-1.76879194511927
H	(1)	2.05386986853127	1.89956078083835	1.01655892092492
C	(1)	0.24292437242723	1.26179938673632	0.04505467985633
C	(1)	-0.44640171797841	1.41318699152796	-1.32047747326180
H	(1)	-0.52655025034288	2.47394988988299	-1.56480833615659
H	(1)	-1.45240444938479	0.99740555038801	-1.28730383586998
H	(1)	0.11229205137596	0.92617952313286	-2.11835461752705
C	(1)	-0.52243193188837	2.06807056990863	1.09747701426414
H	(1)	-1.58464166456804	1.83739078533594	1.09529474127600
H	(1)	-0.40326486482424	3.13081592592589	0.87935070701300
H	(1)	-0.12346847366705	1.87354813472080	2.09391419143063
C	(1)	1.24806459660804	-1.19105281582991	0.07223451858271
C	(1)	0.85294765527942	-1.80977111487524	-1.27796886750677
H	(1)	-0.17957574128110	-2.15528798239722	-1.23800428142133
H	(1)	1.49802947674712	-2.66397837174012	-1.49053980524766
H	(1)	0.94899674378340	-1.10151328518465	-2.09934640530115
C	(1)	1.25372930394826	-2.27937664100149	1.14767678981752
H	(1)	1.43781113547920	-1.84600546729595	2.13158422028526
H	(1)	2.05007240994173	-2.99269699357371	0.92834944858909
H	(1)	0.30405026944399	-2.80797553794661	1.17759604842677
H	(1)	3.65049105580423	1.21334589129470	-0.73325653590211
H	(1)	2.99806775973527	-0.38060199400246	1.02359357360353
H	(1)	1.69459213235675	2.73878746604695	-0.48234630733765
N	(1)	0.21604342811710	-0.17770549250928	0.45955148889221
O	(1)	-0.91379021226543	-0.65731381170775	0.81691959997269
O	(2)	-3.45023426453146	0.29836622009037	0.11975244457892
H	(2)	-2.58990169595232	-0.02704277510781	0.43898452380280
C	(2)	-4.30753755892246	-0.80988901286854	-0.07378877014037
H	(2)	-3.91562161224167	-1.51177157237403	-0.82067274795168
H	(2)	-4.48574217467319	-1.36169624911689	0.85727511394804
H	(2)	-5.26450277326690	-0.42864311036042	-0.43269170238096

Table A29: Cartesian coordinates of 1:1 TEMPO o···$HOCH_3$ computed at UB3LYP-D3(BJ)/def2-TZVP level of theory.

Atom	Fragment	X	Y	Z
C	(1)	-1.65244393081233	-0.86186207120621	1.25215890579359
C	(1)	-2.34515508078859	0.49291272226027	1.27876206908258
C	(1)	-1.29751251397819	1.58849706020882	1.14443577468403
H	(1)	-0.96577271677916	-0.91997222618797	2.10190491641384
H	(1)	-2.88912380933260	0.61268891543732	2.21833440935602
H	(1)	-1.75447756136057	2.57977219993681	1.18486189978117
C	(1)	-0.48087545662921	1.50113624748008	-0.15165283193423
C	(1)	0.78401238836536	2.35120864482099	-0.01355001442136
H	(1)	1.34402522897513	2.37770459018672	-0.94548524758456
H	(1)	1.43480525440669	1.95406829627272	0.76591640425218
H	(1)	0.49804482406746	3.36996570576816	0.25394555994691
C	(1)	-1.29500815209955	1.98339625342727	-1.36271061134124
H	(1)	-0.73913858644442	1.79235725738937	-2.28020525177323
H	(1)	-1.47054964366299	3.05731994585446	-1.27960751759098
H	(1)	-2.26233297831737	1.48782622843192	-1.43326964117135
C	(1)	-0.85772163083392	-1.12046208247165	-0.03497342249933
C	(1)	0.12070785507213	-2.27425937745490	0.19692244050098
H	(1)	0.86927173927380	-1.99788641189387	0.93979218905508
H	(1)	0.63282135691602	-2.54531894144132	-0.72371143693525
H	(1)	-0.43329077032622	-3.14190546458984	0.55930601090921
C	(1)	-1.78573105322120	-1.46241407131589	-1.21093120310380
H	(1)	-2.25249597162858	-2.43345822734707	-1.03666852245940
H	(1)	-1.20749266107756	-1.51547134751757	-2.13296490193663
H	(1)	-2.57770395609669	-0.72601953222625	-1.34057678231343
H	(1)	-3.08932549290116	0.56566563202452	0.48168149249330
H	(1)	-2.37096719266269	-1.67612183892023	1.36977496036060
H	(1)	-0.61046276188341	1.52186378573738	1.99323550188119
N	(1)	-0.05315184418359	0.08825813516639	-0.39238946096369
O	(1)	0.86471227074692	-0.08329687871178	-1.26624218804476
O	(1)	3.07938023259275	-0.33745365871799	0.47444746058024
H	(1)	2.42113963362840	-0.23086849129969	-0.23280130430193
C	(1)	3.96542074895435	-1.37847207006700	0.11143598927542
H	(1)	4.50564605444922	-1.15742127846793	-0.81700093233547
H	(1)	4.69605645210596	-1.48360212671264	0.91451384816839
H	(1)	3.44821972546582	-2.33874552385343	-0.01007856182409

Table A30: Cartesian coordinates of 1:1 TEMPO p···$HOC(CH_3)_3$ computed at UB3LYP-D3(BJ)/def2-TZVP level of theory.

Atom	Fragment	X	Y	Z
C	(1)	2.55394716973031	0.81002868435446	-1.27662339113347
C	(1)	3.51045233592148	-0.30242633769390	-0.87260362192540
C	(1)	2.71072913419454	-1.56133608421356	-0.57080314311702
H	(1)	3.09431684722054	1.72882576885446	-1.51535742690907
H	(1)	4.10800302312373	-0.00602144851305	-0.00707380484661
H	(1)	2.17695684879012	-1.86382682079334	-1.47721249869476
C	(1)	1.69085564252694	-1.38521432733957	0.56331821197542
C	(1)	2.38418984337387	-1.34368111489161	1.93483371509137
H	(1)	1.66244609590013	-1.13231544271424	2.72250020403502
H	(1)	3.17550565964076	-0.59665132871480	1.97140304633284
H	(1)	2.83168142135219	-2.31827631857792	2.13791109213039
C	(1)	0.69489683727243	-2.54718466940524	0.52886433501928
H	(1)	0.02163364596923	-2.53174882995544	1.38219779065470
H	(1)	1.25098528790138	-3.48602963015775	0.54852909163834
H	(1)	0.10109910141212	-2.51660549714708	-0.38557319149011
C	(1)	1.51135086897616	1.14397773025400	-0.20131365678382
C	(1)	2.13033134438729	1.95305189805521	0.94924747038986
H	(1)	3.02768741491311	1.48370072199850	1.34881108473032
H	(1)	1.40841443538641	2.06058584416340	1.75806030734271
H	(1)	2.40039625808122	2.94779813183144	0.59064780312834
C	(1)	0.37265226257127	1.94853871737980	-0.83142112116976
H	(1)	0.78865518389579	2.83432457212440	-1.31441600362532
H	(1)	-0.35035323526362	2.26156987759528	-0.08212514354911
H	(1)	-0.14725868782282	1.35471642002288	-1.58423538813658
H	(1)	4.21742306316079	-0.49584664808866	-1.68244696771030
H	(1)	2.02943158047597	0.50641899462004	-2.18784960459377
H	(1)	3.36805138459433	-2.39040760593269	-0.30036681276187
N	(1)	0.92318566731775	-0.11654031980932	0.35175931114913
O	(1)	-0.15369720120709	0.02782665622452	1.02519899101249
C	(2)	-2.80400542607372	0.12579476888118	3.59350999479972
C	(2)	-1.46723946193875	-0.17351556109332	4.27693100166396
H	(2)	-3.38700558604320	-0.79118383612184	3.49359537815793
H	(2)	-3.38854563675860	0.84949341305061	4.16653813249319
H	(2)	-2.63585314015086	0.53630745748125	2.59535009408615
C	(2)	-1.68736369043557	-0.80386200602044	5.64698305821012
C	(2)	-0.62990333301711	1.10368336350581	4.39494510080172
H	(2)	-2.23788867202891	-0.12752483593178	6.30358192252867
H	(2)	-2.25381830609139	-1.73096414801996	5.54615097808649
H	(2)	-0.72841911776720	-1.03821136637213	6.11226213452159
H	(2)	0.33489483127849	0.87841436321831	4.85300292120580
H	(2)	-0.45123706597075	1.52953002504064	3.40531398535491
H	(2)	-1.13673058535655	1.85556532690905	5.00441523958111
O	(2)	-0.74792852875838	-1.14880620759088	3.51339086732653
H	(2)	-0.60077314668390	-0.78748903446673	2.62087760499861

Table A31: Cartesian coordinates of 1:1 TEMPO o···HOC(CH_3)$_3$ computed at UB3LYP-D3(BJ)/def2-TZVP level of theory.

Atom	Fragment	X	Y	Z
C	(1)	2.66964172499097	0.70700222015519	-1.34860179362496
C	(1)	3.43159414706997	-0.54603171565215	-0.94198211994994
C	(1)	2.43581651972781	-1.64410394000685	-0.59727769463452
H	(1)	3.35307523526644	1.51246332954241	-1.62662696983565
H	(1)	4.09338042689371	-0.34236404478733	-0.09628130358893
H	(1)	1.83613691474405	-1.86527073513441	-1.48521976534797
C	(1)	1.48763591164796	-1.27358110268504	0.55101605950477
C	(1)	2.19789075721168	-1.34230861700015	1.91204672785263
H	(1)	1.54223810465099	-0.95178264070404	2.68983638772374
H	(1)	3.12707497392876	-0.77416337659534	1.92412806129439
H	(1)	2.43453225767664	-2.38159707933770	2.14653088085633
C	(1)	0.29171213366230	-2.22841619199647	0.55122532321537
H	(1)	-0.35103621338649	-2.05500398669819	1.41129295579506
H	(1)	0.66000624983665	-3.25514938543056	0.58933681712819
H	(1)	-0.30619802526634	-2.10188037675293	-0.35147885989260
C	(1)	1.73652335874886	1.24037742880659	-0.25338949845388
C	(1)	2.52338907568114	1.95162296626282	0.85884614726120
H	(1)	3.33484357843096	1.33820723648129	1.24790825881691
H	(1)	1.85367389583676	2.20369010589747	1.68059855157632
H	(1)	2.95494644937570	2.87408458386992	0.46659977095932
C	(1)	0.73147158722392	2.21497713360659	-0.87141415304628
H	(1)	1.27805093007424	2.99457214206315	-1.40503433223198
H	(1)	0.11351620664856	2.68067997500054	-0.10706171261980
H	(1)	0.07491465402344	1.70188655806199	-1.57428294432622
H	(1)	4.07404140685035	-0.87219569427259	-1.76291200478598
H	(1)	2.07042705918039	0.48029767558286	-2.23544340617744
H	(1)	2.94737404150692	-2.56934530044521	-0.32274072496433
N	(1)	0.96176806752952	0.11226407182163	0.35087485729038
O	(1)	-0.05214926159804	0.43910764033767	1.05902407876373
C	(2)	-3.56667597961586	1.66553466265405	0.14884851547244
C	(2)	-3.41441251616547	0.22320004270536	-0.34178315127621
H	(2)	-3.38547189961334	2.36140019174428	-0.67204661087034
H	(2)	-4.56899337442949	1.84648204704253	0.54407066630138
H	(2)	-2.84468392662778	1.87447163133234	0.94155588646441
C	(2)	-4.37623804321457	-0.06407612262756	-1.48830910986872
C	(2)	-3.63129901745906	-0.76067788901703	0.81121513967777
H	(2)	-5.41240440310487	0.05319746706123	-1.16557688642236
H	(2)	-4.18931221799461	0.62102942452420	-2.31686142157391
H	(2)	-4.23693987683293	-1.08425026900080	-1.84981798347363
H	(2)	-3.49561029771409	-1.78512006265574	0.46035768382069
H	(2)	-2.91005720448428	-0.57308873345509	1.60978269786599
H	(2)	-4.63614355731433	-0.66591819105114	1.22933395688211
O	(2)	-2.10044576538304	0.04092943548932	-0.88309895813327
H	(2)	-1.46037408821404	0.20943748526291	-0.17073801942423

Table A32: Cartesian coordinates of 1:1 TEMPO p···HOC_6H_5 computed at UB3LYP-D3(BJ)/def2-TZVP level of theory.

Atom	Fragment	X	Y	Z
C	(1)	3.46154890714554	1.38399686121575	0.23241679060532
C	(1)	3.66468311450320	0.42873706483711	-0.93380348612965
C	(1)	3.22469431343684	-0.96537682462016	-0.51299592421986
H	(1)	4.08818178453849	1.05532786192038	1.06716198433181
H	(1)	4.71772751015481	0.41470924052284	-1.22312781149926
H	(1)	3.38104513662040	-1.68805871610318	-1.31655827825415
C	(1)	1.74949200242294	-1.04851547247245	-0.09476177095461
C	(1)	1.52141715913828	-2.35546365561711	0.66907864483384
H	(1)	1.90057031712055	-3.18190410982936	0.06545846726251
H	(1)	0.46805588840261	-2.53584391751186	0.86624293623000
H	(1)	2.06068315393605	-2.34591176560903	1.61707538147729
C	(1)	0.82248405757683	-0.99658293374104	-1.31905980323258
H	(1)	1.03619261724247	-0.14377088617588	-1.96140678090905
H	(1)	-0.22029041728511	-0.94357035839002	-1.01321752432952
H	(1)	0.95676016503989	-1.90474957871151	-1.90894139368571
C	(1)	2.00675200725940	1.46438442674540	0.71378646149431
C	(1)	1.96707577783318	2.09731880663985	2.10601811026759
H	(1)	0.94442589086138	2.22898561925400	2.45086085836055
H	(1)	2.45601128888136	3.07212965964022	2.06684635957653
H	(1)	2.49634682962095	1.47307474947593	2.82701196251031
C	(1)	1.14432132145871	2.29418258747069	-0.24993545334047
H	(1)	1.21154140917540	1.93881137215051	-1.27670827668168
H	(1)	1.47417504216405	3.33411063012008	-0.22841940188697
H	(1)	0.10051682402400	2.25783952693514	0.05872726632150
H	(1)	3.10858474395082	0.76309424359532	-1.81290147202880
H	(1)	3.78396995798543	2.39572986914369	-0.02313004739985
H	(1)	3.84483457350478	-1.28974169316509	0.32837195143164
N	(1)	1.42278362099325	0.08911640880499	0.82370478178796
O	(1)	0.32875227830788	0.01314127186080	1.48218686805085
O	(2)	-1.84713565689355	-1.63949269464435	1.12451821981432
H	(2)	-1.09404583771603	-1.04048824345449	1.30970911156966
C	(2)	-2.75276496721189	-1.02917300007474	0.32156681239225
C	(2)	-3.81750727112876	-1.79079778415782	-0.16189392239587
C	(2)	-2.65255258796697	0.31820247787189	-0.03258898364884
C	(2)	-4.76526131849410	-1.20853813736724	-0.99090162122779
H	(2)	-3.88356193040243	-2.83283973710025	0.12283802694458
C	(2)	-3.60732690294106	0.88820122114217	-0.86613354743532
H	(2)	-1.83305186074720	0.90803538411937	0.35727985689003
C	(2)	-4.66769269845230	0.13252608815636	-1.35227135720368
H	(2)	-5.58812017840053	-1.80895863173739	-1.35928545524941
H	(2)	-3.52047439506539	1.93454599639471	-1.13316386757928
H	(2)	-5.40976167059428	0.58128677246576	-1.99938467286046

Table A33: Cartesian coordinates of 1:1 TEMPO o···HOC_6H_5 computed at UB3LYP-D3(BJ)/def2-TZVP level of theory.

Atom	Fragment	X	Y	Z
C	(1)	3.28710299310683	0.95777477307372	0.95286718250212
C	(1)	3.72083457225580	-0.49018804093411	1.12763574550463
C	(1)	2.48392145018975	-1.36321713083445	1.27915051147688
H	(1)	2.73816465399053	1.26931724007965	1.84662858628020
H	(1)	4.35177814718835	-0.58393835558068	2.01414982849107
H	(1)	2.75479589551516	-2.41006439975299	1.43240729439091
C	(1)	1.53314586315855	-1.29857152174830	0.07617773520466
C	(1)	0.16223759319123	-1.84271008434305	0.48309378230808
H	(1)	-0.29849306127346	-1.20518073242383	1.23792158030646
H	(1)	0.28814444585756	-2.84248142969955	0.90177512800361
H	(1)	-0.51167979799172	-1.90447627769953	-0.36747048623357
C	(1)	2.07608401727367	-2.10433733911340	-1.11394801306810
H	(1)	1.44447451668436	-1.94414564249660	-1.98712213262660
H	(1)	2.06632268116210	-3.16732308710784	-0.86772017139592
H	(1)	3.09750995713039	-1.82522399982547	-1.36892490622462
C	(1)	2.39570869028500	1.18722375689552	-0.27471661781152
C	(1)	1.67951200535270	2.53283695178869	-0.14077903164226
H	(1)	0.99854048465456	2.52634515657619	0.71090984715581
H	(1)	1.10762466527580	2.76720248491340	-1.03569642997866
H	(1)	2.42352440969201	3.31579822376928	0.01466432333634
C	(1)	3.21431210001471	1.16709099825671	-1.57508376525193
H	(1)	3.87202970385179	2.03735366818452	-1.60377157476656
H	(1)	2.54464446017013	1.20896903716003	-2.43341882999849
H	(1)	3.83187980307223	0.27390738073385	-1.65973519914666
H	(1)	4.32903898261967	-0.81960862834702	0.28153260341866
H	(1)	4.14983200699057	1.62179893923822	0.86564848445340
H	(1)	1.93779131501732	-1.04498218007606	2.17222367318302
N	(1)	1.34758029573348	0.12227443585712	-0.35435426289306
O	(1)	0.38431566295579	0.34245658514278	-1.16739298209195
O	(2)	-1.65670825335374	1.29778427660413	0.40347625662245
H	(2)	-0.99675650429008	1.01644984446162	-0.26220576596040
C	(2)	-2.82486500790709	0.63531490203343	0.21030604621721
C	(2)	-3.02054183349998	-0.23709707951646	-0.86231570931525
C	(2)	-3.85602758519501	0.84629320117520	1.12585343115520
C	(2)	-4.23775834892589	-0.89105778276590	-1.00772920738331
H	(2)	-2.21810199744059	-0.39405586677111	-1.57234982218798
C	(2)	-5.06715501811880	0.18781811129805	0.96768327167236
H	(2)	-3.68975476352452	1.52719881865403	1.95055879724379
C	(2)	-5.26807711590472	-0.68576629254544	-0.09718403785194
H	(2)	-4.38012056999096	-1.56548835479976	-1.84344084428881
H	(2)	-5.86175090427392	0.35919562412121	1.68365074710892
H	(2)	-6.21452061069956	-1.19663018363585	-0.21600506591821

4.3 Structures[31]

UB3LYP/def2-TZVP structures of DTBN and TEMPO 1:2 complexes are shown in Figures A3, A4 and A5, with their relative energies (in kJ mol^{-1}).

For DTBN, the asymmetry of the NO moiety leads to two isomers of similar energy, which are mirror-images of the monomer. For TEMPO, there is no asymmetry and only one enantiomeric complexes is observed.

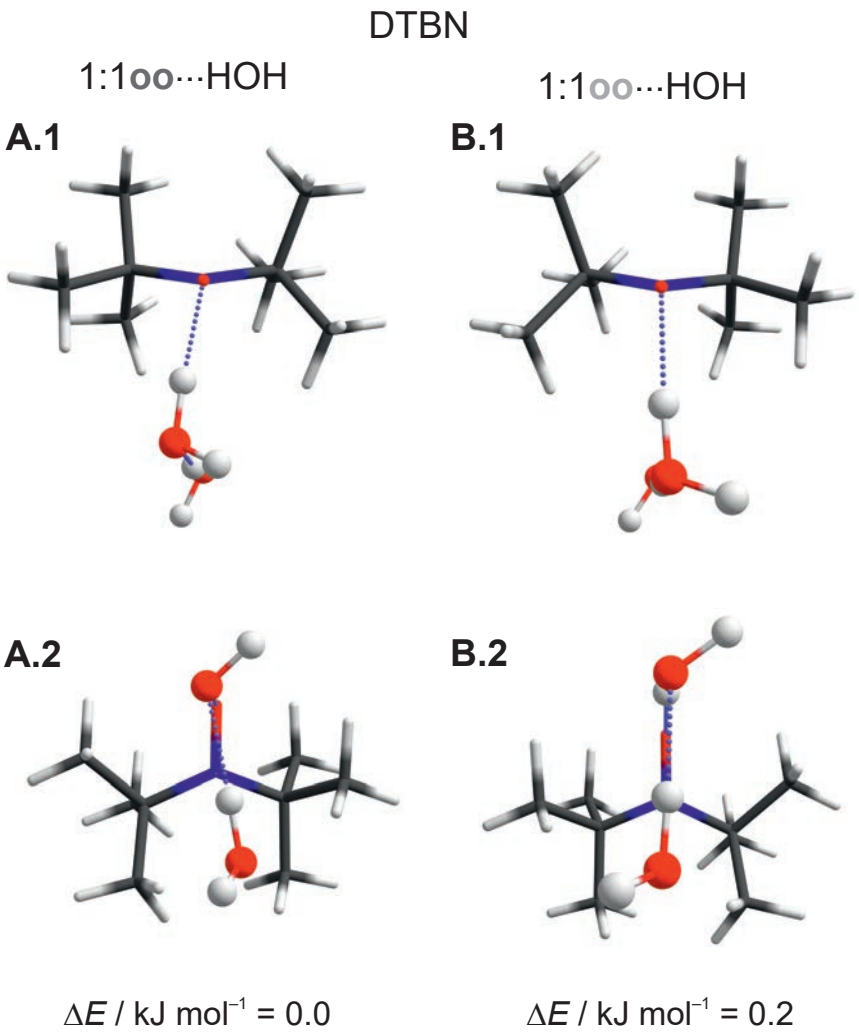

Figure A3: Structure of DTBN 1:2 water complexes (A and B) observed from two different perspectives on the top (A.1 and B.1) and on the bottom (A.2 and B.2) of the figure.[31]

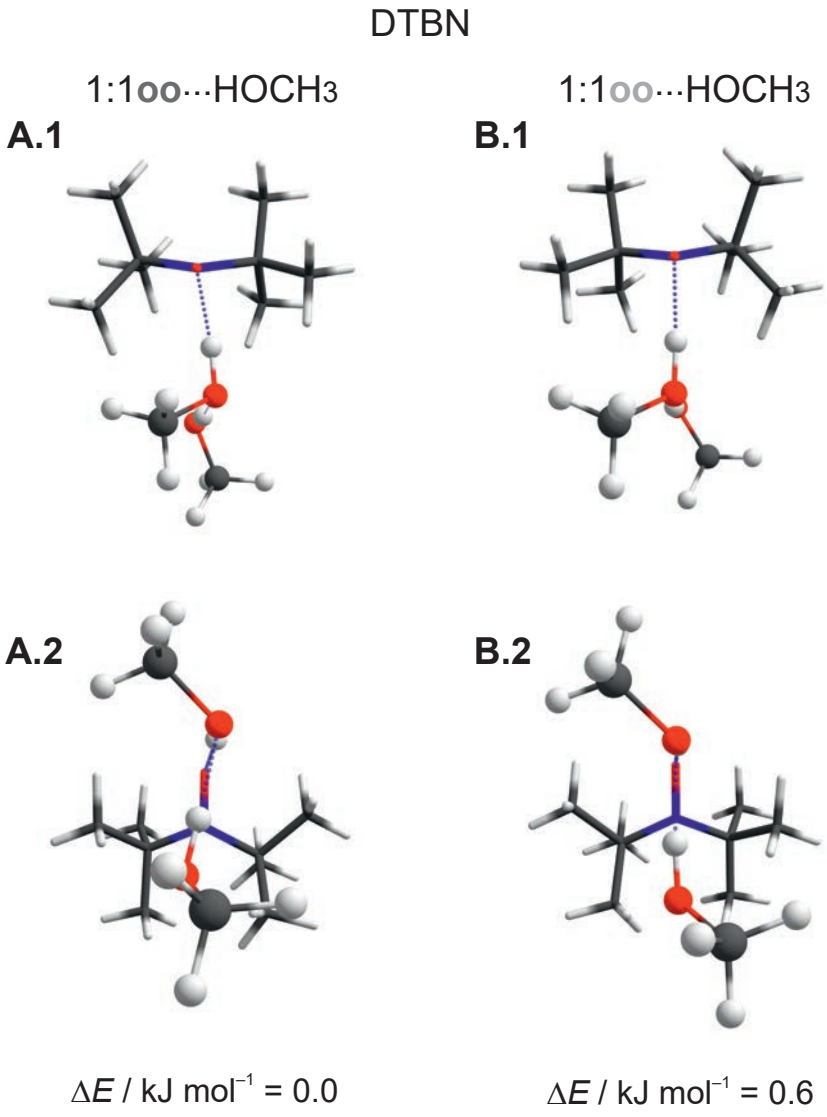

Figure A4: Structure of DTBN 1:2 methanol complexes (A and B) observed from two different perspectives on the top (A.1 and B.1) and on the bottom (A.2 and B.2) of the figure.[31]

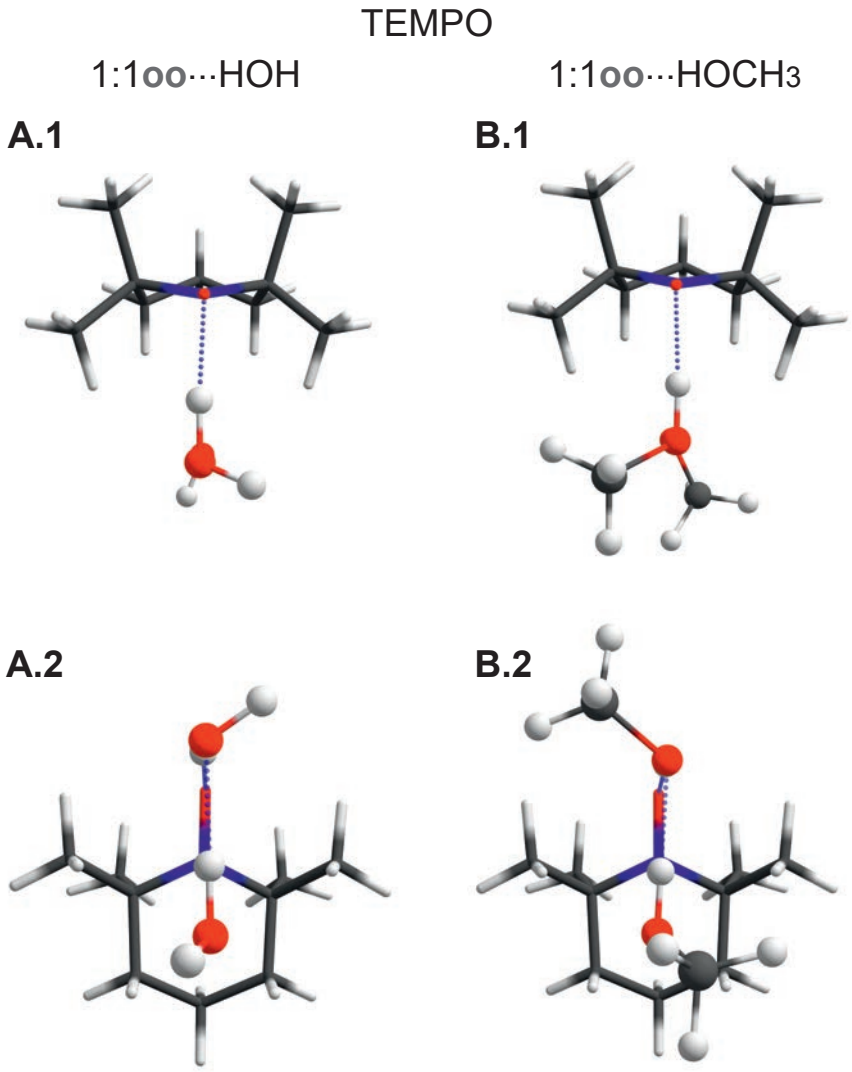

Figure A5: Structure of TEMPO 1:2 water and methanol complexes (A and B) observed from two perspectives on the top (A.1 and B.1) and on the bottom (A.2 and B.2) of the figure.[31]

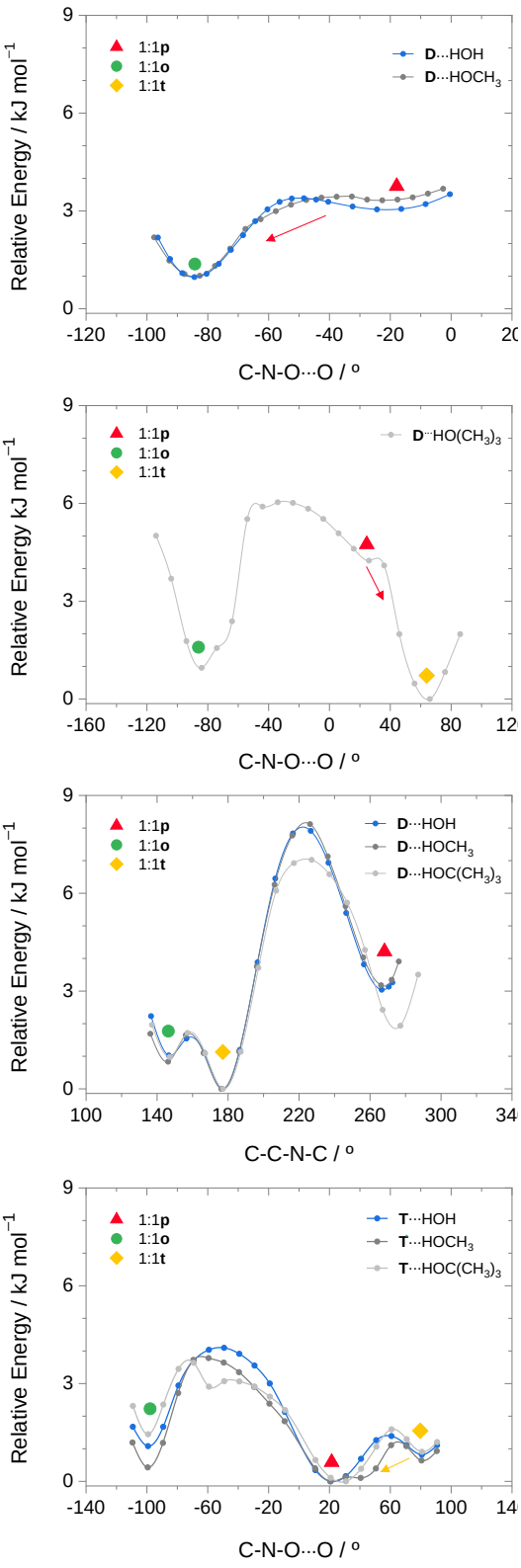

Figure A6: Relaxation barriers between the different isomers of monosolvates of DTBN and TEMPO, revealing that relaxation from p to o/t (red arrows) for DTBN and also from t to p for TEMPO (yellow arrow). For color definitions, see the section 4 of this Thesis.[31]

4.4 Solvation energies

Absolute and relative computed energies are shown in Table A34 for checking purposes for the unrestricted open-shell B3LYP calculations.

Table A34: Electronic energies E_{el} (in E_h), zero-point vibrational energies (in E_h), and relative zero-point corrected relative energies ΔE_0 (in kJ mol^{-1}, conversion factor 2625.49963948 kJ mol^{-1}/E_h) of the DTBN and TEMPO 1:1 and 1:2 complexes obtained at unrestricted open-shell B3LYP-D3(BJ,ABC)/def2-TZVP and DLPNO-CCSDT/aug-cc-pVTZ levels at the B3LYP-D3(BJ,ABC)/def2-TZVP-optimized structures

	E_{el}^{UB3LYP} (E_h)	ZPVE (E_h)	ΔE_0^{UB3LYP} (kJ mol^{-1})	E_{el}^{DLPNO} (E_h)	ΔE_0^{DLPNO} (kJ mol^{-1})
DTBN					
t···HOH	-521.96286462	0.27668926	0.0	-521.21769281	0.0
o···HOH	-521.96251528	0.27661049	0.7	-521.21748477	0.3
p···HOH	-521.96178146	0.27665978	2.8	-521.21690572	2.0
oo···HOH	-598.40683952	0.30182280	0.0	-597.57508481	0.0
oo···HOH	-598.40668750	0.30174471	0.2	-597.57463966	1.0
t···HOCH$_3$	-561.24950408	0.30564064	0.0	-560.43854376	0.0
o···HOCH$_3$	-561.24916050	0.30558674	0.8	-560.43828409	0.7
p···HOCH$_3$	-561.24834478	0.30555387	2.8	-560.43746986	2.7
oo···HOCH$_3$	-676.98087451	0.35931741	0.0	-676.0181413	0.0
oo···HOCH$_3$	-676.98044578	0.35912118	0.6	-676.0177608	0.5
t···HOC(CH$_3$)$_3$	-679.17608407	0.38946091	0.0	-678.1838391	0.0
o···HOC(CH$_3$)$_3$	-679.17572965	0.38934704	0.6	-678.1833769	0.9
p···HOC(CH$_3$)$_3$	-679.17531484	0.38952238	2.2	-678.1829846	2.4
TEMPO					
t···HOH	-560.07574018	0.28533849	0.0	-559.2703389	0.5
o···HOH	-560.07558957	0.28532752	0.4	-559.2704849	0.1
p···HOH	-560.07594089	0.28554610	0.0	-559.2707348	0.0
t···HOCH$_3$	-599.36238799	0.31424650	0.0	-598.4908260	0.7
o···HOCH$_3$	-599.36242930	0.31443855	0.4	-598.4912241	0.1
p···HOCH$_3$	-599.36258800	0.31447788	0.1	-598.4913199	0.0
t···HOC(CH$_3$)$_3$	-717.28907136	0.39819014	0.4	-716.2362657	0.7
o···HOC(CH$_3$)$_3$	-717.28890734	0.39815167	0.7	-716.2362761	0.5
p···HOC(CH$_3$)$_3$	-717.28942010	0.39839686	0.0	-716.2367251	0.0
p'···HOC$_6$H$_5$	-791.08351286	0.36760684	0.9	-789.8887915	1.4
o···HOC$_6$H$_5$	-791.08325220	0.36743067	1.2	-789.8885185	1.7
p···HOC$_6$H$_5$	-791.08388021	0.36761840	0.0	-789.8893473	0.0

4.5 Fragment energies

Table A35: Electronic energies E_{el} (in E_{h}) along with zero-point vibrational energies (in E_{h}) of DTBN, TEMPO, water, methanol, t-butanol and phenol monomers and selected dimers and trimers obtained at closed- and unrestricted open-shell B3LYP-D3(BJ,ABC)/def2-TZVP.

	$E_{\mathrm{el}}^{\mathrm{B3LYP/TZVP}}$ (E_{h})	ZPVE (E_{h})
H_2O monomer	-76.42649306	0.02115550
H_2O dimer	-152.86285904	0.04573284
H_2O trimer	-229.31062345	0.07271290
$HOCH_3$ monomer	-115.71252120	0.05099693
$HOCH_3$ dimer	-231.43594570	0.10426402
$HOCH_3$ trimer	-347.17004218	0.15883233
$HOC(CH_3)_3$ monomer	-233.63844773	0.13502409
$HOC(CH_3)_3$ dimer	-467.29008951	0.27221408
HOC_6H_5 monomer	-307.42934517	0.10422733
HOC_6H_5 dimer	-614.87094233	0.21017281
DTBN monomer	-445.52258443	0.25255897
TEMPO monomer	-483.63642104	0.26144033

4.6 Dissociation Energies

Table A36: Dissociation energies of DTBN and TEMPO solvates (in kJ mol^{-1}), determined by the difference between the electronic energies of the solvates E^{AB} (in kJ mol^{-1}) and the sum of the electronic energies of the 1:0 and 0:1 monomers $E^{A} + E^{B}$ (in kJ mol^{-1}) obtained at closed- and unrestricted open-shell B3LYP-D3(BJ,ABC)/def2-TZVP. The corresponding ZPVE-corrected results are also shown.

DTBN	$E_{el}^{A} + E_{el}^{B}$	$E_{0}^{A} + E_{0}^{B}$	E_{el}^{AB}	E_{0}^{AB}	ΔE_{el}	ΔE_{0}
t···H_2O	-1370377.115	-1369658.478	-1370413.313	-1369686.865	36.2	28.4
o···H_2O	-1370377.115	-1369658.478	-1370412.396	-1369686.155	35.3	27.7
p···H_2O	-1370377.115	-1369658.478	-1370410.469	-1369684.099	33.4	25.6
t···$HOCH_3$	-1473522.567	-1472725.582	-1473560.371	-1472757.911	37.8	32.3
o···$HOCH_3$	-1473522.567	-1472725.582	-1473559.469	-1472757.151	36.9	31.6
p···$HOCH_3$	-1473522.567	-1472725.582	-1473557.327	-1472755.095	34.8	29.5
t···$HOC(CH_3)_3$	-1783137.045	-1782119.446	-1783176.564	-1782154.034	39.5	34.6
o···$HOC(CH_3)_3$	-1783137.045	-1782119.446	-1783175.633	-1782153.403	38.6	34.0
p···$HOC(CH_3)_3$	-1783137.045	-1782119.446	-1783174.544	-1782151.853	37.5	32.4
TEMPO						
t···H_2O	-1470444.979	-1469703.024	-1470478.654	-1469729.498	33.7	26.5
o···H_2O	-1470444.979	-1469703.024	-1470478.258	-1469729.131	33.3	26.1
p···H_2O	-1470444.979	-1469703.024	-1470479.181	-1469729.480	34.2	26.5
t···$HOCH_3$	-1573590.432	-1572770.128	-1573625.734	-1572800.680	35.3	30.6
o···$HOCH_3$	-1573590.432	-1572770.128	-1573625.842	-1572800.284	35.4	30.2
p···$HOCH_3$	-1573590.432	-1572770.128	-1573626.259	-1572800.597	35.8	30.5
t···$HOC(CH_3)_3$	-1883204.909	-1882163.992	-1883242.198	-1882196.750	37.3	32.8
o···$HOC(CH_3)_3$	-1883204.909	-1882163.992	-1883241.768	-1882196.421	36.9	32.4
p···$HOC(CH_3)_3$	-1883204.909	-1882163.992	-1883243.114	-1882197.123	38.2	33.1
p···HOC_6H_5	-2076942.884	-2075982.824	-2076990.442	-2076025.260	47.6	42.4
p'···HOC_6H_5	-2076942.884	-2075982.824	-2076989.478	-2076024.326	46.6	41.5
o···HOC_6H_5	-2076942.884	-2075982.824	-2076988.793	-2076024.104	45.9	41.3

4.7 LED analysis

To determine how intermolecular interactions contribute to the different torsional potentials of water around the N-O moiety in DTBN complexes, a local energy decomposition LED-analysis with DLPNO-CCSD(T)/aug-cc-pVTZ method[25] of London dispersion contributions was performed for the DFT-optimized 1:1 structures (Tables A37, A38, A39). The relative energy results are summarized in Table A40, relative to the most stable structure of each solvate, with and without DFT ZPVE corrections. The results indicate that the relative ZPVE correction is larger for TEMPO solvates, often reaching the same order of magnitude as the relative London dispersion contributions. Therefore, the trends are not discussed in detail, although it is noticeable that for complexes with phenol the London dispersion appears to switch between two p-type structures. For DTBN complexes, the ZPVE corrections are

less conformer dependent and for water and methanol, London dispersion favours t structures over p structures. The p structure is always less stable than t, for the bulky tBuOH solvates, but surprisingly more so without London dispersion. No systematic trends spanning all solvent molecules can be pointed out.

Table A37: Selected results (in E_h) of the LED analysis performed at the stationary points of the 1:1 DTBN complexes at unrestricted open-shell DLPNO-CCSD(T)/aug-cc-pVTZ//UB3LYP-D3(BJ,ABC)/def2-TZVP level.

DTBN	t···HOH	p···HOH	o···HOH
Intrafragment REF. energy:			
Intra fragment 1 (REF.)	-442.7573065	-442.7703945	-442.762830
Intra fragment 2 (REF.)	-76.03750343	-76.03289252	-76.03895266
Interaction of fragments 2 and 1:			
Electrostatics (REF.)	-0.062534701	-0.057779186	-0.05739387
Exchange (REF.)	-0.014267003	-0.011123090	-0.012551217
Dispersion (strong pairs)	-0.005604805	-0.004861762	-0.005659446
Dispersion (weak pairs)	-0.000545353	-0.000462412	-0.000508010
Sum of non dispersive correlation terms:			
Non dispersion (strong pairs)	-2.244406263	-2.244074384	-2.244117794
Non dispersion (weak pairs)	-0.004765617	-0.004774328	-0.004785124
DTBN	t···$HOCH_3$	p···$HOCH_3$	o···$HOCH_3$
Intrafragment REF. energy:			
Intra fragment 1 (REF.)	-442.7533988	-442.7675394	-442.7601312
Intra fragment 2 (REF.	-115.0675475	-115.0626008	-115.0690439
Interaction of fragments 2 and 1:			
Electrostatics (REF.)	-0.066235627	-0.06145750	-0.060183104
Exchange (REF.)	-0.015689296	-0.012051509	-0.01361650
Dispersion (strong pairs)	-0.006578470	-0.005287371	-0.006549331
Dispersion (weak pairs)	-0.000868431	-0.000758636	-0.000818655
Sum of non dispersive correlation terms:			
Non dispersion (strong pairs)	-2.425417711	-2.425236011	-2.425182645
Non dispersion (weak pairs)	-0.004952238	-0.004953941	-0.004986028
DTBN	t···$HOC(CH_3)_3$	p···$HOC(CH_3)_3$	o···$HOC(CH_3)_3$
Intrafragment REF. energy:			
Intra fragment 1 (REF.)	-442.7528284	-442.7631036	-442.7604928
Intra fragment 2 (REF.)	-232.2207066	-232.2158289	-232.2230918
Interaction of fragments 2 and 1:			
Electrostatics (REF.)	-0.068353742	-0.063892714	-0.060854324
Exchange (REF.)	-0.016522026	-0.014707930	-0.014132134
Dispersion (strong pairs)	-0.007835535	-0.008223963	-0.007582220
Dispersion (weak pairs)	-0.001630381	-0.001642262	-0.001572660
Sum of non dispersive correlation terms:			
Non dispersion (strong pairs)	-2.988801968	-2.988459727	-2.988595161
Non dispersion (weak pairs)	-0.005830899	-0.005834088	-0.005836789

Table A38: Selected results (in E_h) of the LED analysis carried out at the stationary points of the 1:1 TEMPO solvates at DLPNO-CCSD(T)/aug-cc-pVTZ level

TEMPO	t···HOH	p···HOH	o···HOH
Intrafragment REF. energy:			
Intra fragment 1 (REF.)	-480.6546869	-480.6657798	-480.6633423
Intra fragment 2 (REF.	-76.03852119	-76.03232582	-76.04081553
Interaction of fragments 2 and 1:			
Electrostatics (REF.)	-0.061153338	-0.059475289	-0.052839170
Exchange (REF.)	-0.014098292	-0.011568815	-0.011696286
Dispersion (strong pairs)	-0.004869395	-0.004779702	-0.004953241
Dispersion (weak pairs)	-0.000562829	-0.00047226	-0.000533904
Sum of non dispersive correlation terms:			
Non dispersion (strong pairs)	-2.392591648	-2.392486622	-2.392416424
Non dispersion (weak pairs)	-0.005207015	-0.005261219	-0.005284910
TEMPO	t···$HOCH_3$	p···$HOCH_3$	o···$HOCH_3$
Intrafragment REF. energy:			
Intra fragment 1 (REF.)	-480.6502307	-480.6633663	-480.6602110
Intra fragment 2 (REF.	-115.068248	-115.0623423	-115.0708819
Interaction of fragments 2 and 1:			
Electrostatics (REF.)	-0.065761478	-0.062525035	-0.055972490
Exchange (REF.)	-0.015620611	-0.012352595	-0.012971215
Dispersion (strong pairs)	-0.005582021	-0.005518503	-0.006004878
Dispersion (weak pairs)	-0.000894144	-0.000800089	-0.000862026
Sum of non dispersive correlation terms:			
Non dispersion (strong pairs)	-2.573527319	-2.573427182	-2.573311708
Non dispersion (weak pairs)	-0.005387701	-0.005439193	-0.005479905
TEMPO	t···$HOC(CH_3)_3$	p···$HOC(CH_3)_3$	o···$HOC(CH_3)_3$
Intrafragment REF. energy:			
Intra fragment 1 (REF.)	-480.6497781	-480.6608265	-480.6605541
Intra fragment 2 (REF.	-232.2212308	-232.2152479	-232.2246057
Interaction of fragments 2 and 1:			
Electrostatics (REF.)	-0.067506215	-0.065446805	-0.057196065
Exchange (REF.)	-0.016619790	-0.014053707	-0.013440133
Dispersion (strong pairs)	-0.007413012	-0.007471197	-0.006929736
Dispersion (weak pairs)	-0.001573479	-0.001563031	-0.001551763
Sum of non dispersive correlation terms:			
Non dispersion (strong pairs)	-3.136619020	-3.136575602	-3.13653382
Non dispersion (weak pairs)	-0.006279348	-0.006328804	-0.006354168

Table A39: Selected results (in E_h) of the LED analysis carried out at the stationary points of the 1:1 TEMPO solvates at DLPNO-CCSD(T)/aug-cc-pVTZ level

TEMPO	t···HOC_6H_5	p···HOC_6H_5	o···HOC_6H_5
Intrafragment REF. energy:			
Intra fragment 1 (REF.)	-480.6550902	-480.6528033	-480.6461734
Intra fragment 2 (REF.)	-305.6345063	-305.6322632	-305.6424592
Interaction of fragments 2 and 1:			
Electrostatics (REF.)	-0.078625582	-0.08038416	-0.077489731
Exchange (REF.)	-0.014842611	-0.01620787	-0.016720264
Dispersion (strong pairs)	-0.007489209	-0.008828952	-0.007630852
Dispersion (weak pairs)	-0.001446703	-0.001573852	-0.001555936
Sum of non dispersive correlation terms:			
Non dispersion (strong pairs)	-3.339684621	-3.339961566	-3.339423483
Non dispersion (weak pairs)	-0.006856432	-0.006823132	-0.006816266

Table A40: Relative electronic energies (ΔE in kJ mol^{-1}) for different 1:1 complex conformations and relative electronic energies without London Dispersion (LD) terms (strong and weak-pairs) obtained from a LED analysis. The calculations were carried out at DLPNO-CCSD(T)/aug-cc-pVTZ//UB3LYP/def2-TZVP level. For comparison, the effect of DFT ZPVE correction on the relative DLPNO-CCSD(T) energies is also given as ΔE_0.

DTBN + H_2O	1:1 t	1:1 p	1:1 o
ΔE	0.0	2.1	0.5
ΔE_0	0.0	2.0	0.3
ΔE (without LD term)	0.1	0.0	0.7
DTBN + $HOCH_3$			
ΔE	0.0	2.8	0.7
ΔE_0	0.0	2.7	0.7
ΔE (without LD term)	0.9	0.0	1.3
DTBN + $HOC(CH_3)_3$			
ΔE	0.0	2.2	1.2
ΔE_0	0.0	2.4	0.9
ΔE (without LD term)	0.0	3.3	0.4
TEMPO + H_2O	1:1 t	1:1 p	1:1 o
ΔE	1.0	0.0	0.7
ΔE_0	0.5	0.0	0.1
ΔE (without LD term)	1.5	0.0	1.3
TEMPO + $HOCH_3$			
ΔE	1.3	0.0	0.3
ΔE_0	0.7	0.0	0.1
ΔE (without LD term)	1.7	0.0	1.7
TEMPO + $HOC(CH_3)_3$			
ΔE	1.2	0.0	1.2
ΔE_0	0.7	0.0	0.5
ΔE (without LD term)	1.4	0.3	0.0
TEMPO + HOC_6H_5	1:1 p'	1:1 p	1:1 o
ΔE	1.5	0.0	2.2
ΔE_0	1.4	0.0	1.7
ΔE (without LD term)	0.0	2.4	1.4

Table A41: Computed wavenumbers of DTBN and TEMPO complexes (in cm^{-1}) with unrestricted open-shell B3LYP-D3(BJ,ABC), B2PLYP-D3 and TPSS-D3(BJ) functionals with both def2-TZVP and QZ basis sets.

Structure	B3LYP def2-QZVP $\tilde{\nu}$	B2PLYP def2-TZVP $\tilde{\nu}$	TPSS def2-TZVP $\tilde{\nu}$	TPSS def2-QZVP $\tilde{\nu}$
DTBN + H_2O				
t···HOH	3592	3614	3426	3435
o···HOH	3610	3640	3454	3457
p···HOH	3608	3634	3449	3454
DTBN + $HOCH_3$				
t···HOCH_3	3594	3608	3415	3424
o···HOCH_3	3617	3638	3443	3452
p···HOCH_3	3613	3629	3445	3457
DTBN + $HOC(CH_3)_3$				
t···H$OC(CH_3)_3$	3587	3584	3403	3415
o···H$OC(CH_3)_3$	3618	3621	3436	3446
p···H$OC(CH_3)_3$	3619	3619	3444	3451
TEMPO + H_2O				
o···HOH	3630	3655	3484	3485
p···HOH	3597	3621	3438	3443
t···HOH_3	3630	3655	3484	3485
TEMPO + $HOCH_3$				
o···HOCH_3	3635	3650	3462	3469
p···HOCH_3	3603	3621	3439	3449
t···HOCH_3	3635	3650	3462	3469
TEMPO + $HOC(CH_3)_3$				
o···H$OCH(CH_3)_3$	3633	3635	3456	3467
p···H$OCH(CH_3)_3$	3603	3601	3426	3438
t···H$OCH(CH_3)_3$	3633	3635	3456	3467
TEMPO + HOC_6H_5				
o···HOC_6H_5	3508	3513	3330	3348
p···HOC_6H_5	3494	3501	3306	3314
p'···HOC_6H_5	3492	3497	3304	3315

4.8 Closed-shell reference data

Table A42: Experimental OH_b stretching wavenumbers of water, methanol, tert-butanol and phenol dimers and trimer and the harmonic B3LYP-D3(BJ)/def2-TZVP computed OH stretching vibrations.

	He-jet [35–39] $\tilde{\nu}$	B3LYP-D3(BJ,ABC)/def2-TZVP $\tilde{\nu}$
OH_b (H_2O dimer)	3602	3666
OH_b (H_2O trimer)	3533	3574/3564
OH_b ($HOCH_3$ dimer)	3575	3647
OH_b ($HOCH_3$ trimer)	3474/3469	3548/3542
OH_b ($HOC(CH_3)_3$ dimer)	3497	3609
OH_b (HOC_6H_5) dimer)	3530	3647

5 Jet-FTIR Experiments (subsection 4.2)[31]

5.1 Measurement details

Gratin Jet measurements[1]:
DTBN hydrate complexes were prepared in supersonic jet expansions through a 0.2 mm × 700 mm slit nozzle at a stagnation pressure of 750 mbar. CaF_2 optics, an optical filter (F20: wavenumber range <4000 cm^{-1}), an InSb/HgCdTe detector, a 150 W tungsten lamp and a VERTEX 70v FTIR spectrometer (scanning speed 140 kHz, double sided mode) were used to probe the gas pulses. A more detailed description of the experimental setup can be found in Ref.[26].

Table A43: The spectra shown in Section 4.1 of the Thesis are the average of # gas pulses recorded on the dates dd/mm/yyyy.

Spectrum	#	Setup	dd/mm/yyyy	Figure
DTBN + H_2O	150	Filet Jet	22/10/2021	15
DTBN + $HOCH_3$	100	Filet Jet	21/09/2021	15
TEMPO + H_2O [1]	900	Gratin Jet	19/01/2021	15
TEMPO + $HOCH_3$	500	Filet Jet	23/04/2021	15
DTBN + $HOC(CH_3)_3$	300	Filet Jet	14/12/2021	16
150 scans (14/12/2021) *plus* 150 scans (15/11/2021)			15/12/2021	
TEMPO + $HOC(CH_3)_3$	125	Filet Jet	19/05/2021	16
TEMPO + HOC_6H_5	575	Filet Jet	11/05/2021	16

6 Matrix-Isolation Experiments (subsection 4.3)

6.1 TEMPO and DTBN IR Spectra

Table A44: Experimental and computed IR spectra of TEMPO monomer.

Experiment [a] Ar, 10 K		Computed [b] $\tilde{\nu}$ (A^{th})
1477	63	1520.0(2.2)
1469	62	1510.7(10.7)
1469	61	1509.7(18.8)
1461	60	1504.7(2.5)
1457	59	1500.0(8.5)
-	58	1496.3(1.8)
-	57	1492.7(0.6)
1448	56	1492.0(3.1)
-	55	1486.0(0.5)
1436	54	1479.0(1.4)
1430	53	1473.6(1.7)
1386	52	1426.4(2.9)
1378	51	1416.9(13.2)
1367	50	1400.2(11.2)
1359	49	1395.6(11.6)
-	48	1393.8(0.1)
-	47	1389.4(1.2)
1342	46	1379.1(10.9)
-	45	1377.2(0.3)
1297	44	1326.3(1.7)
1263	43	1283.3(13.0)
1249	42	1272.3(22.1)
1244	41	1261.9(1.3)
1217	40	1243.2(1.0)
1203	39	1223.3(8.0)
1179	38	1203.9(3.4)
1134	37	1152.1(19.1)
1089	36	1110.9(2.0)
1061	35	1077.3(1.2)
1044	34	1067.0(1.1)
-	33	1054.6(0.1)
-	32	1016.2(0.2)
994	31	1015.5(1.5)
975	30	988.5(6.2)
956	29	973.9(3.4)
931	28	945.0(0.9)
-	27	928.6(0.0)
-	26	886.8(0.0)
857	25	872.0(1.4)
793	24	798.5(2.0)
786	23	794.2(0.4)
634	22	638.7(2.2)
576	21	578.2(0.4)
554	20	560.5(6.7)
531	19	535.3(8.2)

[a]Experimental frequencies (1500-500 cm^{-1}) of TEMPO in Ar matrices at 10 K. [b] Unscaled (U)B3LYP-D3BJ/def2-TZVP harmonic frequencies ($\tilde{\nu}$ in cm^{-1}) and absolute intensities (A^{th} in km mol^{-1}) are also given.

Table A45: Experimental and computed IR spectra of TEMPO monomer.

Experiment [a] Ar, 10 K		Computed [b] $\tilde{\nu}$ (A^{th})
1491	45	1530.8 (4.7)
1482	44	1523.1 (18.4)
1482	43	1514.1 (13.0)
-	42	1510.0 (1.1)
1476	41	1498.9 (2.3)
1460	40	1498.3(7.5)
-	39	1494.0 (0.2)
-	38	1492.3 (1.7)
-	37	1487.5 (0.6)
-	36	1486.2 (1.7)
-	35	1474.4 (0.2)
1448	34	1472.9 (1.6)
1405	33	1439.1 (1.4)
1390	32	1428.5 (20.3)
1373	31	1407.0 (13.4)
1366	30	1402.2 (5.7)
1363	29	1398.8 (12.4)
1357	28	1393.1 (7.2)
1342	27	1375.8 (7.6)
1245	26	1270.9 (21.5)
1239	25	1260.8 (8.1)
1222	24	1243.9 (18.2)
1216	23	1236.7 (6.3)
1204	22	1224.9 (9.4)
1194	21	1216.3 (48.3)
1058	20	1075.1(1.3)
1032	19	1057.4 (0.3)
1026	18	1049.7 (1.3)
1021	17	1043.1 (0.5)
982	16	985.9 (0.4)
-	15	972.3 (0.0)
-	14	968.7 (0.0)
-	13	938.1 (0.5)
927	12	936.6 (1.0)
917	11	928.4 (0.2)
	10	925.9 (0.4)
822	9	824.6 (0.9)
-	8	795.5 (0.4)
625	7	630.4 (2.2)
534	6	545.9 (5.3)
532	5	541.6 (12.0)

[a]Experimental frequencies (1500-500 cm^{-1}) of DTBN in Ar matrices at 10 K. [b] Unscaled (U)B3LYP-D3BJ/def2-TZVP harmonic frequencies ($\tilde{\nu}$ in cm^{-1}) and absolute intensities (A^{th} in km mol^{-1}) are also given.

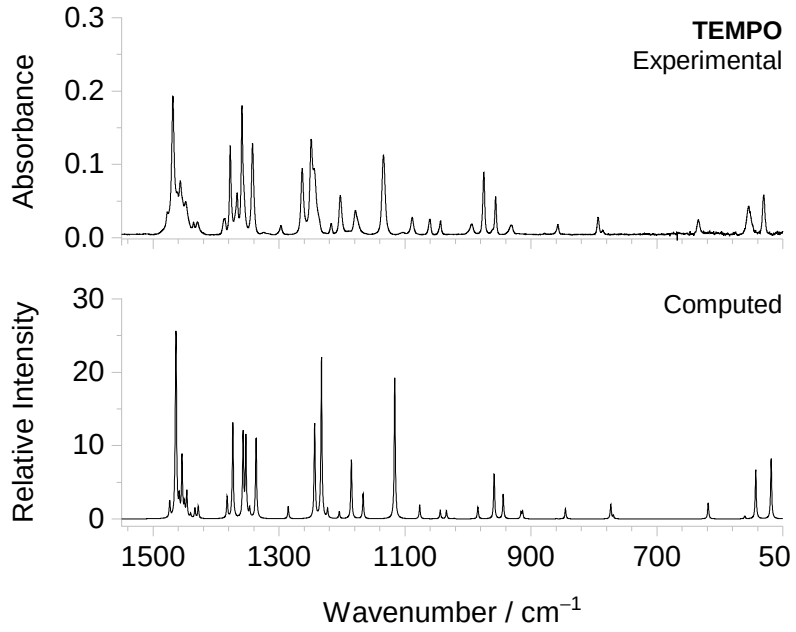

Figure A7: Experimental IR spectrum of matrix-isolated TEMPO monomers in Ar at 10 K and (U)B3LYP-D3BJ/def2-TZVP harmonic spectrum (bottom). The predicted spectrum was scaled by 0.97 factor.

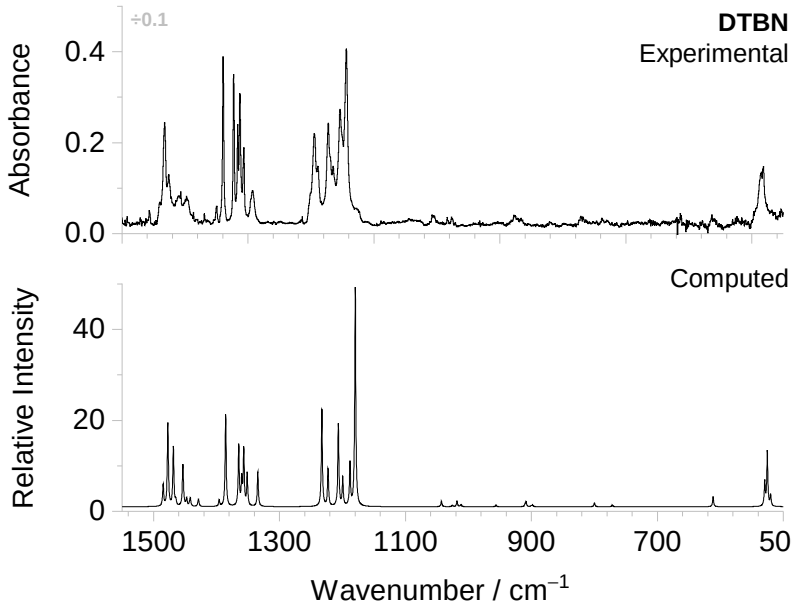

Figure A8: Experimental IR spectrum of matrix-isolated DTBN monomers in Ar at 10 K and (U)B3LYP-D3BJ/def2-TZVP harmonic spectrum (bottom). The predicted spectrum was scaled by 0.97 factor.

7 Spin Densities of TEMPO and DTBN Hydrates

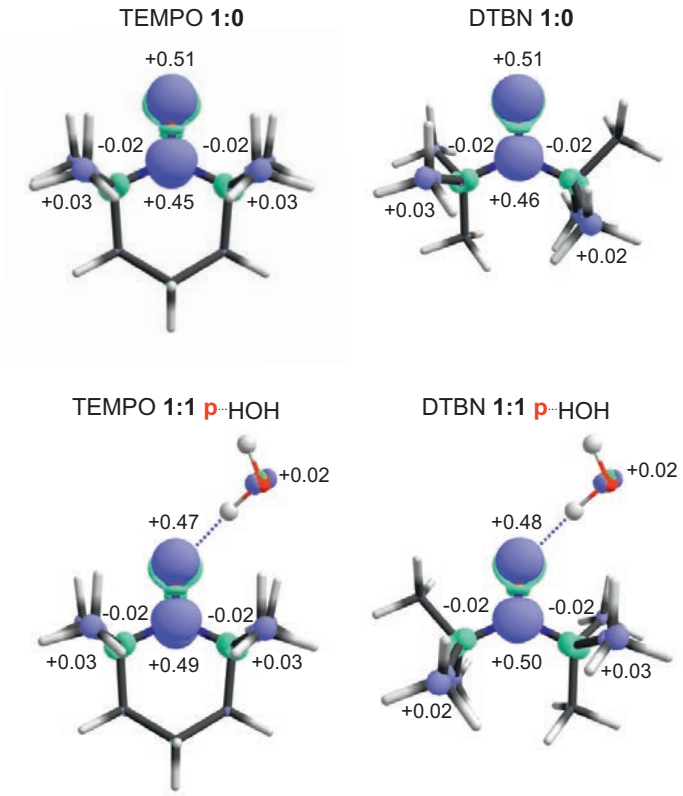

Figure A9: Spin density distributions of TEMPO and DTBN monomers, and TEMPO and DTBN 1:1 hydrates were computed at the (U)B3LYP/def2-TZVP level of theory and evaluated by Natural Population Analysis (NPA). The isosurface plots (spin a coded blue and spin b coded green) have been generated with the isodensity contour of 0.016 e/Bohr.

References

[1] E. M. Brás, T. L. Fischer, M. A. Suhm, *Angew. Chem. Int. Ed.* **2021**, *60*, 19013–19017.
[2] P. Pracht, F. Bohle, S. Grimme, *Phys. Chem. Chem. Phys.* **2020**, *22*, 7169–7192.
[3] S. Grimme, *J. Chem. Theory Comput.* **2019**, *15*, 2847–2862.
[4] C. Bannwarth, S. Ehlert, S. Grimme, *J. Chem. Theory Comput.* **2019**, *15*, 1652–1671.
[5] S. Grimme, C. Bannwarth, P. Shushkov, *J. Chem. Theory Comput.* **2017**, *13*, 1989–2009.
[6] A. D. Becke, *Phys. Rev. A* **1988**, *38*, 3098–3100.
[7] A. D. Becke, *J. Chem. Phys.* **1993**, *98*, 5648–5652.
[8] C. Lee, W. Yang, R. G. Parr, *Phys. Rev. B* **1988**, *37*, 785–789.
[9] F. Weigend, R. Ahlrichs, *Phys. Chem. Chem. Phys.* **2005**, *7*, 3297–3305.
[10] S. Grimme, J. Antony, S. Ehrlich, H. Krieg, *J. Chem. Phys.* **2010**, *132*, 154104.
[11] A. D. Becke, E. R. Johnson, *J. Chem. Phys.* **2005**, *123*, 154101.
[12] E. R. Johnson, A. D. Becke, *J. Chem. Phys.* **2005**, *123*, 024101.
[13] E. R. Johnson, A. D. Becke, *J. Chem. Phys.* **2006**, *124*, 174104.
[14] S. Grimme, S. Ehrlich, L. Goerigk, *J. Comput. Chem.* **2011**, *32*, 1456–1465.
[15] F. Neese, *WIREs Comput. Mol. Sci.* **2018**, *8*, e1327.
[16] C. Riplinger, B. Sandhoefer, A. Hansen, F. Neese, *J. Chem. Phys.* **2013**, *139*, 134101.
[17] C. Riplinger, F. Neese, *J. Chem. Phys.* **2013**, *138*, 034106.
[18] C. Riplinger, P. Pinski, U. Becker, E. F. Valeev, F. Neese, *J. Chem. Phys.* **2016**, *144*, 024109.
[19] Y. Guo, C. Riplinger, D. G. Liakos, U. Becker, M. Saitow, F. Neese, *J. Chem. Phys.* **2020**, *152*, 024116.
[20] R. A. Kendall, T. H. Dunning Jr, R. J. Harrison, *J. Chem. Phys.* **1992**, *96*, 6796–6806.
[21] W. B. Schneider, G. Bistoni, M. Sparta, M. Saitow, C. Riplinger, A. A. Auer, F. Neese, *J. Chem. Theory Comput.* **2016**, *12*, 4778–4792.
[22] G. Bistoni, *WIREs Comput. Mol. Sci.* **2020**, *10*, e1442.
[23] F. Neese, *J. Am. Chem. Soc.* **2006**, *128*, 10213–10222.
[24] *https://sites.google.com/site/orcainputlibrary/coupled-cluster*.
[25] A. Altun, M. Saitow, F. Neese, G. Bistoni, *J. Chem. Theory Comput.* **2019**, *15*, 1616–1632.
[26] H. C. Gottschalk, T. L. Fischer, V. Meyer, R. Hildebrandt, U. Schmitt, M. A. Suhm, *Instruments* **2021**, *5*, 12.
[27] J. Ceponkus, P. Uvdal, B. Nelander, *J. Phys. Chem. A* **2008**, *112*, 3921–3926.
[28] Y. Bouteiller, B. Tremblay, J. Perchard, *Chem. Phys.* **2011**, *386*, 29–40.
[29] K. E. Otto, Z. Xue, P. Zielke, M. A. Suhm, *Phys. Chem. Chem. Phys.* **2014**, *16*, 9849–9858.
[30] T. L. Fischer, T. Wagner, H. C. Gottschalk, A. Nejad, M. A. Suhm, *J. Phys. Chem. Lett.* **2020**, *12*, 138–144.
[31] E. M. Brás, T. L. Fischer, M. A. Suhm, *Phys. Chem. Chem. Phys.* **2023**, *(Submitted)*.
[32] S. Grimme, *J. Chem. Phys.* **2006**, *124*, 034108.
[33] J. Tao, J. P. Perdew, V. N. Staroverov, G. E. Scuseria, *Phys. Rev. Lett.* **2003**, *91*, 146401.
[34] M. J. Frisch, G. W. Trucks, H. B. Schlegel, G. E. Scuseria, M. A. Robb, J. R. Cheeseman, G. Scalmani, V. Barone, G. A. Petersson, H. Nakatsuji, X. Li, M. Caricato, A. V. Marenich, J. Bloino, B. G. Janesko, R. Gomperts, B. Mennucci, H. P. Hratchian, J. V. Ortiz, A. F. Izmaylov, J. L. Sonnenberg, D. Williams-Young, F. Ding, F. Lipparini, F. Egidi, J. Goings, B. Peng, A. Petrone, T. Henderson, D. Ranasinghe, V. G. Zakrzewski, J. Gao, N. Rega, G. Zheng, W. Liang, M. Hada, M. Ehara, K. Toyota, R. Fukuda, J. Hasegawa, M. Ishida, T. Nakajima, Y. Honda, O. Kitao, H. Nakai, T. Vreven, K.

Throssell, J. A. Montgomery, Jr., J. E. Peralta, F. Ogliaro, M. J. Bearpark, J. J. Heyd, E. N. Brothers, K. N. Kudin, V. N. Staroverov, T. A. Keith, R. Kobayashi, J. Normand, K. Raghavachari, A. P. Rendell, J. C. Burant, S. S. Iyengar, J. Tomasi, M. Cossi, J. M. Millam, M. Klene, C. Adamo, R. Cammi, J. W. Ochterski, R. L. Martin, K. Morokuma, O. Farkas, J. B. Foresman, D. J. Fox, Gaussian16 Revision A.03, Gaussian Inc. Wallingford CT, **2016**.

[35] U. Buck, F. Huisken, *Chem. Rev.* **2000**, *100*, 3863–3890.

[36] R. W. Larsen, P. Zielke, M. A. Suhm, *J. Chem. Phys.* **2007**, *126*, 194307.

[37] K. E. Otto, Z. Xue, P. Zielke, M. A. Suhm, *Phys. Chem. Chem. Phys.* **2014**, *16*, 9849.

[38] D. Zimmermann, T. Häber, H. Schaal, M. A. Suhm, *Mol. Phys.* **2001**, *99*, 413–425.

[39] T. Ebata, T. Watanabe, N. Mikami, *J. Phys. Chem.* **1995**, *99*, 5761–5764.

Appendix B

Generation and Characterisation of Sulphur-Centred Radicals

Contents

List of Tables

List of Figures

1 Chemicals

Tab. B1 contains details on the chemicals used for the investigations detailed in Chapter 5 and introduces abbreviations for their referencing in this supplement.

Table B1: List of substances and their abbreviation, along with the CAS number, supplier and purity.

Name	Abbreviation	CAS No.	Supplier	Purity
2,2´ - Dipyridyldisulfide	1	2127-03-9	Sigma Aldrich	$\geq$ 98%
Nitrogen	N_2	7727-37-9	N60 Air Liquide	99.9999%
Argon	Ar	7440-37-1	N60 Air Liquide	99.9999%

2 Computations of Chapter 5

2.1 Methods and keywords

The structures of 2,2'-dipyridyldisulfide (1) were obtained from manual starting structures and from relaxed potential surface energy scans around the C−S−S−C and N−C−S−S dihedral angles, with the B3LYP/def2-TZVP method[1–4], without and with with Grimme's three-body term dispersion correction D3[5] and Becke-Johnson (BJ) damping [6–9] using the Gaussian software package [10]. The structures and vibrational spectra of sulphur-centered radicals was carried out using the unrestricted open-shell variant as described in Table B2. Single point calculations on the B3LYP-D3BJ geometries were carried out using the DPLNO-CCSD(T) [11–14] method with aug-cc-pVTZ[15], and matching auxiliary basis sets, in both closed- and unrestricted open-shell[14] variants, with ORCA software package [16]. For DLPNO calculations, two fragments were defined to prepare the input file, as 1 and 2. The obtained B3LYP-D3 geometries are shown in Tables B1-B8.

Table B2: Methods and keywords applied for closed- and open-shell quantum chemical calculations of 2,2'-dipyridyldisulfide (1), pyridyl-2-thiyl (2) monomer and pairs (2a), and pyridyl-2-thiyl peroxy (5) radicals shown in the Chapter 5 of this Thesis.

Method	Program	Keywords
B3LYP-D3(BJ)	Gaussian 16	`#opt=tight freq b3lyp def2tzvp int=ultrafine empiricaldispersion=gd3bj` (multiplicity = 1)
B3LYP	Gaussian 16	`#opt=tight freq b3lyp def2tzvp int=ultrafine`
(U)B3LYP-D3(BJ)	Gaussian 16	`#opt=tight freq ub3lyp def2tzvp int=ultrafine` (multiplicity = 2 for doublet spin state ,multiplicity = 1 or 3 for singlet or triplet spin states)
(U)B3LYP	Gaussian 16	`#opt=tight freq ub3lyp def2tzvp int=ultrafine`
DLPNO-CCSD(T)	ORCA 4.2.1	`DLPNO-CCSD(T) TightPNO aug-cc-pVTZ aug-cc-pVTZ/C TightSCF LED` (for closed-shell calculations)
DLPNO-CCSD(T)	ORCA 4.2.1	`UHF DLPNO-CCSD(T) TightPNO aug-cc-pVTZ aug-cc-pVTZ/C TightSCF LED` (for unrestricted open-shell calculations)

2.2 Cartesian Coordinates

Selected Cartesian coordinates (in Å) of B3LYP- and B3LYP-D3(BJ)/def2-TZVP computed structures (in Å) of the investigated chemical species in the Chapter 5 of the Thesis. These are given in the Tables B3,B4,B5,B6,B7,B8, B9,B10,B11.

Table B3: Cartesian coordinates of out-out conformer of 2,2'-dipyridyldisulfide 1 computed at (U)B3LYP-D3BJ/def2-TZVP level of theory.

Atom	X	Y	Z
N	0.016008000	3.084306000	0.276854000
C	0.416938000	1.831630000	0.351972000
S	-0.416938000	0.933965000	1.657326000
S	0.416938000	-0.933965000	1.657326000
C	-0.416938000	-1.831630000	0.351972000
N	0.016008000	-3.084306000	0.276854000
C	0.510552000	3.872503000	-0.659721000
C	1.480704000	3.442723000	-1.554579000
C	1.918960000	2.126772000	-1.464043000
C	1.381763000	1.293682000	-0.495388000
C	-0.510552000	-3.872503000	-0.659721000
C	-1.480704000	-3.442723000	-1.554579000
C	-1.918960000	-2.126772000	-1.464043000
C	-1.381763000	-1.293682000	-0.495388000
H	0.136578000	4.889809000	-0.691471000
H	1.878235000	4.118980000	-2.298555000
H	2.673018000	1.749278000	-2.142885000
H	1.701044000	0.267667000	-0.391726000
H	-0.136578000	-4.889809000	-0.691471000
H	-1.878235000	-4.118980000	-2.298555000
H	-2.673018000	-1.749278000	-2.142885000
H	-1.701044000	-0.267667000	-0.391726000

Table B4: Cartesian coordinates of conformer in-out of 2,2'-dipyridyldisulfide 1 computed at B3LYP-D3BJ/def2-TZVP level of theory.

Atom	X	Y	Z
N	1.438355000	0.618471000	-0.635819000
C	1.892686000	-0.344483000	0.147496000
S	0.789377000	-1.663330000	0.651972000
S	-0.726282000	-1.615503000	-0.712449000
C	-1.858020000	-0.359493000	-0.139781000
N	-2.964041000	-0.344641000	-0.872921000
C	2.275990000	1.602145000	-0.969181000
C	3.586947000	1.669913000	-0.521922000
C	4.050466000	0.654042000	0.308503000
C	3.195958000	-0.379212000	0.650866000
C	-3.899932000	0.556407000	-0.575112000
C	-3.771358000	1.467246000	0.463435000
C	-2.605118000	1.437338000	1.220566000
C	-1.619468000	0.512662000	0.918817000
H	1.870909000	2.369511000	-1.619491000
H	4.225565000	2.490776000	-0.817226000
H	5.068983000	0.661596000	0.674911000
H	3.523757000	-1.197043000	1.278659000
H	-4.789186000	0.542387000	-1.195571000
H	-4.559420000	2.177981000	0.670373000
H	-2.460958000	2.133927000	2.036750000
H	-0.698268000	0.466001000	1.478281000

Table B5: Cartesian coordinates of conformer in-in of 2,2′-dipyridyldisulfide 1 computed at B3LYP-D3BJ/def2-TZVP level of theory.

Atom	X	Y	Z
N	0.850679000	1.453204000	-0.412168000
C	-0.144149000	1.822143000	0.373510000
S	-0.675308000	0.756967000	1.708677000
S	0.675308000	-0.756967000	1.708677000
C	0.144149000	-1.822143000	0.373510000
N	-0.850679000	-1.453204000	-0.412168000
C	1.197418000	2.270333000	-1.408495000
C	0.564291000	3.477409000	-1.660584000
C	-0.483773000	3.853936000	-0.825143000
C	-0.850679000	3.018397000	0.213698000
C	-1.197418000	-2.270333000	-1.408495000
C	-0.564291000	-3.477409000	-1.660584000
C	0.483773000	-3.853936000	-0.825143000
C	0.850679000	-3.018397000	0.213698000
H	2.019296000	1.935112000	-2.031772000
H	0.880885000	4.102569000	-2.483908000
H	-1.006400000	4.788970000	-0.981409000
H	-1.658518000	3.277148000	0.885517000
H	-2.019296000	-1.935112000	-2.031772000
H	-0.880885000	-4.102569000	-2.483908000
H	1.006400000	-4.788970000	-0.981409000
H	1.658518000	-3.277148000	0.885517000

Table B6: Cartesian coordinates of thiyl radical 2 computed at B3LYP-D3BJ/def2-TZVP level of theory.

Atom	X	Y	Z
N	-1.16350000	-0.12145000	0.00000000
C	0.00000000	0.51773200	0.00000000
C	1.23818200	-0.13001900	0.00000000
C	1.23913200	-1.51370200	0.00000000
C	0.02718400	-2.19841600	0.00000000
C	-1.14395200	-1.45531800	0.00000000
H	2.15981200	0.43594800	0.00000000
H	2.17702000	-2.05433000	0.00000000
H	-0.00888500	-3.27881500	0.00000000
H	-2.11177300	-1.94412200	0.00000000
S	-0.13968500	2.27311300	0.00000000

Table B7: Cartesian coordinates of pyridyl-2-thiyl radical pairs 2a (planar structure, triplet state) computed at (U)B3LYP-D3BJ/def2-TZVP level of theory.

Atom	X	Y	Z
N	3.907570000	1.005317000	0.000172000
C	2.578415000	0.750302000	0.000063000
S	1.494393000	2.091259000	0.000034000
S	-1.494406000	-2.091269000	-0.000189000
C	-2.578420000	-0.750305000	-0.000099000
N	-3.907576000	-1.005310000	-0.000073000
C	4.736196000	-0.022566000	0.000195000
C	4.319311000	-1.359912000	0.000111000
C	2.959321000	-1.629681000	0.000000000
C	2.071962000	-0.566497000	-0.000025000
C	-4.736194000	0.022581000	-0.000005000
C	-4.319297000	1.359924000	0.000041000
C	-2.959305000	1.629681000	0.000016000
C	-2.071955000	0.566489000	-0.000055000
H	5.795093000	0.215239000	0.000284000
H	5.052072000	-2.155715000	0.000136000
H	2.590929000	-2.647284000	-0.000066000
H	1.004926000	-0.738983000	-0.000107000
H	-5.795093000	-0.215216000	0.000015000
H	-5.052051000	2.155732000	0.000096000
H	-2.590905000	2.647281000	0.000050000
H	-1.004918000	0.738961000	-0.000074000

Table B8: Cartesian coordinates of pyridyl-2-thiyl radical pairs 2a (planar structure, singlet state, from fragment-based calculations) computed at (U)B3LYP-D3BJ/def2-TZVP level of theory.

Atom	X	Y	Z
N(Fragment=2)	-3.126631000	-2.545352000	0.000000000
C(Fragment=2)	-2.132613000	-1.626819000	0.000000000
S(Fragment=2)	-2.568625000	0.041389000	0.000000000
S(Fragment=3)	2.568565000	-0.041407000	0.000000000
C(Fragment=3)	2.132597000	1.626816000	0.000000000
N(Fragment=3)	3.126639000	2.545318000	0.000000000
C(Fragment=2)	-2.790984000	-3.822240000	0.000000000
C(Fragment=2)	-1.467124000	-4.280316000	0.000000000
C(Fragment=2)	-0.442987000	-3.345783000	0.000000000
C(Fragment=2)	-0.772163000	-2.000604000	0.000000000
C(Fragment=3)	2.791031000	3.822219000	0.000000000
C(Fragment=3)	1.467186000	4.280333000	0.000000000
C(Fragment=3)	0.443023000	3.345827000	0.000000000
C(Fragment=3)	0.772157000	2.000638000	0.000000000
H(Fragment=2)	-3.610743000	-4.533446000	0.000000000
H(Fragment=2)	-1.261448000	-5.342359000	0.000000000
H(Fragment=2)	0.594707000	-3.653067000	0.000000000
H(Fragment=2)	0.000000000	-1.244258000	0.000000000
H(Fragment=3)	3.610813000	4.533398000	0.000000000
H(Fragment=3)	1.261539000	5.342381000	0.000000000
H(Fragment=3)	-0.594662000	3.653143000	0.000000000
H(Fragment=3)	-0.000035000	1.244321000	0.000000000

Table B9: Cartesian coordinates of pyridyl-2-thiyl radical pairs 2a (stacked structure, triplet state) computed at (U)B3LYP-D3BJ/def2-TZVP level of theory.

Atom	X	Y	Z
N	-1.455189000	1.120271000	1.120630000
C	-1.131067000	1.291665000	-0.181555000
S	-0.148078000	2.639380000	-0.616351000
S	0.228852000	-2.696253000	-0.483104000
C	1.167642000	-1.303759000	-0.078425000
N	1.756517000	-0.613778000	-1.079361000
C	-2.215209000	0.087271000	1.440969000
C	-2.695765000	-0.843970000	0.515400000
C	-2.359895000	-0.683425000	-0.820751000
C	-1.570891000	0.397460000	-1.179133000
C	2.452764000	0.464407000	-0.763792000
C	2.613377000	0.931154000	0.546343000
C	2.014266000	0.227666000	1.578720000
C	1.284104000	-0.906430000	1.268169000
H	-2.458745000	-0.019651000	2.493195000
H	-3.303365000	-1.674961000	0.846107000
H	-2.699576000	-1.386391000	-1.569184000
H	-1.270269000	0.562395000	-2.202822000
H	2.906135000	1.000850000	-1.590276000
H	3.181350000	1.831570000	0.734570000
H	2.099017000	0.564551000	2.603001000
H	0.787802000	-1.486072000	2.032140000

Table B10: Cartesian coordinates of pyridyl-2-thiyl peroxy radical 5a computed at (U)B3LYP-D3BJ/def2-TZVP level of theory.

Atom	X	Y	Z
N	-1.176475000	-1.236703000	0.000000000
C	-0.292982000	-0.246382000	0.000000000
C	-0.628027000	1.105789000	0.000000000
C	-1.978764000	1.418009000	0.000000000
C	-2.921738000	0.396659000	0.000000000
C	-2.469210000	-0.915883000	0.000000000
H	0.130776000	1.872975000	0.000000000
H	-2.290682000	2.454431000	0.000000000
H	-3.981408000	0.610069000	0.000000000
H	-3.166154000	-1.746001000	0.000000000
S	1.353599000	-0.887324000	0.000000000
O	2.205313000	0.639746000	0.000000000
O	3.498379000	0.499438000	0.000000000

Table B11: Cartesian coordinates of pyridyl-2-thiyl peroxy radical 5c computed at (U)B3LYP-D3BJ/def2-TZVP level of theory.

Atom	X	Y	Z
N	-0.865859000	1.236136000	0.422442000
C	-0.105741000	0.397333000	-0.287243000
C	-0.565707000	-0.820592000	-0.788887000
C	-1.875579000	-1.189983000	-0.515990000
C	-2.674433000	-0.319509000	0.208107000
C	-2.127392000	0.886528000	0.643359000
H	0.089711000	-1.447867000	-1.373861000
H	-2.264687000	-2.133915000	-0.874177000
H	-3.703951000	-0.561324000	0.435360000
H	-2.728823000	1.593309000	1.204175000
S	1.561766000	0.878281000	-0.566006000
O	2.432602000	-0.348586000	0.520557000
O	1.789100000	-1.386203000	0.873372000

2.3 Absolute Energies

Absolute energies are provided in Tables B12, B13 and B14 for checking purposes.

Table B12: Electronic energies E_{el} (in E_h), zero-point vibrational energies (in E_h) of 2,2′-dipyridyldisulfide conformers at B3LYP-D3(BJ)/def2-TZVP and DLPNO-CCSD(T)/aug-cc-pVTZ//B3LYP-D3(BJ)/def2-TZVP levels.

Structure	$E_{el}^{B3LYP\text{-}D3BJ}$	ZPVE	E_{el}^{DLPNO}
out-out	-1292.06008769	0.16019238	-1289.99653371
in-out	-1292.05794490	0.16001347	-1289.99447036
in-in	-1292.05576794	0.15981847	-1289.99225060

Table B13: Electronic energies E_{el} (in E_h), zero-point vibrational energies (in E_h) of radical 2 at unrestricted open-shell (U)B3LYP-D3BJ/def2-TZVP and UHF-DLPNO-CCSD(T)/aug-cc-pVTZ//B3LYP-D3/def2-TZVP levels.

Structure	$E_{el}^{(U)B3LYP\text{-}D3BJ}$	ZPVE	E_{el}^{DLPNO}
2a	-645.97594282	0.07867199	-644.947512865
2a-^{3}p	-1291.97167470	0.15749434	-1289.905134151
2a-^{1}p	-1291.97171876	0.15751034	-1289.892230957
2a-^{3}s	-1291.97739019	0.15769735	-1289.911946242

Table B14: Electronic energies E_{el} (in E_h), zero-point vibrational energies (in E_h) of radical pyridyl-2-thiyl peroxy radical 5 at unrestricted open-shell (U)B3LYP-D3BJ/def2-TZVP level.

Structure	$E_{el}^{(U)B3LYP}$	ZPVE
5a	-796.379762828	0.08439036
5b	-796.376681343	0.08424967
5c	-796.377942798	0.08431647

2.4 Scans

The potential energy suface as a function of C−S−O−O and N−S−C−O dihedral angles was computed to find all the low-lying energy structures of pyridyl-2-thiyl peroxy radical 5 (Figure B1).

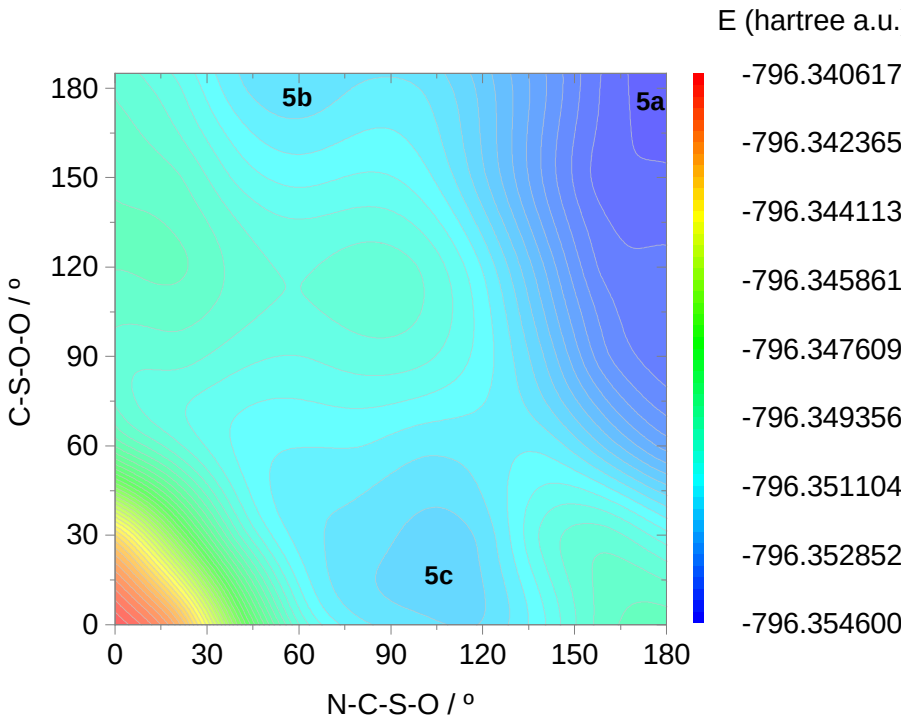

Figure B1: Contour plot of the (U)B3LYP/def2-TZVP potential energy surface for pyridyl-2-thiyl peroxy radicals 5 computed as a function of C-S-O-O and N-S-C-O dihedral angles, incrementally rotated and fixed in steps of 20 degrees. The three minima (5a, 5b, and 5c) indicated in the figure were fully optimized at the same level of theory. The coloured bar ranging from blue to red encodes the absolute energy in hartree, from the lower energies (blue) to higher energies (red). The renderings of 3D structures of the global minimum 5a (dark blue region) and local minima 5b and 5c (light blue regions) can be found in the subsection 5.2.2 of reactions with molecular oxygen (Chapter 5), along with the relative energies in kJ mol^{-1}. The relaxation barrier 5a a 5b is approximately 0.7 kJ mol^{-1}, while it is 1.9 kJ mol^{-1} between 5a and 5c kJ mol^{-1}, and 4.3 kJ mol^{-1} between 5b and 5c. The first may be low enough to allow relaxation of 5b into 5a, which would explain the absence of conformer 5b in the matrix environment.

2.5 Scale factors

To address the overestimation of the calculated harmonic frequencies, multiplicative scaling factors (0.978, 0.976 and 0.984, for B3LYP/def2-TZVP with and without dispersion corrections, and B3LYP/6-311++(3df,3pd), respectively) were applied (Figure B2).

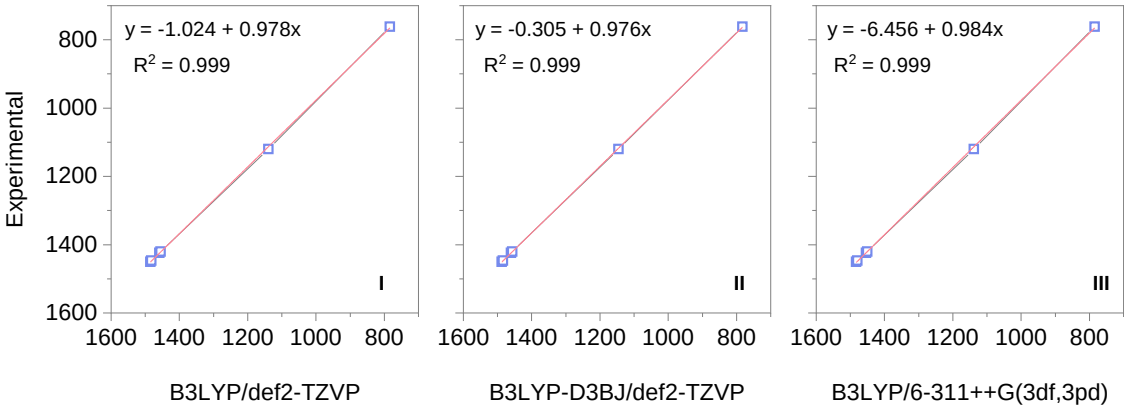

Figure B2: Linear regression of experimental wavenumbers (Y-axis) and computed harmonic wavenumbers (X-axis) for 2,2'-dipyridyldisulfide within the B3LYP and B3LYP-D3BJ/def2-TZVP (I and II, respectively), and B3LYP/6-311++g(3df,3pd) approximations (III). Only the most intense bands in the experimental spectrum were considered.

2.6 Radical Pairs Harmonic Spectra

Table B15: (U)B3LYP-D3BJ/def2-TZVP harmonic spectrum of 2a-^{3}s.

$\tilde{\nu}$	(A^{th})
3221.7	0.7
3217.3	1.5
3206.5	5.3
3205.5	5.2
3190.0	3.0
3189.8	3.0
3157.5	10.4
3148.2	17.5
1592.6	0.4
1588.8	2.6
1576.8	24.6
1573.9	18.4
1465.3	5.1
1463.4	3.4
1441.6	16.7
1440.6	6.5
1321.4	1.0
1319.7	0.5
1275.4	1.4
1272.4	0.5
1177.7	2.1
1177.5	1.6
1123.3	0.5
1120.8	0.1
1096.8	2.2
1096.2	3.1
1063.6	0.9
1062.5	9.4
1015.6	0.1
1014.6	0.4
995.7	7.1
992.9	12.1
988.4	0.9
988.0	1.3
905.2	1.0
903.5	1.2
786.4	54.8
785.3	15.7
754.5	0.1
753.4	0.1
736.7	21.5
734.1	17.5
631.2	5.5
630.7	3.2

Table B16: (U)B3LYP-D3BJ/def2-TZVP harmonic spectrum of 2a-^{1}p

$\tilde{\nu}$	(A^{th})
3203.1	0.0
3202.6	65.6
3197.9	31.7
3197.8	0.0
3183.5	32.4
3183.3	0.0
3150.6	0.0
3150.5	38.2
1590.3	0.0
1590.1	4.5
1575.2	0.0
1574.2	71.0
1462.3	5.7
1461.7	0.0
1446.3	0.0
1443.9	17.9
1325.6	3.6
1325.2	0.0
1276.1	0.0
1273.8	1.6
1181.3	0.0
1178.6	15.3
1123.2	0.0
1123.1	0.2
1103.0	0.0
1098.3	8.2
1060.2	0.0
1059.9	16.5
1027.3	0.1
1024.4	0.0
994.9	0.7
994.3	0.0
990.5	29.1
989.5	0.0
920.4	0.0
919.6	0.1
791.5	0.0
790.7	66.1
754.8	0.0
754.5	0.2
743.4	27.6
740.3	0.0
629.6	0.0
629.1	8.6

2.7 Spectra 5a and 5c

Table B17: Experimental IR spectra of matrix isolated of pyridyl-2-thiyl peroxy radical 5a in O_2-doped N_2 matrices along with the unscaled harmonic (U)B3LYP-D3BJ/def2-TZVP spectra.

Experiment[a] N_2 matrix		Computed[b (U)B3LYP-D3	(U)B3LYP	Approximate Description[c]
-	27	1489.4 (54.6)	1487.6 (54.5)	ring str. + CH bend
1434	26	1459.5 (69.8)	1458.1 (70.1)	ring str.+ CH bend.
1327	25	1315.8 (7.2)	1314.3 (7.6)	ring str. + CH bend.
-	24	1296.2 (0.8)	1294.1 (0.9)	ring str. + CH bend.
-	23	1182.4 (2.8)	1180.5 (2.8)	CH bend. + ring str.
1150	22	1163.7 (55.4)	1158.4 (46.8)	CS str. + CH bend.
1150	21	1149.9 (57.7)	1148.7 (64.9)	OO str. + CS str. + CSO bend. + CH bend.
-	20	1117.4 (6.4)	1114.3 (8.7)	CH bend. + ring str.
1065	19	1069.1 (5.1)	1066.0 (5.6)	CH bend. + ring str.
-	18	1009.9 (0.0)	1010.4 (0.0)	CH o.o. def.
992	17	1008.1 (6.2)	1004.8 (6.2)	ring breathing
-	16	985.4 (0.3)	986.2 (0.3)	CH o.o. def.
-	15	901.6 (0.3)	902.4 (0.3)	CH o.o. def.
765	14	777.3 (50.7)	778.3 (51.7)	CH o.o. def.
-	13	757.1 (6.6)	757.4 (5.7)	CH o.o. def.
749	12	749.1 (10.3)	745.7 (10.4)	CS str. + ring dist.
-	11	638.8 (14.4)	636.6 (15.3)	SO str. + SOO bend.
615	10	620.0 (26.6)	618.1 (26.1)	SOO bend. + CSO bend.
490	9	485.9 (3.8)	486.6 (3.7)	ring. tors.
-	8	453.9 (2.1)	450.6 (2.2)	CS str. + CSO bend. + ring dist.
-	7	405.5 (3.9)	406.1 (3.9)	ring. tors.

Table B18: Experimental IR spectra of matrix isolated of pryridyl-2-thiyl peroxy radical 5c in O_2-doped N_2 matrices along with the unscaled harmonic (U)B3LYP-D3BJ/def2-TZVP spectra.

Experiment[a] N_2 matrix		Computed[b] (U)B3LYP-D3	(U)B3LYP	Approximate Description[c]
-	27	1479.7 (13.2)	1477.7 (13.5)	ring str. + CH bend.
1434	26	1457.4 (19.0)	1456.1 (19.4)	ring str.+ CH bend.
-	25	1315.2 (0.2)	1313.4 (0.1)	ring str. + CH bend.
-	24	1295.4 (2.0)	1292.4 (2.0)	ring str. + CH bend.
1210	23	1216.0 (136.0)	1210.8 (136.1)	OO str. + CS str.
-	22	1181.1 (2.7)	1179.7 (2.7)	CS str. + CH bend.
-	21	1132.4 (13.8)	1127.9 (12.4)	CH bend.
-	20	1111.2 (4.3)	1107.0 (5.7)	CH bend. + ring str.
1065	19	1068.7 (4.8)	1065.3 (4.7)	CH bend. + ring str.
-	18	1018.3 (0.3)	1019.2 (0.3)	ring dist. + CH o.o. def.
992	17	1010.3 (8.5)	1006.6 (8.4)	ring breathing
-	16	987.5 (0.2)	988.4 (0.3)	CH o.o. def.
-	15	917.4 (1.0)	918.3 (0.9)	CH o.o. def.
777	14	790.8 (27.3)	791.9 (27.8)	CH o.o. def.
-	13	755.7 (15.2)	756.1 (14.8)	CH o.o. def.
743	12	749.6 (0.8)	745.5 (0.9)	CS str. + ring dist. + SOO bend.
-	11	635.0 (2.3)	632.4 (2.3)	ring dist. + CS str.
566	10	574.7 (34.0)	572.4 (33.3)	SOO bend. + CSO bend.
-	9	480.1 (1.7)	480.3 (2.0)	SOO bend. + CSO bend.
-	8	419.9 (0.5)	420.3 (0.8)	SO str. + ring tors.
-	7	410.4 (12.2)	407.2 (11.8)	CS str. + OO str. + ring. dist.

References

[1] A. D. Becke, *Phys. Rev. A* **1988**, *38*, 3098–3100.
[2] A. D. Becke, *J. Chem. Phys.* **1993**, *98*, 5648–5652.
[3] C. Lee, W. Yang, R. G. Parr, *Phys. Rev. B* **1988**, *37*, 785–789.
[4] F. Weigend, R. Ahlrichs, *Phys. Chem. Chem. Phys.* **2005**, *7*, 3297–3305.
[5] S. Grimme, J. Antony, S. Ehrlich, H. Krieg, *J. Chem. Phys.* **2010**, *132*, 154104.
[6] A. D. Becke, E. R. Johnson, *J. Chem. Phys.* **2005**, *123*, 154101.
[7] E. R. Johnson, A. D. Becke, *J. Chem. Phys.* **2005**, *123*, 024101.
[8] E. R. Johnson, A. D. Becke, *J. Chem. Phys.* **2006**, *124*, 174104.
[9] S. Grimme, S. Ehrlich, L. Goerigk, *J. Comput. Chem.* **2011**, *32*, 1456–1465.
[10] M. J. Frisch, G. W. Trucks, H. B. Schlegel, G. E. Scuseria, M. A. Robb, J. R. Cheeseman, G. Scalmani, V. Barone, G. A. Petersson, H. Nakatsuji, X. Li, M. Caricato, A. V. Marenich, J. Bloino, B. G. Janesko, R. Gomperts, B. Mennucci, H. P. Hratchian, J. V. Ortiz, A. F. Izmaylov, J. L. Sonnenberg, D. Williams-Young, F. Ding, F. Lipparini, F. Egidi, J. Goings, B. Peng, A. Petrone, T. Henderson, D. Ranasinghe, V. G. Zakrzewski, J. Gao, N. Rega, G. Zheng, W. Liang, M. Hada, M. Ehara, K. Toyota, R. Fukuda, J. Hasegawa, M. Ishida, T. Nakajima, Y. Honda, O. Kitao, H. Nakai, T. Vreven, K. Throssell, J. A. Montgomery, Jr., J. E. Peralta, F. Ogliaro, M. J. Bearpark, J. J. Heyd, E. N. Brothers, K. N. Kudin, V. N. Staroverov, T. A. Keith, R. Kobayashi, J. Normand, K. Raghavachari, A. P. Rendell, J. C. Burant, S. S. Iyengar, J. Tomasi, M. Cossi, J. M. Millam, M. Klene, C. Adamo, R. Cammi, J. W. Ochterski, R. L. Martin, K. Morokuma, O. Farkas, J. B. Foresman, D. J. Fox, Gaussian16 Revision A.03, Gaussian Inc. Wallingford CT, **2016**.
[11] C. Riplinger, B. Sandhoefer, A. Hansen, F. Neese, *J. Chem. Phys.* **2013**, *139*, 134101.
[12] C. Riplinger, F. Neese, *J. Chem. Phys.* **2013**, *138*, 034106.
[13] C. Riplinger, P. Pinski, U. Becker, E. F. Valeev, F. Neese, *J. Chem. Phys.* **2016**, *144*, 024109.
[14] Y. Guo, C. Riplinger, D. G. Liakos, U. Becker, M. Saitow, F. Neese, *J. Chem. Phys.* **2020**, *152*, 024116.
[15] R. A. Kendall, T. H. Dunning Jr, R. J. Harrison, *J. Chem. Phys.* **1992**, *96*, 6796–6806.
[16] F. Neese, *WIREs Comput. Mol. Sci.* **2018**, *8*, e1327.

Appendix C

High Z′ Crystal Structure of the Imidazole Disulfide

CRYSTAL GROWTH & DESIGN

Article

Cite This: *Cryst. Growth Des.* 2018, 18, 4167−4173

pubs.acs.org/crystal

High Z' Crystal Structure of a New Polymorph of a Thioimidazole Disulfide: Importance of Conformational Flexibility

Elisa M. Brás,*[,†] Marta S. C. Henriques,[‡] José A. Paixão,[‡] and Rui Fausto[†]

[†]CQC, Department of Chemistry, University of Coimbra, P-3004-535 Coimbra, Portugal

[‡]CFisUC, Department of Physics, University of Coimbra, P-3004-516 Coimbra, Portugal

Supporting Information

ABSTRACT: A new polymorph of a thioimidazole disulfide (2-[(1*H*-imidazol-2-yl) disulfanyl]-1*H*-imidazole; IDI) was prepared, which exhibits a rare crystal structure with 4 symmetry independent molecules (Z' = 4; Z = 16) and all possible conformers predicted for the isolated molecule within the crystal unit cell. The crystal structure is non-centrosymmetric, *Ia* monoclinic space group, with cell parameters: a = 7.45910(10) Å, b = 44.1680(8) Å, c = 11.3522(2) Å, and β = 103.0240(10)°. The four symmetry independent molecules establish an extensive hydrogen bond network involving NH groups as proton donors and N atoms of neighboring molecules as acceptors. A computational structural investigation of the isolated molecule of the compound was performed at the DFT(B3LYP)/6-311++G(d,p) level of theory in order to characterize in detail its conformational space, and these results were taken into account to evaluate the role of conformational flexibility and intermolecular interactions in the observed crystal packing. The exceptional structural characteristics of the new polymorph were underlined by comparison with those of the previously reported one (*C*2/*c*, monoclinic, Z = 4; Z' = 1/2; Bazargani, M. F.; Talavat, L.; Naderi, S.; Khavasi, H. R. *Acta Crystallogr., Sect. E* **2011**, *67*, o2585).

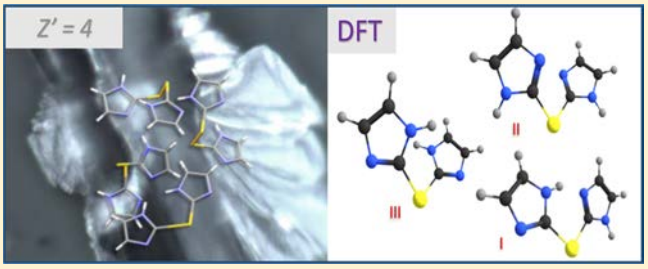

1. INTRODUCTION

Most of the crystals formed from chemically identical molecules can be simply described by defining a molecular building block and then applying the crystallographic symmetry operations of a particular space group to that molecular entity. However, in some crystals, chemically identical molecules are not related to one another by crystallographic symmetry, and occupy distinct independent positions. With Z' being the number of formula units in a crystallographic unit cell divided by the number of independent general positions, these types of crystals correspond to Z' > 1, in opposition to common crystals where Z' = 1.

The first suggested Z' > 1 crystal structures in the Cambridge Structural Database (CSD)[1] are those of the α and β polymorphs of hydroquinone, which were reported in 1926 and 1927, respectively, by Caspari,[2,3] but the real first actual molecular structure determination of a Z' > 1 system was only published 10 years later by Robertson and Woodward, who solved the structure of *trans*-stilbene, showing that the crystal comprises two crystallographically independent half molecules sited on crystallographic inversion centers in $P2_1/a$.[4] Nowadays, around 70,000 organic crystals with Z' > 1 are known (about 9% of the ca. 800,000 structures contained in the CSD),[5−7] those with Z' > 4 being extremely rare (<0.1% in CSD).[5−7]

The reasons leading to the emergence of Z' > 1 crystal structures (or those explaining their uncommonness) have attracted the interest of the scientific community, mostly driven by the key relevance of understanding the properties of organic solid materials with high potential for drug development,[8−10] and also because Z' > 1 crystalline materials are structurally closely related to cocrystals, which are likewise currently a hot topic of research.[11−17] Several recent comprehensive reviews have been published addressing this matter.[5−7,18]

Very interestingly, the idea that there might not be any general "driving force" toward either Z' > 1 or Z' = 1 crystals has recently becoming more and more consensual. As stated in the seminal recent review of Steed and Steed:[7] *"if the optimal interactions are for a Z' > 1 crystal with an intermolecular interaction that is not coincident with crystallographic symmetry, then this interaction will form, [···] independently of the anthropomorphically imposed restraint of symmetry"*. Nevertheless, for each individual system reasons must exist that determine the formation of uncommon Z' > 1 type crystals. The rationalization of such factors, on the other hand, shall contribute to furthering our understanding of the general problem of crystallization.

Most of the Z' > 1 crystals appear to be less stable than their Z' = 1 polymorphs. Also, they have been found to in general exhibit a lower density. These observations have led to the

Received: May 2, 2018
Revised: May 30, 2018
Published: June 6, 2018

DOI: 10.1021/acs.cgd.8b00673
Cryst. Growth Des. 2018, 18, 4167−4173

disputed suggestion that high Z' structures might result from preassociated aggregates in solution.[7,19] According to that proposition, such solution factors can be supposed to dominate nucleation to the point where the solution phase aggregation ultimately is translated into a low-symmetry crystalline metastable phase, while alternative putative structures respecting crystallographic symmetry become inaccessible.

On the other hand, there have been reported several cases where $Z' > 1$ structures are more stable than the corresponding $Z = 1$ forms.[7] A possible explanation for this considers that high Z' structures may offer more convenient orientations of molecules for intermolecular interactions (e.g., straighter and shorter—stronger—hydrogen bonds), in particular, when these have to be made compatible with strong stabilizing intramolecular interactions or in the presence of different synthons exhibiting competing geometrical demands. Besides, it has also been suggested that $Z' > 1$ structures can be favored in the presence of high conformational flexibility, specifically when both compact and extended conformers exist for a given molecule: the lowest energy conformers tend to be more compact due to intramolecular stabilization (e.g., intramolecular H-bonding), while more extended conformers may lack these intramolecular interactions but have a higher molecular surface area available for the establishment of intermolecular interactions.

Though statistical surveys based on CSD available data have pointed out several possible factors for the formation of multiple symmetry independent molecules in a crystal, based on the present state of the knowledge one can only realistically sustain that the ability (or not) of a given chemical system to form stable $Z' > 1$ crystalline forms results from a delicate balance involving several factors, the ultimate goal of making a priori predictions on this domain being still far from reachable. This certainly stresses the need for additional data on chemical systems exhibiting high Z' crystalline forms, and their rationalization.

Herein one describes a fascinating example of a new polymorph of a thioimidazole disulfide {2-[(1*H*-imidazol-2-yl) disulfanyl]-1*H*-imidazole; IDI; Figure 1} exhibiting a high Z' crystalline structure ($Z' = 4$), whose unit cell comprises the whole set of conformers of the molecule (the abundant lowest energy conformer and two high-energy forms not present in solution before crystallization).

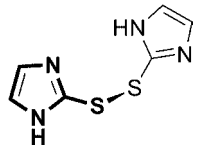

Figure 1. Schematic drawing of the 2-[(1*H*-imidazol-2-yl) disulfanyl]-1*H*-imidazole (IDI) single molecule.

In the next sections of this article, results of a computational structural investigation of the isolated IDI molecule will first be presented, providing a detailed characterization of the conformational space of the molecule. The crystal structure of the new polymorph will then be described and discussed taking into account also the results obtained for the isolated molecules, in order to shed light on the roles of conformational flexibility and intermolecular interactions in the observed crystal packing. The exceptional structural characteristics of the new polymorph will be underlined by comparison with those of the previously reported polymorph, exhibiting $Z' = 1/2$.[20]

2. EXPERIMENTAL AND COMPUTATIONAL METHODS

2-Mercaptoimidazole was purchased from Sigma-Aldrich (crystalline; purity 98%). The disulfide, 2-[(1*H*-imidazol-2-yl) disulfanyl]-1*H*-imidazole, was obtained from the mercaptoimidazole by the air oxidation method.[21−23] A concentrated solution of 2-mercaptoimidazole in tetrahydrofuran (THF) was prepared and the solvent was allowed to slowly evaporate at room temperature. A mixture of two crystals was obtained, the major component being the original mercaptoimidazole and the minor the disulfide. Crystals of the latter suitable for single crystal X-ray analysis were harvested and their structure determined using a Bruker APEX II diffractometer with graphite monochromated Mo Kα (λ = 0.71073 Å) excitation. Absorption corrections were performed using SADABS,[24] and the structural refinements were done using the SHELXL-2016/6 package.[25] The summary of the data collection, refinement details, and the main crystallographic results are given in the Supporting Information. A CIF file containing supplementary crystallographic data was deposited at the Cambridge Crystallographic Data Centre with reference CCDC 1541935.

Calculations were undertaken at the density functional theory (DFT) level of theory, using the Gaussian 09 suite of programs.[26] The B3LYP functional,[27,28] together with the double-ζ polarized, augmented with diffuse functions in both hydrogen and heavy atoms 6-311++G(d,p) basis set,[29] was used in the calculations. Calculations for the compound in the presence of solvent (tetrahydrofuran; THF) were done using the universal Solvation Model based on solute electron density and on a continuum model of the solvent defined by the bulk dielectric constant and atomic surface tensions (SMD) of Truhlar and co-workers.[30]

3. RESULTS AND DISCUSSION

3.1. Conformational Analysis of the Isolated IDI Molecule. The conformational space of the isolated IDI molecule was investigated through quantum chemical calculations undertaken at the DFT(B3LYP)/6-311++G(d,p) level

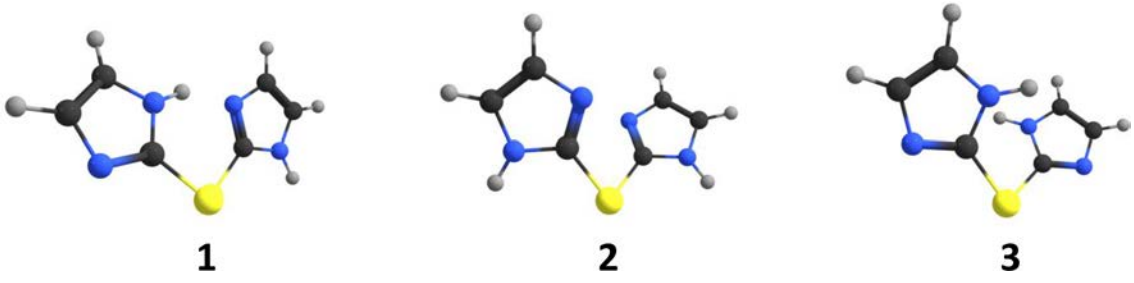

Figure 2. B3LYP/6-311++G(d,p) optimized geometries of the three conformers of IDI. The values of the conformationally relevant C−S−S−C and N(H)−C−S−S dihedral angles are shown in Table 1, together with the relevant energy data.

DOI: 10.1021/acs.cgd.8b00673
Cryst. Growth Des. 2018, 18, 4167−4173

of theory. A detailed conformational search was done by doing relaxed potential energy scans over the conformationally relevant dihedral angles (defined about the C−S and S−S bonds). Three different conformers were found, which are depicted in Figure 2. Their relative energies and conformation-defining dihedral angles are provided in Table 1.

Table 1. Geometrical Parameters (Conformation Defining Dihedral angles; °), Energies (Electronic Energies with and without Zero-Point Correction, ΔE(ZPE), ΔE, and Gibbs Energy, $\Delta G°$; kJ mol^{-1}) and Dipole Moments (μ; Debye) of the Optimized Geometries of IDI Conformers in Gas Phase and in THF

	IDI conformers		
	1	**2**	**3**
	Isolated Molecule (gas phase)		
Dihedral Angles			
C−S−S−C	84.3	75.7	78.4
N(H)−C−S−S	−58.2/119.5	77.5/77.5	−100.3/-100.3
ΔE (ZPE)	-	20.8	22.1
ΔE	-	22.8	23.8
$\Delta G°$	-	15.2	16.7
μ	6.30	1.08	6.28
	in THF		
Dihedral Angles			
C−S−S−C	83.2	85.5	84.6
N(H)−C−S−S	−56.7/120.1	83.8/83.8	−92.1/-92.1
ΔE (ZPE)	-	8.5	9.7
ΔE	-	9.7	9.3
$\Delta G°$	-	4.9	9.8
μ	8.64	2.84	9.66

The conformers contrast essentially in the relative orientation of the imidazole rings, though the C−S−S−C dihedral angle also differs slightly from one conformer to the other. The most stable conformer (form **1**; C_1 symmetry) has the imidazole rings oriented in such a way that the hydrogen atom connected to the nitrogen atom of one of the rings points to the inside of the molecule, while for the other ring the hydrogen points to the outside of the molecule. This arrangement of the imidazole rings allows for the establishment of an intramolecular hydrogen bond interaction between the NH moiety of one ring and the unprotonated nitrogen atom of the second ring (see Figure 2), the N−H, H···N, and N−N···H hydrogen bond parameters being 1.025 Å, 2.020 Å, and 153.6°, respectively. On the other hand, the higher energy conformers **2** and **3** are C_2 symmetry forms, and have the imidazole rings oriented in a way that the NH groups are both pointing to the outside or the inside of the molecule, respectively. Thus, in these forms, the NH···N stabilizing interaction present in the most stable conformer is replaced by destabilizing N/N or NH/HN interactions, respectively (Figure 2). Because of these structural features, conformer **1** is considerably more stable than forms **2** and **3**, which are higher in energy than the conformational ground state by 22.8 and 23.8 kJ mol^{-1}, respectively (when corrected by zero-point vibrational energy, these values reduce slightly to 20.8 and 22.1 kJ mol^{-1}). Very interestingly, for the isolated molecules, the entropy of the higher-energy forms is higher than that of the most stable conformer (458 and 456 J mol^{-1} K^{-1} in **2** and **3**, respectively, vs 435 J mol^{-1} K^{-1} in **1**) as could be expected, because this latter form has a more rigid structure due to the presence of the intramolecular NH···N hydrogen bond. This is also shown in the relative frequencies of the τS−S and τC−S torsional vibrations, which are 82.6/42.8/90.6 cm^{-1}, 23.4/36.3/46.0 cm^{-1}, and 23.7/41.2/42.8 cm^{-1}, respectively, for **1**, **2**, and **3**; i.e., the torsional coordinates are considerably less flexible in conformer **1** than in both **2** and **3**. Because of the larger entropy of conformers **2** and **3**, compared to **1**, the relative Gibbs energies of the conformers are closer, with conformers **2** and **3** having Gibbs energies that are higher than that of form **1** by 15.2 and 16.7 kJ mol^{-1}, respectively (i.e., about 30% smaller when compared with the corresponding relative electronic energies). In any case, the Gibbs energies of conformers **2** and **3** are still considerably large, and these values lead to expected populations of these forms in room temperature (gas phase) conformational equilibrium that are negligible (∼0.3% in total).

Calculations were also performed for the compound in the presence of solvent (THF) by placing the solute in a cavity within the solvent reaction field. For these calculations, the SMD model was used, since it has been shown to properly consider solvation energies.[30] Compared to the gas phase calculations, those considering the solvent predicted only minor changes in the structural parameters of the conformers. The C−S−S−C and N(H)−C−S−S dihedral angles, which correspond to the most flexible coordinates, took the values 83.2/−56.7/120.1°, 85.5/83.8/83.8°, and 84.6/−92.1/−92.1°, respectively for conformers **1**, **2**, and **3** (compare these values with those shown in Table 1 for the isolated molecules). On the other hand, the relative energies change substantially, reducing to less than half compared to the values calculated for the molecules in vacuo (see Table 1). The striking result is that the entropy effects are distinct from those discussed above for the molecules in vacuo. In THF solution, the entropy of conformer **2** is considerably larger than those of forms **1** and **3**, which in turn are nearly equal. The explanation for this comes from the fact that conformer **2** is considerably less polar (calculated dipole moment in gas phase and THF solution: 1.08 and 2.84 D) than forms **1** and **3** (6.30/8.64 D and 6.28/9.66 D for **1** and **3**, respectively), so that its interaction with the solvent is less important allowing the molecule to keep its intrinsic torsional flexibility. On the other hand, the stronger dipolar interactions with solvent in **1** and **3** (and, as discussed above, also the intramolecular H-bond interaction in **1**) reduce the torsional flexibility in these two conformers (the absence of the intramolecular H-bond in **3** is compensated by the larger dipole moment of this conformer, resulting in similar entropies for **1** and **3**).

Taking into account the calculated relative Gibbs energies of the three conformers, the conformational composition of the compound in THF solution at room temperature can be estimated as 86.5% (**1**), 11.9% (**2**), and 1.6% (**3**), i.e., it is predicted that, though conformer **1** still strongly dominates in the equilibrium, the population of conformer **2** also becomes also relevant, while that of conformer **3** is still very small. These calculations were performed because the crystallization of the studied compound in the present study was made from a THF solution, and we wanted to roughly estimate the relative abundance of the conformers in the media prior to crystallization to investigate any possible implications on the structure of the crystal. We will return to this subject in the next section.

3.2. Structure of Crystalline IDI. Neat solid crystalline IDI has been investigated previously by Bazargani et al.[20] The

DOI: 10.1021/acs.cgd.8b00673
Cryst. Growth Des. 2018, 18, 4167−4173

material was prepared by stirring 2-mercaptoimidazole with thallium(I) acetate in a 2:1 molar ratio, in methanol. Suitable crystals for X-ray analysis were obtained by slow evaporation from the methanol solution after 1 week. The structure was determined at room temperature, the crystal being monoclinic, space group $C2/c$, with a = 14.083(3) Å, b = 6.3928(13) Å, c = 9.922(2) Å, and β = 122.29(3)°, and four molecules per unit cell. The asymmetric unit of the crystal contains one-half-molecule and a 2-fold rotation axis bisects the S−S bond. The individual molecules assume a conformation similar to that of conformer **2**, exhibiting a C_2 symmetry, with the C−S−S−C and N(H)−C−S−S dihedral angles being 83.62(17)/86.3(2)/86.3(2)°, respectively. In this crystal, intermolecular N−H···S hydrogen bonds result in the formation of a linear chain along the c-direction, and additional $\pi-\pi$ interactions between imidazole rings of adjacent chains in the a-direction result in the formation of the supramolecular structure.[20] The packing diagram exhibited by this crystal (from now on designated as polymorph I) is shown in Figure 3, which has been built based on the CIF file accompanying the original publication.

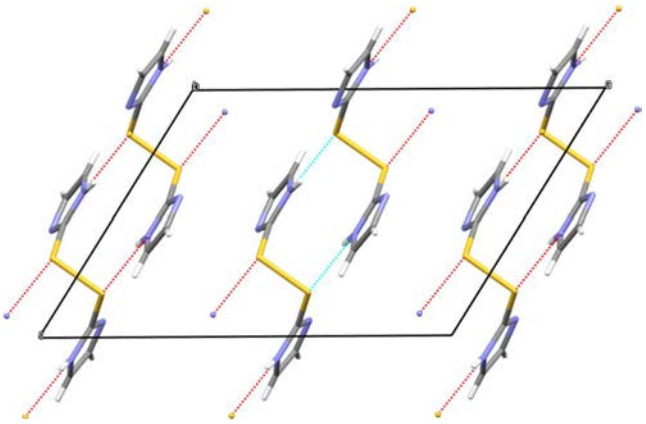

Figure 3. Packing of IDI polymorph I, viewed along the b axis, and with hydrogen bonds shown as dashed lines. The picture was made based on the CIF file accompanying the original publication.[20]

The crystals obtained in the present investigation were found to correspond to a new polymorph of the compound, from now on designated as polymorph II. The structure of the newly synthesized polymorph was found to be considerably more complex than that of polymorph I. The analyzed crystal was a 2-fold rotational twin through the (1 0 3) reciprocal vector or [101] direct vector. It was found to belong to the noncentrosymmetric *Ia* monoclinic space group, with Z = 16 and cell parameters: a = 7.45910(10) Å, b = 44.1680(8) Å, c = 11.3522(2) Å, and β = 103.0240(10)° (Figure 4). The unit cell

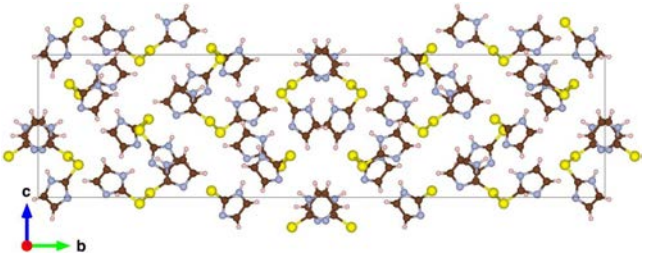

Figure 4. Projection of the crystal structure of IDI polymorph II along the a axis of the unit cell.

contains four symmetry independent molecules (Z' = 4), which assume different conformations. These nonequivalent molecules have been denoted as A−D in Figure 5, which shows the asymmetric unit of the crystal, and in Figure 6, where they have been depicted individually using a common reference perspective to allow a better comparison between their structures.

The crystal structure of polymorph II exhibits several fascinating features, which are emphasized when it is compared with the simpler structure of polymorph I. First, polymorph II exhibits a complex unit cell, with a large number of molecules (Z = 16), which is 4 times larger than the number of molecules in the unit cell of polymorph I (Z = 4). Also, the major stabilizing intermolecular interactions in the two polymorphs are different. While, as mentioned above, in polymorph I intermolecular N−H···S hydrogen bonds play the major role in crystal structure stabilization, polymorph II is stabilized by an extensive three-dimensional network of hydrogen bonds involving the NH groups as proton donors and the bare N atoms as acceptors (N−H···N). A total of 8 strong hydrogen bonds per asymmetric unit could be located in the crystal of polymorph II, which exhaust the molecules' full ability for H-bonding (see Table 2). It is also interesting to note that the N−H···N interactions present in polymorph II are intrinsically more directional than the N−H···S ones (N−H···N hydrogen bonds can be expected to be stronger than N−H···S bonds due to the higher basicity of the N atom compared to S). The existence of more directional intermolecular interactions in the crystal of polymorph II is in agreement with the suggestion[7] that such a feature favors formation of high Z' crystals as a means to optimize competing symmetry-incompatible interactions.

The most interesting structural features of the crystal of polymorph II (Table 3) are, however, (i) the fact that it belongs to the rare set of crystals with $Z' > 1$, exhibiting four symmetry independent molecules (Z' = 4); (ii) the fascinating feature that in the crystal asymmetric unit, the four distinct molecules assume conformations that exhaust the set of possible conformers for the isolated IDI molecule. In fact, while molecules C and D in the crystal are both in a conformation similar to that of the most stable conformer for the isolated molecule (**1**), molecules B and A are similar to the higher energy conformers **2** and **3**, respectively (compare Figures 1 and 6).

In the crystal, all molecules have their 4 H-bond valences fulfilled (two H-bond donor and two H-bond acceptor sites, at the protonated and unprotonated nitrogen atoms, respectively). This means that the NH···N intramolecular hydrogen bond characteristic of conformer **1** (as isolated species) is broken in molecules C and D in the crystal, and replaced by two intermolecular hydrogen bonds. This fact makes the energetic balance associated with the establishment of the intermolecular H-bonds less favorable for C/D than for both A and B molecules, which are in conformation **2** and **3**, respectively, and require only minor structural rearrangements for participation in the intermolecular H-bond network of the crystal. The simultaneous observation of the three conformers of IDI in polymorph II crystal structure can then be considered as a compromise between the greater intrinsic stability of the isolated conformer **1**, and the more efficient in energetic terms and facile packing achieved by the higher energy conformers **2** and **3**.

DOI: 10.1021/acs.cgd.8b00673
Cryst. Growth Des. 2018, 18, 4167−4173

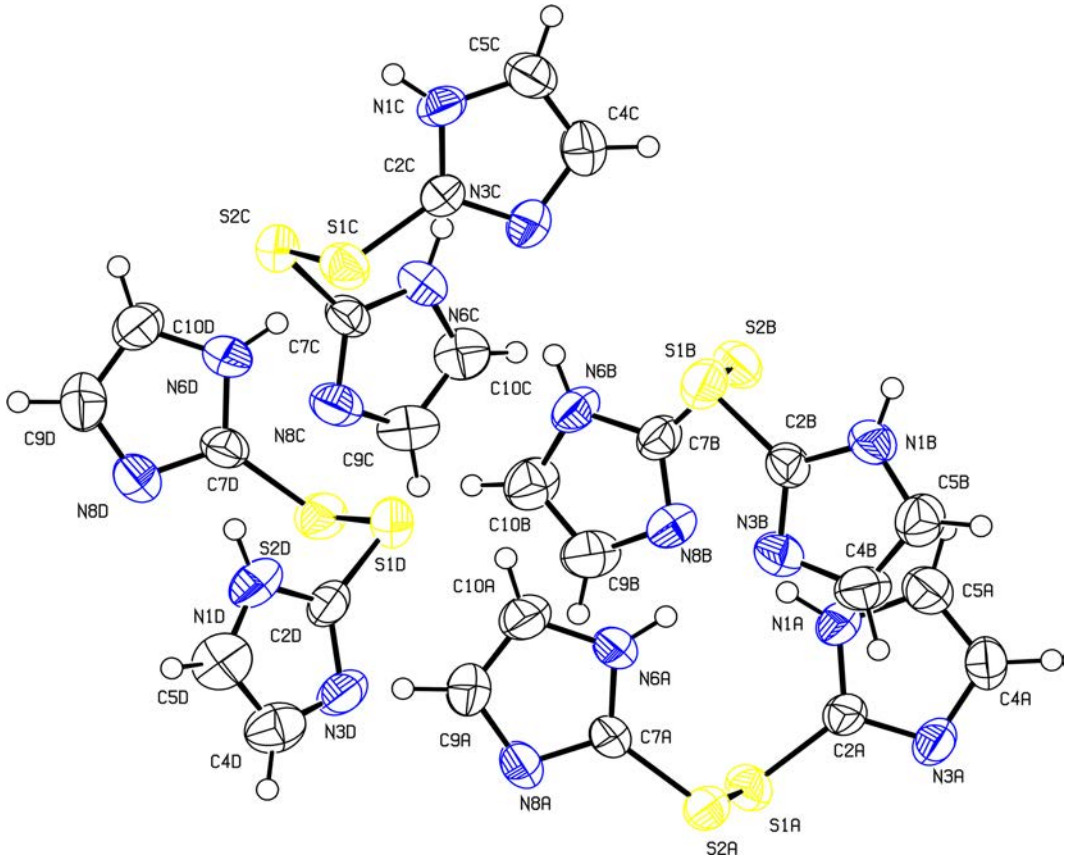

Figure 5. ORTEP drawing of the four symmetry independent molecules of IDI polymorph II, with the adopted atom labeling scheme.

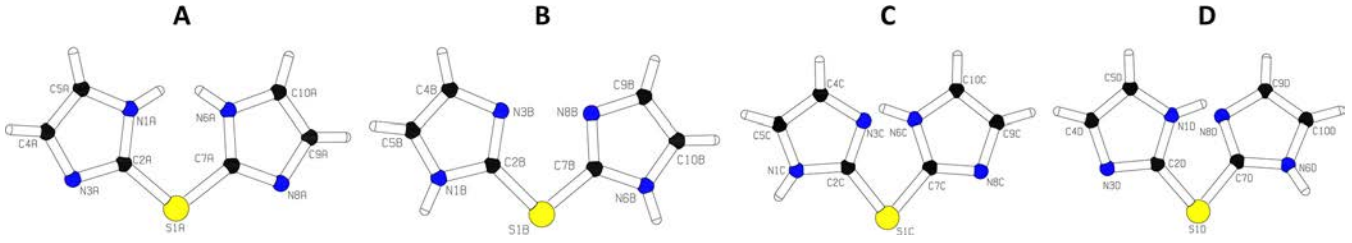

Figure 6. Four symmetry independent molecules of IDI polymorph II viewed along the S−S bond. C−S−S−C, and N(H)−C−S−S torsion angles are A (100.77(19)°, −87.7(3)°, −85.2(4)°); B (95.49(18)°, 91.4(3)°, 95.2(4)°); C: (77.81(18)°, 84.7(3) °, −91.1(3)°); D: (80.21(19)°, −92.1(4)°, 81.0(3)°).

Table 2. Distances and Angles of Intermolecular Hydrogen Bonds in IDI Crystal Structures[a]

Hydrogen Bond		
D−H···*A*	*D*···*A* (Å)	*D*−H···*A* (°)
Polymorph II		
N1(A)-H1(A)···N8(B)	2.783 (4)	169.8
N6(A)-H6(A)···N3(B)	2.795 (5)	168.1
N1(B)−H1(B)···N3(A)$^{(i)}$	2.827 (4)	171.0
N6(B)−H6(B)···N3(C)	2.813 (5)	169.7
N1(C)−H1(C)···N3(D)$^{(ii)}$	2.778 (5)	163.3
N6(C)−H6(C)···N8(A)$^{(ii)}$	2.806 (5)	170.7
N1(D)−H1(D)···N8(D)$^{(iii)}$	2.787 (5)	171.6
N6(D)−H6(D)···N8(C)$^{(iv)}$	2.781 (4)	167.9
Polymorph I[20]		
N−H···S$^{(v)}$	3.227 (3)	153.0

[a]Symmetry codes: (i) 1 + *x*, 1/2 + *y*, 1/2 + *z*; (ii) *x*, *y*, 1 + *z*; (iii) 1/2 + *x*, −*y*, *z*; (iv) 1 + *x*, *y*, *z*. (v) *x*, −*y*, *z* + 1/2.[20]

It is interesting to note that, as already mentioned, in polymorph I the molecules exist as conformer **2**, which constitutes additional evidence that intermolecular interactions in IDI can easily overrule the intrinsic relative stability of the conformers. Furthermore, the fact that conformer **2**, which has a rather small population in equilibrium in solution (negligible in gas phase), is the only constituting unit in polymorph I and is also observed in polymorph II, indicates that, for this molecule, the conformational arrangement of the molecules prior to aggregation does not govern their final conformation in the crystals. The high torsional flexibility of the molecule (as measured by the τS−S and τC−S torsional frequencies; see above) is certainly a determining factor allowing conformational relaxation upon aggregation to take place easily.

CONCLUSIONS

A new polymorph of (2-[(1*H*-imidazol-2-yl) disulfanyl]-1*H*-imidazole was synthesized and its structure determined by

DOI: 10.1021/acs.cgd.8b00673
Cryst. Growth Des. 2018, 18, 4167−4173

Table 3. Summary of Crystal Data for Polymorph II

	Polymorph II
Formula	$C_6H_6N_4S_2$
Formula weight	198.27
Crystal system	Monoclinic
Space group	*Ia*
a, *b*, *c* (Å)	7.45910(10), 44.1680(8), 11.3522(2)
α, β, γ (deg)	90, 103.0240(10), 90
V	3643.81(11)
Z, *Z*′	16, 4
D_{calc} (g/cm^3)	1.446
μ (mm^{-1})	0.534
F(000)	1632
Crystal size	0.17 × 0.20 × 0.40
N_{ref}, N_{par}	8371, 434
Data Collection	
Temperature (K)	293(2)
λ (Å)	0.71073
θ (min, max)	2.8, 27.5
h, *k*, *l*	−9:9, −56:57, −14:14
N_{ref}, N_{par}	8371, 434
Refinement	
R_1 ($I > 2\sigma$), wR_2 ($\|F\|^2$, all), *S*	0.0322, 0.0827, 1.03
$\Delta\rho$ (min, max) (e/Å^3)	−0.20, 0.18
Twin fraction	0.346(2)

single crystal XRD. The crystal results to be a high *Z*′ structure with four symmetry independent molecules (*Z*′ = 4) in the unit cell. Very interestingly, the whole set of possible conformers for the isolated IDI molecule are comprehended in the asymmetric unit, with two molecules assuming a conformation similar to the most stable conformer for the isolated molecule, and the two remaining molecules assuming a conformation identical to each one of the two higher energy conformers.

In the crystal, the two molecules similar to the most stable conformer of IDI exhaust their H-bond valence, establishing four intermolecular H-bonds, whose formation implies the cleavage of the intramolecular N−H···H hydrogen bond that characterizes the structure of the conformer as an isolated species. This fact can be considered as a reason justifying the presence of the higher-energy conformers in the structure of the studied crystal, since in those cases the energetic demand associated with the aggregation of the molecules is smaller (there is no need to break any intramolecular H-bond, but just minor structural rearrangements). Evidently, the conformational changes taking place during aggregation, in particular, the conversion of the most stable conformer (largely dominant in solution) into the higher energy forms, can be facilitated by the high torsional flexibility of the molecule, as reflected in the low frequency torsional τS−S and τC−S vibrations. The greater ease of the higher energy conformers to pack can also be concluded from the fact that in the previously studied[20] polymorph of the compound a high energy conformer is the only form present in the crystal, even though its expected population in equilibrium before crystallization is very small. On the other hand, this is also an indication that, for the investigated molecule, the conformational arrangement of the molecules prior to aggregation does not govern their final conformation in the crystals.

Finally, it shall be also stressed that the observation of the new polymorph with a high *Z*′ structure, where the intermolecular interactions (N−H···H) are stronger and more directional than those existing in polymorph I of the compound (N−H···S), comes in line with the proposition[7] that this is a relevant feature facilitating formation of these type of less frequent crystalline structures.

■ ASSOCIATED CONTENT

Supporting Information

The Supporting Information is available free of charge on the ACS Publications website at DOI: 10.1021/acs.cgd.8b00673.

Summary of data collection, refinement details, and crystallographic results (PDF)

Accession Codes

CCDC 1541935 contains the supplementary crystallographic data for this paper. These data can be obtained free of charge via www.ccdc.cam.ac.uk/data_request/cif, or by emailing data_request@ccdc.cam.ac.uk, or by contacting The Cambridge Crystallographic Data Centre, 12 Union Road, Cambridge CB2 1EZ, UK; fax: +44 1223 336033.

■ AUTHOR INFORMATION

Corresponding Author

*E-mail: embras@qui.uc.pt.

ORCID

Elisa M. Brás: 0000-0003-1365-3628

Rui Fausto: 0000-0002-8264-6854

Notes

The authors declare no competing financial interest.

■ ACKNOWLEDGMENTS

Financial support from Project PTDC/QEQ-QFI/3284/2014 − POCI-01-0145-FEDER-016617, funded by the Portuguese "Fundação para a Ciência e a Tecnologia" (FCT) and FEDER/COMPETE 2020-EU is acknowledged. The Coimbra Chemistry Centre (CQC) and the Center of Physics of the University of Coimbra (CFisUC) are supported by FCT, through the projects UI0313/QUI/2013 and UID/FIS/04564/2016, also cofunded by FEDER/COMPETE 2020-EU. E.B. acknowledges FCT and CMAR for the Research Grant CCMAR/BI/0013/2017, awarded under the Project PTDC/MAR-BIO/4132/2014.

■ REFERENCES

(1) Groom, C. R.; Bruno, I. J.; Lightfoot, M. P.; Ward, S. C. *Acta Crystallogr., Sect. B: Struct. Sci., Cryst. Eng. Mater.* **2016**, *72*, 171.
(2) Caspari, W. A. *J. Chem. Soc.* **1926**, *129*, 2944.
(3) Caspari, W. A. *J. Chem. Soc.* **1927**, *0*, 1093.
(4) Robertson, J. M.; Woodward, I. *Proc. Roy. Soc. London A* **1937**, *162*, 568.
(5) Steed, J. W. *CrystEngComm* **2003**, *5*, 169.
(6) Desiraju, G. R. *CrystEngComm* **2007**, *9*, 91.
(7) Steed, K. M.; Steed, J. W. *Chem. Rev.* **2015**, *115*, 2895.
(8) Mahapatra, S.; Thakur, S. T.; Joseph, S.; Varughese, S.; Desiraju, G. R. *Cryst. Growth Des.* **2010**, *10*, 3191.
(9) Roszak, K.; Katrusiak, A.; Katruziak, A. *Cryst. Growth Des.* **2016**, *16*, 3947.
(10) Chattopadhyay, B.; Hemantha, H. P.; Narendra, N.; Sureshbabu, V. V.; Warren, J. E.; Helliwell, M.; Mukherjee, A. K.; Mukherjee, M. *Cryst. Growth Des.* **2010**, *10*, 2239.
(11) Vishweshwar, P.; McMahon, J. A.; Bis, J. A.; Zaworotko, M. J. *J. Pharm. Sci.* **2006**, *95*, 499.
(12) Aakeröy, C. B.; Salmon, D. J. *CrystEngComm* **2005**, *7*, 439.

DOI: 10.1021/acs.cgd.8b00673
Cryst. Growth Des. 2018, 18, 4167−4173

(13) Good, D. J.; Rodríguez-Hornedo, N. *Cryst. Growth Des.* **2009**, *9*, 2252.
(14) Friščić, T.; Jones, W. *Cryst. Growth Des.* **2009**, *9*, 1621.
(15) Cincic, D.; Friščić, T.; Jones, W. *J. Am. Chem. Soc.* **2008**, *130*, 7524.
(16) Childs, S. L.; Stahly, G. P.; Park, A. *Mol. Pharmaceutics* **2007**, *4*, 323.
(17) Anderson, K. M.; Probert, M. R.; Goeta, A. E.; Steed, J. W. *CrystEngComm* **2011**, *13*, 83.
(18) Taylor, R.; Cole, J. C.; Groom, C. R. *Cryst. Growth Des.* **2016**, *16*, 2988.
(19) Davey, R. J.; Allen, K.; Blagden, N.; Cross, W. I.; Lieberman, H. F.; Quayle, M. J.; Righini, S.; Seton, L.; Tiddy, G. J. T. *CrystEngComm* **2002**, *4*, 257.
(20) Bazargani, M. F.; Talavat, L.; Naderi, S.; Khavasi, H. R. *Acta Crystallogr., Sect. E: Struct. Rep. Online* **2011**, *67*, o2585.
(21) Garcia Ruano, J. L.; Parra, A.; Alemán, J. *Green Chem.* **2008**, *10*, 706.
(22) Nagy, P. *Antioxid. Redox Signal.* **2013**, *18*, 1623.
(23) Winterbourn, C. C.; Hampton, M. B. *Free Radical Biol. Med.* **2008**, *45*, 549.
(24) *SADABS* v 2004/1; Bruker AXS Inc.: Madison, WI, USA, 2001.
(25) Sheldrick, G. M. *Acta Crystallogr., Sect. C: Struct. Chem.* **2015**, *71*, 3.
(26) Frisch, M. J.; Trucks, G. W.; Schlegel, H. B.; Scuseria, G. E.; Robb, M. A.; Cheeseman, J. R.; Scalmani, G.; Barone, V.; Mennucci, B.; Petersson, G. A.; Nakatsuji, H.; Caricato, M.; Li, X.; Hratchian, H. P.; Izmaylov, A. F.; Bloino, J.; Zheng, G.; Sonnenberg, J. L.; Hada, M.; Ehara, M.; Toyota, K.; Fukuda, R.; Hasegawa, J.; Ishida, M.; Nakajima, T.; Honda, Y.; Kitao, O.; Nakai, H.; Vreven, T.; Montgomery, Jr., J. A.; Peralta, J. E.; Ogliaro, F.; Bearpark, M.; Heyd, J. J.; Brothers, E.; Kudin, K. N.; Staroverov, V. N.; Kobayashi, R.; Normand, J.; Raghavachari, K.; Rendell, A.; Burant, J. C.; Iyengar, S. S.; Tomasi, J.; Cossi, M.; Rega, N.; Millam, J. M.; Klene, M.; Knox, J. E.; Cross, J. B.; Bakken, V.; Adamo, C.; Jaramillo, J.; Gomperts, R.; Stratmann, R. E.; Yazyev, O.; Austin, A. J.; Cammi, R.; Pomelli, C.; Ochterski, J. W.; Martin, R. L.; Morokuma, K.; Zakrzewski, V. G.; Voth, G. A.; Salvador, P.; Dannenberg, J. J.; Dapprich, S.; Daniels, A. D.; Farkas, Ö.; Foresman, J. B.; Ortiz, J. V; Cioslowski, J.; Fox, D. J. *Gaussian 09*; Gaussian Inc: Wallingford, CT. 2009.
(27) Becke, A. D. *Phys. Rev. A* **1988**, *38*, 3098.
(28) Lee, C. T.; Yang, W. T.; Parr, R. G. *Phys. Rev. B: Condens. Matter Mater. Phys.* **1988**, *37*, 785.
(29) McLean, A. D.; Chandler, G. S. *J. Chem. Phys.* **1980**, *72*, 5639.
(30) Marenich, A. V.; Cramer, C. J.; Truhlar, D. G. *J. Phys. Chem. B* **2009**, *113*, 6378.

DOI: 10.1021/acs.cgd.8b00673
Cryst. Growth Des. 2018, 18, 4167−4173

Appendix D

Photoinduced Reactivity of an Endoperoxide: Detection of Triplet Diradical Intermediates

Contents

List of Tables

List of Figures

The Appendix D is based on the previously published article:

E. M. Brás, L. I. L. Cabral, P. S. M. Amado, M. Abe, R. Fausto, M. L. S. Cristiano, Photoinduced Reactivity in a Dispiro-1,2,4-trioxolane: Adamantane Ring Expansion and First Direct Observation of the Long-Lived Triplet Diradical Intermediates., *J. Phys. Chem. A*, 2020, 124, 21, 4202-4210.

1 Chemicals[1]

Adamantane-2-spiro-3'-8'-oxo-1',2',4'-trioxaspiro[4,5]decane 1 was obtained by Griesbaum coozonolysis[2–4] reactions between O-methyl 2-adamantanone oxime and the 4-substituted cyclohexanone. Ozone (produced with an ozone generator Sander Labor-Ozonizator 301.7 (0.5 L/min O2, 140 V) was passed through a solution of dichloromethane at - 78 ° C and flushed into a solution of O-methyl 2-adamantanone oxime (1.00 g, 5.58 mmol) and 1,4-cyclohexanedione (0.65 g, 5.58 mmol) in pentane (60 mL) and dichloromethane (40 mL) at 0 ° C. After consumption of the starting material, the solution was flushed with nitrogen for 5 min and concentrated under reduced pressure at room temperature to give a crude material. Purification by flash chromatography using a mixture of EtOAc/n-hexane, gave the pure compound as a colorless solid (0.66 g, 42% yield): m.p. 127-128 ° C; 1H-NMR (400 MHz, $CDCl_3$): δ 1.69-2.02 (m, 14H), 2.14 (t, J = 6.9 Hz, 4H), 2.51 (t, J = 7.0 Hz, 4H) ppm; ^{13}C-NMR (100 MHz, $CDCl_3$): 25.9, 26.31, 31.09, 32.59, 34.25, 35.70, 36.18, 37.35, 106.46, 111.95, 208.90 ppm; MS (EI, m/z): 278.9 [M]+.
The *O*-methyl 2-adamantanone oxime (precursor of 1) was obtained as follows: to a solution of 2-adamantanone (4.00 g, 26.63 mmol) in methanol (20 mL), under stirring, was added pyridine (3.40 mL, 42.03 mmol) and methoxylamine hydrochloride (2.846 g, 34.08 mmol). The reaction mixture was stirred at room temperature for 72 h. The final mixture was concentrated and then diluted with dichloromethane (20 mL) and water (30 mL). The organic layer was separated, and the aqueous layer was washed with dichloromethane (2x20 mL). The combined organic layers were washed with aqueous HCl (1 M; 20 mL x2), then with brine (20 mL). The final organic extract was dried with $MgSO_4$, filtered, then concentrated under reduced pressure to give *O*-methyl-2-adamantanone oxime (4.20 g, 88 % yield) as a colorless solid (m.p. 69-70 ° C). ^{1}H-NMR (400 MHz, $CDCl_3$): δ 3.81 (s, 3H), 3.46 (s,1H), 2.54 (s, 1H), 2.00 - 1.78 (m, 12H) ppm. ^{13}C NMR (101 MHz, $CDCl_3$) δ: 166.74, 60.96, 39.03, 37.64, 36.52, 36.24, 29.53, 27.85 ppm. MS (MALDI-TOF, m/z): 180.02 [M]+.

4-Oxahomoadamantan-5-one 4, was synthesized using the procedure described by Renoud-Grappin et al.[5].To a suspension of 2-adamantanone (0.5 g, 3.33 mmol) and $NaHCO_3$ (0.31 g, 3.66 mmol) in anhydrous dichloromethane (10 mL) was added a solution of *m*-chloroperoxyben -zoic acid (*m*-CPBA) (0.86 g, 4.99 mmol) in anhydrous dichloromethane (5 mL). The reaction mixture was stirred at room temperature, in the dark, until consumption of the starting compound. Then the organic mixture was washed with water (3x15 mL), brine (2x15 mL) and dried over with $MgSO_4$. The organic layer was then evaporated to dryness under reduced pressure. Purification of the residue by flash chromatography using a mixture of EtOAc/n-hexane, gave the required product as a white solid (0.35 g, 63 % yield): m.p: 288-290 ° C. ^{1}H NMR (400 MHz, $CDCl_3$): δ = 4.49 (tt, J = 4.4, 2.4 Hz, 1H), 3.10 â 3.05 (m, 1H), 2.16 â 1.58 (m, 12H). ^{13}C NMR (101 MHz, $CDCl_3$): δ = 178.99, 73.17, 41.24, 35.78, 33.82, 30.96, 25.85. HRMS (CI, m/z) calcd for $C_{10}H_{15}O_2$ (M+H)+: 167.1067; found 167.1072.

1,4-Cyclohexanedione 5 was purchased from Sigma Aldrich UK and used without further purification. All compounds prepared were kept in the freezer and shielded from the light during storage, remaining stable under these conditions.

2 Computations of Chapter 6[1]

2.1 Cartesian Coordinates

Table D1: Cartesian coordinates of conformer 1A of peroxide 1 computed at B3LYP/6-311++G(3df,3pd) level of theory.

Atom	X	Y	Z
C	4.248705	0.260359	0.219177
H	4.944712	-0.401821	0.741436
H	4.839276	1.085952	-0.187019
C	3.194559	0.799417	1.201852
H	3.688119	1.337431	2.014325
C	3.551985	-0.500310	-0.922473
H	4.299138	-0.883472	-1.621066
C	2.744790	-1.674767	-0.342610
H	3.406088	-2.365821	0.185799
H	2.266372	-2.239291	-1.144536
C	2.385757	-0.373508	1.783081
H	1.646760	-0.009426	2.497764
H	3.045283	-1.059765	2.319731
C	1.687670	-1.141744	0.644434
H	1.089157	-1.959686	1.047552
C	0.744361	-0.180458	-0.086880
C	2.238178	1.751033	0.461840
H	2.791907	2.597372	0.048288
H	1.497680	2.156059	1.152700
C	2.592990	0.446940	-1.663394
H	3.146814	1.283138	-2.097013
H	2.103639	-0.076036	-2.486073
C	1.538563	0.994097	-0.682826
H	0.840359	1.649662	-1.204113
O	-0.295435	0.288060	0.777977
O	0.033613	-0.925076	-1.082266
O	-1.166535	-0.132452	-1.247234
C	-1.537324	0.104893	0.114300
C	-2.291576	-1.085271	0.710528
C	-2.364354	1.385118	0.150849
C	-3.668525	-1.285357	0.058039
H	-2.402027	-0.903612	1.781027
H	-1.682376	-1.979783	0.594121
C	-3.746510	1.211729	-0.498968
H	-2.476514	1.662273	1.200097
H	-1.803005	2.179863	-0.337885
C	-4.482872	-0.006094	0.032152
H	-4.242683	-2.057458	0.565923
H	-3.524882	-1.600412	-0.979875
H	-4.368065	2.091602	-0.346482
H	-3.622458	1.072007	-1.577079
O	-5.634355	0.042561	0.3962460

Table D2: Cartesian coordinates of 1B of peroxide 1 and computed at B3LYP/6-311++G(3df,3pd) level of theory.

Atom	X	Y	Z
C	-3.947020	-0.976462	-0.037306
H	-4.522303	-1.359909	0.809822
H	-4.566276	-1.109083	-0.928500
C	-2.634850	-1.766283	-0.185205
H	-2.856092	-2.826225	-0.329309
C	-3.633234	0.515623	0.168964
H	-4.563921	1.077664	0.273594
C	-2.783832	0.692728	1.439557
H	-3.326714	0.324646	2.313553
H	-2.575702	1.749612	1.613145
C	-1.782683	-1.590263	1.083819
H	-0.856946	-2.161445	1.002472
H	-2.320123	-1.967665	1.957083
C	-1.468016	-0.097388	1.298943
H	-0.841879	0.037436	2.181969
C	-0.690360	0.420408	0.083845
C	-1.846665	-1.236374	-1.395852
H	-2.430036	-1.361258	-2.311240
H	-0.922920	-1.802653	-1.522666
C	-2.843833	1.048155	-1.038957
H	-3.434550	0.944620	-1.952372
H	-2.628610	2.109970	-0.913481
C	-1.530927	0.257624	-1.194453
H	-0.953917	0.643887	-2.035114
O	0.575534	-0.236425	-0.043541
O	-0.329385	1.781419	0.333832
O	0.831592	1.944167	-0.518004
C	1.574216	0.767612	-0.213215
C	2.460379	0.456347	-1.413314
C	2.398729	0.930100	1.065243
C	3.318276	-0.794594	-1.164134
H	1.832001	0.321164	-2.291917
H	3.102443	1.320302	-1.594093
C	3.237706	-0.323063	1.355898
H	1.731102	1.149345	1.896063
H	3.052009	1.794648	0.932050
C	4.068852	-0.741125	0.156565
H	4.035349	-0.949652	-1.967436
H	2.662672	-1.669646	-1.125126
H	3.899710	-0.176072	2.206740
H	2.566067	-1.154244	1.590820
O	5.239536	-1.028376	0.244158

Table D3: Cartesian coordinates of 4-oxahomoadamantan-5-one 4 computed at B3LYP/6-311++G(3df,3pd) level of theory.

Atom	X	Y	Z
C	-1.851176	-1.143844	0.000000
H	-2.880559	-0.775858	0.000000
H	-1.903972	-2.235383	0.000000
C	-1.112108	-0.650698	1.253927
H	-1.635735	-1.002797	2.145869
C	-1.112108	-0.650698	-1.253927
H	-1.635735	-1.002797	-2.145869
C	-1.112108	0.884443	-1.275177
H	-2.141636	1.236445	-1.383517
H	-0.556740	1.267250	-2.133553
C	-1.112108	0.884443	1.275177
H	-0.556740	1.267250	2.133553
H	-2.141636	1.236445	1.383517
C	0.307960	-1.233265	1.274922
H	0.236889	-2.320322	1.363523
H	0.852837	-0.885592	2.155253
C	0.307960	-1.233265	-1.274922
H	0.236889	-2.320322	-1.363523
H	0.852837	-0.885592	-2.155253
C	1.120431	-0.923835	0.000000
H	2.004785	-1.557923	0.000000
C	-0.547781	1.514191	0.000000
H	-0.792400	2.575115	0.000000
O	0.902084	1.561622	0.000000
C	1.714371	0.481323	0.000000
O	2.903030	0.667292	0.000000

Table D4: Cartesian coordinates of conformer 5A of 1,4-cyclohexanedione 5 computed at B3LYP/6-311++G(3df,3pd) level of theory.

Atom	X	Y	Z
C	0.062145	1.462478	0.000000
C	0.335137	0.694764	1.281987
C	0.335137	0.694764	-1.281987
C	-0.335137	-0.694764	1.281987
H	1.419373	0.566988	1.362503
H	0.008144	1.294612	2.128420
C	-0.335137	-0.694764	-1.281987
H	1.419373	0.566988	-1.362503
H	0.008144	1.294612	-2.128420
C	-0.062145	-1.462478	0.000000
H	-0.008144	-1.294612	2.128420
H	-1.419373	-0.566988	1.362503
H	-0.008144	-1.294612	-2.128420
H	-1.419373	-0.566988	-1.362503
O	0.335137	-2.602788	0.000000
O	-0.335137	2.602788	0.000000

Table D5: Cartesian coordinates of conformer 5B of 1,4-cyclohexanedione computed at B3LYP/6-311++G(3df,3pd) level of theory.

Atom	X	Y	Z
C	0.000000	0.000000	1.503902
C	-0.322813	1.247142	0.695162
C	0.322813	-1.247142	0.695162
C	0.322813	1.247142	-0.695162
H	-0.037549	2.119961	1.279800
H	-1.413244	1.283813	0.597565
C	-0.322813	-1.247142	-0.695162
H	1.413244	-1.283813	0.597565
H	0.037549	-2.119961	1.279800
C	0.000000	0.000000	-1.503902
H	0.037549	2.119961	-1.279800
H	1.413244	1.283813	-0.597565
H	-1.413244	-1.283813	-0.597565
H	-0.037549	-2.119961	-1.279800
O	0.000000	0.000000	-2.710798
O	0.000000	0.000000	2.710798

Table D6: Cartesian coordinates of conformer 5C of 1,4-cyclohexanedione computed at B3LYP/6-311++G(3df,3pd) level of theory.

Atom	X	Y	Z
C	1.292405	0.775091	0.383336
C	0.000000	1.409472	-0.100076
C	-1.292405	0.775091	0.383336
C	-1.292405	-0.775091	0.383336
H	0.000000	-1.409472	-0.100076
H	1.292405	-0.775091	0.383336
C	-1.452694	1.153073	1.397238
H	-2.100177	1.170012	-0.227927
H	-1.452694	-1.153073	1.397238
C	-2.100177	-1.170012	-0.227927
H	2.100177	-1.170012	-0.227927
H	1.452694	-1.153073	1.397238
H	2.100177	1.170012	-0.227927
H	1.452694	1.153073	1.397238
O	0.000000	-2.399061	-0.792274
O	0.000000	2.399061	-0.792274

2.2 Structures and energies of 4 and 5[1]

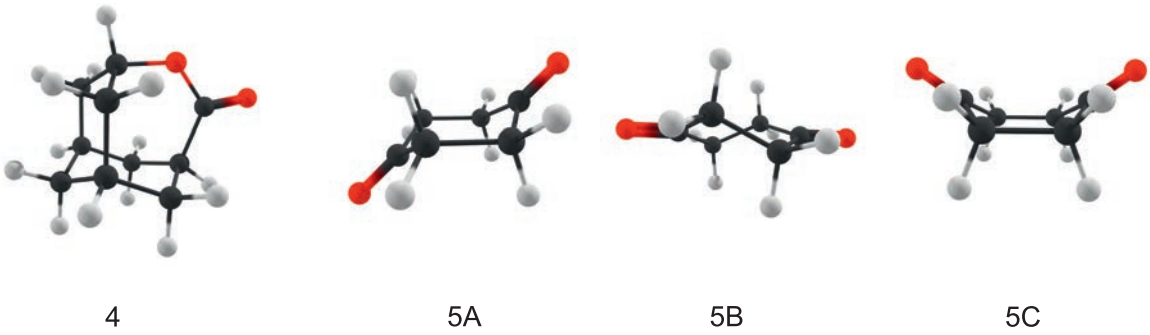

Figure D1: B3LYP/6-311++G(3df,3pd) optimized structures of 4-oxahomoadamantan-5-one 4, and of the three conformers of 1,4-cyclohexanedione 5. Reprinted and adapted from E. M. Brás, L. I. L. Cabral, P. S. M. Amado, M. Abe, R. Fausto, M. L. S. Cristiano, Photoinduced Reactivity in a Dispiro-1,2,4-trioxolane: Adamantane Ring Expansion and First Direct Observation of the Long-Lived Triplet Diradical Intermediates., *J. Phys. Chem. A*, 2020, 124, 21, 4202-4210. Copyright 2020 American Chemical Society.

Table D7: B3LYP/6-311++G(3df,3pd) and M06-2X/6-311++G(3df,3pd) computed energies of 4-oxa-homoadamantan-5-one 4 1,4-cyclohexanedione 5 (5A,5B and 5C conformers) with zero-point energies (ZPVE) and estimated room temperature (298.15 K) per cent populations in the gas phase equilibrium.

B3LYP	4	5A	5B	5C
E / hartree	-540.1494392	-384.0403014	-384.0404968	-384.0318899
E / kJ mol^{-1}	-1418162.3527273	-1008297.8114045	-1008298.3244088	-1008275.7268301
ZPVE/ kJ mol^{-1}	601.4504	344.5485	342.6121	342.2655
E / kJ mol^{-1} with (ZPVE)	-1417560.9023273	-1007953.2629045	-1007955.7123088	-1007933.4613301
E / kJ mol^{-1}	-	2.45	0.0	22.25
Pop. (298.15 K)	100.0 %	27.1 %	72.9 %	0.0 %
M06-2X	4	5A	5B	5C
E/ hartree	-539.9285172920	-383.8745007	-383.8748659	-383.8651966
E/ kJ mol^{-1}	-1417582.3222000	-1007862.5015695	-1007863.4605543	-1007838.0736628
ZPE/ kJ mol^{-1}	607.9650	348.4905	346.6623	346.6689
E/ kJ mol^{-1} with (ZPVE)	-1416974.3572000	-1007514.0110695	-1007516.7982544	-1007491.4047628
E/ kJ mol^{-1}	-	2.79	0.0	25.39
Pop. (298.15 K)	100.0 %	24.5 %	75.5 %	0.0 %

3 Matrix-isolation Experiments[1]

3.1 IR spectra of matrix-isolated 1

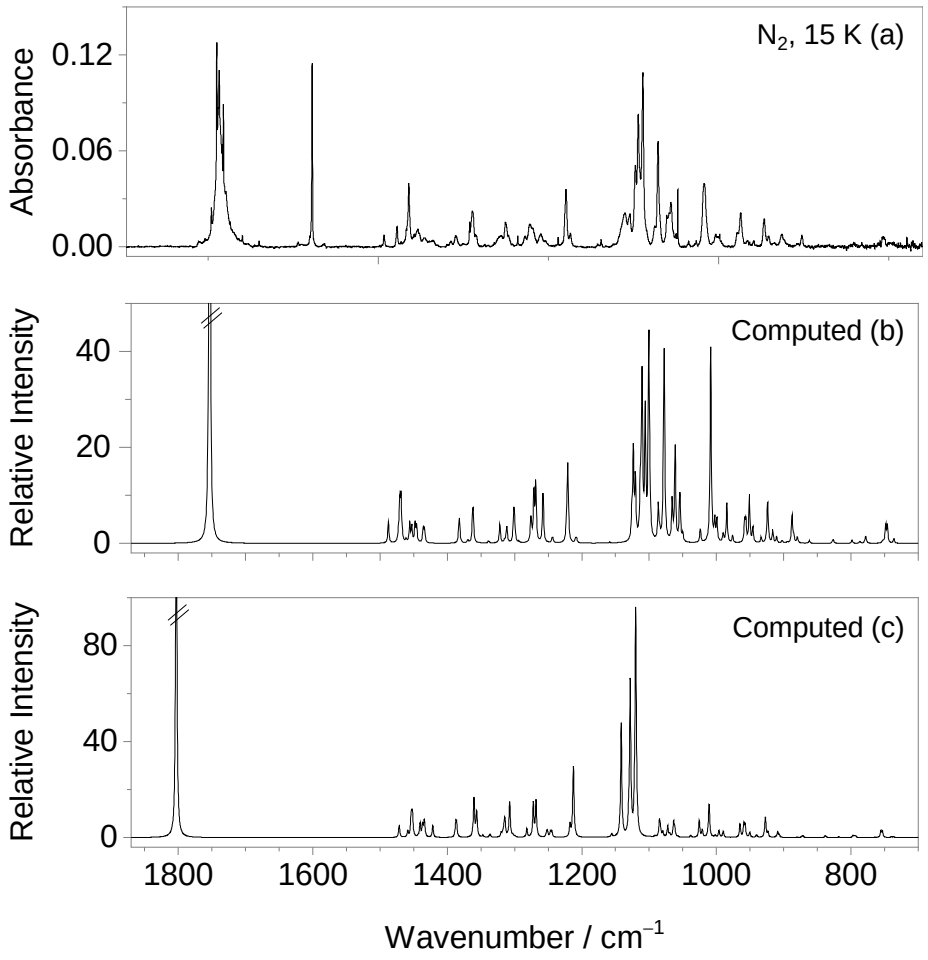

Figure D2: Infrared spectra of 1: (a) isolated in a N2 matrix (15 K); (b), (c) computed at the B3LYP and M06-2X/6-311++G(3df,3pd) levels. The computed IR spectra are shown as the 1:1 sum of the spectra of the two conformers of 1 (1A and 1B) and were scaled as referred in the msin text. Reprinted and adapted from E. M. Brás, L. I. L. Cabral, P. S. M. Amado, M. Abe, R. Fausto, M. L. S. Cristiano, Photoinduced Reactivity in a Dispiro-1,2,4-trioxolane: Adamantane Ring Expansion and First Direct Observation of the Long-Lived Triplet Diradical Intermediates., *J. Phys. Chem. A*, 2020, 124, 21, 4202-4210. Copyright 2020 American Chemical Society.

Table D8: IR spectra (in the 1800-630 cm^{-1} spectral range) of matrix-isolated 1 (at 15 K) along with the computed harmonic vibrational frequencies (cm^{-1}) and intensities (km mol^{-1}; in parenthesis) at both B3LYP and M06-2X/6-311+G(3df,3pd) levels.

Experiment		B3LYP		M06-2X	
Ar matrix[a]	N_2 matrix[a]	1A	1B	1A	1B
1746/1736/1726 (vs)	1745/1737/1734/1728/1724 (vs)	1759 (281)	1759 (277)	1805 (291)	1805 (289)
1472 (m)	1473 (m)	1492 (7)	1492 (7)	1473 (8)	1473 (8)
		1475 (12)	1477 (6)	1455 (13)	1460 (8)
1455 (s)	1459/1455 (s)	1473 (14)	1475 (12)	1454 (8)	1455 (13)
		1472 (3)	1473 (14)	1453 (12)	1453 (15)
-	-	1466 (1)	1466 (1)	1446 (1)	1445 (1)
1446/1442 (m)	1447/1443 (m)	1461 (0.03)	1460 (6)	1439 (0.2)	1442 (18)
		1457 (10)	1460 (7)	1438 (15)	1439 (0.1)
1439/1431 (w)	1440/1433 (w)	1452 (13)	1450 (11)	1436 (14)	1435 (12)
1423/1419 (w)	1423/1420 (w)	1440 (9)	1438 (9)	1423 (8)	1423 (8)
1394/1389/1385 (m)	1393/1386 (m)	1387 (10)	1386 (10)	1389 (17)	1388 (17)
1375 (vw)	1376 (vw)	1374 (1)	1373 (1)	1362 (28)	1362 (26)
		1367 (17)	1366 (13)	1358 (19)	1357 (17)
1365/1360/1356 (vw)	1366/1362/1357 (vw)	1365 (1)	1365 (1)	1354 (0.02)	1355 (0.2)
		1361 (1)	1361 (0.1)	1348 (1)	1349 (1)
-	-	1356 (0.2)	1355 (0.1)	1339 (1)	1338 (0.2)
1344 (vw)	1344/1339 (vw)	1343 (1)	1342 (1)	1338 (2)	1337 (2)
-	1330 (vw)	1335 (0.1)	1334 (0.1)	1321 (5)	1321 (1)
-	-	1332 (0.02)	1332 (0.01)	1319 (5)	1317 (9)
1321/1319 (s)	1322/1319 (s)	1326 (6)	1326 (7)	1316 (12)	1316 (11)
1315/1311/1308 (m)	1313/1309 (m)	1319 (1)	1319 (1)	1313 (0.1)	1313 (1)
		1316 (6)	1315 (6)	1312 (1)	1311 (0.2)
1303 (vw)	1303 (vw)	1305 (9)	1305 (10)	1309 (25)	1308 (24)
		1304 (8)	1304 (5)	1304 (2)	1305 (1)
1283 (s)	1284 (s)	1280 (10)	1279 (8)	1283 (4)	1283 (7)
1277/1271 (m)	1277/1272 (m)	1275 (33)	1272 (37)	1274 (46)	1269 (48)
1259/1253 (m)	1261/1255 (m)	1261 (16)	1262 (19)	1254 (0.1)	1255 (1)
1244 (vw)	1245/1243 (vw)	1248 (2)	1247 (3)	1248 (7)	1246 (8)
1224 (s)	1224 (s)	1226 (5)	1226 (9)	1219 (5)	1219 (13)
		1225 (26)	1224 (26)	1214 (49)	1214 (46)
1218 (vw)	1218 (vw)	1213 (3)	1211 (3)	1213 (4)	1212 (3)
1165 (vw)	1166 (vw)	1162 (0.2)	1162 (0.4)	1156 (1)	1157 (3)
1136/1133/1130 (m)	1138/1130 (m)	1129 (15)	1128 (11)	1143 (122)	1143 (31)
		1127 (52)	1124 (39)	1131 (23)	1129 (35)
		1116 (10)	1117 (25)	1129 (169)	1123 (5)
1122 (s)	1122 (s)	1114 (67)	1114 (11)	1120 (61)	1121 (276)
		1114 (40)	1114 (1)	1101 (0.1)	1101 (0.1)
1117/1111 (s)	1118/1111 (s)	1109 (84)	1104 (126)	1099 (0.2)	1100 (0.3)
1111 (s)	1111 (s)	1103 (4)	1102 (26)	1093 (1)	1092 (1)
1093 (m)	1094 (m)	1090 (23)	1088 (5)	1086 (20)	1084 (11)
1088 (s)	1089 (s)	1082 (48)	1081 (99)	1079 (0.2)	1081 (7)
		1065 (62)	1069 (27)	1074 (15)	1071 (4)
1072/1070 (m)	1073/1069 (m)	1058 (22)	1057 (14)	1065 (19)	1063 (11)
		1053 (2)	1053 (3)	1058 (0.4)	1058 (1)
1034 (w)	1033 (w)	1027 (6)	1028 (3)	1039 (3)	1039 (0.3)
1021 (s)	1021 (s)	1012 (64)	1011 (67)	1027 (22)	1022 (10)
1005/1004 (w)	1004/1001 (w)	1002 (15)	1006 (14)	1012 (21)	1012 (29)
		993 (3)	993 (3)	1005 (0.4)	1003 (3)
1000 (w)	999 (w)	988 (27)	979 (4)	997 (4)	997 (6)
973 (w)	973 (w)	959 (13)	961 (14)	991 (3)	991 (6)
967/958 (m/w)	968/958/957 (m/w)	949 (10)	954 (31)	960 (17)	966 (17)
948 (w)	948 (w)	936 (3)	936 (1)	951 (7)	958 (15)
933/926 (m/w)	935/926 (m/w)	926 (20)	927 (12)	942 (3)	941 (1)
917/908 (vw/w)	918/907/904 (vw/w)	913 (4)	919 (8)	928 (19)	929 (11)
885/884/878 (vw)	885/878 (vw)	888 (4)	890 (19)	908 (3)	910 (7)
		882 (0.2)	883 (4)	881 (0.2)	881 (0.5)
		881 (0.4)	881 (0.2)	874 (1)	873 (0.3)
841 (vw)	841 (vw)	830 (1)	829 (2)	839 (1)	838 (2)
807/801 (vw)	807/801 (vw)	801 (1)	801 (1)	819 (1)	819 (1)
		789 (1)	789 (1)	798 (1)	798 (1)
789 (vw)	790 (vw)	780 (3)	781 (3)	794 (2)	796 (2)
764 (vw)	763 (vw)	756 (1)	754 (1)	766 (0.2)	765 (0.2)
757 (w)	758 (w)	748 (11)	751 (11)	754 (8)	756 (9)
		738 (2)	739 (1)	738 (1)	741 (1)
670 (vw)	670 (vw)	668 (1)	667 (3)	667 (2)	668 (3)
639/630 (vw)	638/630 (vw)	633 (1)	636 (3)	641 (3)	641 (3)

[a] Bands indicated in color are assigned to individual conformers (blue to 1A and green to 1B); those in black color are assigned to the both forms. Experimental intensities are given in qualitative terms: vs - very strong, s - strong, m - medium, w - weak, vw - very weak; non-observed features are indicated by a hyphen.

3.2 UV-vis absorption spectrum of 1

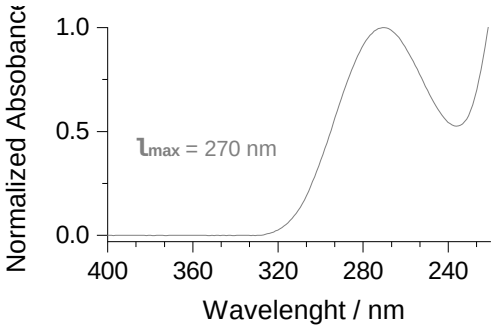

Figure D3: UV-vis absorption spectrum of 1 in ethanol solution. Reprinted and adapted from E. M. Brás, L. I. L. Cabral, P. S. M. Amado, M. Abe, R. Fausto, M. L. S. Cristiano, Photoinduced Reactivity in a Dispiro-1,2,4-trioxolane: Adamantane Ring Expansion and First Direct Observation of the Long-Lived Triplet Diradical Intermediates., *J. Phys. Chem. A*, 2020, 124, 21, 4202-4210. Copyright 2020 American Chemical Society.

3.3 IR spectra of photo-generated 4 and 5

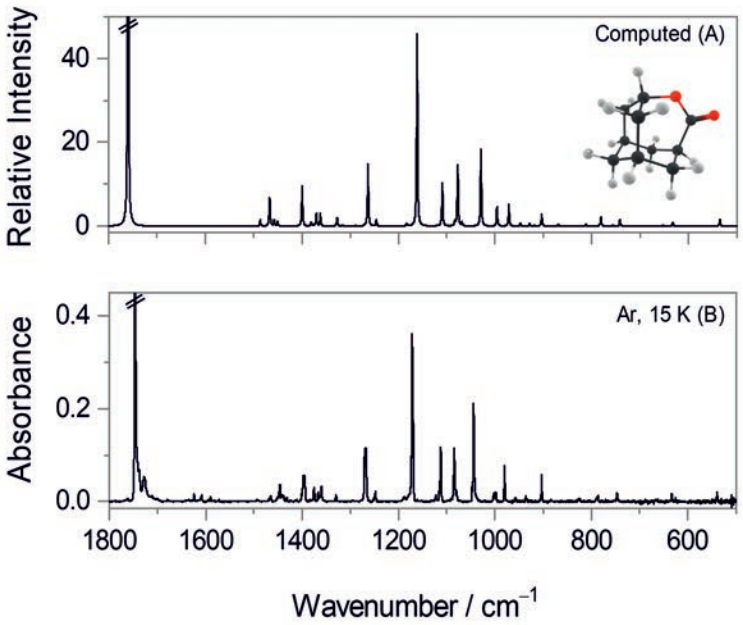

Figure D4: (A) B3LYP/6-311++G(3df,3pd) infrared computed spectra of 4-oxahomoadamantan-5-one 4. (B) Experimental infrared spectra of matrix isolated authentic sample of oxahomoadamantan-5-one 4 isolated in argon matrix. Reprinted and adapted from E. M. Brás, L. I. L. Cabral, P. S. M. Amado, M. Abe, R. Fausto, M. L. S. Cristiano, Photoinduced Reactivity in a Dispiro-1,2,4-trioxolane: Adamantane Ring Expansion and First Direct Observation of the Long-Lived Triplet Diradical Intermediates., *J. Phys. Chem. A*, 2020, 124, 21, 4202-4210. Copyright 2020 American Chemical Society.

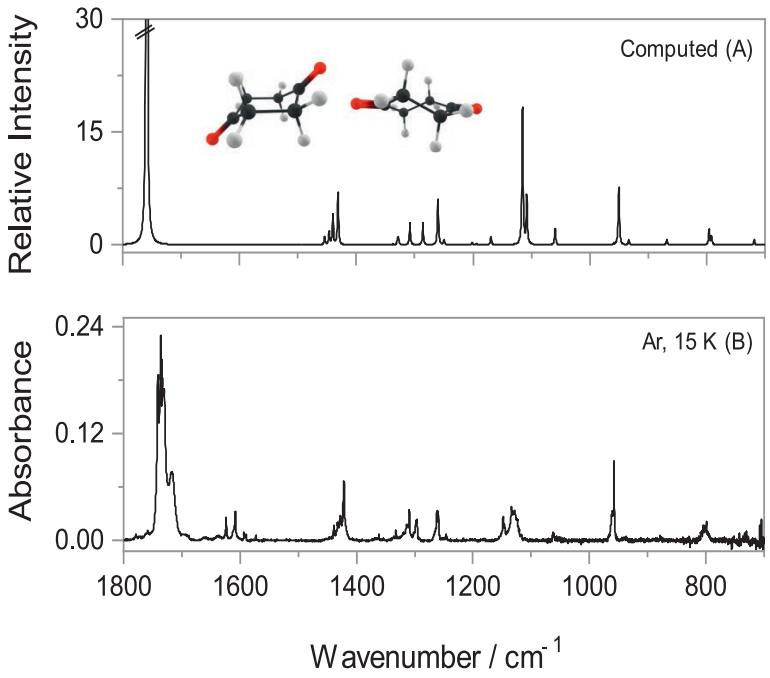

Figure D5: (A) B3LYP/6-311++G(3df,3pd) infrared computed spectra of 1,4-cyclohexanedione 5 . (B) Experimental infrared spectra of matrix isolated authentic sample of 1,4-cyclohexanedione 5 (isomers 5A and 5B) isolated in an argon matrix. Reprinted and adapted from E. M. Brás, L. I. L. Cabral, P. S. M. Amado, M. Abe, R. Fausto, M. L. S. Cristiano, Photoinduced Reactivity in a Dispiro-1,2,4-trioxolane: Adamantane Ring Expansion and First Direct Observation of the Long-Lived Triplet Diradical Intermediates., *J. Phys. Chem. A*, 2020, 124, 21, 4202-4210. Copyright 2020 American Chemical Society.

Table D9: Experimental IR spectra (1800-450 cm^{-1}) of the photogenerated 4-oxahomoadamantan-5-one 4 (in Ar and N2 matrices; 15 K) with the experimental IR spectrum of the authenthic sample (N_2 and Ar matrices; 15 K). B3LYP/6-311+G(3df,3pd) and M06-2X/6-311+G(3df,3pd) computed harmonic vibrational frequencies (cm^{-1}) and intensities (in parenthesis; km mol^{-1}) are also shown. .

Photolysis of 1 Ar matrix[a]	authentic N_2 matrix[a]	authentic Ar matrix[a]	B3LYP	sym.	M06-2x	sym
1736/1730 (vs)	1737/1734/1730/1728/1726 (vs)	1747 (vs)	1757 (407)	A'	1805 (437)	A'
1465 (w)	1467 (w)	1465 (w)	1484 (5)	A'	1469 (6)	A'
1446 (m)	1448 (m)	1446 (m)	1466 (12)	A"	1449 (13)	A"
			1465 (13)	A'	1448 (16)	A'
1442 (w)	-	1442/1439 (w)	1456 (4)	A'	1440 (2)	A'
1432 (w)	-	1431 (w)	1449 (3)	A"	1432 (3)	A"
1401/1397 (m)	1402/1399 (m)	1401/1395 (m)	1398 (31)	A'	1407 (55)	A'
-	-	-	1381 (0.1)	A"	1378 (1)	A"
1376 (w)	1376 (vw)	1376/1375 (w)	1379 (3)	A'	1372 (15)	A'
			1374 (1)	A"	1364 (2)	A"
1368 (w)	1368 (w)	1366 (w)	1369 (9)	A'	1360 (12)	A'
1361 (w)	-	1363/1360 (w)	1360 (9)	A'	1355 (5)	A'
-	1357(vw)	1356 (w)	1349 (0.1)	A"	1335 (0.2)	A"
1341 (w)	-	1340 (w)	1339 (0.01)	A"	1331 (6)	A'
1332 (w)	1333 (w)	1330/1329 (w)	1326 (6)	A'	1323 (0.1)	A"
-	-	1320 (w)	1315 (0.5)	A'	1319 (0.1)	A'
			1314 (0.5)	A"	1319 (1)	A"
1294 (vw)	-	1294 (w)	1287 (0.3)	A"	1293 (1)	A"
1272 (m)	1273 (m)	1270/1268 (m)	1263 (1)	A"	1272 (90)	A"
			1262 (47)	A'	1268 (1)	A"
1250/1249 (w)	1251 (m)	1248/1247 (w)	1245 (5)	A'	1247 (11)	A'
1188 (w)	1189 (vw)	1188 (w)	1182 (2)	A"	1180 (142)	A'
1175/1172 (vs)	1176/1173 (vs)	1172/1170 (vs)	1160 (145)	A'	1179 (2)	A"
-	-	-	1131 (0.001)	A"	1119 (0.04)	A"
-	-	1122 (w)	1120 (0.5)	A"	1114 (30)	A'
1113 (m)	-	1116/1113 (m)	1108 (33)	A'	1108 (1)	A"
-	-	1092 (w)	1082 (4)	A"	1092 (1)	A"
1088 (m)	1083 (vw)	1086/1085 (m)	1076 (47)	A'	1079 (34)	A'
-	-	1079 (w)	1068 (3)	A"	1076 (4)	A"
-	-	-	1044 (0.01)	A"	1060 (32)	A'
1044 (s)	1044 (s)	1047/1044 (s)	1028 (59)	A'	1058 (0.4)	A"
1007/1000 (m)	1001/1000 (m)	1002/998 (w)	995 (15)	A'	989 (5)	A'
980 (m)	980 (m)	980 (m)	971 (16)	A'	979 (8)	A'
-	-	957 (w)	947 (2)	A'	952 (3)	A'
936 (vw)	-	935 (w)	928 (2)	A"	933 (2)	A"
-	-	-	919 (1)	A"	926 (1)	A"
905 (s)	905 (s)	904 (m)	903 (9)	A'	898 (10)	A'
-	-	884 (vw)	869 (1)	A'	884 (0.3)	A'
-	-	-	855 (0.02)	A"	851 (0.3)	A"
826 (vw)	826 (vw)	826 (vw)	811 (2)	A'	823 (2)	A'
788 (w)	-	787 (w)	781 (7)	A'	783 (6)	A'
-	-	779 (vw)	770 (0.2)	A"	778 (0.1)	A"
771(vw)	771 (vw)	771 (vw)	756 (1)	A'	769 (1)	A'
749 (w)	750 (vw)	748 (w)	741 (5)	A"	749 (6)	A"
-	-	662 (vw)	652 (1)	A'	668 (0.4)	A'
634 (vw)	-	634 (vw)	632 (3)	A"	628 (3)	A"
-	-	-	565 (0.3)	A'	562 (1)	A'
540 (vw)	541 (vw)	539 (w)	534 (5)	A'	537 (5)	A'

[a] Experimental intensities are given in qualitative terms: vs - very strong, s - strong, m - medium, w - weak, vw - very weak; non-observed features are indicated by a hyphen.

Table D10: Experimental IR spectra (1800-600 cm^{-1}) of the photogenerated 1,4-cyclohexanedione 5 (Ar and N2 matrices; 15 K) with the experimental IR spectrum of the authentic sample (Ar matrix; 15 K). B3LYP/6-311+G(3df,3pd) and M06-2X/6-311+G(3df,3pd) computed harmonic vibrational frequencies (cm^{-1}) and intensities (in parenthesis; km mol^{-1}) are also shown.

Photolysis of 1 Ar matrix[a]	authentic N_2 matrix[a]	authentic Ar matrix[a]	5A B3LYP	sym.	M06-2x	5B B3LYP	sym.	M06-2x
1736/1730 (vs)	1737/1734 1730/1728 1726 (vs)	1744/1737 1735/1730/1718 (vs)	1760 (458)	Bu	1806 (478)	1759 (468)	B1	1805 (494)
		1428 (w)	1459 (0)	Ag	1444 (0)	1440 (17)	B3	1427 (20)
1422 (m)	1423 (m)	1439 (m)	1454 (15)	Bu	1439 (17)	1438 (0)	A	1426 (0)
		1432/1422 (m/s)	446 (24)	Au	1432 (28)	1431 (30)	B2	1418 (31)
-	-	-	1443 (0)	Bg	1425 (0)	1429 (0.1)	B1	1414 (1)
1337 (vw)	-	1336 (w)	1338 (1)	Bu	1332 (0)	1330 (3)	B1	1320 (5)
1337 (vw)	-	1336 (w)	1337 (0)	Bg	1318 (0.4)	1328 (4)	B3	1310 (2)
1315/1313 (m)	-	1313 (m)	1300 (0)	Ag	1292 (0)	1308 (13)	B2	1307 (28)
1300/1299 (m)	1300/1299 (m)	1298/1296 (m)	1286 (40)	Au	1291 (55)	1293 (0)	A	1288 (0)
1261/1260 1244 (w)	-	1262/1260/1246 (m/w)	1250 (9)	Au	1232 (9)	1260 (28)	B2	1249 (28)
-	-	-	1226 (0)	Ag	1212 (0)	1222 (0)	A	1210 (0)
-	-	-	1197(0)	Bg	1194 (0)	1202 (1)	B3	1192 (2)
-	- 1181	(vw)	1194 (3)	Bu	1178 (3)	1169 (5)	B3	1164 (3)
1149/1147 1126/1125 (w/m)	1150/1127 (w)	1148/1146 1134/1128/1125(m)	1108 (88)	Au	1116 (69)	1115 (83)	B2	1129 (68)
-	-	-	1085(0)	Ag	1076 (0)	1070 (0.3)	B1	1056 (0.2)
1062 (w)	1063 (vw)	1062 (w)	1051 (0)	Bg	1036 (0)	1060 (10)	B2	1054 (6)
-	-	-	986 (0)	Ag	989 (0)	997 (0)	A	999 (0)
961/959 (m)	961 (m)	961/959 (m)	959 (2)	Bu	956 (1)	950 (32)	B2	948 (33)
961/959/ 940 (m/vw)	961/941 (m/vw)	961/959/940 (m/vw)	951 (11)	Au	952 (17)	933 (3)	B1	929 (2)
-	-	-	868 (10)	Au	869 (6)	857 (0)	A	849 (0)
799 (w)	780 (vw)	802 (w)	791 (15)	Bu	786 (12)	796 (10)	B3	790 (9)
-	-	-	726 (0)	Bg	731 (0)	719 (3)	B1	727 (2)
-	-	-	719 (0)	Ag	727 (0)	697 (0)	A	711 (0)
-	-	-	709 (0.1)	Bu	715 (0.3)	587 (0.1)	B3	589 (0.2)
-	-	-	590 (0)	Ag	599 (0)	533 (15)	B1	518 (15)

[a] Bands indicated in color are assigned to individual conformers (blue to 5A and green to 5B); those in black color are assigned to the both forms. Experimental intensities are given in qualitative terms: vs - very strong, s - strong, m - medium, w - weak, vw - very weak; non-observed features are indicated by a hyphen.

References

[1] E. M. Brás, L. I. L. Cabral, P. S. M. Amado, M. Abe, R. Fausto, M. L. S. Cristiano, *The Journal of Physical Chemistry A* **2020**, *124*, PMID: 32375479, 4202–4210.
[2] K. Griesbaum, X. Liu, A. Kassiaris, M. Scherer, *Liebigs Annalen* **1997**, *1997*, 1381–1390.
[3] K Griesbaum, *ChemInform* **1998**, *29*, no–no.
[4] Y. Dong, Y. Tang, J. Chollet, H. Matile, S. Wittlin, S. A. Charman, W. N. Charman, J. S. Tomas, C. Scheurer, C. Snyder, B. Scorneaux, S. Bajpai, S. A. Alexander, X. Wang, M. Padmanilayam, S. R. Cheruku, R. Brun, J. L. Vennerstrom, *Bioorganic Medicinal Chemistry* **2006**, *14*, Tetrahedron Prize for Creativity in Organic Chemistry 2005: B. Giese, 6368–6382.
[5] R. Krishnan, J. S. Binkley, R. Seeger, J. A. Pople, *The Journal of chemical physics* **1980**, *72*, 650–654.